

## DYNAMIC STABILITY OF A THREE-LAYER BEAM – GENERALISATION OF THE SANDWICH STRUCTURE THEORY

Krzysztof MAGNUCKI\*<sup>✉</sup>, Ewa MAGNUCKA-BLANDZI\*\*<sup>✉</sup>

\*Łukasiewicz Research Network - Poznan Institute of Technology, 6 Ewarysta Estkowskiego St. 61-755 Poznan, Poland

\*\*Institute of Mathematics, Poznan University of Technology, ul. Piotrowo 3a, 60-965 Poznan, Poland

krzysztof.magnucki@pit.lukasiewicz.gov.pl, ewa.magnucka-blandzi@put.poznan.pl

received 12 November 2022, revised 24 May 2023, accepted 30 May 2023

**Abstract:** The work focuses on the dynamic stability problem of a simply supported three-layer beam subjected to a pulsating axial force. Two analytical models of this beam are developed: one model takes into account the non-linear hypothesis of cross-section deformation, and the other takes into account the standard "broken line" hypothesis. Displacements, strains and stresses for each model are formulated in detail. Based on the Hamilton principle, equations of motion are determined for each of these models. These systems of two differential equations for each model are approximately solved with the consideration of the axial pulsating force, and the fundamental natural frequencies, critical forces and the Mathieu equation are determined. Detailed studies are performed for an exemplary family of beams. The stable and unstable regions are calculated for the three pulsating load cases. The values of fundamental natural frequencies and critical forces of exemplary beams calculated from two models are compared.

**Key words:** three-layer beam, fundamental natural frequency, unstable regions, mathematical modelling, shear effect

### 1. INTRODUCTION

Sandwich constructions initiated in the mid-twentieth century have been intensively improved and are being used in aerospace, automotive, railway and shipbuilding industries. There are many scientific and research works on stability and free vibrations of sandwich beams. Ray and Kar [1] presented the parametric instability of a three-layer symmetrical sandwich beam subjected to periodic axial loading. Nine different boundary conditions were considered. The influence of the shear parameter on static buckling loads was considered, and the influence of the shear parameter and the core thickness parameter on the areas of parametric instability was investigated. Yeh et al. [2] studied the problem of dynamic stability of a sandwich beam with an electrorheological liquid core subjected to an axial dynamic force. The influence of natural frequency, static buckling loads and loss factors on the dynamic stability of a sandwich beam was investigated. In addition, the areas of instability of the studied beam were calculated using the harmonic balance method and the finite element method. Yang et al. [3] used the finite element method to study the vibration and dynamic stability of a moving sandwich beam. It was assumed that the damping layer is linearly viscoelastic and almost incompressible. Taking into account the numerical results, it was shown that the forced damping layer stabilises the movable layered beam. Lin and Chen [4] used the finite element method to study the problems of dynamic stability of spinning pre-twisted sandwich beams with a limited damping layer, subjected to periodic axial loads. For a viscoelastic material, a complex representation of the modulus was used. The influence of the pre-twisted angles, spinning speed, core thickness, shear parameter, core loss factor and constraint layer stiffness on unstable regions was discussed. Many different plate theories

were described by Carrera and Brischetto [5]. Bending and vibration of sandwich structures were assessed. The kinematics of the classical and other theories (higher order, zigzag, layered and mixed) were described. Reddy [6] reformulated the classical and shear theories of beam and plate deformations using non-local differential Eringen constitutive relations and non-linear von Karman strains. Theoretical studies described in the article can be used to determine the influence of geometric non-linearity and non-local constitutive relations on the bending response. Misiurek [7] studied the dynamic response of a finite, simply supported sandwich beam subjected to a force moving at a constant speed. The main goal of the work was to show that the aperiodic part of the solution can be presented in a closed form, instead of an infinite form (an infinite series). Based on the Tymoshenko beam theory, Chen et al. [8] studied the behaviour of non-linear natural vibrations of a porous sandwich beam deformable under the influence of shear. The beam consisted of two facing layers and a functionally graded porous core, which contains internal pores with different porosity distributions. The authors assumed that the elastic modulus and mass density change along the thickness direction in terms of porosity coefficients and mass density. Grygorowicz and Magnucka-Blandzi [9] described the static and dynamic stability of a simply supported sandwich beam with a metal foam core. Mathematical modelling of the problem was presented. The displacement field was formulated based on the broken line hypothesis and the assumed non-linear hypothesis. Using the Hamilton principle, the equations of motion were obtained. Critical loads, areas of instability, natural frequencies of the beam and static and dynamic equilibrium paths were calculated analytically and verified numerically. Kolakowski and Teter [10] reviewed papers on static and dynamic buckling and post-buckling behaviours of thin-walled structures. Based on the analytical-numerical method, the static buckling stresses, natural

frequencies, equation coefficients describing the post-buckling equilibrium path and the dynamic response of the plate structure subjected to a compressive load and/or bending moment were determined. In addition, all buckling modes and post-buckling behaviour of thin-walled columns made of different materials were described. Sayyad and Ghugal [11] developed a unified shear deformation theory for the analysis of shear-deformable composite beams and plates. To account for the transverse shear deformation effect, the authors expanded the theory with different shape functions (parabolic (PSDT), trigonometric (TSDT), hyperbolic (HSDT) and exponential (ESDT)) in terms of thickness coordinates. To verify the accuracy and effectiveness of the authors' theory, the obtained results were compared with the exact elasticity solution and other higher order shear deformation theories. Sayyad and Ghugal [12] provided a critical literature review on bending, buckling and free vibration analysis of isotropic, laminated and shear-deformable beams based on equivalent theories (single-layer theories, layer-wise theories, zig-zag theories and exact elastic solution). In addition, the literature on finite element modelling of laminated and sandwich beams was reviewed based on classical and refined theories. Finally, for reference to researchers of the subject, the displacement fields of various equivalent single-layer and layer-wise theories were summarised. Based on the Grigolyuk-Chulkov hypothesis and the modified couple stress theory, Avrejcewicz et al. [13] developed a mathematical model of three-layer beams. The authors took into account the movements of the layers at the micro- and the nano-scale. Based on the Hamilton principle, the equations of motion and the boundary/initial conditions for the displacement of the beams were obtained. Smyczyński and Magnucka-Blandzi [14] considered the stability analysis of a simply supported five-layer beam. The beam consisted of two facings, a core and two tie layers between the facings and the core. Based on the Hamilton principle and the formulated non-linear hypothesis of beam cross-section deformation, a system of four stability equations was derived. Then, the system was approximately solved, and critical loads, free vibrations and areas of instability were determined. Sayyad and Ghugal [15] used the theory of trigonometric shear and normal strain to study the bending, buckling and vibration responses of shear-deformable composite laminated beams and sandwich beams. The main goal of this theory was to take into account the effects of transverse shear and normal strain. According to this theory, the shear stresses on the top and bottom surfaces were equal to zero (zero shear stress conditions were met without applying a shear correction factor). Numerical results for deflections, stresses, natural frequencies and critical buckling loads for isotropic, laminated and sandwich beams were presented. Magnucka-Blandzi and Magnucki [16] presented a mathematical model of a simply supported sandwich beam subjected to three-point bending. To describe the problem, the authors adopted the appropriate hypothesis of flat cross-section deformation. An important feature of this analytical beam model was that it included the shear effect of the facings and was reduced to a classic sandwich beam described by two differential equilibrium equations. Al-shujairi and Mollamahmutoglu [17] studied the dynamic stability of a functionally graded (FG) size-dependent layered microbeam subjected to parametric axial excitation. The authors considered various boundary conditions, including thermal effects. The material properties of the FG part of the multilayer microbeam varied depending on the thickness of the beam. The problem was solved numerically. The original contribution to the article was to determine the parametric instability regions of the FG microbeam under different

boundary conditions and with different effects. In a review, Birman and Kardomateas [18] described contemporary trends in theoretical developments, innovative designs and modern applications of layered structures. Examples of problems faced by engineers and designers of sandwich structures were considered, including typical failures, responses to various loads, environmental effects and fire. Example applications of sandwich structures were concentrated in the aerospace, civil and marine engineering, electronics and biomedicine industries. Li et al. [19] discussed the non-linear amplitude-frequency response and the unstable boundary and the dynamic responses of an axially moving viscoelastic layer beam at low- and high-frequency fundamental resonances and compared them. Sayyad and Ghugal [20] presented a literature review on the modelling and analysis of functionally graded sandwich beams using the theory of elasticity, analytical methods and numerical methods based on classical and refined theories of shear deformation, citing 250 references. In addition, suggestions for future research into the analysis of functionally graded sandwich beams were made. Sayyad and Ghugal [21] presented an analysis of the static behaviour of curved FG sandwich beams. For the bending analysis of vertically curved beams, the sinusoidal beam theory was used, taking into account the influence of transverse normal stresses/strains. Sayyad and Avhad [22] presented closed form Navier-type solutions for static bending, elastic buckling and free vibration analysis of functionally graded (FG) symmetrical layered beams using the theory of deformation under hyperbolic shear. Eloy et al. [23] investigated numerically and experimentally sandwich panels with carbon-epoxy composite coatings and a magnetorheological elastomer honeycomb core. Based on the results, it was noticed that the honeycomb sandwich panel shifted the natural frequencies due to the increase of the induced magnetic field, especially for the shape of the first mode. Chen et al. [24] extended the model of a higher order shear-deformable mixed beam element with a rational distribution of shear stresses to the vibration analysis of functionally graded beams. The authors discussed the load-frequency relationship of functionally graded sandwich beams. The results showed that in addition to the axial force, the bending moment exerted a significant difference in the vibration frequency of the functionally graded beams. Tewelde and Krawczuk [25] presented a review of the literature on non-linear effects caused by the closure of cracks in the structure, i.e. beam and plate structures. After analysing various methods, the advantages, disadvantages and perspectives of a number of non-linear vibration methods for detecting structural damage were discussed. In addition, recommendations were made for future researchers.

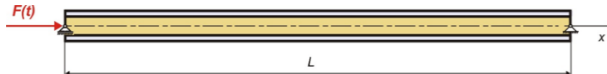


Fig. 1. Scheme of the beam subjected to a pulsating axial force

The subject of the study is a simply supported three-layer beam of length  $L$ , width  $b$  and total depth  $h$  subjected to a pulsating axial force  $F$  (Fig. 1). A novelty in this work is the individual hypothesis-theory of deformation of the plane cross section, which is assumed for beam modelling taking into account the shear effect in layers. The main purpose of the work is to analytically determine the fundamental natural frequencies, critical loads and unstable regions of this beam. This work is a continuation/development of the study presented in the proceedings of the

8th International Conference on Coupled Instabilities in Metal Structures [26].

## 2. MATHEMATICAL MODEL OF THE BEAM

A non-linear hypothesis of a planar cross-section deformation is assumed. This hypothesis takes into account the shear effect in each layer of this beam and is a generalisation of the standard "broken line" hypothesis. The deformation shape of the planar cross section is a curved line perpendicular to the outer surfaces of the beam (Fig. 2). Thus, this hypothesis satisfies the necessary condition of zeroing the shear stresses on these surfaces.

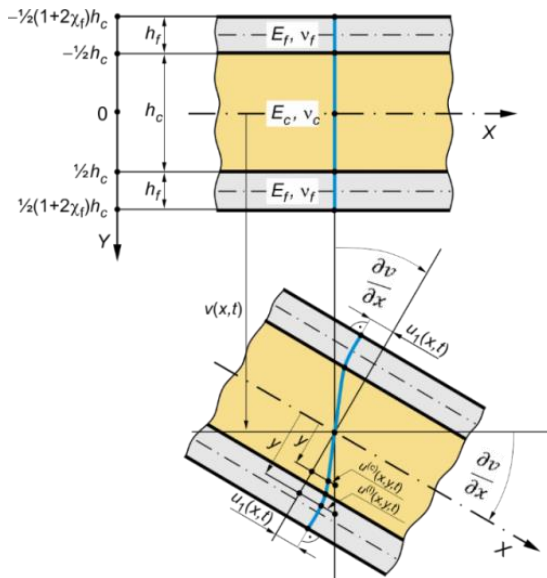


Fig. 2. Scheme of the deformation of a planar cross section of the three-layer beam – the non-linear hypothesis

The total height of the beam equals

$$h = 2h_f + h_c,$$

where  $h_f, h_c$  denote thicknesses of the outer layers and the middle layer (core), respectively.

Moreover, the following notation is introduced:

- $\eta = y/h_c$  – dimensionless coordinate,
- $\tilde{u}_1(x, t) = u_1(x, t)/h_c$  – dimensionless displacement,
- $\chi_f = h_f/h_c$  – parameter,
- $k_f \in \langle 0, 1 \rangle$  – coefficient (real number),
- $\beta_c \in \langle 0, 1 \rangle$  – coefficient (real number),
- $E_f, E_c$  – Young modulus of facings and core,
- $\nu_f, \nu_c$  – Poisson ratio of facings and core,
- $\rho_f, \rho_c$  – mass densities of facings and core.

So, the total mass density of the beam is as follows:

$$\rho_b = \rho_c + 2\rho_f\chi_f.$$

Based on the assumed theory, longitudinal displacements are formulated separately for each layer, i.e. for

$$\text{upper layer: } -(1 + 2\chi_f)/2 \leq \eta \leq -1/2$$

$$u^{(u)}(x, y, t) = -h_c \left[ \eta \frac{\partial v}{\partial x} + f_d^{(u)}(\eta) \tilde{u}_1(x, t) \right], \quad (1)$$

where

$$f_d^{(u)}(\eta) = \left\{ - \left[ 3 - 4 \left( \frac{\eta}{1+2\chi_f} \right)^2 \right] \frac{\eta}{1+2\chi_f} \right\}^{k_f},$$

middle layer (core):  $-1/2 \leq \eta \leq 1/2$

$$u^{(c)}(x, y, t) = -h_c \left[ \eta \frac{\partial v}{\partial x} - 2f_d^{(c)}(\eta) \tilde{u}_1(x, t) \right], \quad (2)$$

where

$$f_d^{(c)}(\eta) = c_f \frac{3-4\beta_c\eta^2}{3-\beta_c} \eta, \quad c_f = \left[ \frac{1+6(1+\chi_f)\chi_f}{(1+2\chi_f)^3} \right]^{k_f},$$

lower layer:  $1/2 \leq \eta \leq (1 + 2\chi_f)/2$

$$u^{(l)}(x, y, t) = -h_c \left[ \eta \frac{\partial v}{\partial x} - f_d^{(l)}(\eta) \tilde{u}_1(x, t) \right], \quad (3)$$

where

$$f_d^{(l)}(\eta) = \left\{ 3 - 4 \left( \frac{\eta}{1+2\chi_f} \right)^2 \right\} \frac{\eta}{1+2\chi_f}^{k_f}.$$

The non-linear deformation functions  $f_d^{(u)}(\eta)$ ,  $f_d^{(c)}(\eta)$  and  $f_d^{(l)}(\eta)$  existing in these expressions are developed taking into account the conditions of continuity between layers and conditions of perpendicularity to the outer surfaces of the beam.

A linear relationship between strains and displacements is assumed, so the strains for each layer are as follows:

$$\varepsilon_x = \frac{\partial u}{\partial x}, \quad \gamma_{xy} = \frac{\partial v}{\partial x} + \frac{\partial u}{h_c \partial \eta}.$$

Then, taking into account the aforementioned expressions and expressions (1)–(3), the strains are determined.

Hence, the stresses are determined by using the following formulas:

$$\text{upper layer: } -(1 + 2\chi_f)/2 \leq \eta \leq -1/2$$

$$\sigma_x^{(u)} = E_f \cdot \varepsilon_x^{(u)}, \quad \tau_{xy}^{(u)} = \frac{E_f}{2(1+\nu_f)} \cdot \gamma_{xy}^{(u)},$$

middle layer (core):  $-1/2 \leq \eta \leq 1/2$

$$\sigma_x^{(c)} = E_c \cdot \varepsilon_x^{(c)}, \quad \tau_{xy}^{(c)} = \frac{E_c}{2(1+\nu_c)} \cdot \gamma_{xy}^{(c)},$$

lower layer:  $1/2 \leq \eta \leq (1 + 2\chi_f)/2$

$$\sigma_x^{(l)} = E_f \cdot \varepsilon_x^{(l)}, \quad \tau_{xy}^{(l)} = \frac{E_f}{2(1+\nu_f)} \cdot \gamma_{xy}^{(l)}.$$

Then, the elastic strain energy

$$\begin{aligned} U_\varepsilon &= \frac{1}{2} b h_c \cdot \\ &\cdot \int_0^L \left\{ E_f \int_{-\frac{1}{2}+2\chi_f}^{-\frac{1}{2}} \left\{ [\varepsilon_x^{(u)}]^2 + \frac{1}{2(1+\nu_f)} [\gamma_{xy}^{(u)}]^2 \right\} d\eta \right\} dx + \\ &+ E_c \int_{-\frac{1}{2}}^{\frac{1}{2}} \left\{ [\varepsilon_x^{(c)}]^2 + \frac{1}{2(1+\nu_c)} [\gamma_{xy}^{(c)}]^2 \right\} d\eta + \\ &+ E_f \int_{\frac{1}{2}}^{\frac{1+2\chi_f}{2}} \left\{ [\varepsilon_x^{(l)}]^2 + \frac{1}{2(1+\nu_f)} [\gamma_{xy}^{(l)}]^2 \right\} d\eta \right\} dx, \end{aligned}$$

the kinetic energy

$$T = \frac{1}{2} (2\rho_f\chi_f + \rho_c) b h_c \int_0^L \left( \frac{\partial v}{\partial t} \right)^2 dx,$$

the work of the load

$$W = \frac{1}{2} F \int_0^L \left( \frac{\partial v}{\partial x} \right)^2 dx$$

are derived.

Based on the Hamilton principle,

$$\delta \int_{t_1}^{t_2} [T - (U_\varepsilon - W)] dt = 0, \quad (4)$$

two differential equations of motion are obtained in the following form:

$$\begin{cases} \rho_b b h_c \frac{\partial^2 v}{\partial t^2} + E_c b h_c^3 \left( C_{vv} \frac{\partial^4 v}{\partial x^4} - C_{vu} \frac{\partial^3 \tilde{u}_1}{\partial x^3} \right) + \frac{\partial^2 v}{\partial x^2} F(t) = 0 \\ C_{vu} \frac{\partial^3 v}{\partial x^3} - C_{uu} \frac{\partial^2 \tilde{u}_1}{\partial x^2} + C_u \frac{\tilde{u}_1(x, t)}{h_c^2} = 0 \end{cases} \quad (5)$$

where  $C_{vv}$ ,  $C_{vu}$ ,  $C_{uu}$  and  $C_u$  are – dimensionless coefficients.

These coefficients are as follows:

$$C_{vv} = \frac{1}{12} [1 + 2e_f (3 + 6\chi_f + 4\chi_f^2) \chi_f],$$

$$C_{vu} = \frac{1}{10} [c_f \frac{5-\beta_c}{3-\beta_c} + 20e_f I_1],$$

$$C_{uu} = 2e_f I_2 + \frac{c_f^2}{35} (105 - 42\beta_c + 5\beta_c^2),$$

$$C_u = \frac{e_f}{1+v_f} I_3 + \frac{6}{5(1+v_f)} c_f^2 \frac{15-10\beta_c+3\beta_c^2}{(3-\beta_c)^2},$$

where

$$e_f = \frac{E_f}{E_c}, \quad I_1 = \int_{\frac{1}{2}}^{\frac{1}{2}+\chi_f} \eta f_d^{(l)}(\eta) d\eta,$$

$$I_2 = \int_{\frac{1}{2}}^{\frac{1}{2}+\chi_f} [f_d^{(l)}(\eta)]^2 d\eta,$$

$$I_3 = \int_{\frac{1}{2}}^{\frac{1}{2}+\chi_f} \left[ \frac{df_d^{(l)}}{d\eta} \right]^2 d\eta.$$

### 3. NATURAL FREQUENCY AND UNSTABLE REGIONS

The system of two differential equations (5) is approximately solved with the use of two assumed functions:

$$v(x, t) = v_a(t) \sin \left( \pi \frac{x}{L} \right), \quad \tilde{u}_1(x, t) = \tilde{u}_{1a}(t) \cos \left( \pi \frac{x}{L} \right), \quad (6)$$

where  $v_a(t)$  and  $\tilde{u}_{1a}(t)$  are time-dependent functions.

These functions identically satisfy the boundary conditions:

$$v(0, t) = v(L, t) = 0, \quad \frac{d\tilde{u}_1}{dx} \Big|_{x=0} = \frac{d\tilde{u}_1}{dx} \Big|_{x=L} = 0.$$

The loading force – the pulsating force – is in the following form:

$$F(t) = F_m + F_a \cos(\theta t), \quad (7)$$

where  $F_m$ ,  $F_a$  and  $\theta$  are mean value, amplitude and frequency of the force, respectively. Substituting functions (6) and (7) into equation (5), and after a simply transformation, the Mathieu equation is obtained:

$$\frac{d^2 v_a}{dt^2} + \Omega^2 [1 - 2\mu \cos(\theta t)] v_a(t) = 0, \quad (8)$$

where

$$v_a(t) = \bar{v}_a \sin(\omega t), \quad v_a \text{ – deflection amplitude},$$

$$\Omega^2 = \omega^2 (1 - \alpha_m), \quad \mu = \frac{1}{2} \cdot \frac{\alpha_a}{1 - \alpha_m},$$

$$\alpha_m = \frac{F_m}{F_{CR}}, \quad \alpha_a = \frac{F_a}{F_{CR}},$$

$$\omega^2 = \left( \frac{\pi}{\lambda} \right)^4 \frac{10^{12}}{(1+2\chi_f)^2} (1 - C_{sv}) C_{vv} \frac{E_c}{\rho_b h^2},$$

$$F_{CR} = \left( \frac{\pi}{\lambda} \right)^2 (1 - C_{sv}) \frac{C_{vv}}{(1+2\chi_f)^3} E_c b h,$$

$$C_{sv} = \max_{\beta_c, k_f} \left\{ \frac{\pi^2}{C_{vv}} \cdot \frac{C_{vu}^2}{\pi^2 C_{uu} + \lambda_c^2 C_u} \right\}, \quad \lambda_c = \frac{L}{h_c}.$$

Using the aforementioned notations, unstable regions can be described by the following inequalities:  
the first unstable region

$$2\Omega \sqrt{1 - \mu} \leq \theta \leq 2\Omega \sqrt{1 + \mu}, \quad (9)$$

the second unstable region

$$\Omega \sqrt{1 - 2\mu^2} \leq \theta \leq \Omega \sqrt{1 + \frac{1}{3}\mu^2}. \quad (10)$$

### Sample Calculations

Detailed studies are carried out for an exemplary family of three-layer beams. Stable and unstable regions are calculated for the three load cases – pulsating forces.

The geometric dimensions of the beams are as follows:

$h = 20$  mm – total depth,

$L = 600$  mm – length,

$\lambda = L/h = 30$  – relative length,

and the following mechanical properties are considered:

$E_f = 65\,000$  MPa – Young modulus in facings,

$\nu_f = 0.33$  – Poisson ratio in facings,

$E_c = 1\,200$  MPa – Young modulus in the core,

$\nu_c = 0.3$  – Poisson ratio in the core,

$\rho_f = 2\,600$  kg/m<sup>3</sup> – mass density in facings,

$\rho_c = 350$  kg/m<sup>3</sup> – mass density in the core.

The fundamental natural frequency

$$\omega = \left( \frac{\pi}{\lambda} \right)^2 \frac{10^6}{1+2\chi_f} \sqrt{(1 - C_{sv}) C_{vv} \frac{E_c}{\rho_b h^2}}, \quad (11)$$

and the dimensionless critical force

$$\tilde{F}_{CR} = \frac{F_{CR}}{E_c b h} = \left( \frac{\pi}{\lambda} \right)^2 (1 - C_{sv}) \frac{C_{vv}}{(1+2\chi_f)^3}, \quad (12)$$

are calculated and specified in Tab. 1.

**Tab. 1.** Dimensionless coefficients  $\beta_c$ ,  $k_f$ , shear coefficient  $C_{sv}$ , fundamental natural frequency  $\omega$  and dimensionless critical force  $\tilde{F}_{CR}$

$\chi_f$	$\frac{1}{18}$	$\frac{2}{16}$	$\frac{3}{14}$	$\frac{4}{12}$	$\frac{5}{10}$
$\beta_c$	0.1097	0.06230	0.04127	0.02798	0.01847
$k_f$	0.07041	0.04187	0.03263	0.02862	0.02698
$C_{sv}$	0.03488	0.05871	0.07476	0.08358	0.08552
$\omega \left[ \frac{1}{s} \right]$	881.8	976.3	987.5	969.9	941.2
$\tilde{F}_{CR}$	0.01359	0.02318	0.03038	0.03575	0.03971

Three load cases are taken into account (LC-1, LC-2, LC-3) – according to the parameter values given in Tab. 2.

**Tab. 2.** Dimensionless coefficients, natural frequency and dimensionless critical force ( $\lambda = 30$ )

Load case	LC-1	LC-2	LC-3
$\alpha_a$	0.5	1.0	1.5
$\alpha_m$	0.5	0.25	0.1
$\mu$	1/2	2/3	5/6

Then, the following unstable regions are determined for the following:

- first load case LC-1 (Fig. 3)
  - the first unstable region (9):

$$\omega \leq \theta \leq \sqrt{3} \cdot \omega,$$

- the second unstable region (10):

$$\frac{1}{2} \cdot \omega \leq \theta \leq \frac{1}{2} \sqrt{\frac{13}{6}} \cdot \omega,$$

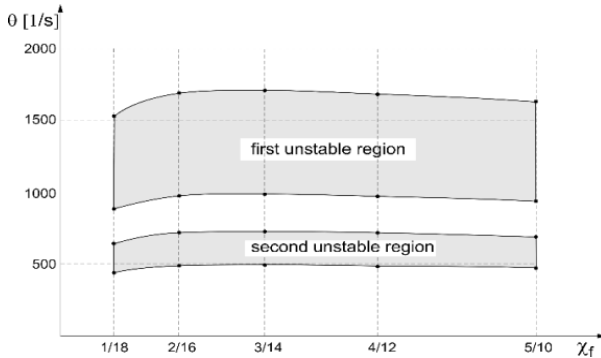


Fig. 3. Unstable regions for the first load case (LC-1)

- second load case LC-2 (Fig. 4)
  - the first unstable region (9):

$$\omega \leq \theta \leq \sqrt{5} \cdot \omega,$$

- the second unstable region (10):

$$\frac{\sqrt{3}}{6} \cdot \omega \leq \theta \leq \frac{\sqrt{31}}{6} \cdot \omega,$$

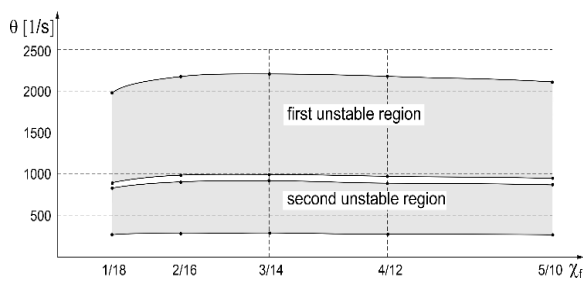


Fig. 4. Unstable regions for the second load case (LC-2)

- third load case LC-3 (Fig. 5)
  - the first unstable region (9)

$$\frac{\sqrt{15}}{5} \cdot \omega \leq \theta \leq \frac{\sqrt{165}}{5} \cdot \omega,$$

- the second unstable region does not exist (10).

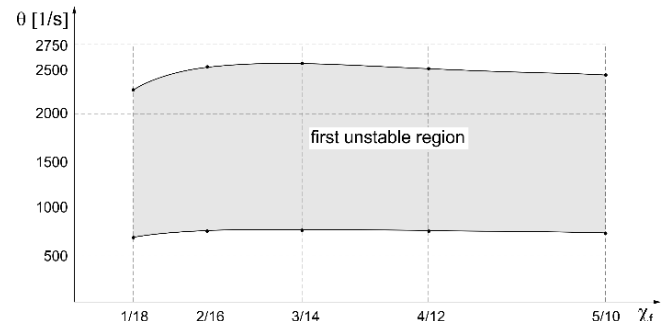


Fig. 5. Unstable regions for the third load case (LC-3)

#### 4. CLASSICAL MODEL OF THE BEAM

The classical beam model is a particular case of the beam model presented in Section 2, i.e. it is a simplification of the mathematical model. Therefore, the deformation of the plane cross section of the sandwich beam, taking into account the “broken line” hypothesis-theory, is shown in Fig. 6.

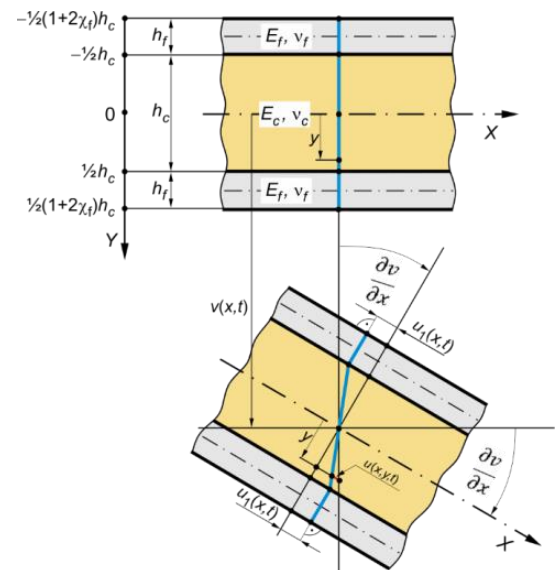


Fig. 6. Scheme of the deformation of a plane cross section of the beam – the standard “broken line” hypothesis-theory

Thus, the displacements, strains and stresses in the successive layers of the beam are as follows:

- upper layer:  $-(1 + 2\chi_f)/2 \leq \eta \leq -1/2$

$$u^{(u)}(x, y, t) = -h_c \left[ \eta \frac{\partial v}{\partial x} + \tilde{u}_1(x, t) \right] \quad (13)$$

$$e_x^{(u)}(x, y, t) = -h_c \left[ \eta \frac{\partial^2 v}{\partial x^2} + \frac{\partial \tilde{u}_1}{\partial x} \right], \quad \gamma_{xy}^{(u)}(x, y, t) = 0 \quad (14)$$

$$\sigma_x^{(u)}(x, y, t) = -E_f h_c \left[ \eta \frac{\partial^2 v}{\partial x^2} + \frac{\partial \tilde{u}_1}{\partial x} \right], \quad \tau_{xy}^{(u)}(x, y, t) = 0 \quad (15)$$

- core:  $-1/2 \leq \eta \leq 1/2$

$$u^{(c)}(x, y, t) = -h_c \eta \left[ \frac{\partial v}{\partial x} - 2\tilde{u}_1(x, t) \right] \quad (16)$$

$$\varepsilon_x^{(c)}(x, y, t) = -h_c \eta \left[ \frac{\partial^2 v}{\partial x^2} - 2 \frac{\partial \tilde{u}_1}{\partial x} \right], \quad \gamma_{xy}^{(c)}(x, t) = 2\tilde{u}_1(x, t) \quad (17)$$

$$\sigma_x^{(c)}(x, y, t) = -E_c h_c \eta \left[ \frac{\partial^2 v}{\partial x^2} - 2 \frac{\partial \tilde{u}_1}{\partial x} \right], \quad (18)$$

$$\tau_{xy}^{(c)}(x, t) = \frac{E_c}{1+v_c} \tilde{u}_1(x, t)$$

– lower layer:  $1/2 \leq \eta \leq 1/2 + \chi_f$

$$u^{(l)}(x, y, t) = -h_c \left[ \eta \frac{\partial v}{\partial x} - \tilde{u}_1(x, t) \right] \quad (19)$$

$$\varepsilon_x^{(l)}(x, y, t) = -h_c \left[ \eta \frac{\partial^2 v}{\partial x^2} - \frac{\partial \tilde{u}_1}{\partial x} \right], \quad \gamma_{xy}^{(l)}(x, y, t) = 0, \quad (20)$$

$$\sigma_x^{(l)}(x, y, t) = -E_f h_c \left[ \eta \frac{\partial^2 v}{\partial x^2} - \frac{\partial \tilde{u}_1}{\partial x} \right], \quad \tau_{xy}^{(l)}(x, y, t) = 0. \quad (21)$$

Based on the Hamilton principle (4), two differential equations of motion are obtained in form (5), where dimensionless coefficients of a sandwich beam are as follows:

$$C_{vv} = \frac{1}{12} [1 + 2e_f \chi_f (3 + 6\chi_f + 4\chi_f^2)],$$

$$C_{vu} = \frac{1}{6} [1 + 6e_f \chi_f (1 + \chi_f)],$$

$$C_{uu} = \frac{1}{3} (1 + 6e_f \chi_f), \quad C_u = \frac{2}{1+v_c}, \quad e_f = \frac{E_f}{E_c}, \quad \chi_f = \frac{h_f}{h_c}.$$

The fundamental natural frequency  $\omega$  [1/s] and the dimensionless critical force  $\tilde{F}_{CR}$  have identical forms (11) and (12), where the dimensionless coefficient is as follows:

$$C_{sv} = \frac{\pi^2}{C_{vv}} \cdot \frac{C_{vu}^2}{\pi^2 C_{uu} + \lambda_c^2 C_u}.$$

Detailed calculations are performed for sample data from section 4. The values of the dimensionless coefficient  $C_{sv}$ , the fundamental natural frequency  $\omega$  [1/s] and the dimensionless critical force  $\tilde{F}_{CR}$  are specified in Tab. 3.

**Tab. 3.** Results of analytical calculations of the exemplary beams

$\chi_f$	$\frac{1}{18}$	$\frac{2}{16}$	$\frac{3}{14}$	$\frac{4}{12}$	$\frac{5}{10}$
$C_{sv}$	0.03534	0.05927	0.07519	0.08374	0.08531
$\omega \left[ \frac{1}{s} \right]$	881.6	976.0	987.2	969.9	941.3
$\tilde{F}_{CR}$	0.01358	0.02316	0.03037	0.03574	0.03972

As a result of comparing the values of the fundamental natural frequencies  $\omega$  [1/s] and the dimensionless critical forces  $\tilde{F}_{CR}$  calculated based on the generalised model (Tab. 1) and the classical sandwich beam model (Tab. 3), it is easy to see that these differences are negligible. Thus, the unstable regions calculated with consideration of two models of sandwich beams are identical.

## 5. CONCLUSIONS

Summing up the research presented in this article, the following conclusions can be drawn:

- the assumed non-linear hypothesis-theory of deformation of a plane cross section of the beam takes into account the shear effect in the facings, so it is a generalisation of the "broken

line" hypothesis, in which the shear effect in the facings is omitted,

- the influence of the shear effect in the beam facings on the values of the fundamental natural frequency  $\omega$  and the critical load-force  $\tilde{F}_{CR}$  is negligibly small, which is easy to see when comparing their values specified in Tabs 1 and 3,
- the influence of the three-layer beam structure, i.e. the ratio of the thickness of the facings to the thickness of the core (value of the parameter  $\chi_f$ ), on the values of the fundamental natural frequency  $\omega$  and the critical load force  $\tilde{F}_{CR}$  is significant (Tabs 1 and 3), which is graphically presented in Figs 7 and 8.



**Fig. 7.** Fundamental natural frequency

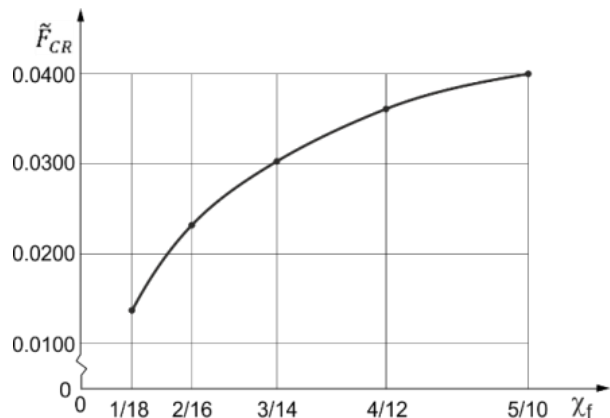


**Fig. 8.** Critical load-force

Therefore, based on the aforementioned, it can be concluded that when examining critical loads, fundamental natural frequencies and unstable regions, it is sufficient to apply the "broken line" hypothesis.

## REFERENCES

1. Ray KR, Kar C. Parametric instability of a sandwich beam under various boundary conditions. *Computers & Structures*. 1995;55(5): 857-870.
2. Yeh J-Y, Chen L-W, Wang C-C. Dynamic stability of a sandwich beam with a constrained layer and electrorheological fluid core. *Composite Structures*. 2004;64(1):47-54.
3. Yang W-P, Chen L-W, Wang C-C. Vibration and dynamic stability of a traveling sandwich beam. *Journal of Sound and Vibration*. 2005;285(3):597-614.

4. Lin C-Y, Chen L-W. Dynamic stability of spinning pre-twisted sandwich beams with a constrained damping layer subjected to periodic axial loads. *Composite Structures*. 2005;70(3):275-286.
5. Carrera E, Brischetto S. A survey with numerical assessment of classical and refined theories for the analysis of sandwich plates. *Applied Mechanics Reviews*. 2009;62:01080-1-17
6. Reddy JN. Nonlocal nonlinear formulations for bending of classical and shear deformation theories of beams and plates. *International Journal of Engineering Science*. 2010;48:1507-1518.
7. Misiurek K, Śniady P. Vibrations of sandwich beam due to a moving force. *Composite Structures*. 2013;104:85-93.
8. Chen D, Kitipornchai S, Yang J. Nonlinear free vibration of shear deformable sandwich beam with a functionally graded porous core. *Thin-Walled Structures*. 2016;107:39-48.
9. Grygorowicz M, Magnucka-Blandzi E. Mathematical modeling for dynamic stability of sandwich beam with variable mechanical properties of core. *Applied Mathematics and Mechanics*. 2016;37(10):1361-1374.
10. Kolakowski Z, Teter A. Coupled static and dynamic buckling modeling of thin-walled structures in elastic range: Review of selected problems. *Acta Mechanica et Automatica*. 2016;10(2):141-149.
11. Sayyad AS, Ghugal YM. A unified shear deformation theory for the bending of isotropic, functionally graded, laminated and sandwich beams and plates. *International Journal of Applied Mechanics*. 2017;9(1):1750007.
12. Sayyad AS, Ghugal YM. Bending, buckling and free vibration of laminated composite and sandwich beams: A critical review of literature. *Composite Structures*. 2017;171:486-504.
13. Awrejcewicz J, Krysko VA, Pavlov SP, Zhigalov MV, Krysko AV. Mathematical model of a three-layer micro- and nano-beams based on the hypotheses of the Grigolyuk-Chulkov and the modified couple stress theory. *International Journal of Solids and Structures*. 2017;117:39-50.
14. Smyczynski M, Magnucka-Blandzi E. Stability and free vibrations of the three layer beam with two binding layers. *Thin-Walled Structures*. 2017;113:144-150.
15. Sayyad AS, Ghugal YM. Effect of thickness stretching on the static deformations, natural frequencies, and critical buckling loads of laminated composite and sandwich beams. *Journal of the Brazilian Society of Mechanical Sciences and Engineering*. 2018;40(6):No 296.
16. Magnucka-Blandzi E, Magnucki K. Mathematical modelling of a sandwich beam with consideration of the shear effect in the faces – three-point bending. Eighth International Conference of Thin-Walled Structures – ICTWS 2018, Lisbon, Portugal, 24-27 July, 2018.
17. Al-shujairi M, Mollamahmutoğlu Ç. Dynamic stability of sandwich functionally graded micro-beam based on the nonlocal strain gradient theory with thermal effect. *Composite Structures*. 2018;201: 1018-1030.
18. Birman V, Kardomateas GA. Review of current trends in research and applications of sandwich structures. *Composites Part B: Engineering*. 2018;142:221-240.
19. Li YH, Dong YH, Qin Y, Lv HW. Nonlinear forced vibration and stability of an axially moving viscoelastic sandwich beam. *International Journal of Mechanical Sciences*. 2018;138-139:131-145.
20. Sayyad AS, Ghugal YM. Modeling and analysis of functionally graded sandwich beams: A review. *Mechanics of Advanced Materials and Structures*. 2019;26(21):1776-1795.
21. Sayyad AS, Ghugal YM. A sinusoidal beam theory for functionally graded sandwich curved beams. *Composite Structures*. 2019;226:111246.
22. Sayyad AS, Avhad PV. On static bending, elastic buckling and free vibration analysis of symmetric functionally graded sandwich beams. *Journal of Solid Mechanics*. 2019;11(1):166-180.
23. Eloy FS, Gomes GF, Ancialetti Jr. AC, Cunha Jr. SS, Bombard AJF, Junqueira DM. A numerical-experimental dynamic analysis of composite sandwich beam with magnetorheological elastomer honeycomb core. *Composite Structures*. 2019;209:242-257.
24. Chen S, Geng R, Li W. Vibration analysis of functionally graded beams using a higher-order shear deformable beam model with rational shear stress distribution. *Composite Structures*. 2021;277:114586.
25. Tewelde SA, Krawczuk M. Nonlinear vibration analysis of beam and plate with closed crack: A review. *Acta Mechanica et Automatica*. 2022;16(3):274-285.
26. Magnucki K., Magnucka-Blandzi E. Dynamic stability of a three-layer beam – Generalization of the sandwich structures theory. *Proceedings of the 8th International Conference on Coupled Instabilities in Metal Structures*, Lodz University of Technology, Poland, July 12-14, 2021.

"The paper is developed based on the scientific activity of the Łukasiewicz Research Network – Poznan Institute of Technology, Rail Vehicles Center, and the scientific activity of the Institute of Mathematics, Poznan University of Technology".

Krzysztof Magnucki:  <https://orcid.org/0000-0003-2251-4697>

Ewa Magnucka-Blandzi:  <https://orcid.org/0000-0002-6349-5579>



This work is licensed under the Creative Commons BY-NC-ND 4.0 license.

# INFLUENCE OF FLUID RHEOLOGY ON BLOOD FLOW HAEMODYNAMICS IN PATIENT-SPECIFIC ARTERIAL NETWORKS OF VARIED COMPLEXITY – IN-SILICO STUDIES

Zbigniew TYFA<sup>\*</sup>, Piotr REOROWICZ<sup>\*</sup>, Damian OBIDOWSKI<sup>\*</sup>, Krzysztof JÓZWIK<sup>\*</sup>

<sup>\*</sup>Faculty of Mechanical Engineering, Lodz University of Technology,  
Żeromskiego 116 St., 90-924 Łódź, Poland

[zbiqniev.tyfa@p.lodz.pl](mailto:zbiqniev.tyfa@p.lodz.pl), [piotr.reorowicz@p.lodz.pl](mailto:piotr.reorowicz@p.lodz.pl), [damian.obidowski@p.lodz.pl](mailto:damian.obidowski@p.lodz.pl), [krzysztof.jozwik@p.lodz.pl](mailto:krzysztof.jozwik@p.lodz.pl)

received 30 March 2023, revised 5 June 2023, accepted 28 June 2023

**Abstract:** Results obtained with computational fluid dynamics (CFD) rely on assumptions made during a pre-processing stage, including a mathematical description of a fluid rheology. Up to this date there is no clear answer to several aspects, mainly related to the question of whether and under what conditions blood can be simplified to a Newtonian fluid during CFD analyses. Different research groups present contradictory results, leaving the question unanswered. Therefore, the objective of this research was to perform steady-state and pulsatile blood flow simulations using eight different rheological models in geometries of varying complexity. A qualitative comparison of shear- and viscosity-related parameters showed no meaningful discrepancies, but a quantitative analysis revealed significant differences, especially in the magnitudes of wall shear stress (WSS) and its gradient (WSSG). We suggest that for the large arteries blood should be modelled as a non-Newtonian fluid, whereas for the cerebral vasculature the assumption of blood as a simple Newtonian fluid can be treated as a valid simplification.

**Key words:** blood rheology; CFD; non-Newtonian blood flows; arterial systems

## 1. INTRODUCTION

Computational fluid dynamics (CFD) tools can be considered as numerical simulations that help predict and analyse the physical behaviour and complex phenomena occurring in fluid flows by solving equations of fluid mechanics, i.e. energy, mass and momentum conservation. As far as simulations of blood flow are concerned, CFD can provide an insight into the flow structures of a given patient without exposing him or her to any health risks. Furthermore, in-silico analyses can provide valuable preoperative information to help medical professionals plan and perform surgery. However, it should not be left unmentioned that the results of any numerical simulation depend heavily on initial assumptions made during a pre-processing stage. Apart from the complexity of the arterial system or the inflow and outflow boundary conditions, one such assumption is a mathematical description of the rheology of the fluid.

In fluid mechanics, there are three fundamental parameters of any fluid, namely heat conductivity, density and viscosity. Since the main heat transfer occurs in capillaries, not arteries, in the vast majority of CFD studies blood flow is modelled as isothermal and adiabatic – there is no heat transfer, and thus the first parameter (heat conductivity) can be neglected. In terms of density, blood is usually considered to be an incompressible fluid (although it carries O<sub>2</sub> and CO<sub>2</sub>). Its density is in the range of 1,030–1,070 kg/m<sup>3</sup> [1].

The last parameter, viscosity, can be described as the resistance of a fluid to flow. Resistive viscous forces arise due to mutual attractive forces between fluid particles. In terms of bio-flows, the importance of viscosity is related to the fact that it par-

tially controls the blood flow through arteries and veins. For instance, a higher haematocrit value (ratio of red blood cells in blood) results in a viscosity increase and, consequently, higher resistances for the flow [2]. In general, blood is a complex fluid that exhibits non-Newtonian shear-thinning behaviour. This means that its viscosity varies when subjected to external stress – the higher the shear rate, the lower the viscosity. This can be observed when the blood velocity is high or when the vessel cross-section is relatively small. Shear-thinning phenomenon occurs at higher shear rates because erythrocytes and other blood cells begin to deform under applied stress. Otherwise, they form aggregates that increase the attractive forces between them, leading to a higher viscosity and, consequently, higher flow resistance [2].

The non-Newtonian properties of blood are significant at lower values of shear rate – it is claimed that after exceeding the 100 s<sup>-1</sup> threshold, blood can be treated as a simple Newtonian fluid of constant viscosity [3,4]. Similarly, as with any experimental study of living tissue, varied research groups have obtained different results regarding the shear-thinning behaviour of blood. This is due to the fact that blood is a patient-specific fluid (its parameters depend on numerous factors such as sex, age, diet, general hydration, medications taken, etc.), and thus all its physical properties vary widely among the human population. Therefore, dozens of different mathematical formulas describing blood have appeared in the literature. Tab. 1 and Fig. 1 present the most common rheological models that are widely used for in-silico studies of blood flow.

As stated before, the non-Newtonian properties of blood are significant at lower values of shear rates, i.e. <100 s<sup>-1</sup> [3,4]. It is claimed that shear rates are high in large arteries or vessels characterised by high blood flow and relatively small size. Therefore, it

is hypothesised that the Newtonian assumption is valid for the majority of human arteries [2]. However, the shear rate can vary throughout the entire cardiac cycle from 0 s<sup>-1</sup> to 1,000 s<sup>-1</sup>, and thus the assumption of a non-Newtonian shear-thinning fluid seems to be mandatory to obtain the most realistic numerical results [9]. Therefore, many scientists have analysed the influence of blood rheology on CFD data. Unfortunately, there is no clear answer as to whether blood can be simplified to a Newtonian fluid – each research group has presented slightly different results and drawn contradictory conclusions.

**Tab. 1.** The most common rheological models of blood used in CFD

Blood model	Mathematical formula	
Newtonian (NEWT)	$\eta = 0.00345 \text{ Pa} \cdot \text{s}$ $\eta = 0.0035 \text{ Pa} \cdot \text{s}$	(1)
Power Law (PL)	$\eta = k \cdot (\dot{\gamma})^{n-1}$ where: $k = 0.017 \text{ kg} \cdot \text{m}^{-1} \cdot \text{s}^{-1.292}$ ; $n = 0.708$	(2)
Quemada (QUE)	$\eta = \eta_p \cdot (1 - \frac{K \cdot HTC}{2})^{-2}$ $K = \frac{k_0 + k_\infty \cdot (\dot{\gamma}/\dot{\gamma}_c)^{0.5}}{1 + (\dot{\gamma}/\dot{\gamma}_c)^{0.5}}$ where: $\eta_p = 0.00127 \text{ Pa} \cdot \text{s}$ ; $k_0 = 4.0$ ; $k_\infty = 1.5$ ; $\dot{\gamma}_c = 5.0 \text{ s}^{-1}$	(3)
Modified PL (MPL) (1,5–8)	$\begin{cases} \eta = 0.55471 \text{ Pa} \cdot \text{s} & \text{for } \dot{\gamma} \leq 0.001 \\ \eta = \eta_0 \cdot (\dot{\gamma})^{n-1} & \text{for } 0.001 \leq \dot{\gamma} < 327 \\ \eta = 0.00345 \text{ Pa} \cdot \text{s} & \text{for } \dot{\gamma} \geq 327 \end{cases}$ where: $\eta_0 = 0.035 \text{ kg} \cdot \text{m}^{-1} \cdot \text{s}^{-1.4}$ ; $n = 0.6$	(4)
Carreau (CAR)	$\eta = \eta_\infty + (\eta_0 - \eta_\infty) \cdot (1 + (\lambda \cdot \dot{\gamma})^2)^{\frac{n-1}{2}}$ where: $\eta_\infty = 0.0035 \text{ Pa} \cdot \text{s}$ ; $\eta_0 = 0.056 \text{ Pa} \cdot \text{s}$ ; $\lambda = 3.313005 \text{ s}$ ; $n = 0.3568$ ;	(5)
Casson (CAS)	$\eta = (\sqrt{\eta_c} + \sqrt{\frac{\tau_c}{\dot{\gamma}}})^2$ where: $\eta_c = 0.00414 \text{ kg} \cdot \text{m}^{-1} \cdot \text{s}^{-1}$ ; $\tau_c = 0.0038 \text{ kg} \cdot \text{m}^{-1} \cdot \text{s}^{-2}$	(6)
Cross (CRO)	$\eta = \eta_\infty + \frac{\eta_0 - \eta_\infty}{1 + (\lambda \cdot \dot{\gamma})^a}$ where: $\eta_\infty = 0.0035 \text{ Pa} \cdot \text{s}$ ; $\eta_0 = 0.0364 \text{ Pa} \cdot \text{s}$ ; $\lambda = 0.38 \text{ s}$ ; $a = 1.45$	(7)
K-L (KL)	$\eta = \frac{1}{\dot{\gamma}} \cdot (\tau_c + \eta_c \cdot (a_2 \cdot \sqrt{\dot{\gamma}} + a_1 \cdot \dot{\gamma}))$ where: $\tau_c = 0.005 \text{ Pa}$ ; $\eta_c = 0.0035 \text{ Pa}$ ; $a_1 = 1.0 \text{ s}$ ; $a_2 = 1.19523 \text{ s}^{0.5}$	(8)

One of the first numerical studies of rheology was proposed by Gijzen et al. [10]. Their research showed that the non-Newtonian fluid (Carreau–Yasuda model) has a considerable effect on the flow velocity in the carotid arteries when compared to the results for a simple Newtonian fluid. Thus, this indicates that the rheology of blood plays a critical role in the ability of the numerical solver to properly approximate the flow distribution. Shinde et al. [11] stated that if shear stress is meant to be considered as a predictor of atherosclerosis development, a non-Newtonian fluid should be assumed. In contrast, Boyd and Buick [12], who also analysed the carotid artery as well, concluded that the non-Newtonian properties of blood can be neglected due to small relative differences between rheological models. Mendieta et al.

[13] suggested that Newtonian fluid is a reasonable assumption when analysing averaged shear stress, oscillatory shear index and general flow distribution. The next CFD study using the carotid artery was prepared by Razavi et al. [14], who analysed the influence of Newtonian and six non-Newtonian models on flow haemodynamics. After performing a series of transient simulations, they found that even at high velocities (and consequently high shear rates), considerable differences were detectable for Power Law and Walburn–Schneck models. Razavi et al. [14] concluded that the Power Law overestimated wall shear stress (WSS) values at both low and high shear rates, while the Generalized Power Law and modified Casson models appeared to underestimate the non-Newtonian behaviour. According to this scientific group, the Carreau and Carreau–Yasuda models are the most appropriate rheological approximations of the human blood flow in the carotid artery. Furthermore, their research has shown that the assumption of pulsatile flow is mandatory for the study of recirculation phenomena, which can lead to drastic changes in shear rates and, consequently, in viscosity – such an analysis cannot be performed for the steady-state simulations [14].

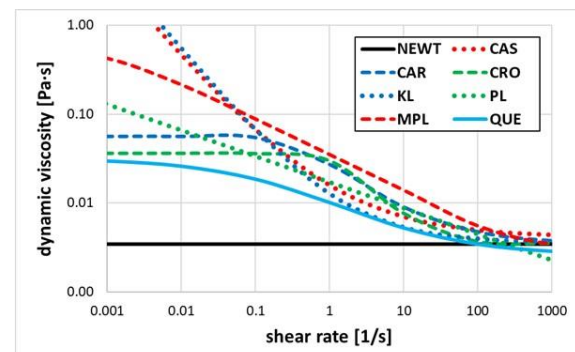


**Fig. 1.** Dynamic viscosity dependence on shear rate (logarithmic plots)  
– the most common rheological blood models

In 2004 and 2006 Johnston et al. [4,15] carried out steady-state and pulsatile blood flow simulations in patient-specific coronary arteries. The results of these studies showed that the shear stress distribution at the arterial walls was consistent for all rheological models (Newtonian, Power Law, Carreau, Casson, Walburn–Schneck and Generalized Power Law), although magnitudes varied. For the steady-state simulations, Johnston et al. observed that the WSS differences between the rheological models became less distinct as the inlet velocity increased (associated with a concomitant increase in shear rate).

To quantitatively compare the viscosity differences between each non-Newtonian and Newtonian model, this research group introduced two parameters: local and global non-Newtonian importance factors. These parameters are described more thoroughly in the further part of this paper. The results indicated that for the flows characterised by medium to high shear rates, the Newtonian model is a valid approximation. By comparing steady-state and transient results, Johnston et al. concluded that the Newtonian blood model is a reliable assumption for approximately 70% of the cardiac cycle. During the remaining 30%, the flow was characterised by relatively lower velocity, which increased the viscosity and consequently WSS values. Therefore, they suggested that the Newtonian model may be a reasonable and sufficient approximation for transient simulations [15]. However, they emphasised that the non-Newtonian model of blood should be used for in-depth

studies focussing on local haemodynamics, such as vortex formation.

To evaluate the impact of the rheological model on haemodynamics within the largest vessel of the human organism, Karimi et al. [16] generated a patient-specific model of the aorta consisting of ascending aorta, aortic arch and initial region of descending aorta. They performed transient simulations and investigated the following blood models: Newtonian, Casson, K-L, Modified Casson, Carreau, Carreau–Yasuda, Cross, Power Law, Modified Power Law and Generalized Power Law. It was ascertained that the Cross model generates significantly different WSS and velocity distributions at diastole (when shear rates are low) when compared to other non-Newtonian models. Moreover, this thorough and extensive research proved that blood rheology affects the flow solution, while the Newtonian assumption tends to underestimate WSS values [16].

Caballero and Lain [2] investigated the influence of rheology in a slightly more complex geometry of the aorta, since it extended up to the abdominal region. They performed steady-state and transient in-silico analyses in which the blood was described by the following rheological models: Newtonian, Carreau, Power Law and Herschel–Buckley. Similar to the previous studies, they found that the WSS distribution was consistent across all rheological cases, but WSS magnitudes varied, especially at lower inlet velocities. For medium to high shear rates, little differences were observed. Their results indicated that Carreau and Herschel–Buckley models tended to overestimate WSS at high velocities, while the Newtonian model underestimated WSS at low flow rates. Moreover, when they compared the cycle-averaged results for all rheological models, there were hardly any differences in WSS and the global non-Newtonian importance factor, indicating that the non-Newtonian model assumption is not of great significance for pulsatile flow. Therefore, Caballero and Lain [2] concluded that the Newtonian model is a suitable assumption for the transient analysis.

Shortly thereafter, Doost et al. [3] analysed haemodynamics within patient-specific geometry of the left ventricle. During transient simulations, blood was modelled as Newtonian and non-Newtonian fluid (described by Carreau, Casson, Generalized Power Law, K-L and Cross equations). It has been shown that the choice of the specific rheological model has a considerable influence on the obtained results. For instance, each mathematical description of blood resulted in different numbers and sizes of small vortices. The results of the K-L and Cross models produced lower WSS values than pure Newtonian fluid, whereas the WSS values for the other rheological models were significantly higher [3].

Considering all the aforementioned information (derived from the available literature), it can be concluded that there is no clear answer whether blood can be simplified to a Newtonian fluid for in-silico investigations or whether it has to be considered as a specific non-Newtonian fluid. Each research group presents different results and varied conclusions, and thus the answer remains ambiguous. Therefore, the main objective of this research was to evaluate the influence of the chosen blood model on the numerical data by performing steady-state and pulsatile blood flow simulations relying on eight different blood models in patient-specific geometries of varying complexity. This could help to answer three open hypotheses:

- blood can be simplified to a Newtonian fluid in large arteries and small vessels with high blood flow;

- blood can be simplified to a Newtonian fluid for cycle-averaged and steady-state investigations;
- regardless of vessel size, when blood flow is characterised by low intensity, the effect of viscosity variation is so pronounced that the use of shear rate-dependent models is recommended.

## 2. MATERIALS AND METHODS

To accomplish all of the objectives of the following research, numerous separate steps had to be taken. Firstly, one had to prepare several patient-specific geometries of varying complexity. Then, volumetric meshes of sufficient quality had to be generated. Finally, the authors performed steady-state and pulsatile blood flow simulations, considering blood washout analysis. All these steps are briefly described in the further part of this paper.

### 2.1. Patient-specific geometries

As described earlier, blood viscosity depends on numerous factors, including the topology of the flow channels, and thus it was decided to carry out an analysis of blood rheology in geometries of varying complexity: a simple bifurcation of the common carotid artery (CCA), the entire aorta with major branches and a complex system of intracranial arteries. All patient-specific models (see Fig. 2) were reconstructed from biomedical imaging that was subjected to image segmentation procedures. Model retrieval methods were performed in a custom software called Anatomical Model Reconstructor (AMR) developed at the Institute of Turbomachinery (Lodz University of Technology, Poland).

The first step was to import Digital Imaging and Communications in Medicine (DICOM) images obtained by angiography computed tomography (angio-CT) into the AMR software. Then, each voxel in the dataset was divided into eight sub-voxels to improve automatic segmentation procedures. To visualise arteries filled with a contrast agent (to distinguish them from surrounding tissues), a specific preset of the windowing operation was used. Then, the region growing method was used to perform image segmentation for the entire image set. Unfortunately, each 3D mask required further manual processing. The main shortcomings were related to the separation of bone structures from the arterial lumen and the addition of smaller branches of intracranial vessels that were omitted during the automatic image segmentation. Once a 3D binary mask was completed and stored for all the regions of interest (lumens of the selected blood vessels), a 3D surface geometry of the given arterial network was extracted from it. The voxelised model (with staircase-like topology) was smoothed with expert smoothing parameters to obtain an anatomically correct model while preserving the overall topology. Then, each arterial branch was clipped in its proximal or distal part to obtain perpendicular cross-sections for the outlet and inlet surfaces. The next step was to cover each open channel with a planar surface using an automated capping method. This means that each opening or hole detected in the wall of the model was automatically filled with a simple planar surface that was treated as a separate 3D object. Finally, each relevant 3D surface model, i.e. the artery wall and all capping boundaries, was saved to a selected folder as a separate file stored in stereolithography (STL) format. Fig. 2 depicts a comparison of all three patient-specific models, generated in the custom-developed AMR software, that were used during this research.

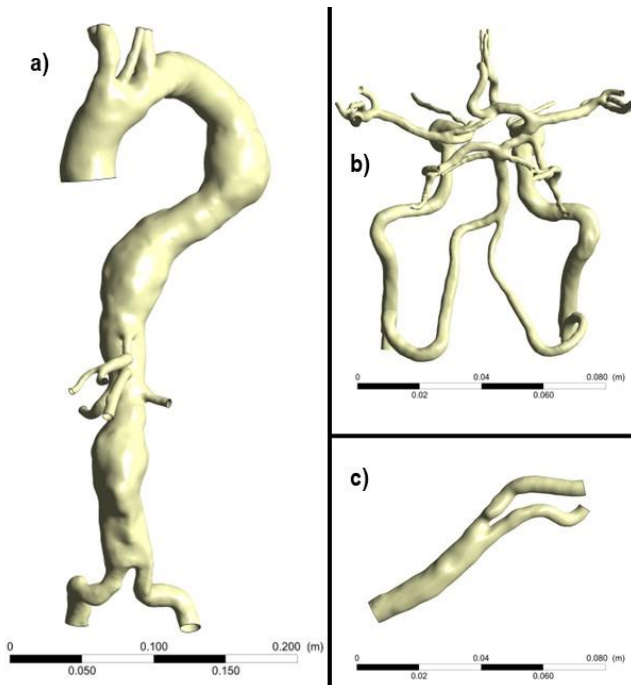


**Fig. 2.** Patient-specific models used during in-silico investigations: (a) entire aorta with major branches; (b) complex intracranial arterial system; (c) carotid artery bifurcation

## 2.2. Numerical domain: volumetric meshes

High-quality volumetric meshes were generated in the ANSYS ICEM (Ansys Inc. Canonsburg, USA) package, based on prepared STL objects. They consisted of unstructured tetrahedral elements in the free-flow regime as well as prismatic elements embedded in an inflation layer. The inflation layer was composed of 16 sublayers – such a number was chosen after thorough sensitivity tests performed for each geometry type. Specific macro files were used for the mesh generation – such scripts were automatically prepared in the AMR software. Another aspect, also covered by a prepared script, focussed on the mesh metrics – each Delaunay mesh was subjected to additional smoothing and refinement to ensure that the resulting mesh was of high quality. This process was repeated thrice for tetrahedral elements and twice additionally for tetrahedral and prismatic elements. With each successive iteration, the ICEM mesh quality measure was increased.

Before focussing on target numerical simulations, it was necessary to ensure that a discretisation error due to the mesh density was negligible. Therefore, specific mesh independence tests (MITs), both asymptotic and parametric, were performed beforehand [17]. It was decided that the mesh for the carotid artery should comprise approximately two million elements, while the mesh for the intracranial arterial network should be composed of approximately six million elements. For the whole aorta, the coarsest mesh was chosen for further numerical analyses (consisting of about eight million elements).

## 2.3. Numerical domain: simulation settings

In all simulations, i.e. steady-state and transient, the flow was assumed to be adiabatic and isothermal, while blood was treated

as an incompressible fluid with constant density (1,045 kg/m<sup>3</sup>) and varying viscosity, as defined by eight specific models, which are presented in Tab. 1. The flow simulations were performed using the pressure-based ANSYS CFX (Ansys Inc. Canonsburg, USA) solver. The Reynolds-averaged Navier–Stokes (RANS) equations were calculated with the k- $\omega$  Shear Stress Transport (SST) turbulence model. Each steady-state simulation was considered complete when it either reached the convergence criteria (10<sup>-6</sup>) or exceeded 500 iterations. The steady-state boundary conditions are listed in Tab. 2, while the transient boundary conditions for the inlet cross-sections are shown in Fig. 3. A Prandtl velocity profile was set at the inlet cross-section in the aorta case study, whereas parabolic profiles were used for all the others. Static gauge pressure was set for each opening cross-section even in transient analyses, where the values were the same as in steady-state case studies. The reason for this simplification is the fact that the walls of the numerical domain were rigid, and thus the flow distribution depended only on the pressure gradient between the outlet surfaces.

**Tab. 2.** Steady-state boundary conditions used for the CFD analyses

Case	Inlet cross-section max. velocity [m/s]				Opening cross-sections pressure [kPa]
Entire aorta with major branches	0.12				Right SA 13.00
	0.12				Right CCA 13.00
	0.12				Left CCA 12.90
	0.12				Left SA 13.015
	0.12				HA 13.00
	0.12				GA 13.00
	0.12				SMA 13.00
	0.12				Left RA 12.95
	0.12				Right RA 12.95
	0.12				Left CIA 13.01
CCA	0.85				Right CIA 13.02
	0.85				ICA 14.00
	0.85				ECA 14.00
Cerebral arteries	LICA	LVA	RICA	RVA	All cerebral arteries
	0.365	0.275	0.370	0.155	11.00

CCA, common carotid artery; CIA, common iliac artery; GA, gastric artery; HA, hepatic artery; LICA, left internal carotid artery; LVA, left vertebral artery; RA, renal artery; RICA, right internal carotid artery; RVA, right vertebral artery; SA, subclavian artery; SMA, superior mesenteric artery.

In addition, the blood washout phenomenon has been analysed in transient simulations, as it allows the detection of regions prone to stagnation and clotting since thrombus is expected to occur in regions of low velocity, low shear stress and non-washed-out areas [18,19]. In these studies, the washout analysis is based on the principle that “old blood” occupies an entire volume of the fluid domain at the beginning of the simulation. Then, “new blood” begins to flow inside the numerical domain, pushing “old blood” out of the domain according to the specification of the inlet boundary condition. No mixing of the two separate fluids (within a

single mesh element) was assumed. Both fluids were characterised by the same rheological properties.

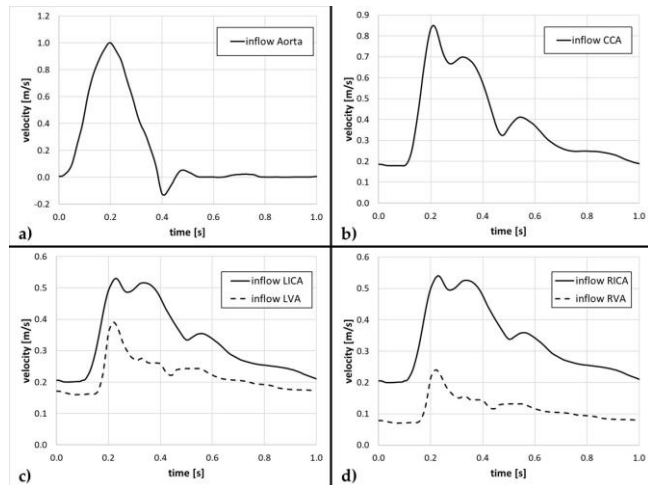


**Fig. 3.** Transient boundary conditions set on the inlet cross-sections in each analysed case study: (a) entire aorta; (b) carotid artery bifurcation; (c)–(d) intracranial arteries

The plots depicted in Fig. 3 are limited to just a single cardiac cycle for a higher clarity, but multiple cycles were simulated in the CFD analyses: 7 for the CCA bifurcation, 10 for the aorta and 5 for the cerebral vasculature. We wanted to minimise the influence of the initial conditions on the final results and to analyse a sufficient number of cardiac cycles required for a reliable blood washout analysis. Tab. 3 presents some parameters used for further comparison of the results.

**Tab. 3.** Chosen parameters used during the results' analysis

Parameter	Mathematical formula
Time-averaged WSS (TAWSS) Shear stress averaged for one full cardiac cycle.	$\text{TAWSS} = \frac{1}{T} \int_0^T  \vec{\tau}_w  dt \quad (9)$
WSS spatial gradient (WSSG) Determines regions of spatial changes in shear stress magnitude. High WSSG might indicate region prone to formation of atheromatous plaque or aneurysm growth.	$\text{WSSG} = \sqrt{\left(\frac{\partial \vec{\tau}_{w,m}}{\partial m}\right)^2 + \left(\frac{\partial \vec{\tau}_{w,n}}{\partial n}\right)^2} \quad (10)$
Time-averaged WSSG (TAWSSG) WSSG averaged for full cardiac cycle.	$\text{TAWSSG} = \frac{1}{T} \int_0^T \text{WSSG} dt \quad (11)$
Oscillatory shear index (OSI) Gives insight about the direction changes of shear forces throughout the cardiac cycle. High local OSI and low WSS show regions susceptible to plaque aggregation and instances of blood stagnation.	$\text{OSI} = 0.5 \cdot \left(1 - \frac{\left \int_0^T \vec{\tau}_w dt\right }{\int_0^T  \vec{\tau}_w  dt}\right) \quad (12)$

Local and global non-Newtonian importance factors ( $I_L$ and $I_G$ ) Describe local/global differences between dynamic viscosity produced by Newtonian and non-Newtonian fluids.	$I_L = \frac{\eta}{\eta_\infty} \quad (13)$
	$\bar{I}_G = \frac{1}{N} \frac{[\sum_N (\eta - \eta_\infty)^2]^{1/2}}{\eta_\infty} \quad (14)$

### 3. RESULTS

To evaluate the influence of the rheological blood model on the numerical solution, numerous simulations were performed on a chosen geometry, i.e. CCA bifurcation, intracranial arterial network and entire aorta. Since eight different blood models were investigated for each selected reconstruction, a total of 48 simulations were performed (24 steady-state and 24 transient ones). To present the results clearly, each geometry is discussed separately. Besides an analysis of the most common flow parameters, i.e. velocity, wall shear stress (WSS) and flow distribution, several other haemodynamic indicators were estimated as well. To calculate them for steady-state and transient simulations, specific algorithms written in a high-level programming language (Python) were prepared. Thus, one could analyse TAWSS, OSI, WSSG, TAWSSG, IL and IG, which are described in Tab. 3.

However, before proceeding to the analysis of the rheology influence on the numerical data, it was decided to perform an initial validation of the results obtained. For this reason, the authors compared the basic haemodynamic parameters (estimated for Newtonian case studies) with the clinical and statistical research.

#### 3.1. Results validation

Tabs. 4 and 5 provide information on the maximum velocity and Reynolds numbers recorded during peak systole for the CCA bifurcation and the entire aorta case studies. Moreover, Tab. 5 outlines data related to the relative blood distribution through three control surfaces: the common carotid artery and two renal arteries.

**Tab. 4.** Initial validation of the numerical data for the CCA bifurcation case study at systole peak – control plane located at CCA segment

Max. velocity [m/s]		Reynolds number [-]	
CFD data	Reference	CFD data	Reference
0.87	0.84* 0.89** 0.75*** 0.90**** 0.85*****	606	460 [5] 500 [20] 968 [21]

\*Averaged value for female control group [22]  
\*\*Averaged value for male control group [22]  
\*\*\*Value measured during resting conditions [23]  
\*\*\*\*Value measured during exercise [23]  
\*\*\*\*\*Value coming from ultrasonography examination [24]

As can be seen, all the obtained results are in good agreement with the literature data – there are hardly any significant

discrepancies. It is worth mentioning that estimated Reynolds numbers (representing physiological in-vivo cases) seem to be low enough to treat the flow as laminar. This suggests that RANS closed with the k- $\omega$  SST turbulence model is not recommended for the assumed flows. However, it has to be stated that we simulated pulsatile blood flow in geometries with complex topology (consisting of numerous junctions and high curvature), which can affect the flow directioning. Thus, there was a high probability of occurrence of specific flow phenomena, such as flow separation and formation of recirculation zones. Therefore, treating the flow as a purely laminar one (which is suitable for fully developed flows that do not occur in the human circulatory system) might be an oversimplification. Moreover, as presented in Tabs. 4 and 5, the obtained results are consistent with the literature data, which proves that the numerical domain assumptions were correct.

**Tab. 5.** Initial validation of the numerical data for the entire aorta case study and several chosen control surfaces

	Relative blood distribution with respect to the inflow		Reynolds number at systole peak [-]	
Location	CFD data	Reference	CFD data	Reference
CCA	10.6%	8.5% (25)	844	460 [5] 500 [20] 968 [21]
Left RA	7.72%	8.6% (25)	673	400–1,100
Right RA	7.25%	8.6% (25)	800	[26]

CCA, common carotid artery; RA, renal artery.

Regarding the cerebral vasculature, it was decided to analyse the symmetry of blood supply between both hemispheres of the brain and its relation to the cardiac output (Tab. 6). Since the spatial geometry was limited to intracranial arteries (it did not start at the aorta), it was decided to assume 70 cm<sup>3</sup> as a reference for physiological cardiac output [27]. Moreover, the authors presented volume flow rates at three main control surfaces located at the left and right middle cerebral arteries as well as at the basilar artery (Tab. 7).

**Tab. 6.** Initial validation of the numerical data for the cerebral vasculature case study – part one

Location	Blood volume delivered in one full cardiac cycle [cm <sup>3</sup> ]	Relative ratio	Referential ratio
Left hemisphere	4.869	50.1% of the inflow	50%–50% (symmetry)
Right hemisphere	4.851	49.9% of the inflow	
Full vasculature	9.720	13.89% of the physiological cardiac output (70 cm <sup>3</sup> ) 14.4% of the cardiac output [25] 13%–15% of the cardiac output [30]	15% of the cardiac output [28,29]

**Tab. 7.** Initial validation of the numerical data for the cerebral vasculature case study – part two

Location	Volume flow rate [cm <sup>3</sup> /min]	
	CFD data	Reference
Basilar artery	178	182 ± 56 [31] 138 ± 41 [32] 145 ± 41 [33]
Left middle cerebral artery	160	159 ± 28 [32] 146 ± 31 [33]
Right middle cerebral artery	138	146 ± 28 [32] 146 ± 31 [33]

As shown in Tab. 6, the CFD-estimated flow distribution represents a physiologically correct blood supply. Not only is the flow distributed symmetrically between both hemispheres of the brain (50.1% for the left hemisphere and 49.9% for the right one), but also the total volume of blood supply, i.e. 9.72 cm<sup>3</sup>, represents approximately 14% of the physiological cardiac output. Thus, we confirmed that our results correlate well with clinical observations [25,28–30].

Regarding the volume flow rates at three control planes (see Tab. 7), the obtained results are again in a correct physiological range. For example, the reference volume flow rate through the left middle cerebral artery is reported to be 159 ± 28 cm<sup>3</sup>/min [32], whereas the result obtained from our simulations is equal to 160 cm<sup>3</sup>/min.

Considering all the presented information, it can be concluded that the performed in-silico analyses of blood flow in each arterial configuration (i.e. CCA bifurcation, entire aorta and cerebral vasculature), resemble the natural, physiological haemodynamics. Thus, the presented numerical simulations can be considered as successfully validated.

### 3.2. Common carotid artery bifurcation

The first analysed aspect was the flow distribution across the numerical domain. For this purpose, three control planes were created at the distal part of the common carotid artery (CCA), the internal carotid artery (ICA) and the external carotid artery (ECA) – for steady-state simulations, the area-averaged velocity was examined, while for transient ones, the blood volume delivered throughout the entire cardiac cycle was calculated (Tab. 8). Based on the presented data, it can be concluded that the influence of the blood model on the flow distribution seems to be negligible for the majority of the case studies. The highest differences were obtained for the Power Law and K-L models, at 2.8% and 1.7%, respectively. For the Carreau, Cross, Modified Power Law and Quemada models, hardly any discrepancies could be observed. Within this group, the highest deviation was circa 0.5%. Conducted steady-state and transient simulations indicate that the flow distribution within the CCA bifurcation model is not affected significantly by the rheological blood model; however, some alterations occur. This suggests that blood can be simplified to a Newtonian fluid when analysing a CCA bifurcation. To prove the aforementioned statement, an additional analysis of further haemodynamic parameters was required. Tab. 9 outlines area-averaged wall shear stress (AAWSS) and area-averaged spatial gradient of wall shear stress (AAWSSG) calculated for the model walls. Additionally, average and maximum time-averaged wall

shear stress (TAWSS) and shear index (OSI) values are shown as well.

**Tab. 8.** Blood distribution analysis for the CCA bifurcation geometry

Control plane	Blood model							
	NEWT	CAR	CAS	CRO	KL	MPL	PL	QUE
Avg. velocity [m/s]	0.386	0.385 (-0.3%)	0.385 (-0.3%)	0.386 (0.0%)	0.385 (-0.3%)	0.386 (0.0%)	0.386 (0.0%)	0.386 (0.0%)
	0.779	0.777 (-0.3%)	0.772 (-0.9%)	0.779	0.767 (-1.5%)	0.779	0.801 (2.8%)	0.782 (0.4%)
	0.541	0.543 (0.4%)	0.546 (0.9%)	0.541 (0.0%)	0.550 (1.7%)	0.542 (0.2%)	0.528 (-2.4%)	0.539 (-0.4%)
Blood vol. [cm <sup>3</sup> ]	12.004 (0.0%)							
	5.436	5.408 (-0.5%)	5.380 (-1.0%)	5.433 (-0.1%)	5.345 (-1.7%)	5.415 (-0.4%)	5.521 (1.6%)	5.446 (0.2%)
	6.569	6.597 (0.4%)	6.626 (0.9%)	6.572 (0.0%)	6.660 (1.4%)	6.590 (0.3%)	6.485 (1.3%)	6.560 (-0.1%)

Based on the data presented in Tab. 8, it can be concluded that all the parameters related to the shear stress depend on the chosen blood model. The absolute differences of the AAWSS seem to be marginal; however, they represent a significant relative variation. Thus, if a larger inflow was assumed, the absolute differences could be higher. Nevertheless, the highest AAWSS values occurred at peak systole due to the highest shear rates. Simultaneously, the absolute differences between AAWSS were the largest among all blood models, exceeding 3.5 Pa (over 40%) for the Power Law model case study. In terms of maximum TAWSS differences, the highest ones were obtained for the Power Law model (circa 20 Pa, i.e. 47%) and for the KL model (circa 12 Pa, i.e. 28%). For steady-state and transient analyses, the Newtonian fluid model underestimated AAWSS, TAWSS and AAWSSG parameters, which is in agreement with several scientific studies [2,16].

**Tab. 9.** Shear-related parameters for the CCA bifurcation geometry

Parameter	Blood model								
	NEWT	CAR	CAS	CRO	KL	MPL	PL	QUE	
Steady-state	AAWSS [Pa]	6.52	6.71 (2.9%)	7.35 (12.7%)	6.52 (0.0%)	8.12 (24.5%)	6.48 (-0.6%)	4.21 (-35.4%)	6.13 (-6.0%)
	AAWSSG [Pa/m]	0.779	0.777 (-0.3%)	0.772 (-0.9%)	0.779 (0.0%)	0.767 (-1.5%)	0.779 (0.0%)	0.801 (2.8%)	0.782 (0.4%)
Systole peak	AAWSS [Pa]	8.92	9.19 (3.0%)	10.11 (13.3%)	8.93 (0.1%)	11.24 (26.0%)	8.89 (-0.3%)	5.33 (-40.2%)	8.32 (-6.7%)
	AAWSSG [Pa/m]	4,156	4,187 (0.7%)	4,546 (9.4%)	4,156 (0.0%)	4,964 (19.4%)	4,131 (-0.6%)	2,215 (-46.7%)	3,847 (-7.4%)
Full cycle	Avg. TAWSS [Pa]	3.27	3.42 (4.6%)	3.73 (14.1%)	3.27 (0.0%)	4.13 (26.3%)	3.30 (0.9%)	2.31 (-29.4%)	3.12 (-4.6%)
	Max. TAWSS [Pa]	42.97	43.94 (2.3%)	48.96 (13.9%)	42.99 (0.0%)	54.89 (27.7%)	42.49 (-1.1%)	22.72 (-47.1%)	39.33 (-8.5%)
	Avg. OSI [-]	0.156	0.151 (-3.2%)	0.151 (-3.2%)	0.156 (0.0%)	0.149 (-4.5%)	0.150 (-3.8%)	0.154 (-1.3%)	0.154 (-1.3%)

The next analysed parameters were those related to viscosity: local and global non-Newtonian importance factors (IL and IG,

respectively), as indicated in Tab. 10 and Fig. 4. If the value of the IL parameter differs from 1.0, it is possible to observe regions of the non-Newtonian flow. However, this requires a graphical representation of the analysed case – calculating a simple average value of IL does not provide meaningful information about the global influence of the rheological model. Thus, the second parameter introduced, IG, considers a relative difference in viscosity values (for each mesh node), which is averaged. After thorough numerical analyses, Johnston et al. [4] concluded that the most optimal cut-off value of IG for coronary arteries is 0.25. Below this value, the flow can be treated as Newtonian. For large arteries, a threshold value of 0.15 has been established [16].

**Tab. 10.** Viscosity-related parameters for the CCA bifurcation geometry

Parameter	Blood model								
	NEWT	CAR	CAS	CRO	KL	MPL	PL	QUE	
Steady-state	Avg. IL [-]	1.00	1.16	1.31	1.04	1.53	1.18	0.73	0.99
	IG [-]	0.00	0.15	0.21	0.14	0.35	0.32	0.32	0.09
Systole start	Avg. IL [-]	1.00	1.31	1.39	1.07	1.58	1.43	1.11	1.11
	IG [-]	0.00	0.25	0.27	0.16	0.39	0.44	0.25	0.13
Systole peak	Avg. IL [-]	1.00	1.10	1.27	1.01	1.49	1.06	0.62	0.94
	IG [-]	0.00	0.10	0.18	0.02	0.33	0.17	0.32	0.07

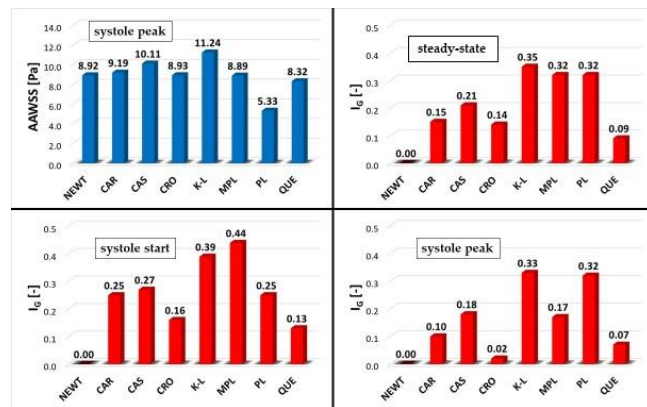


**Fig. 4.** AAWSS and IG parameters for the selected stages of the cardiac cycle – CCA bifurcation case studies; all rheological models of blood

Both steady-state and transient simulations outline significant deviations from the Newtonian fluid. The largest differences occur at low shear rates, i.e. at the beginning of systole. However, even at high shear rates, the results show meaningful, non-negligible discrepancies. Solely the Cross and Quemada models present proneness to Newtonian behaviour. Comparing the calculated data for steady-state analyses, the IG parameter is the highest for K-L, Modified Power Law and Power Law models (exceeding the value of 0.30), while the lowest one was obtained for the Quemada model, i.e. 0.09. The remaining blood models resulted in the IG parameter equal to approximately 0.15–0.20. Since the cut-off value of the IG parameter is claimed to be 0.15 for larger vessels,

it can be concluded that all analysed blood models, except the Quemada one, show a considerable non-Newtonian character. As far as the transient simulations are concerned, similar characteristics can be observed as for the steady-state simulations, although only for the beginning of systole. This phase of the cardiac cycle is characterised by low shear rates where the blood viscosity is extremely susceptible to mathematical description. All blood models, except for Quemada, resulted in IG values greater than 0.15.

However, when systole peak occurs, meaningful changes in the IG parameter can be observed. For instance, in the Carreau and Cross models, IG drops below 0.1, whereas in the Casson and Modified Power Law models it is reduced from 0.27 and 0.44 to 0.18 and 0.17, respectively. In summary, the changes in IG resulting from varying shear rates (a consequence of varying flow velocity) indicate that the non-Newtonian behaviour of blood depends on phase of the cardiac cycle.

### 3.3. Entire aorta with major branches

The same results analyses were performed for the entire aorta case studies; however, to make the paper more concise, it was decided to present only the most interesting data. Thus, Tabs. 11 and 12 contain information on the selected haemodynamic parameters, i.e. blood volume delivered to specific regions of the fluid domain (P1 – gastric artery; P2 – superior mesenteric artery; P3 – left renal artery) and IL and IG parameters, as well as the maximum WSS detected at the walls. Figs. 5 and 6 depict a qualitative comparison of the selected data.

Focussing on the flow distribution, the largest difference was found at the superior mesenteric artery for the K-L blood model (6% underestimation, i.e. circa 0.35 cm<sup>3</sup>, when compared to the Newtonian reference model). For the other models, the differences varied up to 3%–4%. It can be concluded that flow distribution is not significantly affected by the mathematical description of the blood rheology, but some alternations might occur. Thus, it seems that blood can be simplified to the Newtonian fluid model when the entire aorta geometry is analysed.

**Tab. 11.** A quantitative analysis of the chosen parameters for the entire aorta geometry: part 1

Control plane	Blood vol [cm <sup>3</sup> ]	Blood model							
		NEWT	CAR	CAS	CRO	KL	MPL	PL	QUE
P1	2.014	2.036 (1.1%)	2.056 (2.1%)	2.005 (-0.5%)	2.050 (1.8%)	1.998 (-0.8%)	1.997 (-0.9%)	2.023 (0.4%)	
	9.675	9.407 (-2.8%)	9.302 (-3.9%)	9.634 (-0.4%)	9.106 (-5.9%)	9.338 (-3.5%)	9.863 (1.9%)	9.642 (-0.3%)	
	6.971	6.887 (-1.2%)	6.916 (-0.8%)	6.978 (0.1%)	6.860 (-1.6%)	6.760 (-3.0%)	6.824 (-2.1%)	6.960 (-0.2%)	
Steady-state; max. WSS [Pa]	11.71	12.85 (9.7%)	13.96 (19.2%)	11.94 (2.0%)	15.53 (32.6%)	12.89 (10.1%)	8.64 (-26.2%)	11.52 (-1.6%)	
Systole start; max. WSS [Pa]	6.50	7.05 (8.4%)	7.84 (20.6%)	6.94 (6.8%)	8.64 (33.0%)	7.61 (17.0%)	4.98 (-23.3%)	6.56 (0.9%)	
Systole peak; max. WSS [Pa]	129.53	132.35 (2.2%)	143.96 (11.1%)	130.56 (0.8%)	159.42 (23.1%)	130.38 (0.7%)	70.13 (-45.9%)	120.90 (-6.7%)	
Max. TAWSS [Pa]	19.65	20.30 (3.3%)	22.22 (13.1%)	19.85 (1.0%)	24.66 (25.5%)	20.01 (1.8%)	11.19 (-43.0%)	18.40 (-6.4%)	

**Tab. 12.** A quantitative analysis of the chosen parameters for the entire aorta geometry: part 2

Parameter	Blood model							
	NEWT	CAR	CAS	CRO	KL	MPL	PL	QUE
Systole start; $l_L$ [-]	1.00	1.63	1.57	1.26	1.74	2.27	1.53	1.32
Systole peak; $l_L$ [-]	1.00	1.17	1.32	1.03	1.55	1.11	0.79	1.00
Steady-state; $l_L$ [-]	0.00	1.20	7.90	1.46	1.93	3.34	0.46	0.31
Systole start; $l_G$ [-]	0.00	0.23	0.13	0.18	0.20	0.97	0.18	0.08
Systole peak; $l_G$ [-]	0.00	0.02	0.04	0.00	0.10	0.03	0.04	0.00

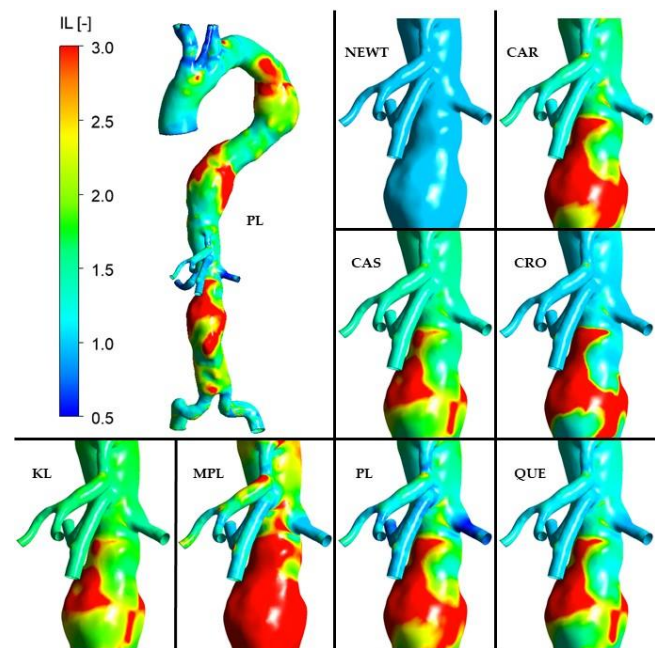


**Fig. 5.** Distribution of the IL parameter at the walls of the entire aorta case studies; all rheological models of blood

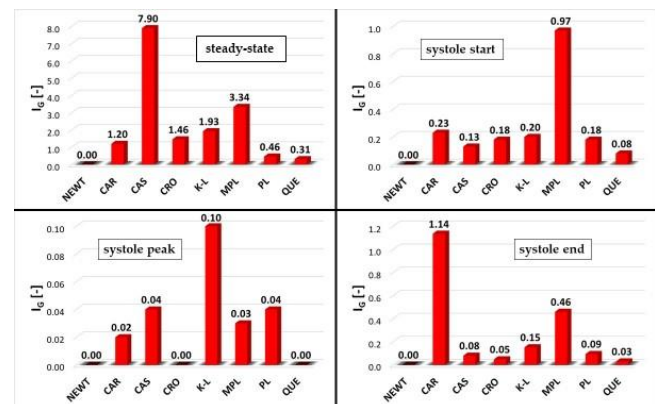


**Fig. 6.** The IG parameter for the selected stages of the cardiac cycle – entire aorta case studies; all rheological models of blood

A qualitative comparison of the WSS distribution also showed no significant changes between the blood models as well. However, when focussing on a quantitative comparison of WSS magnitudes as well as on IL and IG analysis, contrary observations

could be made. As shown in Tab. 11, the relative variation of the maximum WSS and TAWSS parameters was extremely high. The highest difference, obtained for the Power Law model at systole peak, was approximately 46%. The majority of the remaining differences, both for area-averaged and maximum WSS, were in the 5%–20% range. Therefore, it can be concluded that the rheological model of blood has a significant, non-negligible influence on haemodynamic parameters. This statement was further confirmed by IL and IG analysis. Concentrating on the former parameter, it can be concluded that not only the magnitudes varied, but also the general distribution was influenced by the chosen rheological model. Thus, the dynamic viscosity of the blood located in a direct vicinity of the arterial walls varied considerably in all case studies. As far as the IG parameter is concerned, a significant influence of the cardiac cycle phase on its values could be observed. At the beginning of systole, when shear rates were relatively low, almost all blood models produced IG values above the 0.15 threshold. The Casson and Quemada models were the only exceptions – the IG parameter was equal to 0.13 and 0.08, respectively. The highest value was obtained for the Modified Power Law model – it almost reached 1.00. Thus, this mathematical description is the most prone to the non-Newtonian character at the beginning of systole. At systole peak, none of the blood models reached a threshold value. Therefore, it could be concluded that at systole peak, i.e. at high shear rates, all mathematical descriptions show a high susceptibility to the Newtonian behaviour. During end-systole, the highest IG values were obtained for the Carreau and Modified Power Law models, amounting to 1.14 and 0.46, respectively. The IG parameters for the remaining blood models were characterised by values lower than 0.15.

### 3.4. Intracranial arterial system

During the blood distribution analysis, all outlet cross-sections were categorised into separate groups supplying different regions of the brain, i.e. anterior and middle parts of the left/right lobe and the posterior part of the left/right lobe. Tab. 13 shows the data obtained from the transient simulations, i.e. the blood volume delivered throughout the full cardiac cycle. As can be seen, the flow distribution remained almost unchanged – all differences did not exceed 1%. The largest discrepancies occurred in the K-L model, where the blood supply in the posterior part of the left lobe was limited by 0.8%. However, such small differences prove that flow distribution does not depend on the chosen blood model. It means that blood can be simplified to the Newtonian fluid model when analysing intracranial vessels. An additional analysis of parameters related to shear stresses was performed to prove this statement (Tab. 14).

Similar to the CCA bifurcation analysis, it can be seen that the absolute differences of the AAWSS, AAWSSG and TAWSS parameters are negligible, although their percentage variations are high. The Power Law and Quemada models seem to underestimate all the parameters related to the shear stress, i.e. AAWSS, AAWSSG, TAWSS and OSI. The flow solution obtained for the Cross model showed that this mathematical description is by far the most similar to the Newtonian behaviour – the results were extremely similar to the those obtained for the reference case study. Excluding the K-L and Quemada models, the remaining ones appear to result in negligible absolute differences in AAWSS, AAWSSG and TAWSS. Additionally, the general distri-

bution of the shear-related parameters was almost identical in each case study, making a sole qualitative comparison insufficient. Fig. 7 shows a WSS comparison for two models that were characterised by the highest visual discrepancies.

Tab. 13. A quantitative analysis of the blood distribution in the cerebral vasculature case studies

	Blood volume delivered during full cardiac cycle [cm <sup>3</sup> ]							
	NEWT	CAR	CAS	CRO	KL	MPL	PL	QUE
Left lobe; anterior and middle	3.445	3.438 (-0.2%)	3.437 (-0.2%)	3.445 (0.0%)	3.434 (-0.3%)	3.433 (-0.3%)	3.430 (-0.4%)	3.441 (-0.1%)
Left lobe; posterior	1.424	1.421 (-0.2%)	1.417 (-0.5%)	1.424 (0.0%)	1.411 (-0.8%)	1.426 (0.1%)	1.427 (0.2%)	1.426 (0.1%)
Right lobe; anterior and middle	3.304	3.314 (0.3%)	3.311 (0.2%)	3.306 (0.1%)	3.310 (0.2%)	3.318 (0.4%)	3.319 (0.5%)	3.311 (0.2%)
Right lobe; posterior	1.547	1.551 (0.3%)	1.553 (0.4%)	1.548 (0.1%)	1.557 (0.6%)	1.547 (0.0%)	1.547 (0.0%)	1.548 (0.1%)

Tab. 14. A quantitative analysis of shear-related parameters in the cerebral vasculature case studies

Parameter	Blood model								
	NEWT	CAR	CAS	CRO	KL	MPL	PL	QUE	
Steady-state	AAWSS [Pa]	2.94	3.13 (6.5%)	3.44 (17.0%)	2.95 (0.3%)	3.85 (31.0%)	2.94 (0.0%)	2.22 (-24.5%)	2.83 (-3.7%)
	AAWSSG [Pa/m]	1,776	1,791 (0.9%)	1,934 (8.9%)	1,774 (-0.1%)	2,099 (18.2%)	1,743 (-1.8%)	1,200 (-32.4%)	1,670 (-6.0%)
Systole peak	AAWSS [Pa]	4.82	5.12 (6.2%)	5.65 (17.2%)	4.83 (0.2%)	6.38 (32.4%)	4.79 (-0.6%)	3.34 (-30.7%)	4.57 (-5.2%)
	AAWSSG [Pa/m]	3,004	3,051 (1.6%)	3,297 (9.8%)	3,002 (-0.1%)	3,600 (19.8%)	2,972 (-1.1%)	1,868 (-37.8%)	2,808 (-6.5%)
Full cycle	Avg. TAWSS [Pa]	2.29	2.47 (7.9%)	2.71 (18.3%)	2.30 (0.4%)	3.03 (32.3%)	2.32 (1.3%)	1.79 (-21.8%)	2.22 (-3.1%)
	Avg. OSI [-]	0.204	0.204 (0.0%)	0.204 (0.0%)	0.204 (0.0%)	0.204 (0.0%)	0.204 (0.0%)	0.203 (-0.5%)	0.204 (0.0%)

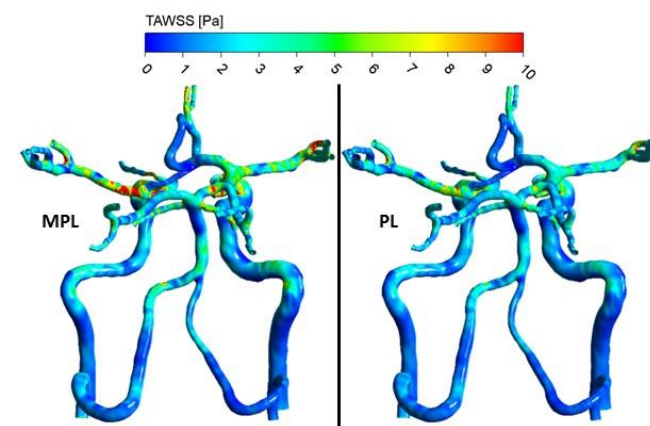
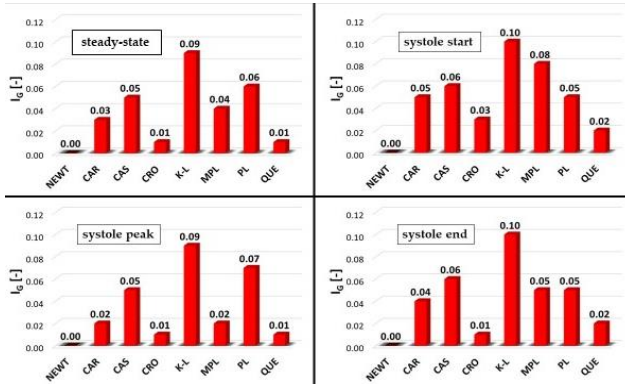


Fig. 7. TAWSS distribution at the walls of intracranial arteries – comparison of two selected rheological models: Modified Power Law (MPL) and Power Law (PL)

Therefore, the conducted analyses indicate that blood can be simplified to the Newtonian fluid model in numerical simulations of blood flow within the intracranial arteries. This was further supported by a thorough analysis of the IG parameter (see Fig. 8).



**Fig. 8.** The IG parameter for the selected stages of the cardiac cycle – cerebral vasculature case studies; all rheological models of blood

Contrary to the analysis performed for the CCA bifurcation and entire aorta case studies, the IG parameter for the intracranial arteries seemed to be independent of shear rate – it remained identical at both low and high shear rates. The only exception was MPL – it decreased from 0.08 (for the beginning of systole) to 0.02 (for the systole peak). The highest value of IG was obtained for the K-L model, which means that this mathematical description showed the highest non-Newtonian proneness among all investigated blood models. Moreover, regardless of the rheological model of blood, simulation type and cardiac cycle stage, all IG values were far below the threshold value of 0.15. Therefore, it can be concluded that the Newtonian model assumption of blood is a sufficient and valid approach to simulate blood flows within cerebral vasculature models.

### 3.5. Blood washout analysis

The final part of this research was devoted to an investigation of whether blood rheology affects the blood washout. If the remaining volume of “old blood” changed due to a mathematical description of fluid rheology, then it could be concluded that blood has to be modelled as non-Newtonian fluid in every CFD analysis. The reason behind this statement is the fact that non-washed-out blood is related to stagnation zones in which blood could start clotting. Tab. 15 presents the ratio of “old blood” that remained in the fluid domain at the last timestep of each simulation and Tab. 16 shows absolute differences of “old blood” volume, whereas Fig. 9 depicts time-dependent trends for Newtonian fluid – waveforms just for a single blood model are depicted for a clearer representation.

Firstly, it can be easily observed that the larger the model, the longer the blood washout phenomenon – for the CCA bifurcation almost the entire volume of “old blood” (~98%) was washed out during the first two cycles, whereas for the aorta case studies it took 10 cycles to reach nearly 95% of “old blood” washout. Regarding the differences in “old blood” volume remaining in the numerical domain at the end of each simulation, the relative differences seemed to be marginal – the highest discrepancy was found for the aorta geometry for the KL blood model: approximately 0.7%. Thus, such small differences suggest that blood rheology has almost no influence on the blood washout phenomenon. However, when comparing the absolute differences, slightly contrary conclusions could be drawn. For the CCA bifurcation and intracranial arteries, these differences were negligible (far below

0.01 cm<sup>3</sup>), whereas for the aorta case studies they were significant, i.e. reaching almost 4 cm<sup>3</sup>. This difference in blood volume indicated regions that could be prone to blood stagnation and, consequently, blood clotting. By applying a simple Newtonian fluid, such an observation could not be deduced.

**Tab. 15.** The percentage ratio of “old blood” volume with respect to the entire fluid domain volume at the end of each simulation

	Ratio of “old blood” that remained in the fluid domain [%]							
	NEWT	CAR	CAS	CRO	KL	MPL	PL	QUE
CCA bifurcation	0.37	0.41	0.41	0.39	0.42	0.40	0.31	0.39
Entire aorta	5.03	5.36	5.66	5.09	5.74	5.46	4.52	4.94
Intracranial arteries	0.60	0.62	0.62	0.64	0.64	0.67	0.52	0.61

**Tab. 16.** The absolute differences of “old blood” volume with respect to the volume estimated for Newtonian blood model

	Difference of “old blood” volume [cm <sup>3</sup> ]							
	NEWT	CAR	CAS	CRO	KL	MPL	PL	QUE
CCA bifurcation	-	0.002	0.002	0.001	0.002	0.001	-0.002	0.001
Entire aorta	-	1.759	3.359	0.320	3.785	2.293	-2.719	-0.480
Intracranial arteries	-	0.002	0.002	0.004	0.004	0.007	-0.008	0.001

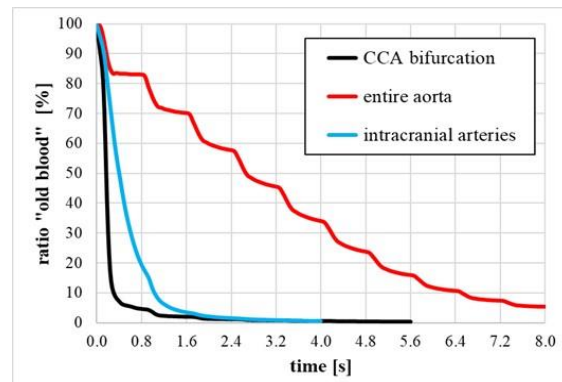


**Fig. 9.** The ratio of non-washed-out blood vs time – the Newtonian blood model case studies

### 3.6. Shear rate analysis

To observe the local influence of the rheological model of blood on the numerical data related to the flow characteristics, it was decided to perform an investigation of the shear rate at numerous control planes. Such an approach was presented in the work of Apostolidis et al. [34], who performed transient simulations of the blood flow in the left coronary artery and analysed the differences between the results obtained for the Newtonian and Casson viscoelastic models of blood. Additionally, they proposed a new approach towards setting outlet boundary conditions that attempts to preserve consistency with the pressure/flow predictions while being more computationally efficient.

To maintain the clarity of this paper, the results are presented for only one control plane per each case study. For the CCA bifurcation case study, a distal fragment of the ICA was chosen.

For the entire aorta case study, we decided to focus on the superior mesenteric artery (SMA), whereas in the cerebral vasculature, a cross-section of the left middle cerebral artery (MCA) was selected. Figs. 10, 11 and 12 outline a qualitative comparison of the shear rate for three selected rheological models of blood, i.e. Newtonian, Casson and Modified Power Law. The results were extracted from the time step corresponding to the late diastole, when velocity and shear rate were the lowest, whereas the non-Newtonian proneness was the highest. Apart from a qualitative comparison of shear rate, we decided to present a relative difference (expressed as a percentage) between non-Newtonian and Newtonian models. All differences below 10% were considered insignificant. Therefore, a dark blue colour represents regions where the shear rate differences were negligible. The quantitative data of this analysis are presented in Tab. 17.

**Tab. 17.** Analysis of relative differences in shear rate

Control surface	Max. difference		Avg. difference	
	NEWT vs CAS	NEWT vs MPL	NEWT vs CAS	NEWT vs MPL
ICA	114.0%	30.9%	12.6%	5.2%
SMA	116.8%	113.3%	24.0%	34.4%
MCA	86.5%	17.8%	8.5%	1.6%

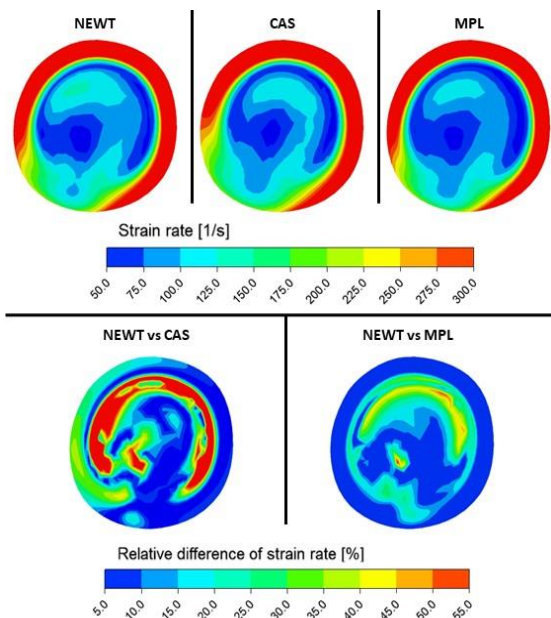


**Fig. 10.** The shear rate distribution and its relative differences at the ICA plane for three rheological models of blood – the CCA bifurcation case

By analysing the quantitative and qualitative data presented in Tab. 17 and Figs. 10, 11 and 12, it can be concluded that the rheological model of blood influenced the shear rate in each case study. Focussing on the maximum differences, the highest discrepancies were found for the superior mesenteric artery (SMA), exceeding 115%. Regarding the average differences, the highest ones were once again found at the SMA control surface (24.0% and 34.4% for Casson and Modified Power Law models, respectively). The lowest discrepancies were observed at MCA surface for Modified Power Law model – i.e. 1.6%. It is interesting to note that the differences in shear rate for the MPL model were visible only in the free-flow regime and not in the boundary layer. For the other control surfaces and rheological models, differences could

be observed both in the free-flow regime and in the boundary layer. Additionally, the discrepancies were significant, confirming all the former conclusions that blood should not be modelled as a simple Newtonian fluid.

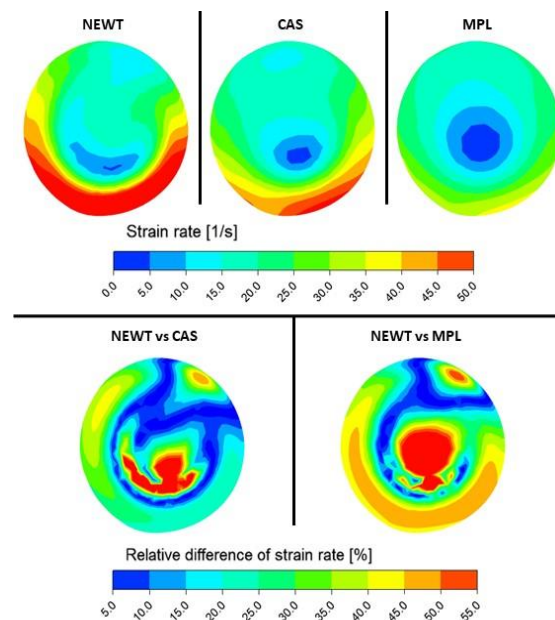


**Fig. 11.** The shear rate distribution and its relative differences at the SMA for three rheological models of blood – the entire aorta case

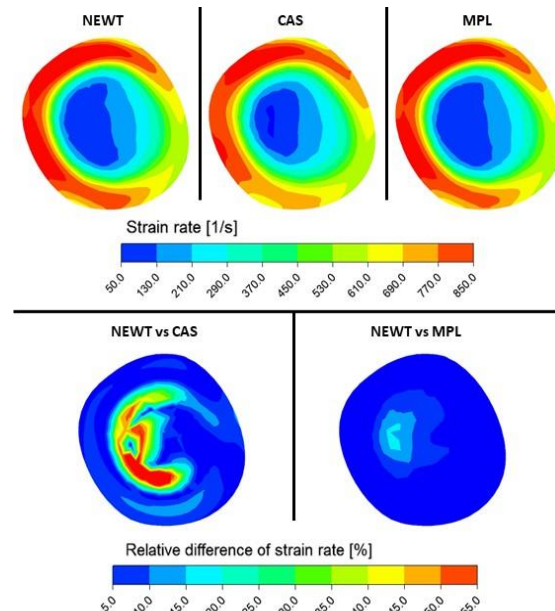


**Fig. 12.** The shear rate distribution and its relative differences at the left MCA for three rheological models of blood – the cerebral vasculature study

#### 4. DISCUSSION

The vast majority of studies available in the literature present the results of blood flow simulations in a specific fragment of the arterial system. We, on the other hand, decided to carry out a research (dedicated to numerical analyses of blood flows characterised by different rheological models of blood) using three ge-

ometries of varying complexity and location in the circulatory system. This allowed us to consider a possible influence of the arterial system complexity on the numerical data. Moreover, to generate as much data as possible, we decided to analyse a large number of different haemodynamic parameters and other possible bioindicators to ensure that the conclusions we drew were correct and adequately supported. It should be emphasised that we coupled rheology analyses with simulating the blood washout phenomenon. Unfortunately, there are no other literature data with which we could compare such results – this indicates an innovative approach towards rheology investigations. Furthermore, one of the analysed parameters was the shear rate. This investigation showed that the viscosity models have a significant effect on the shear rate, especially for the common carotid artery and the entire aorta case studies. Similar observations, i.e. non-negligible differences between Casson and Newtonian models, were presented in the work of Apostolidis et al. [34]. However, they simulated blood flow in the other blood vessel, i.e. the coronary artery, and thus a direct comparison between the two data sets could not be made.

Conducted steady-state and transient simulations indicate that the flow distribution within the CCA bifurcation model was not significantly affected by the rheological blood model; however, some changes occurred. Similarly, Mendieta et al. [13] did not observe drastic changes – flow rate and flow patterns were similar between case studies. This is in contrast to the work of Gijzen et al. [10], who claimed that there is a considerable difference in velocity distribution between the Newtonian and Carreau–Yasuda models. According to their research, the non-Newtonian fluid was characterised by a flattened axial velocity profile and lower velocity gradients. However, no quantitative comparison was presented, and thus it is not clear whether the differences exceed 2%, 5% or 10%. Moreover, we did not see any significant differences in the “old blood” volume remaining in the numerical domain at the end of the simulation. The largest deviation was far below 0.01 cm<sup>3</sup>. This suggests that rheology does not play a critical role in simulating blood flows in CCA models. Although the flow distribution was almost unaffected by the blood rheology (except for the Power Law model), we noticed a significant difference in the shear rate during the quantitative and qualitative evaluation. Additionally, high values of IG and IL parameters suggested that the blood model affected the flow haemodynamics. This statement and most of the presented results are in agreement with the findings of Shinde et al. [11], Razavi et al. [14], Gharahi et al. [35] and Moradieghamahi et al. [36]. The Newtonian fluid model underestimated AAWSS, TAWSS and AAWSSG parameters, which is consistent with the research of Caballero and Lain [2]. The K-L model overestimated the aforementioned parameters, while the Cross model seemed to be the most prone to Newtonian behaviour – results were almost identical to those obtained for the Newtonian fluid. Similar to the work of Moradieghamahi et al. [36], the AAWSS values were the smallest for Newtonian fluid among all models (Power Law is an exception), while the OSI was the largest.

As far as entire aorta case studies are concerned, the flow distribution was not significantly affected by the blood rheology; however, some changes could be observed. Thus, it appears that blood can be simplified to the Newtonian fluid model when the entire aorta geometry is analysed. The research of Karimi et al. [16] suggests that the Cross model generates considerably different velocity distributions at lower shear rates (during diastole), which is opposed to the results of the performed simulations. Despite negligible differences in flow distribution, blood washout

analysis showed significant discrepancies between rheological models of blood, reaching nearly 4 cm<sup>3</sup> for the K-L model. By simplifying blood to a Newtonian fluid, it would not be possible to detect regions characterised by blood stagnation and blood clotting. Moreover, it turned out that we obtained non-negligible differences in the magnitude of the shear rate at several control planes. The largest discrepancy exceeded 115% for the Casson model at the superior mesenteric artery. A thorough analysis of the IG parameter showed that the intensity of the rheological model influence varied, depending on the cardiac cycle phase. At the beginning of systole, almost all blood models produced IG values above 0.15, i.e. above the threshold value presented by Karimi et al. [16]. Therefore, treating blood as a simple Newtonian fluid might be an oversimplification. When comparing the absolute differences among area-averaged WSS and TAWSS, they appeared to be marginal. This may indicate that the blood rheology influence is negligible in the aorta model, which is in agreement with the research of Caballero et al. [2]. Additionally, after qualitative analysis of WSS and TAWSS distributions, these authors concluded that the assumption of the non-Newtonian fluid is not necessary under pulsatile flow, since hardly any differences were visible in the figures. Such conclusions are consistent with the results of this research. However, when the maximum WSS values were analysed quantitatively, no higher absolute differences could be observed, reaching even 60 Pa. Therefore, despite small absolute differences of AAWSS and similar WSS distributions at the model wall, high differences in the maximum WSS and high percentage variation of all parameters suggest that blood should be modelled as a shear-thinning fluid for the aorta.

In terms of intracranial arteries, the flow distribution remained nearly unchanged – all differences did not exceed 1%. Thus, it was demonstrated that the flow distribution does not depend on the chosen blood model. Additionally, hardly any differences could be detected in blood washout analysis, suggesting that blood can be treated as a Newtonian fluid when intracranial vessels are analysed. Such a result is in agreement with the work of Razavi et al. [37], who claimed that Newtonian fluid is a sufficient simplification of the blood model when it comes to the cerebral vasculature. Moreover, not only negligible differences in flow distribution were obtained, but also WSS, TAWSS and WSSG did not change significantly when compared to the reference case. A similar observation could be made when analysing the shear rate at the investigated cross-sections. For example, the average difference between MPL and Newtonian models was only 1.6%. Additionally, the shear rate changes could only be observed in the free-flow regime, and thus they did not influence the parameters related to the stress exerted on the arterial walls (pressure and WSS). Furthermore, the IG results were far below the thresholds suggested by two research teams, which supports the aforementioned statement [4,16]. Oliveira et al. [38] noticed a 50% overestimation of the maximum WSS values at intracranial aneurysm walls. However, when TAWSS and AAWSS were considered, the relative differences decreased to less than 7%. Nevertheless, they concluded that the non-Newtonian assumption of blood is recommended when investigating the maximal WSS and OSI at systole peak.

## 5. CONCLUSIONS

We present a comprehensive study in which we analysed the influence of eight different rheological models of blood on the

numerical results. To ensure that valid conclusions were drawn, we performed in-silico investigations of blood flows in geometries of varying complexity (CCA bifurcation, entire aorta and cerebral vasculature). Thus, our research was not limited to only one type of the arterial configuration. Furthermore, this study was based on the analysis of numerous haemodynamic parameters and bioindicators, including flow distribution, WSS, TAWSS, WSSG, OSI, IG, IL and shear rate. Moreover, we coupled the rheology assessment with the blood washout phenomenon.

The main conclusion of this research is that all haemodynamic parameters, and their variation resulting from different blood models, are strictly related to the model geometry and imposed boundary conditions. The results obtained during this research indicate that blood can be simplified to the Newtonian fluid model when cerebral vasculature is analysed, whereas for the CCA bifurcation and large vessels network it should be modelled as a shear-thinning fluid. Therefore, regardless of the geometry topology, boundary conditions and simulation type, it is more advisable to provide formulas that describe the non-Newtonian behaviour of blood. Otherwise, the simulation might be oversimplified while the results might be underestimated.

## REFERENCES

1. Reorowicz P, Obidowski D, Kłosinski P, Szubert W, Stefanczyk L, Jóźwik K. Numerical simulations of the blood flow in the patient-specific arterial cerebral circle region. *J Biomech.* 2014;47(7):1642–51.
2. Caballero AD, Lain S. Numerical simulation of non-Newtonian blood flow dynamics in human thoracic aorta. *Comput Methods Biomed Engin.* 2015;18(11):1200–16.
3. Doost SN, Zhong L, Su B, Morsi YS. The numerical analysis of non-Newtonian blood flow in human patient-specific left ventricle. *Comput Methods Programs Biomed* [Internet]. 2016;127:232–47. Available from: <http://dx.doi.org/10.1016/j.cmpb.2015.12.020>
4. Johnston BM, Johnston PR, Corney S, Kilpatrick D. Non-Newtonian blood flow in human right coronary arteries: Steady state simulations. *J Biomech.* 2004;37(5):709–20.
5. Jodko D, Jeckowski M, Tyfa Z. Fluid structure interaction versus rigid-wall approach in the study of the symptomatic stenosed carotid artery: Importance of wall compliance and resilience of loose connective tissue. *Int J Numer Method Biomed Eng.* 2022;38(8):1–23.
6. Reorowicz P, Tyfa Z, Obidowski D, Wiśniewski K, Stefanczyk L, Jóźwik K, et al. Blood flow through the fusiform aneurysm treated with the Flow Diverter stent – Numerical investigations. *Biocybern Biomed Eng.* 2022;42(1):375–90.
7. Tyfa Z, Obidowski D, Reorowicz P, Stefanczyk L, Fortuniak J, Jóźwik K. Numerical simulations of the pulsatile blood flow in the different types of arterial fenestrations: Comparable analysis of multiple vascular geometries. *Biocybern Biomed Eng.* 2018;38(2):228–42.
8. Wiśniewski K, Tomasik B, Tyfa Z, Reorowicz P, Bobeff EJ. Porous Media Computational Fluid Dynamics and the Role of the First Coil in the Embolization of Ruptured Intracranial Aneurysms. *J Clin Med.* 2021;10(7):1348.
9. Cho YI, Kensey KR. Effects of the non-Newtonian viscosity of blood on flows in a diseased arterial vessel. Part 1: Steady flows. *Biorheology.* 1991;28(3–4):241–62.
10. Gijssen FJH, Van De Vosse FN, Janssen JD. The influence of the non-Newtonian properties of blood on the flow in large arteries: steady flow in a carotid bifurcation model. *J Biomech.* 1999;32(7):705–13.
11. Shinde S, Mukhopadhyay S, Mukhopadhyay S. Investigation of flow in an idealized curved artery: comparative study using cfd and fsi with newtonian and non-newtonian fluids. *J Mech Med Biol* [Internet]. 2022;22:2250010. Available from: <https://doi.org/10.1142/S0219519422500105>
12. Boyd J, Buick JM. Comparison of Newtonian and non-Newtonian flows in a two-dimensional carotid artery model using the lattice Boltzmann method. *Phys Med Biol.* 2007;52(20):6215–28.
13. Mendieta JB, Fontanarosa D, Wang J, Paritala PK, McGahan T, Lloyd T, et al. The importance of blood rheology in patient-specific computational fluid dynamics simulation of stenotic carotid arteries. *Biomech Model Mechanobiol* [Internet]. 2020;19(5):1477–90. Available from: <https://doi.org/10.1007/s10237-019-01282-7>.
14. Razavi A, Shirani E, Sadeghi MR. Numerical simulation of blood pulsatile flow in a stenosed carotid artery using different rheological models. *J Biomech* [Internet]. 2011;44(11):2021–30. Available from: <http://dx.doi.org/10.1016/j.jbiomech.2011.04.023>
15. Johnston BM, Johnston PR, Corney S, Kilpatrick D. Non-Newtonian blood flow in human right coronary arteries: Transient simulations. *J Biomech.* 2006;39(6):1116–28.
16. Karimi S, Dabagh M, Vasava P, Dadvar M, Dabir B, Jalali P. Effect of rheological models on the hemodynamics within human aorta: CFD study on CT image-based geometry. *J NonNewton Fluid Mech* [Internet]. 2014;207:42–52. Available from: <http://dx.doi.org/10.1016/j.jnnfm.2014.03.007>
17. Celik IB, Ghia U, Roache PJ, Freitas CJ, Coleman H, Raad PE. Procedure for estimation and reporting of uncertainty due to discretization in CFD applications. *J Fluids Eng Trans ASME.* 2008;130(7):0780011–4.
18. Obidowski D, Reorowicz P, Witkowski D, Sobczak K, Jóźwik K. Methods for determination of stagnation in pneumatic ventricular assist devices. *Int J Artif Organs.* 2018;41(10):653–63.
19. Rayz VL, Boussel L, Lawton MT, Acevedo-Bolton G, Ge L, Young WL, et al. Numerical modeling of the flow in intracranial aneurysms: Prediction of regions prone to thrombus formation. *Ann Biomed Eng.* 2008;36(11):1793–804.
20. Logerfo FW, Nowak MD, Quist WC. Structural details of boundary layer separation in a model human carotid bifurcation under steady and pulsatile flow conditions. *J Vasc Surg.* 1985;2(2):263–9.
21. Subramaniam T, Rasani MR. Pulsatile CFD Numerical Simulation to investigate the effect of various degree and position of stenosis on carotid artery hemodynamics. *J Adv Res Appl Sci Eng Technol.* 2022;26(2):29–40.
22. Nagai Y, Kemper MK, Earley CJ, Metter EJ. Blood-flow velocities and their relationships in carotid and middle cerebral arteries. *Ultrasound Med Biol.* 1998;24(8):1131–6.
23. Pomella N, Wilhelm EN, Kolyva C, González-Alonso J, Rakobowchuk M, Khir AW. Common Carotid Artery Diameter, Blood Flow Velocity and Wave Intensity Responses at Rest and during Exercise in Young Healthy Humans: A Reproducibility Study. *Ultrasound Med Biol.* 2017;43(5):943–57.
24. Soleimani E, Mokhtari-Dizaji M, Fatouraei N, Saberi H. Assessing the blood pressure waveform of the carotid artery using an ultrasound image processing method. *Ultrasonography.* 2017;36(2):144–52.
25. Lantz BM, Forester JM, Link DP, Holcroft JW. Regional distribution of cardiac output: normal values in man determined by video dilution technique. *Am J Roentgenol.* 1981;137(5):903–7.
26. Stein PD, Sabbah HN, Anbe DT, Walburn FJ. Blood velocity in the abdominal aorta and common iliac artery of man. *Biorheology.* 1979;16(3):249–55.
27. Bruss ZS, Raja A. Physiology, Stroke Volume. In: StatPearls Publishing; 2022.
28. Czernicki Z. Fizjologia mózgowego przepływu krwi. In: Czepko R, editor. Wybrane zagadnienia diagnostyki i leczenia malformacji naczyniowych ośrodkowego układu nerwowego. Uniwersytet Jagielloński - Wydawnictwo Uniwersytetu Jagiellonskiego; 2007. 15–20.

29. Xing CY, Tarumi T, Liu J, Zhang Y, Turner M, Riley J, et al. Distribution of cardiac output to the brain across the adult lifespan. *J Cereb Blood Flow Metab.* 2017;37(8):2848–56.
30. Majka J. Fizjologia krążenia mózgowego. In: Szczudlik A, Czonkowa A, Kwieciński H, Słowiak A, editors. *Udar mózgu.* 1st ed. Kraków: Wydawnictwo Uniwersytetu Jagiellońskiego; 2007:26–41.
31. Seidel E, Eicke BM, Tettborn B, Krummenauer F. Reference values for vertebral artery flow volume by duplex sonography in young and elderly adults. *Stroke.* 1999;30(12):2692–6.
32. Amin-Hanjani S, Du X, Pandey DK, Thulborn KR, Charbel FT. Effect of age and vascular anatomy on blood flow in major cerebral vessels. *J Cereb Blood Flow Metab.* 2015;35(2):312–8.
33. Zarrinkoob L, Ambarki K, Wåhlin A, Birgander R, Eklund A, Malm J. Blood flow distribution in cerebral arteries. *J Cereb Blood Flow Metab.* 2015;35(December 2014):648–54.
34. Apostolidis AJ, Moyer AP, Beris AN. Non-Newtonian effects in simulations of coronary arterial blood flow. *J NonNewton Fluid Mech [Internet].* 2016;233:155–65. Available from: <http://dx.doi.org/10.1016/j.jnnfm.2016.03.008>
35. Gharahi H, Zambrano BA, Zhu DC, DeMarco JK, Baek S. Computational fluid dynamic simulation of human carotid artery bifurcation based on anatomy and volumetric blood flow rate measured with magnetic resonance imaging. *Int J Adv Eng Sci Appl Math.* 2016;8(1):46–60.
36. Moradieghamah J, Sadeghiseraj J, Jahangiri M. Numerical solution of the Pulsatile, non-Newtonian and turbulent blood flow in a patient specific elastic carotid artery. *Int J Mech Sci [Internet].* 2019;150(October 2017):393–403. Available from: <https://doi.org/10.1016/j.ijmecsci.2018.10.046>
37. Razavi SE, Farhangmehr V, Zendeali N. Numerical investigation of the blood flow through the middle cerebral artery. *BiolImpacts [Internet].* 2018;8(3):195–200. Available from: <https://doi.org/10.15171/bi.2018.22>
38. Oliveira IL, Santos GB, Gasche JL, Militzer J, Baccin CE. Non-Newtonian Blood Modeling in Intracranial Aneurysm Hemodynamics: Impact on the Wall Shear Stress and Oscillatory Shear Index Metrics for Ruptured and Unruptured Cases. *J Biomech Eng [Internet].* 2021;143(7):071006. Available from: <https://doi.org/10.1115/1.4050539>

This work has been accomplished under the part of the research project No. LIDER/12/0056/L-10/18/NCBR/2019 financed by Polish National Centre for Research and Development.

Zbigniew Tyfa:  <https://orcid.org/0000-0001-9870-8370>

Reorowicz Piotr:  <https://orcid.org/0000-0003-0585-0488>

Obidowski Damian:  <https://orcid.org/0000-0002-8950-6424>

Jóźwik Krzysztof:  <https://orcid.org/0000-0002-7596-3691>



This work is licensed under the Creative Commons BY-NC-ND 4.0 license.

# THE INNOVATIVE POST-WELD FINISHING METHOD AND NON-STANDARD CUTTING TOOL FOR CARRYING OUT THIS METHOD

Olha Dvirna\*

\*Faculty of Marine Engineering, Department of Engineering Sciences, Gdynia Maritime University,  
ul. Morska 81-87, 81-225 Gdynia, Poland

[o.dvirna@wm.ugm.edu.pl](mailto:o.dvirna@wm.ugm.edu.pl)

received 31 December 2022, revised 30 June 2023, accepted 6 July 2023

**Abstract:** The most common method of post-weld finishing is grinding with an abrasive tool. This finishing method leads to the occurrence of faults on the treated surface: locations missed or hardened twice, structural notches and stretching residual stress in the surface layer. The faults mentioned lead to the creation and development of ordinary as well as fatigue cracks, seizing or other damage. In addition, grinding is a process that often involves manual labour, which significantly increases the time required for finishing the procedure. Moreover, it is impossible to automate this process. Also, grinding is a process that is damaging for both people and the environment. In contrast to grinding and other processes of post-weld surface finishing, the innovative method, which is the subject of this article, does not have the faults and inconveniences of the previously mentioned techniques. The post-weld surface finishing method by moving of the innovative multi-edge cutting tool along the weld bead is presented in this article. In this method, machining allowance is treated as the weld bead height, which is flush-removed with the base material in one step during one pass of the cutting tool. The adjacent teeth height of changing and increasing according to the direction of feed and the difference in height between the first and last teeth are equal to the weld bead height. The number of cutting teeth necessary to flush-finish the weld bead with the base metal surface depends on the difference in the first and last teeth height and how it is divided. The tooth length is greater than half of the distance between the adjacent cutting teeth, which enables finishing the heterogeneous post-weld surface with many defects and increased hardness. The innovative method is characterised by short machining time of the weld bead and provides an accurate, efficient and economical process.

**Key words:** weld bead surface, physical model, broaching, multi-edge cutting tool

## 1. INTRODUCTION

In industrial enterprises, the most common method of post-weld finishing of surfaces is grinding with an abrasive tool of different shapes and using different abrasive materials. This finishing method leads to the occurrence of faults on the treated surface. The faults include locations missed or hardened twice, which creates structural notches in the surface layer, while also collecting residual stress (stretching) in these locations. The faults mentioned lead to the creation and development of ordinary as well as fatigue cracks and seizing and other damage. During the operation of welded constructions, the fatigue limit can be reduced, which can result in the destruction of the welded elements [1]. In addition, grinding is a process that often involves manual labour, which significantly increases the time required for finishing and impossibility of automating this process. Also, grinding is a process that is damaging for both people and the environment and necessitates the use of additional protective measures.

The innovative post-weld finishing method is a process of mechanical cutting, in which weld bead is removed flush with the base material in one pass of the tool. This process is characterised by the short machining time of the weld and high efficiency. In addition, this tool ensures a low level of deviations in terms of shape and position as well as exceptionally high machining accuracy and high quality of the surface layer with a surface roughness  $R_a = 0.32-2.5 \mu\text{m}$ . While helpful in eliminating unwanted welding defects on the bead surface due to the presence of cutting tool of

the last two teeth of the same height and special geometry, the material removed in the form of chips accumulates in the chip flutes between adjacent blades. The shape and dimensions of the flutes depend on the shape, dimensions and properties of the weld bead material, the bead length and the feed per cutting edge. The feed value results from the design of the tool, with a gradual increase in the cutting teeth height, equivalent to the difference between adjacent edges (increment per one tooth). Wear of a properly designed tool is slow as its edges have a long service life thanks to the increased resistance to shock loads caused by increased tooth length. The work of the tool can be carried out on horizontal and vertical presses or machines of various types and designs. Depending on where the force is applied to the tool, it will be subjected to stretching or compression. The post-weld surface finishing method offers cost-effective machining, eliminating the need for skilled operators. Moreover, it demonstrates the capability to cut multiple weld beads arranged consecutively (continuous cutting) and enables the potential automation of the finishing process.

In the Polish patent document [2] can be seen a method and a device for grinding external longitudinal welds that involve grinding off the weld at a tangent to the surface of the external longitudinal weld and also along the weld with at least three passes of the grinder head preceded by rotation of the weld. The grinding equipment consists of a grinder head seated snugly in a support, a motor unit and a positioning device. The grinder head is fitted with a contact roller that is perpendicular to the line of the external

longitudinal weld and comprises a tension roller, grinding tape, guide roller and pressure spring.

In patent document [3] can be seen a method and a milling machine for machining ridge welds of roller elements that have been joined together. The method involves movement of the ridge milling machine in a flat position, using chains, around the circumference of the connected cylindrical elements placed on a rotator, with the milling cutter's end mill removing the excess from the ridge of the weld previously placed on the joint of the elements that have been joined together. The milling machine consists of a housing, a hydraulic drive block for the cutter with a mechanism for regulating the depth of the milling, a hydraulic drive block for turning the wheels used for moving the milling machine to the lateral surface of the joined roller sections using chains, rollers leading the miller along the weld groove, a mechanism for correcting the movement of the cutter along the ridge of the weld and a mechanism for pulling the chains.

The application in the literature [4] discloses a method and device for machining a joint between two elements, in which a connecting material in the form of a weld is applied along the joint, then the joint of the connecting material is machined to a given cross-sectional shape by a profile cutting tool moved along the joint, and removing the outer layer from it, while at the same time clearing the machined outer layer by suction. What is advantageous is that a polyurethane-based sealant can be used as the connecting material. The tool that is appropriate for this purpose includes a suction nozzle with a suction opening and a cutting tool mounted on its edge; this tool can remove and guide the upper weld layer of the connecting material into the suction opening for removal to the outside.

In German patent document [5], it can be seen that the invention is related to a deforming and cutting broaching tool which has cutting and calibrating teeth and a deforming element fitted in front of the cutting teeth. The patent describes several design solutions of deforming and cutting tool for broaching holes and grooves. The main idea is the design of the deforming element with projections which result in a deforming and cutting broach, with the aid of which longitudinal grooves are formed on the surface to be machined, dividing this surface into sections which are limited in width. These sections are then machined from the incisors with continuous cutting edges. The width of the separated chip corresponds to the width of the respective section. As a result, the otherwise indispensable execution of chip separation grooves on the cutting teeth of the broach is eliminated. Owing to the omission of rapidly wearing angular sections of the cutting edges, the service life of the cutting teeth is significantly increased. In addition, the design of the cutting teeth with a continuous cutting edge contributes to reducing the workload in the manufacture and sharpening of the deforming and cutting broach. Since the height of the projections of the deforming element essentially determines the overall infeed of the cutting teeth, the compaction of the metal takes place in the depth of the grooves thereby formed, and the cutting teeth of the broach cut off sections of uncompact metal, which makes it possible to cut not only soft metals but also be able to process metals with greater hardness. Most advantageously, these forming and cutting broaches can be used for machining bores as well as for machining grooves and flat, stepped surfaces.

However, the design solutions of the forming and cutting broaches presented in this patent cannot be used for post-weld surface finishing, although they have similar elements. First of all, during post-weld surface finishing, it is not permissible to pen-

trate deep into the base material and form a groove on the weld surface. The weld bead can only be removed flush with the base material. Otherwise, the welded joint loses its reliability. Therefore, the tool for post-weld surface finishing must be designed in such a way that the difference in the first and last teeth height is equal to the weld bead height and the teeth width is equal to the maximum of the weld bead width. The total number of teeth necessary to finish flush the weld bead with the base metal surface must depend on the weld bead height (the difference in the first and last teeth height).

In addition, the tool teeth must have a specific geometry and an increased tooth length, so that the cutting process can occur without destruction of the cutting edge in interrupted cutting conditions with shock loads. The last teeth of the tool described in the patent are the calibration teeth. They serve to reduce the roughness of the machined surface. However, when processing a weld, the surface roughness is not of great importance. A much more important challenge is the elimination of fractures, craters, pores and other weld defects. In contrast to the solutions shown in this patent, the method which is the subject of this invention satisfies all the requirements described above.

In contrast to the grinding and other modern methods of post-weld surface finishing, the process of weld bead broaching, which is the subject of this article, does not have the faults and inconveniences found previously [6, 7].

## 2. RESEARCH MATERIALS AND METHODOLOGY

For processing various complex surfaces of different dimensions, shape and quality within one machining cycle (e.g. welded surfaces), it is necessary to use a non-standard cutting tool with a specialised design adapted to specific conditions: a multi-edged tool for post-weld surface finishing, thanks to the appropriate shape and cutting teeth location, correctly adjusted to the finishing conditions on the basis of strength calculations. This tool is used in the following conditions: intermittent cutting caused by the shape and properties of the weld bead surfaces, uneven machining allowance, variable number of simultaneously working (active) edges, discontinuity of the machining process, periodically changing or impact loads on the cutting, heterogeneity of the weld bead material and increase in tool wear.

These types of finishing conditions are characterised by variable loads on the cutting tool due to a cyclical cutting of the edges into the bead when the cutting force changes from  $P_{min} = 0$  to  $P_{max}$ , causing non-cyclic loads.

The invention makes it possible to finish complex weld bead surfaces of various shapes and dimensions, various grades of steel and alloys, as well as automating the process, increasing efficiency and reducing the labour intensity of the machining process.

A tool which is a physical model of the broaching process was used for the research in the first phase [8–10]. Therefore, in order to carry out the research, a cutting tool of a special design was manufactured with changing cutting elements made of high-speed steel SW7M (HS6-5-2); then it underwent heat treatment (hardening at a temperature of 1,250°C and tempering at a temperature of 560°C to a hardness of HRC 62–65). The cutting element geometry was identical to the innovative cutting tool geometry which was used for weld bead broaching [10]. Four samples with the dimensions shown in Fig. 1. made of S235JR steel were prepared for testing.

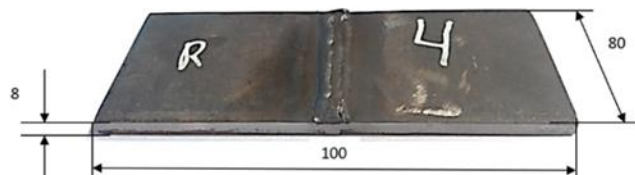


Fig. 1. Test sample displaying dimensions in millimetres

Samples were prepared for machining on the SZ-400 Planer, with welded samples using the different methods before and after planning, as shown in Fig. 2.

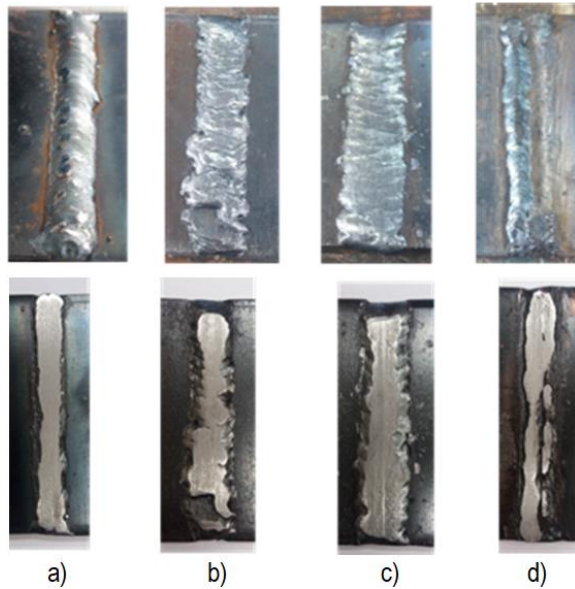


Fig. 2. Welded beads before and after planning: a) semi-automatic welding machine, welding amperage  $I_{weld} \approx 95A$ ; b) semi-automatic welding machine, CO2,  $I_{weld} \approx 110A$ ; c) semi-automatic welding machine, CO2; Corefil 100R Metalweco wire  $\varnothing 1.2$  mm;  $I_{weld} \approx 90 - 110A$ ; d) manual metal arc welding (MMA),  $I_{weld} \approx 90A$

The experiment has shown a stable cutting process with good quality of the treated surface. Therefore, we started the second phase of the research related to the calculation and design of the non-standard multi-edge cutting tool, the fixture for its fastening and the choice of the machine for testing of the innovative method in an industrial environment.

### 3. CALCULATIONS AND DESIGN

In order to prepare the multi-edged tool for post-weld surface finishing intended for machining a specific batch of weld-joints, it is necessary to design it using existing calculation methods [11–17], but also applying new non-standard solutions.

In order to calculate and design the multi-edged tool, a set of welded joints were prepared using various welding methods (MMA, MIG, TIG). The test samples were made of S235JR steel and were prepared for testing as shown in Fig. 3.

First of all, the machining allowance  $q_p$  is determined. When finishing the weld bead flush with the base metal surface, the allowance  $q_p$  is treated as the weld bead height  $H_s$  (Fig. 4), which is limited by the surfaces of the finished object  $a_p$  and the weld

bead  $a_s$  and is equal to the difference in the first and last cutting teeth height.

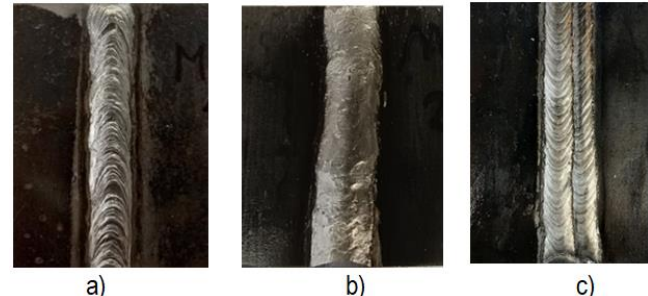


Fig. 3. Welded joints produced using various welding methods: a) MMA; b) MIG; c) TIG

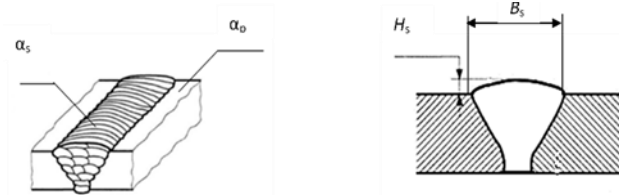


Fig. 4. Weld bead elements

In order to determine the machining allowance  $q_p$  it is necessary to measure the weld beads height  $H_s$ , then statistical analysis of measuring results is carried out. Before calculation and designing of the cutting tool, the maximum dimensions of the weld beads are determined for processed seams in the batch. On the basis of the analysis performed, the extreme weld bead height  $H_s$  and the weld bead width  $B_s$  are determined (Fig. 4). In the welded samples under consideration, the maximum weld bead height  $H_{smax} = 3$  mm and the maximum weld bead width  $B_{smax} = 15$  mm. Consequently, the machining allowance  $q_p = H_{smax} = 3$  mm. After determining the machining allowance  $q_p$ , the value of the feed per tooth  $a$  (thickness of cut layer) needs to be established. The division of the allowance at rectilinear edges is the division of the allowance thickness on the total width of the machining (Fig. 5).

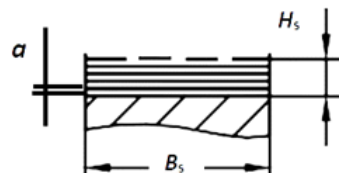


Fig. 5. Division of machining allowance at rectilinear cutting edges

In the example, the thickness of the layer being cut is  $a = 0.2$  mm. Its value was selected with reference to the shape and geometry cutting teeth, the type of the material being processed and the technical capabilities of the machine tool (press).

The next step in the design of the tool is to determine the geometry of the cutting edge. For finishing flat surfaces, cutting teeth are made with an inclination of angle  $\omega^\circ$ , which reduces the concentration of the cutting force on the cutting edge. The angle of inclination of the cutting edges can be  $0^\circ$ ,  $10^\circ$ ,  $15^\circ$  or  $20^\circ$  [14].

The direction of chip flow depends on the inclination angle of the edge and should ensure free removal of chips from the surface of the workpiece without the interaction of the cut material (chips) with adjacent cutting teeth. After selecting the angle of

inclination of the cutting edge, a checking process to determine whether the value of the lateral cutting force  $P_x$ , arising at  $\omega \neq 0^\circ$  (Fig. 6), will not push the cutting tool away.

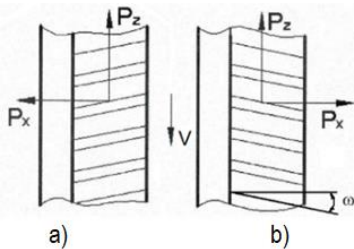


Fig. 6. The system of cutting forces in tools with the inclination of the cutting edges [14]

In the case shown in Fig. 6a, the direction of the side force  $P_x$  will press the cutting tool against the tool body and will not adversely affect the machining process. However, in the case shown in Fig. 6b, the direction of the side force  $P_x$  will cause repulsion, which may have a negative impact on the machining accuracy and will require the use of additional equipment (compensators). However, the use of inclined edges complicates the tool-making process and increases the time required and cost. For these reasons,  $\omega = 0^\circ$  was assumed [14].

To ensure reliable operation of the tool under shock loads, it was necessary to strengthen the teeth of the tool. The approximate value of the cutting teeth pitch  $P_p$  is determined using the formula:

$$P_p = (2.25 \dots 3)\sqrt{L} \quad (1)$$

where  $L$  is the weld bead length in millimetres, ensuring trouble-free chip removal.

At the same time, tooth length dimension  $g$  was increased, strengthening the cutting edge, without changing the length of flute  $k$ , which is set using the following formula:

$$k = (1.05 \dots 0.95)\sqrt{L} \quad (2)$$

The edge height  $h$  is determined in the range:

$$h = (0.55 \dots 0.7)\sqrt{L} \quad (3)$$

The rake angle  $\gamma$  of the cutting edges is determined depending on the type and properties of the processed material. A rake angle of  $\gamma = 20^\circ$  is used. The application angle  $\alpha$  is determined depending on the machining stage [15]: stripping blades  $\alpha = 3^\circ$ ; cutting edges  $\alpha = 2 \dots 3^\circ$ ; finishing edges  $\alpha = 1^\circ$  and spare edges  $\alpha = 0^\circ 30'$ . In the example, the application angle is  $\alpha = 3^\circ$  [14].

The remaining parameters of cutting tooth are determined using the formula:

$$g = P_p - k, \quad r = (0.5 \dots 0.6)h, \quad R = (0.65 \dots 0.8)P_p \quad (4)$$

where  $P_p$  is the pitch value of cutting teeth,  $g$  is the tooth length,  $k$  is the flute length,  $r$  is the radius of the bottom of the flute and  $h$  is the edge height.

After determining the geometry of the cutting teeth, the strength of the multi-edged tool for post-weld surface finishing is checked, depending on the cutting forces. Changes in cutting force values when machining welded surfaces can be caused by the difference in the height of the removed weld, a variable number of simultaneously working (active) teeth, a change in the

properties (heterogeneity) of the processed post-weld material, and the formation and disappearance of build-ups in the chip formation process.

Depending on the value of the change in cutting force  $F$ , there are three varieties of tool load [11]: constant, periodically varying from  $F_{min}$  to  $F_{max}$  and pulsating.

The variation of the tool load can be determined by the following coefficients:

- load constancy factor  $u$ :

$$u = \frac{F_s}{F_a} \quad (5)$$

where  $F_s$  is the average value of the cutting force and  $F_a$  is the amplitude of the cutting force.

$$F_s = \frac{F_{max} + F_{min}}{2}, \quad F_a = \frac{F_{max} - F_{min}}{2} \quad (6)$$

- the load variation coefficient  $e$  is the inverse of the load constancy coefficient:

$$e = \frac{1}{u} = \frac{F_a}{F_s} \quad (7)$$

- load cycle asymmetry coefficient  $r$ :

$$r = \frac{F_{min}}{F_{max}} \quad (8)$$

- the dynamic load factor  $\zeta$  is the inverse of the load cycle asymmetry factor:

$$\zeta = \frac{1}{r} = \frac{F_{max}}{F_{min}} \quad (9)$$

In the process of innovative weld finishing, we assume tool loads periodically varying from  $F_{min}$  to  $F_{max}$ . This variation depends on the number of simultaneously working (active) edges contained in the range from

$$Z_{min} = 2 \text{ to } Z_{max} = 8, \text{ where } Z_{max} = Z_{min} + 1.$$

The load variation coefficients will be [11,12]:

$$u = \frac{F_s}{F_a} = \frac{F_{max} + F_{min}}{F_{max} - F_{min}} = \frac{F_z Z_{max} + F_z Z_{min}}{F_z Z_{max} - F_z Z_{min}} =$$

$$= \frac{F_z (Z_{min} + 1) + F_z Z_{min}}{F_z (Z_{min} + 1) - F_z Z_{min}} = 2Z_{min} + 1;$$

$$e = \frac{1}{u} = \frac{F_a}{F_s} = \frac{1}{2Z_{min} + 1};$$

$$r = \frac{F_{min}}{F_{max}} = \frac{Z_{min}}{Z_{min} + 1};$$

$$\zeta = \frac{1}{r} = \frac{F_{max}}{F_{min}} = \frac{Z_{min} + 1}{Z_{min}} \quad (10)$$

The numerical values of the coefficients are shown in Tab. 1.

Tab. 1 Numerical values of coefficients of variation of tool loading

Number of simultaneously operating edge	Load variation coefficients			
	$u$	$e$	$r$	$\zeta$
from 1 ....2	5	0,200	0,667	1,500
3	7	0,143	0,750	1,333

4	9	0,111	0,800	1,250
5	11	0,090	0,833	1,200
6	13	0,077	0,857	1,167
7	15	0,067	0,875	1,143
8 to 10	17	0,059	0,889	1,125

From the analysis of the above numerical dependence of the coefficient values, the obvious conclusion is that as the number of simultaneously working (active) edges increases, the load variation decreases.

As shown above, the cutting force when machining post-weld surfaces varies from  $F_{min}$  to  $F_{max}$ . On the other hand, the cutting force can take over not only positive values, but also be zero  $F_{min} \geq 0$ . At the moment when the active blades of the cutting tool lose contact with the machined surface, the value of the cutting force of the smallest  $F_{min} = 0$ . The actual change in forces takes place only in the positive range, and the stresses on the tool material caused by the action of such a cutting force will carry the same character.

$$F \in [0 - F_{max}], \sigma \in [0 - \sigma_{max}] \quad (11)$$

Unilateral alternating stresses  $\sigma_j$  can be compared with the fatigue strength  $Z_j$  of the tool material. Then the allowable es  $k_j$  are determined relative to the fatigue strength after assuming a certain value of the safety factor  $x_z$ :

$$\sigma_j = \frac{F_{max}}{A} \leq k_j, \quad k_j = \frac{Z_j}{x_z} = \frac{0.6 \cdot 2100}{4,85} = 260 \text{ MPa} \quad (12)$$

The value of the fatigue strength for unilateral stresses of high-speed steel (approximately) is expressed in relation to the static strength  $R_m$  with the relation  $Z_j = (0.5 \dots 0.75)R_m$ .

For the design of the tool, we adopted the material high-speed steel SW7M (HS6-5-2) subjected to heat treatment (quenching at 1,250°C and tempering at 560°C to hardness HRC 62–65). For this material, we assume an intermediate value  $Z_j = 0,6R_m$  and an ultimate strength 2,100 MPa.

We determine the safety factor  $x_z$  from the formula:

$$x_z = \beta\gamma\delta = 1.72 \cdot 1.39 \cdot 2.03 = 4.85 \quad (13)$$

where  $\beta$  is the stress concentration factor ( $\beta = 1.72$ ), it depends on the condition of the surface layer;  $\gamma$  is the tool size factor ( $\gamma = 1.39$ ) and  $\delta$  is the actual safety factor ( $\delta = 2.03$ ).

The actual safety factor can be expressed by the product of four partial coefficients:

$$\delta = \delta_I \delta_{II} \delta_{III} \delta_{IV} = 1.35 \cdot 1.05 \cdot 1.3 \cdot 1.1 = 2.03 \quad (14)$$

where  $\delta_I$  is the material strength spread factor ( $\delta_I = 1.35$ );  $\delta_{II}$  is the material control quality factor ( $\delta_{II} = 1.05; 1.1; 1.15$ );  $\delta_{III}$  is the tool validity factor ( $\delta_{III} = 1.3$ );  $\delta_{IV}$  is the machining quality factor (rough machined ( $\delta_{IV} = 1.04 \dots 1.07$ ) or raw ( $\delta_{IV} = 1.07 \dots 1.1$ )). All values of the coefficients are selected for the conditions of approximation for broaching (pushing) of post-weld surfaces with the SW18 high-speed steel tool based on the data in the publication [12].

When designing a pushover, it is necessary to check the conditions of compressive strength and buckling.

The compressive stress that occurs in the pusher material should be less than its permissible value:

$$\sigma_c = \frac{F}{A} \leq k_c \quad (15)$$

where  $\sigma_c$  is the compressive stress;  $F$  is the compressive force of the pusher;  $A$  is the area of the dangerous smallest section and  $k_c$  is the permissible compressive stress.

When the compressed tool has a high slenderness the danger of buckling arises. The slenderness of the pusher is determined from the formula:

$$\lambda = L \sqrt{\frac{A}{J_A}} \quad (16)$$

where  $L$  is the length of the pusher and  $J_A$  is the moment of inertia in  $\text{mm}^4$  of the dangerous cross-sectional area  $A = BH \text{ mm}^2$ .

Taking into account that the moment of inertia of a rectangular section is:

$$J_A = \frac{BH^3}{12} \quad (17)$$

is determined:

$$\lambda^2 = 12L^2 \frac{BH}{BH^3} = \frac{12L^2}{H^2} \quad (18)$$

Elastic buckling of the pusher occurs when the critical value of compressive stress is reached, calculated from Euler's formula:

$$R_{kr} = \frac{k_0 E}{\lambda^2} \quad (19)$$

where  $k_0$  is a coefficient that depends on how the ends of the pusher are fixed ( $k_0 = 9.87$ ),  $E$  is the the longitudinal modulus of elasticity for high-speed steel  $E = 2.2 \cdot 10^5 \text{ MPa}$ .

After calculating the permissible compressive stresses and buckling of the pusher, the lower value from these calculations is taken for further design.

The final design stage involves the creation of a dimension table for the teeth of the multi-edged tool, determining its total length and preparing a shop drawing for the tool. Before creating the table, it is necessary to determine the nominal values of the total height of the cross-section for each tooth.

The final design stage involves the creation of a dimension table for the teeth of the multi-edged tool, determining its total length and preparing a shop drawing for the tool. Before creating the table, it is necessary to determine the nominal values of the total height of the cross-section for each tooth.

The value of the section height of each successive tooth increases by the value of the feed per one tooth  $a$  (thickness of the cut layer). So the height of the  $H_i$  – tooth is given by the formula:

$$H_i = H_1 + (i - 1) \quad (20)$$

The table is filled in until the shop drawing is started and it contains the numbers of all the teeth in turn, their height with deviations and the value of the application angle  $\alpha^\circ$  as appropriate for each group of the teeth (Tab. 2).

The total number of teeth  $Z_o$  necessary to finish flush the weld bead with the base metal surface is dependent on the weld bead height (the difference in the first and last teeth height – machining allowance  $q_p$ ):

$$Z_o = \frac{q_p}{a} + 1 \quad (21)$$

where  $a$  is the thickness of the cut layer in millimetres.

Tab. 2. Parameters of cutting teeth

Angle of application	$\alpha = 3^\circ$																
Deviation	- 0.02																
Tooth number	1	2	3	4	5	6	7	8	9	10	11	12	13	14	15	16	17
Tooth height $H_i$ , mm	30.0	30.2	30.4	30.6	30.8	31.0	31.2	31.4	31.6	31.8	32.0	32.2	32.4	32.6	32.8	33.0	33.0

The one in the above dependence results from the fact that the first tooth is made of the same dimensions as the leading part, so it does not participate in the cutting process. The total number of teeth was increased by adding the penultimate and last teeth, which have the same height to eliminate crack, craters, pores and other weld defects.

The cutting tool is then manufactured in a traditional manner in accordance with the calculated parameters and specific cutting tooth geometry [10–12]. It is mounted in the machine tool or press holder, and moved along the weld bead. The weld bead can only be removed flush with the base material. Otherwise, the welded joint loses its reliability.

#### 4. TECHNOLOGY DEVELOPMENT

The thesis of the process of creating an innovative method is effective removal of the weld root (face) in open areas with different types of welded joints with a guarantee of maintaining shape accuracy and high requirements to the quality of the surface layer while ensuring the safety of work and the non-obtrusiveness of the process to man and the environment. According to the stated thesis, several important assumptions were formulated, which were taken into account during the development of innovative weld finishing technology:

- the machining process of the cutting tool that is the subject of the present invention is a machining process of chip machining, in which the entire machining allowance must be cut within one pass of the tool;
- such a process is to provide a short weld machining cycle time and high productivity;
- the tool is to provide low deviations in shape and position and high machining accuracy and surface layer quality with a surface roughness of no more than  $R_a = 0.32\text{--}2.5$  [ $\mu\text{m}$ ];
- the invention must make it possible to machine complex weld surfaces of different dimensions, from different steels and alloys;
- the method is to increase productivity and reduce the labour intensity of the machining process.

The Hydraulic Broaching machines BM25 NARGESA was chosen for the implementation of this technology. The machine BM25, has been thought for small medium productions and is characterised by its great versatility, reliability, easy use, fast setting up, effectiveness and incorporates all safety devices according to CE regulations. The majority characteristics of the machine are motor power – 2,2 Kw; 3-phased tension – 230/400 V; hydraulic power – 10 t; max. broaching capacity – 25 mm; working speed – 24 mm/s; return speed – 54 mm/s and bench dimensions – 420 mm x 420 mm.

The specialised device shown in Fig. 7 was designed and manufactured for homing and fixing the sample (welded joint) and the cutting tool.

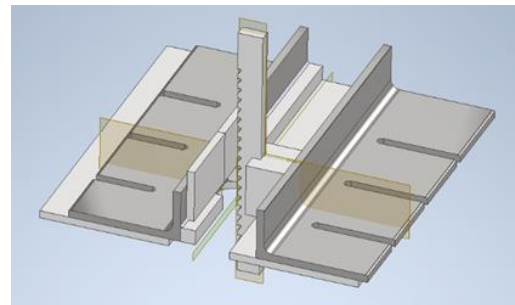


Fig. 7. The device for realising the innovative post-weld finishing method [18]

As a result of the design and calculations, the weld beads finishing technology was developed in accordance with the innovative method (Fig. 8).

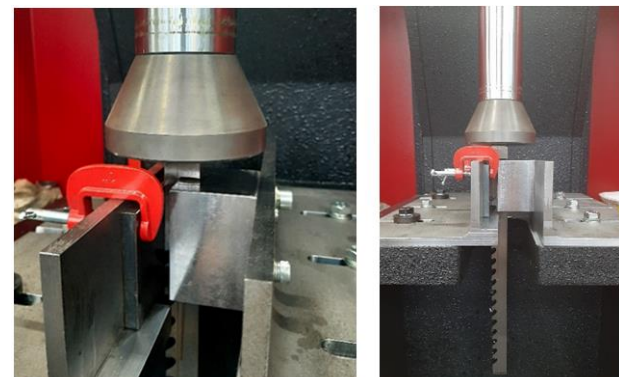


Fig. 8. Finishing of the butt weld joint using the innovative method and tool [18, 19]

In order to verify (test) the developed technology, samples of butt welded joints were made of different materials: unalloyed structural steel, stainless steel and aluminium alloy were subjected to mechanical treatment. The samples after removing the weld face according to the innovative method are shown in Fig. 9.

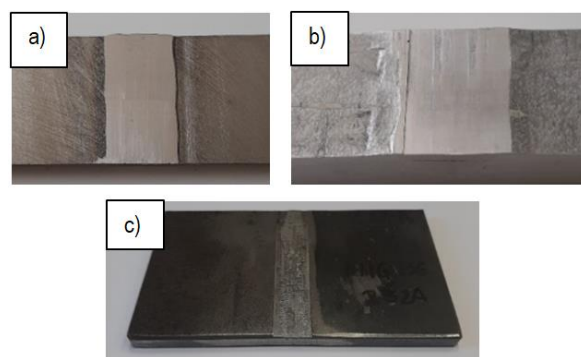


Fig. 9. Weld bead after the finishing [18, 19]: a) stainless steel 1.3964; b) aluminium alloy PA47(7020); c) unalloyed steel S235JR

After conducting extensive testing of the innovative method, numerous benefits and advantages have been unveiled:

- short processing time;
- high productivity and high accuracy;
- low deviations in shape and position;
- high quality of the surface layer;
- the possibility of automating the process;
- reduction of production costs;
- low environmental nuisance;
- applicability of the weld processing solution in a wide range of products from different steels and alloys;
- does not require complex machinery;
- short implementation process;
- the possibility of machining welds of different shapes and dimensions, made by many welding methods.

The proposed method of post-weld surface finishing will find wide application in the production processes of welded structure elements and subassemblies and machine parts made using welded methods. The data of the world-wide solution can be successively used in various industries, that is: marine engineering, aerospace, armament, railroad and other mechanical engineering industries.

## 5. CONCLUSIONS

The innovative method is characterised by the short machining time of the weld bead and high efficiency. In addition, the innovative multi-edge cutting tool is used for weld bead finishing and ensures a low level of deviations in terms of shape and position as well as exceptionally high machining accuracy and high quality of the surface layer. While helpful in eliminating welding defects on the bead surface due to the presence on cutting tool of the last two teeth of the same height and special geometry of cutting teeth, wear of a properly designed tool is slow as its edges have a long service life thanks to increased resistance to shock loads caused by specialised tooth geometry based on strength calculations. The innovative weld bead finishing method provides economical machining, not requiring qualified operators, as well as the ability to cut many weld beads set in a row (continuous cutting), and the possibility of automating the finishing process. The versatility of the solution allows for the post-weld surface broaching of various types of steel and alloys using the overwhelming majority of welding methods. This solution exhibits no detrimental effects on individuals or the surrounding environment, while also complying with all emission standards and regulations. This invention provides accurate, efficient and economical post-weld finishing.

## REFERENCES

1. Ferenc K, Ferenc J. Welded structures. Connections. Warsaw: Wydawnictwo Naukowe PWN ; 2018: 460 (in Polish).
2. Szal A, Orzech K, Klich J, Szwed W, Kalisz K, Bodynek P. A method for grinding the longitudinal welds of the outer cargos and a device for grinding the longitudinal welds of the outer cargos. Patent No. 166176, dated 03.07.1991 (in Polish).
3. Cyfka D, Subocz K. Milling machine for machining the weld ridge. Patent No. 174051, dated 13.01.1998 (in Polish).

4. Bratt G, Martinsson H, Nordstroem M, Ostgren A. Method and device for machining a joint between two components. Patent No. 327604, dated 20.12.1996 (in Polish).
5. Dworow JI, Orlow WE. Deforming and cutting broach. Publication DE 26 12 323, filing date: March 23, 1976 (in German).
6. Dvirna O. Cutting tool for post weld surface finishing. Utility model № 146641, 10.03.2021.
7. Dvirna O. Method of post weld surface finishing. Utility model № 146640, 10.03.2021.
8. Kowalczyk L. Physical modelling of metal forming processes. Random: Publishing House of the Institute of Exploitation Technology; 1995: 371 (in Polish).
9. Dvirna O. Cutting Tool. Patent № 65776, 11.12.2011.
10. Dvirna O. The physical modelling of high speed broaching of the heat-resistant steels for studies surface layer quality. Journal of KONES. 2019; 26(3): 23-29. Available from: [https://kones.eu/ep/2019/vol26/no3/23-30\\_JOK\\_2019\\_NO.3\\_VOL.26\\_ISSN\\_1231-4005-DVIRNA.pdf](https://kones.eu/ep/2019/vol26/no3/23-30_JOK_2019_NO.3_VOL.26_ISSN_1231-4005-DVIRNA.pdf).
11. Dvirna O. Influence of the cutting tool properties on the treatment surface quality in the heat resistant steel broaching. Materials, technologies, constructions: special purpose processes. Stalowa Wola: Oficyna Wydawnicza Politechniki Rzeszowskiej. 2019: 27-38. Available from: [https://www.worldcat.org/title/materials-technologies-constructions-special-purpose-processes/oclc/1150663530&referer=brief\\_results](https://www.worldcat.org/title/materials-technologies-constructions-special-purpose-processes/oclc/1150663530&referer=brief_results)
12. Górski E, Harasymowicz J. Fundamentals of cutting tool design together with technological issues. Warsaw: Wydawnictwa Naukowe PWN; 1980: 608 (in Polish).
13. Kunstetter S. Fundamentals of cutting tool design. Warsaw: Wydawnictwa Naukowo-Techniczne; 1980: 505 (in Polish).
14. Gawlik E, Gil S, Zagórski K. Design of technological processes of machining. Cracow: Wydawnictwa AGH; 2019: 318 (in Polish).
15. Demidov VV, Kireev GI, Smirnov MY. Calculation and design of broaches. Ulyanovsk: Ural State Technical University; 2005: 79 (in Russian).
16. Collection of thematic information materials: Drawing of heat-resistant materials. Edited by Vilkul V.V. Nikolaev: ONTiZAPP; 2009: 277 (in Ukrainian).
17. Dvirna O, Zembrzuska N. Technological methods of ensuring the reliability of lock connections in marine gas turbines. Journal of KONBiN. 2022; 52 (3): 149-163. Available from: [http://www.journal.itwl.pl/images/2022/52v3/09%20Journal-Volume\\_52\\_Issue\\_3\\_149\\_164\\_page.pdf](http://www.journal.itwl.pl/images/2022/52v3/09%20Journal-Volume_52_Issue_3_149_164_page.pdf) (in Polish)
18. Dvirna O. Multi-tool fixing set for post-weld finishing surfaces, application of multi-tool fixing set for post-weld finishing surfaces and method of manufacturing multi-tool fixing set for post-weld finishing surfaces. Patent application for invention No. P.443376 dated 30.12.2022 (in Polish)
19. Dvirna O. A method of finishing post-welding surfaces and a tool for implementing this method. Application for Patent for Invention No. P.433166 dated 07.03.2020 (in Polish)

This research was funded by Innovation Incubator 4.0 Polish Ministry of Education and Science, grant number UMG-05 (RWK/II 4.0/5/12/2020).

Olha Dvirna:  <https://orcid.org/0000-0002-6018-1400>



This work is licensed under the Creative Commons BY-NC-ND 4.0 license.

## AN ADAPTIVE PID CONTROL SYSTEM FOR THE ATTITUDE AND ALTITUDE CONTROL OF A QUADCOPTER

Leszek CEDRO<sup>\*</sup>, Krzysztof WIECZORKOWSKI<sup>\*</sup>, Adam SZCZEŚNIAK<sup>\*</sup>

<sup>\*</sup>Faculty of Mechatronics and Mechanical Engineering, Kielce University of Technology,  
Aleja Tysiąclecia Państwa Polskiego 7, 25-314 Kielce, Poland

[lcedro@tu.kielce.pl](mailto:lcedro@tu.kielce.pl), [KWieczorkowski@interia.pl](mailto:KWieczorkowski@interia.pl), [a.szczesniak@tu.kielce.pl](mailto:a.szczesniak@tu.kielce.pl)

received 25 May 2023, revised 6 September 2023, accepted 12 September 2023

**Abstract:** In adaptive model-based control systems, determining the appropriate controller gain is a complex and time-consuming task due to noise and external disturbances. Changes in the controller parameters were assumed to be dependent on the quadcopter mass, which was the process variable. A nonlinear model of the plant was used to identify the mass, employing the weighted recursive least squares (WRLS) method for online identification. The identification and control processes involved filtration using differential filters, which provided appropriate derivatives of signals. Proportional integral derivative (PID) controller tuning was performed using the Gauss–Newton optimisation procedure on the plant. Differential filters played a crucial role in all the developed control systems by significantly reducing measurement noise. The results showed that the performance of classical PID controllers can be improved by using differential filters and gain scheduling. The control and identification algorithms were implemented in an National Instruments (NI) myRIO-1900 controller. The nonlinear model of the plant was built based on Newton's equations.

**Key words:** UAV drone, mechatronics, adaptive control systems

### 1. INTRODUCTION

The quadrotor has many benefits, such as being highly manoeuvrable, having a small size and simple structure and being able to take off and land vertically. It can also fly at low speeds and stay stationary in the air [1]. However, with six degrees of freedom and only controlled by four inputs, it brings complexity to its position and attitude control [2–4].

A good position and attitude controller are crucial to designing and controlling such a complex system. In control, extensive research has been undertaken for linear and nonlinear control techniques applied to the system. Among them, we find proportional integral derivative (PID) [5–7], linear quadratic regulator (LQR) [8, 9], backstepping control (BC) [10] and sliding mode control (SMC) [11–14]. Controllers (other than PID) are described, for example, in a study mentioned in Ref. [15] (a neural network-based controller). The PID controller is the most commonly used control technique and successfully implemented in the existing system. The PID controller's popularity is due to its simple structure, being easy to design and being easy to tune with satisfactory practical implementation performance [16].

In a study mentioned in Ref. [17], the PID controller with an extended Kalman filter was used to control and stabilise the quadrotor's altitude and attitude angle. The extended Kalman filter was used to filter out the sensor and system noises to stabilise the quadrotor's altitude (3.8 [s]) and attitude angle (5.8 [s]).

A comparative study between PID, proportional derivative (PD) and SMC controllers was conducted [13]. The simulation result showed that the SMC controller has a faster stabilisation time of approximately <3 [s] than PD and PID controllers. Nonetheless, it produces a large pitch and roll angle, making it unfavourable in the real-world condition.

In a study mentioned in Ref. [18], a nonlinear PID-type controller was presented to guarantee the motion control of the quadrotor. The existence of gains was proven by using a Lyapunov-like analysis [19–21], where the quadrotor system's nonlinear dynamics were considered. The authors concluded that the nonlinear PID-type controller they proposed could give better performance than conventional PID and sliding mode controllers since it can provide better tracking accuracy.

A minimal amount of research presents actual experimental results – most of them are simulations only. Outstanding results of aggressive trajectory tracking by a quadcopter have been described in the study mentioned in Ref. [22]. The authors proposed a multi-layer control structure: a combination of PD controllers, incremental nonlinear dynamic inversion (INDI) controllers and exploitation of the differential flatness of the quadcopter dynamics. The complete control system tracked the position and yaw angle and their derivatives of up to fourth order, specifically velocity, acceleration, yaw rate and yaw acceleration.

National Instruments (NI) company products, especially their embedded myRIO-1900 devices, are exceptionally well-suited for handling advanced processing tasks needed in complex and demanding applications, including the practical deployment of various flight control systems for unmanned aerial vehicles (UAVs) [23]. With its well-designed architecture and robust onboard features such as a three-axis accelerometer, analogue IO extensions and a Wi-Fi module, the myRIO-1900 platform represents a highly promising embedded solution for the real-world implementation of diverse and intricate flight control systems. Additionally, the associated LabVIEW Real-Time (RT) software tool capitalises on deterministic execution and ensures the highest level of reliability.

The implementation of the developed adaptive procedure was made possible, thanks to the dual-core processor, which, in RT, handled the variable mass identification procedure on one core and the control procedure on the other.

Adaptive controllers are control systems that can adjust their parameters or structure based on changes in the system or environment. The primary goal of adaptive controllers is to maintain system performance and stability under varying operating conditions, such as changes in load, disturbances or system parameters. Adaptive controllers can be divided into two groups: controllers with gain scheduling, where parameters are scheduled using predefined look-up tables, and self-tuning controllers, where parameters are continuously estimated and updated online.

An adaptive control system based on a model is a type of control system that uses a mathematical model of the system being controlled to adjust its parameters in RT. The mathematical model is usually a simplified representation of the plant, which allows for a better understanding of the system's behaviour and can be used to predict how it will respond to changes in the control inputs.

Adaptive control systems have been successfully applied in a wide range of applications, including robotics, aerospace and manufacturing. However, developing an accurate model of the system can be challenging, and the system's performance may be limited by the accuracy of the model.

Gain scheduling refers to a system where the controller parameters depend on the measured operating conditions. Gain scheduling is effective for systems whose dynamics changes with changing operating conditions. Gain scheduling involves modifying the gains of P, I and D terms according to the state of the system. This method works best for systems whose changes in dynamics can be predicted so that the predetermined gains can be calculated and applied. Thus, it is possible to define multiple sets of PID parameters for gain scheduling.

Adaptive control is commonly used to control plants where considerable changes in the operating conditions occur. The variations may be due to disturbances or changes in the plant parameters. One of the ways to handle this problem is to apply continuous adjustment of the control parameters according to the plant parameters. The variable parameter can be measured or assessed by identification [24]. In the case of a quadcopter, the variable parameter is its total mass. The mass of a plant may change when it is used for transport purposes; it will increase when it carries a payload. The mass is an important factor affecting the optimal setpoints of the quadcopter controllers. The control process can be largely improved by employing controllers with gain scheduling. The mass, used as a process variable, can be assessed through online identification; there is no need to employ additional sensors. This approach is easy to implement for any plant, and it is not necessary to change its design.

This study analyses the dynamics of a UAV with four rotors [25], where adaptive controllers are PID controllers with gain scheduling. The identification of the process variable, i.e. drone mass, involved nonlinear parametrisation and differential filtration to obtain appropriate signals and their derivatives.

In this publication, the authors have addressed several key topics:

They developed a method for tuning PID controller parameters specifically tailored for a quadcopter.

They conducted experimental trials to carefully select the parameters of differential filters. This step is crucial to ensure the stable operation of the control system and accurate identification of the quadcopter's mass.

The authors also proposed an innovative on-line identification method for determining the quadcopter's mass using differential filters. This method allows for RT mass estimation during flight.

Furthermore, they developed a control system that incorporates gain scheduling, and this system utilises the insights gained from the implementation of differential filters. The gain scheduling aspect ensures that the controller adapts to varying conditions.

Studies in this area have investigated the effectiveness of various control methods, such as LQRs [26, 27], sliding mode controllers [28, 29] and fuzzy logic controllers [30, 31]. The most commonly used type of controllers is PID controllers. Although they are common in quadcopters [32–34], it is still problematic to choose appropriate PID settings. One way to deal with this problem is to optimise the control criteria, e.g. error integral. In this study, the desired setpoints of PID controllers were selected by optimising the integral criterion. All the experiments were carried out for a quadcopter mounted on a test rig, which had four degrees of freedom. The control system was composed of four PID controllers responsible for altitude, roll, pitch and yaw. The control system was built using an NI myRIO-1900 controller and LabVIEW software [35].

## 2. MATHEMATICAL MODEL OF THE QUADCOPTER DYNAMICS

During mathematical modelling (Fig. 1), physical parameters are described in three different systems, i.e. the Earth system (EF), robot system (local BF) and auxiliary system (SF). The relationship between the EF, BF and SF is shown in Fig. 1b. In the notation of the mathematical model, all physical quantities, except Euler angles, are expressed in the local coordinate system BF. Euler angles are the angles between the system of BF and SF (or EF).

The mathematical model was derived using Newton's equations of motion. The quadcopter (Fig. 1a) is assumed to have six degrees of freedom.

The drone's altitude and attitude  $q$  coordinates, represented by the vector (1), consist of six parameters. The first three parameters determine the drone's position in space, while the other three determine its orientation or rotations:

$$q = [x \ y \ z \ \varphi \ \theta \ \psi]^T \quad (1)$$

where  $x, y, z$  are position coordinates and  $\varphi, \theta, \psi$  are roll, pitch and yaw about the respective coordinate axes.

The first step is to theoretically determine the angular velocity in the local coordinate system, in the same way as that described in a previous study mentioned in Ref. [36]:

$$\Omega = \begin{bmatrix} \omega_x \\ \omega_y \\ \omega_z \end{bmatrix} = \begin{bmatrix} \dot{\varphi} \\ \dot{\theta} \\ \dot{\psi} \end{bmatrix} + R_x \begin{bmatrix} 0 \\ \dot{\theta} \\ 0 \end{bmatrix} + R_x R_y \begin{bmatrix} 0 \\ 0 \\ \dot{\psi} \end{bmatrix} \quad (2)$$

where  $R_x$  is the rotation matrix for a rotation by the angle  $\varphi$  about the x axis,  $R_y$  is the rotation matrix for a rotation by the angle  $\theta$  about the y axis,  $R_z$  is the rotation matrix for a rotation by the angle  $\psi$  about the z axis and  $\omega_x, \omega_y, \omega_z$  are angular velocities in the local coordinate system, which can be written in the following matrix form:

$$\Omega = P_1 \dot{\Theta} \quad (3)$$

where

$$P_1 = \begin{bmatrix} 1 & 0 & -\sin\theta \\ 0 & \cos\varphi & \sin\varphi\cos\theta \\ 0 & -\sin\varphi & \cos\varphi\cos\theta \end{bmatrix}, \dot{\Theta} = \begin{bmatrix} \dot{\varphi} \\ \dot{\theta} \\ \dot{\psi} \end{bmatrix} \quad (4)$$

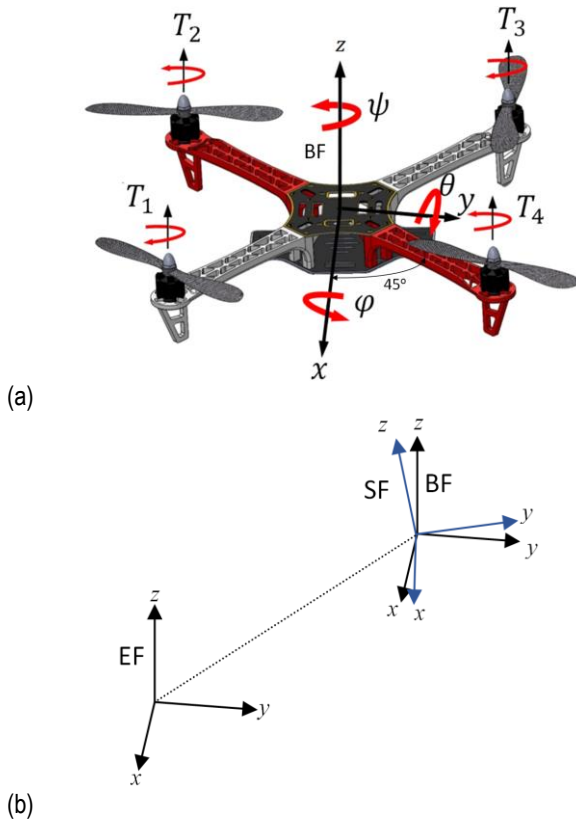


Fig. 1. Quadcopter (a) and modelling systems (b)

The next step is to calculate the inverse of the matrix  $P_1$

$$P_2 = (P_1)^{-1} = \begin{bmatrix} 1 & \sin\varphi \tan\theta & \cos\varphi \tan\theta \\ 0 & \cos\varphi & -\sin\varphi \\ 0 & \sin\varphi \sec\theta & \cos\varphi \sec\theta \end{bmatrix} \quad (5)$$

Finally, knowing the matrix  $P_2$ , which is dependent on the angular velocity of the auxiliary coordinate system, we can define the Euler rates as follows:

$$\dot{\Theta} = P_2 \Omega \quad (6)$$

The next step is to define the linear acceleration using Newton's second law of motion. The general form equation for linear acceleration can be expressed using vectors:

$$ma = F - F_g - F_{Co} - F_{Cw} \quad (7)$$

where  $m$  is the quadcopter mass,  $a$  is the linear acceleration matrix,  $F$  is the sum of thrusts produced by all the motors,  $F_g$  is the gravitational force,  $F_{Co}$  are Coriolis forces resulting from the quadcopter rotations and  $F_{Cw}$  are Coriolis forces resulting from the rotors rotations.

As can be seen from Eq. (7), the constraint is the force decreased by the gravitational force and the Coriolis forces. The gravitational force Eq. (8) can be defined as a force projected from the local coordinate system to the auxiliary system. The gravitational acceleration  $g$  is thus multiplied by the total mass of the quadcopter and the rotation matrix  $P_2$ :

$$F_g = P_2 m \begin{bmatrix} 0 \\ 0 \\ g \end{bmatrix} = \begin{bmatrix} -mg\sin\theta \\ mg\sin\varphi\cos\theta \\ mg\cos\varphi\cos\theta \end{bmatrix} \quad (8)$$

The first of the Coriolis forces results from the rotation of the entire quadcopter:

$$F_{Co} = 2m \Omega \times v = 2m \begin{bmatrix} v_z\omega_y - v_y\omega_z \\ v_x\omega_z - v_z\omega_x \\ v_y\omega_x - v_x\omega_y \end{bmatrix} \quad (9)$$

where  $v$  is the linear velocity matrix and  $v_x, v_y, v_z$  are linear velocities in the local coordinate system.

The second of the Coriolis forces results from the rotations of the rotors:

$$F_{Cw} = 2m_w \Omega_w \times v = 2m_w \begin{bmatrix} -v_y(\omega_1 + \omega_2 + \omega_3 + \omega_4) \\ v_x(\omega_1 + \omega_2 + \omega_3 + \omega_4) \\ 0 \end{bmatrix} \quad (10)$$

where the sum of rotors angular velocity matrix  $\Omega_w$  can be expressed as follows:

$$\Omega_w = \begin{bmatrix} 0 \\ 0 \\ \omega_1 + \omega_2 + \omega_3 + \omega_4 \end{bmatrix} \quad (11)$$

Where  $\omega_i$  is the angular velocity of the  $i$ -th motor.

The lift  $F$ , being the sum of thrusts produced by all the motors, is generated vertically upwards along the drone's vertical axis  $Z$ ; it is described by the following formula (12):

$$F = \begin{bmatrix} 0 \\ 0 \\ F_Z \end{bmatrix} = \begin{bmatrix} 0 \\ 0 \\ T_1 + T_2 + T_3 + T_4 \end{bmatrix} \quad (12)$$

where  $F$  is the vector of sum of thrust of all motors and  $T_i$  is the thrust force of the  $i$ -th motor.

The next step is to calculate angular acceleration. This effect can be described mathematically using Euler's equation of rigid-body motion. The general vector form of Euler's equation can be written as follows:

$$\tau = \frac{dL}{dt} + \Omega \times L \quad (13)$$

where  $L$  is the angular momentum and  $\tau$  is the thrust moment.

It is also true that for a rigid body,

$$L = I \Omega \quad (14)$$

where  $I$  is described by the following matrix:

$$I = \begin{bmatrix} J_x & 0 & 0 \\ 0 & J_y & 0 \\ 0 & 0 & J_z \end{bmatrix} \quad (15)$$

where  $J_x, J_y, J_z$  are moments of inertia about the respective coordinate axes.

The inertia matrix  $I$  for the quadcopter can be diagonalised in a matrix transform due to the symmetry of the quadcopter's geometry. Therefore, the inertia matrix  $I$  is assumed to be expressed in Eq. (15) during the derivation.

Thus, substituting Eq. (13) into Eq. (14) and assuming that the moment of inertia is constant, we have the following expression:

$$\tau = I \dot{\Omega} + \Omega \times (I \Omega) \quad (16)$$

Eq. (16) needs to be adjusted because the motors and rotors cause the gyroscopic effect [37, 38]. This effect is described by the fundamental equation of the gyroscope:

$$\tau_{gyro} = \Omega \times L_p \quad (17)$$

The angular momentum vector  $L_p$  is determined by multiplying the moment of inertia of the rotor ( $I_w$ ) by the rotor's angular velocity in the axis where the rotation occurs ( $\Omega_w$ ):

$$L_p = I_w \Omega_w = \begin{bmatrix} 0 \\ 0 \\ I_w (\omega_1 + \omega_2 + \omega_3 + \omega_4) \end{bmatrix} \quad (18)$$

Knowing  $L_p$  and  $\Omega$ , we can expand Eq. (17) as follows:

$$\begin{aligned} \tau_{gyro} &= \begin{bmatrix} \omega_x \\ \omega_y \\ \omega_z \end{bmatrix} \times \begin{bmatrix} 0 \\ 0 \\ I_w (\omega_1 + \omega_2 + \omega_3 + \omega_4) \end{bmatrix} = \\ &= \begin{bmatrix} \omega_y I_w (\omega_1 + \omega_2 + \omega_3 + \omega_4) \\ -\omega_x I_w (\omega_1 + \omega_2 + \omega_3 + \omega_4) \\ 0 \end{bmatrix} \end{aligned} \quad (19)$$

With the gyroscopic torque being in the vector form, Euler's Eq. (13) can be upgraded and described by using the following formula:

$$\tau = I \dot{\Omega} + \Omega \times (I \Omega) + \tau_{gyro} \quad (20)$$

In Eq. (20), the unknown quantity is the angular acceleration; thus, after transformations, it can be written as follows:

$$\dot{\Omega} = I^{-1}(\tau - \Omega \times (I \Omega) - \tau_{gyro}) \quad (21)$$

For the configuration coordinates responsible for the rotations  $\varphi$ ,  $\theta$  and  $\psi$ , the thrust moments  $\tau$  are expressed in the form of moments  $M_\varphi$ ,  $M_\theta$  and  $M_\psi$ , Eqs. (22–24), respectively:

$$M_\varphi = (-T_1 - T_2 + T_3 + T_4) \frac{l}{\sqrt{2}} \quad (22)$$

$$M_\theta = (-T_1 + T_2 + T_3 - T_4) \frac{l}{\sqrt{2}} \quad (23)$$

$$M_\psi = \sum_{i=1}^4 M_i \quad (24)$$

where  $l$  is the distance between the  $i$ -th motor and the centre of gravity of the drone.

Equations (22–24) demonstrate that the ability of the quadcopter to be controlled is influenced by the thrust force generated in the  $z$  direction  $F_z$  as well as the rotational moments  $M_\varphi$ ,  $M_\theta$  and  $M_\psi$ . The thrust of the  $i$ -th motor  $T_i$  is determined by calculating the square of the angular velocity of the  $i$ -th rotor and multiplying it by a gain correction factor  $b$ :

$$T_i = b \omega_i^2 \quad (25)$$

The moment on the  $i$ -th motor shaft  $M_i$  can be calculated from the angular velocity of the  $i$ -th rotor Eq. (26):

$$M_i = d \omega_i^2 \quad (26)$$

where  $b$ ,  $d$  are correction factors.

The axes of the body coordinate system do not coincide with the quadcopter rotor arms and are rotated by the  $\frac{\pi}{4}$  angle around the body  $z$  axis (Fig. 1). After substituting Eqs (25) and (26) into Eqs (22–24) and multiplying them by the rotation matrix for the  $\frac{\pi}{4}$  angle, we obtain

$$\tau = \begin{bmatrix} M_\varphi \\ M_\theta \\ M_\psi \end{bmatrix} = \begin{bmatrix} \frac{lb(-\omega_1^2 - \omega_2^2 + \omega_3^2 + \omega_4^2)}{\sqrt{2}} \\ \frac{lb(-\omega_1^2 + \omega_2^2 + \omega_3^2 - \omega_4^2)}{\sqrt{2}} \\ d(\omega_1^2 - \omega_2^2 + \omega_3^2 - \omega_4^2) \end{bmatrix} \quad (27)$$

Knowing the other terms and forces, we can write the model of the quadcopter in the following way. The first part of the model refers to linear acceleration, which is defined in the local coordinate system:

$$\begin{aligned} a = \begin{bmatrix} \ddot{x} \\ \ddot{y} \\ \ddot{z} \end{bmatrix} &= \begin{bmatrix} 0 \\ 0 \\ \frac{b}{m}(\omega_1^2 + \omega_2^2 + \omega_3^2 + \omega_4^2) \end{bmatrix} - \begin{bmatrix} -g \sin \theta \\ g \sin \varphi \cos \theta \\ g \cos \varphi \cos \theta \end{bmatrix} + \\ &- 2 \begin{bmatrix} v_z \omega_y - v_y \omega_z \\ v_x \omega_z - v_z \omega_x \\ v_y \omega_x - v_x \omega_y \end{bmatrix} - 2 \frac{m_w}{m} \begin{bmatrix} -v_y(\omega_1 + \omega_2 + \omega_3 + \omega_4) \\ v_x(\omega_1 + \omega_2 + \omega_3 + \omega_4) \\ 0 \end{bmatrix} \end{aligned} \quad (28)$$

where  $m_w$  is the mass of propellers and rotors.

The second part represents Euler rates, which will be used to determine changes in the orientation of the quadcopter local system in relation to that of the auxiliary system:

$$\dot{\Theta} = \begin{bmatrix} \dot{\varphi} \\ \dot{\theta} \\ \dot{\psi} \end{bmatrix} = \begin{bmatrix} \omega_x + \omega_y \sin \varphi \tan \theta + \omega_z \cos \varphi \tan \theta \\ \omega_y \cos \varphi - \omega_z \sin \varphi \\ \omega_y \sin \varphi \sec \theta + \omega_z \cos \varphi \sec \theta \end{bmatrix} \quad (29)$$

The last part is directly related to angular accelerations:

$$\begin{aligned} \dot{\Omega} = \begin{bmatrix} \dot{\omega}_x \\ \dot{\omega}_y \\ \dot{\omega}_z \end{bmatrix} &= \begin{bmatrix} \frac{lb}{J_x \sqrt{2}} (-\omega_1^2 - \omega_2^2 + \omega_3^2 + \omega_4^2) \\ \frac{lb}{J_y \sqrt{2}} (-\omega_1^2 + \omega_2^2 + \omega_3^2 - \omega_4^2) \\ \frac{d}{J_x} (\omega_1^2 - \omega_2^2 + \omega_3^2 - \omega_4^2) \end{bmatrix} + \\ &- \begin{bmatrix} \frac{1}{J_x} (\omega_y \omega_z (J_z - J_y)) \\ \frac{1}{J_y} (\omega_x \omega_z (J_x - J_z)) \\ \frac{1}{J_z} (\omega_x \omega_y (J_y - J_x)) \end{bmatrix} + \\ &- \begin{bmatrix} \frac{1}{J_x} (\omega_y I_w (\omega_1 + \omega_2 + \omega_3 + \omega_4)) \\ \frac{1}{J_y} (-\omega_x I_w (\omega_1 + \omega_2 + \omega_3 + \omega_4)) \\ 0 \end{bmatrix} \end{aligned} \quad (30)$$

The relationships between the angular velocities  $\omega_i$  of the motors and the respective control signals  $U_i$  are given as follows:

$$\begin{aligned} \begin{bmatrix} U_1 \\ U_2 \\ U_3 \\ U_4 \end{bmatrix} &= \begin{bmatrix} b & b & b & b \\ -\frac{bl}{\sqrt{2}} & 0 & \frac{bl}{\sqrt{2}} & 0 \\ 0 & \frac{bl}{\sqrt{2}} & 0 & -\frac{bl}{\sqrt{2}} \\ d & -d & d & -d \end{bmatrix} \begin{bmatrix} \omega_1^2 \\ \omega_2^2 \\ \omega_3^2 \\ \omega_4^2 \end{bmatrix} \\ \mathbf{U} &= [U_1 \ U_2 \ U_3 \ U_4]^T \end{aligned} \quad (31)$$

### 3. IDENTIFICATION METHOD

One of the most popular and effective methods of identification is the least squares (LS) method, which is based on the processing of input and output signals [39].

High-quality control under static and dynamic conditions can be achieved using microchip-based methods. However, these

require precise information on the actual values of the parameters of the mathematical model of the system [40–44].

In this study, specially developed low-pass filters and low-pass differentiating filters were employed to filter inputs and outputs to obtain signals and their derivatives required in the identification process.

Since the proposed control method involves identifying one parameter, i.e. the quadcopter mass, the formulae to describe this case will be provided further in this article. Consider a model as follows:

$$v_k = w_k p \quad (32)$$

where  $p$  is the unknown parameter,  $v_k$  and  $w_k$  are scalar signals and  $k = 0, 1, \dots$  are successive time instants.

The LS algorithm uses plant variables that were recorded over a long enough period of time interval  $k = 0, 1, \dots, N - 1$ .

This approach is known as the recursive LS algorithm with exponential forgetting or the weighted recursive least squares (WRLS) algorithm [45].

The WRLS algorithm minimises an objective function by exponentially forgetting older data

$$J_k(p) = \sum_{i=1}^k \lambda^{k-i} (v_i - w_k p)^2 \quad (33)$$

with respect to the parameter  $p$ , where  $\lambda$  is a constant satisfying the inequality  $0 < \lambda < 1$ . Let  $\hat{p}_k$  represent a value of the parameter  $p$  for which  $dJ_k(p)/dp = 0$ . Using a simple transformation, we get

$$\hat{p}_k = \hat{p}_{k-1} + \gamma_k w_k (v_k - w_k \hat{p}_{k-1}) \quad (34)$$

$$\gamma_k^{-1} = \lambda \gamma_{k-1}^{-1} + w_k^2, k = 1, 2, \dots \quad (35)$$

In criterion Eq. (33), the components dependent on the past measurement data are multiplied by the factor  $\lambda^{k-1}$ . This implies that when the estimate of  $p$  is determined, the past measurement data are less important than the present data. The parameter  $\lambda$  is called a forgetting factor.

Suppose that the plant equation satisfies relationship Eq. (32) depending on the plant input and output [45].

It is assumed that parameter estimates will be updated immediately after a certain number of signal samples  $N$ . The aim is to derive a recursive equation for determining parameter estimates  $p_m$  for the time instants lying in the interval  $\alpha(m) = [(m-1) \cdot N, m \cdot N - 1], m = 1, 2, \dots$

Define the following objective function:

$$J_m(p) = \sum_{j=1}^m \lambda^{m-j} (v_i - w_k p_j) \quad (36)$$

$$\hat{p}_m = \hat{p}_{m-1} + \gamma_m \sum_{i \in \alpha(m-1)} w_i (v_i - w_i \hat{p}_{m-1}) \quad (37)$$

$$\gamma_m^{-1} = \lambda \gamma_{m-1}^{-1} + \sum_{i \in \alpha(m-1)} w_i^2, m = 1, 2, \dots \quad (38)$$

Generally, it is assumed that  $\gamma_0^{-1} = \varepsilon$  for  $\varepsilon$  ranging  $10^3 - 10^6$ . Small initial values of the scalar  $\gamma_0^{-1}$  ensure immediate convergence of the estimates to the real values of the parameters at the beginning of the algorithm.

#### 4. SELECTING THE SETPOINTS FOR PID CONTROLLERS

The usual method to adjust the parameters of a controller is through a trial and error method, but this process can be time-consuming and tiresome. It is essential to tune the controller's parameters properly to get optimal performance, but the traditional way may not always provide the best solution.

Furthermore, the control designer can never tell which exact parameters are the optimal solution for the controller [46]. To overcome the issue of the tedious trial and error method of tuning controller parameters, many researchers have started using optimisation tools in their work to find the optimal values of the controller parameters easily.

The advantages of these optimisations are that they are independent problem structures [47]. Different algorithms have been used to obtain the optimal parameters of the controllers. Among them, we can find the genetic algorithm (GA) [48], ant colony optimisation (ACO) [49], artificial bee colony (ABC) [50] and cuckoo search (CS) [51, 52].

In their research study, Imane and Mostafa investigated how to optimise the gain parameter of a PID controller for altitude and attitude angle control of a quadrotor [53]. They used two optimisation methods, RM and GA, to obtain the optimal gain parameter.

Erkol [47] conducted a study on the optimal tuning of PID control for attitude and hover control of the quadrotor. The study used various optimisation techniques, including ABC, particle swarm optimisation (PSO), GA and the Ziegler–Nichols method. The findings indicate that controllers based on ABC and GA perform the best in terms of integral absolute error (IAE) and root mean square error (RMSE), while the ZN method results in the worst performance.

Tuning the PID controllers responsible for the quadcopter control requires selecting their setpoints:  $K_{Pi}$ ,  $K_{Ii}$  and  $K_{Di}$ . From Eq. (39), it is clear that the number of parameters sought can be reduced from 12 to 9. Because of the drone symmetry, it can be assumed that the drone can be rotated by the  $\varphi$  angle around the body x axis and by the  $\theta$  angle around the body y axis by using PID controllers with the same setpoints. As the quadcopter mounted on the test rig has a limited number of degrees of freedom, the q vector is defined as follows:

$$q = [z \quad \varphi \quad \theta \quad \psi]^T. \text{ Thus,}$$

$$U_i = K_{Pi} e_i + K_{Ii} \int e_i(\tau) d\tau + K_{Di} \dot{e}_i, i = 1, 2, 3, 4 \quad (39)$$

$$e_1 = z_z - z, e_2 = \varphi_z - \varphi, e_3 = \theta_z - \theta, e_4 = \psi_z - \psi \quad (40)$$

$$q_z = [z_z \quad \varphi_z \quad \theta_z \quad \psi_z]^T, e = [e_1 \quad e_2 \quad e_3 \quad e_4]^T$$

where

$z_z$ ,  $\varphi_z$ ,  $\theta_z$  and  $\psi_z$  are setpoints.

The choice of the best PID parameters is dependent on various factors, including the dynamic response of the plant, as well as on the control objectives determined by the operator. The selection task can be difficult and time-consuming when the controller setpoints are set manually and software is used to optimise the PID parameters. The methods that do not require creating a mathematical model include autotuning employed in controllers with automatic setpoint selection. However, automatic setpoint selection systems may not be able to handle the measurement noise, which in the case of a quadcopter is considerable. In this study, the tests of automatic tuning of PID setpoints for the drone were not repeatable, and the desired level of confidence was not reached. High levels of measurement noise affected the estimates of the process variable.

Because of the nonlinearity of the plant, i.e. a quadcopter with multiple input and multiple output (MIMO), and high levels of measurement noise generated by the quadcopter, the number of setpoint selection methods that can be used is limited. In this case, setpoint selection generally involves optimising the control criteria (integral criteria); it does not require a mathematical model.

The diagram in Fig. 2 shows the optimisation of the setpoints of the PID controllers achieved by employing a minimisation algorithm. The Gauss–Newton algorithm [54] is used to minimise the target function  $J = \int \frac{1}{2} \|e\|^2 d\tau$ .

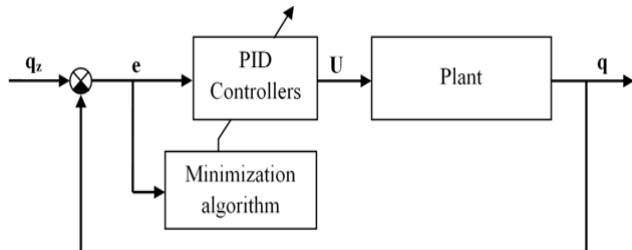


**Fig. 2.** Diagram of the optimisation of the PID controller setpoints.

PID, proportional integral derivative.

The optimisation of the setpoints was performed in LabVIEW for the plant shown in Fig. 3. An MPU-6050 sensor was employed to measure angular positions in three axes. The height  $z$  that the quadcopter reached was measured using a linear variable differential transducer (LVDT). The quadcopter is equipped with MT2216 II 810KV brushless motors CW CCW with 1045 propellers. The range of the quadcopter's tested mass is 1.65–2.0 kg, and the allowable change in altitude is within the range of 0–0.15 m. The test setup is powered by a voltage of 12 V provided by two power supplies (62A each).



**Fig. 3.** Test rig with the quadcopter

To work correctly, the minimisation algorithm requires determining the initial values of setpoints and their ranges. The optimisation procedure performed for nine parameters can be much easier if the range is defined based on the simulation data and a priori knowledge. Ultimately, the setpoints of the PID controllers were estimated for three mass values, which will be the basis to calculate the final values of the setpoints for the mass identified using the adaptive algorithm (Tab. 1).

**Tab. 1.** PID gains obtained using the optimisation procedure

<b>m [kg]</b>	<b>PID controllers</b>	<b>K<sub>P</sub></b>	<b>K<sub>I</sub></b>	<b>K<sub>D</sub></b>
1.65	1	0.4200	0.01360	0.3999
	2 and 3	0.0700	0.00990	0.0200
	4	0.0300	0.00009	0.0219
1.72	1	0.5249	0.02835	0.4000
	2 and 3	0.0700	0.00999	0.0200
	4	0.0299	0.00099	0.0220
1.79	1	0.6300	0.03255	0.4000
	2 and 3	0.0700	0.01000	0.0200
	4	0.0400	0.00100	0.0200

PID, proportional integral derivative

To check the stability of drone control, various methods and tools can be used. One of the most commonly used methods is analysing the step or impulse response of the drone to the given control signals. This involves introducing a sudden change in the control signal and then observing how the drone reacts and how quickly it achieves stability. Another method is to examine the dynamic characteristics of the drone, such as speed, acceleration and rotation angles, depending on the control signals. For drones, an important factor for stability is height control, which can be checked by observing the drone's behaviour during maintaining constant altitude or during takeoff and landing. For more advanced drone control systems, computer simulations can also be used to test the system's performance in various conditions and scenarios.

The proposed drone control systems in this article were tested for stability at different operating points. The observation of the drone's dynamics and maintaining a constant altitude confirmed the stability of the developed control systems for the settings presented in Tab. 1 and the intermediate settings resulting from their linear interpolation.

## 5. ADAPTIVE ATTITUDE AND ALTITUDE CONTROL SYSTEM

This article presents a simpler solution using gain scheduling adaptive control systems. The experiments were conducted under laboratory conditions.

For the analysed plant, the setpoints of the controllers were adjusted depending on the change in the drone mass, which is the process variable (Fig. 4). The setpoints of the controllers for intermediate mass are determined from the linear interpolation between the basic setpoints given in Tab. 1.

The drone mass was estimated by identification, which involved using a WRLS algorithm and derivatives of signals, obtained by means of differential filtration [55].

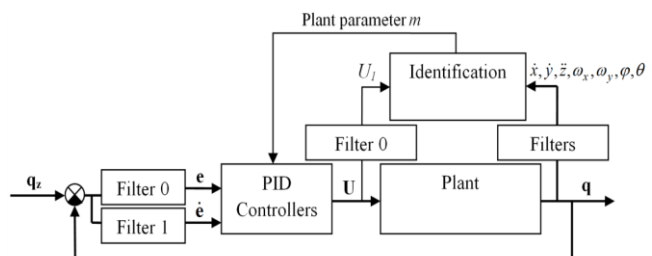


**Fig. 4.** Adaptive control system PID, proportional integral derivative

In the diagram given in Fig. 4, the Filters block contains three filters that perform low-pass filtering and first- and second-order differentiation. The PID Controllers block includes a set of parameters (Tab. 1) and performs linear interpolation based on the leading variable  $m$ . Linear interpolation of PID controller parameters is only possible within the provided set of parameters (Tab. 1). To limit measurement noise for individual signals, low-pass filters are implemented in the Filter 0 blocks. The Filter 1 block contains a differentiating filter that simultaneously calculates signal derivatives and reduces measurement noise.

The identification process uses Eq. (41), where the mass is estimated using the WRLS procedure:

$$U_1 = m\ddot{z} + mg\cos(\theta)\cos(\varphi) + 2m(\omega_x\dot{y} - \omega_y\dot{x}) \quad (41)$$

The next step involves parametrising the model Eq. (41) to ensure accurate identification. The parameter of the model can be determined as follows:

$$p = m, g = 9.81 \quad (42)$$

With a given parameter determined in this way, Eq. (41) takes the following form:

$$U_1 = p\ddot{z} + p9.81\cos(\theta)\cos(\varphi) + 2p(\omega_x\dot{y} - \omega_y\dot{x}) \quad (43)$$

As can be seen, Eq. (43) is linear with respect to the parameter  $p$ . Using Eq. 43, we obtain

$$v = w \quad (44)$$

where

$$v = U_1, w = \ddot{z} + 9.81\cos(\theta)\cos(\varphi) + 2(\omega_x\dot{y} - \omega_y\dot{x}).$$

The parameter estimates are updated every  $N = 129$  samples at  $\Delta = 0.004$ s. The identification process required preparing special derivatives of signals and eliminating most of the measurement noise. The advantage of the differential filters is that they ensure good estimation of the derivatives of signals and also help reduce the measurement noise [56]. In this study, differential filters were used not only in the identification procedure but also to assess  $e$  and  $\dot{e}$  signals. The test results suggest a considerable improvement in the control process, where  $e$  and  $\dot{e}$  signals were obtained through filtration using a low-pass filter (Filter 0) and a differential filter (Filter 1) (Tab. 2). The use of the filters in the control algorithm required selecting the right parameters to ensure a small delay as well as good estimation of signals and their derivatives. The experimentally selected parameters of the filters used in the PID algorithm were as follows: boundary frequency  $\Omega_g = 0.08$ [rad/s] and total bandwidth of FIR filters  $2 \cdot M_f + 1 = 7$ .

The procedure to identify the quadcopter mass at a sudden change in mass (29 [s],  $m + 70$  g) is accurate, taking only several seconds (Fig. 5).

The initial mass identification outliers resulted from the quadcopter lift off the ground ( $z = 0$  [m]) and high initial values of the matrix  $y_0^{-1}$ . Very good results were obtained when the WRLS algorithm governed by the forgetting factor  $\lambda = 0.98$  was applied. The value of this factor has a considerable influence on the rate at which the procedure responds to a change in the actual mass. The high value of this factor is responsible for slow changes in the mass and high precision in the determination of its value, which has a beneficial effect on the control stability. The NI myRIO-1900 controller, with low computational capacity, was responsible for controlling the quadcopter and estimating its mass. The WRLS identification procedure was initiated every 2 Hz. This

frequency (used to determine the mass) was optimal for the controller, and it allowed us to collect the right amount of data to ensure the stability of the WRLS procedure. As the stability of the mass identification procedure is essential, the signals and their derivatives were estimated with high precision. Thus, the filters used in this procedure had settings different from the filters employed in the PID control algorithm. The best results were reported for the following filter parameters:  $\Omega_g = 0.2$ [rad/s] boundary frequency and the total bandwidth of the FIR filters being  $2 \cdot M_f + 1 = 129$ .

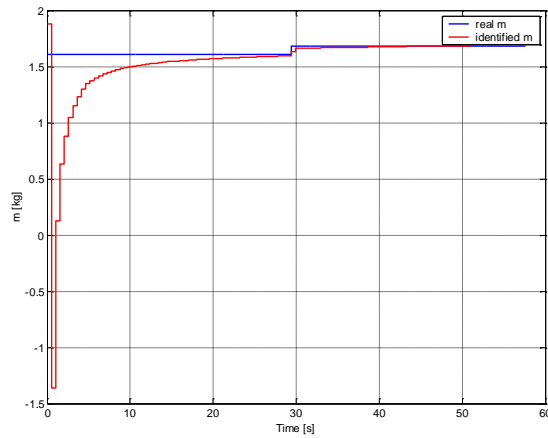


Fig. 5. Identification of the quadcopter mass

From Tab. 2, it is clear that the control output values obtained for PID controllers with gain scheduling (adaptive PID controllers) are better than those reported for PID controllers with fixed gains, which ensures a considerable improvement in the control quality. Figure 6 illustrates the control of the  $z$  variable, for which the changes were the most favourable.

The remaining responses of the quadcopter with constant and variable PID controllers parameters are presented in Figs. 7–9. Changes in individual PID controllers gains with gain scheduling are shown in Figs. 10–12.

Tab. 2. Control quality IAE for the different PID control systems

Controller	IAE $e_1$	IAE $e_2$	IAE $e_3$	IAE $e_4$	IAE $e$
Fixed gains	0.00542761	0.0244549	0.0293129	0.3711150	0.43031041
Fixed gains with filtration	0.00517794	0.0404676	0.0407506	0.2188910	0.30528714
Gain scheduling	0.00485863	0.0304711	0.0374924	0.1112040	0.18402613

IAE, integral absolute error; PID, proportional integral derivative

The developed control algorithm with a leading variable is simpler to implement than model-based adaptive methods. It is characterised by stability and accurate identification of the leading variable, which in this case is the quadcopter's mass. Based on the identified mass, the controller performs linear interpolation of the provided controller parameters from Tab. 1. Both the original parameters and the interpolated parameters were tested for stability.

The resistance of the control algorithm to external disturbances was evaluated by briefly applying an external force to the structure of the hovering quadcopter, thereby displacing it from its equilibrium position. Mass identification was solely based on the

dynamics equation for  $\ddot{z}$  (41), resulting in a significantly simpler procedure than other adaptive algorithms that rely on a full model. Since the controller is based on stable and verified parameters regarding external disturbances, the control algorithm with a leading variable does not require additional on-line stability checks. This approach ensures the stability of the developed control system, which may not always be achievable in adaptive control systems based on full model identification.

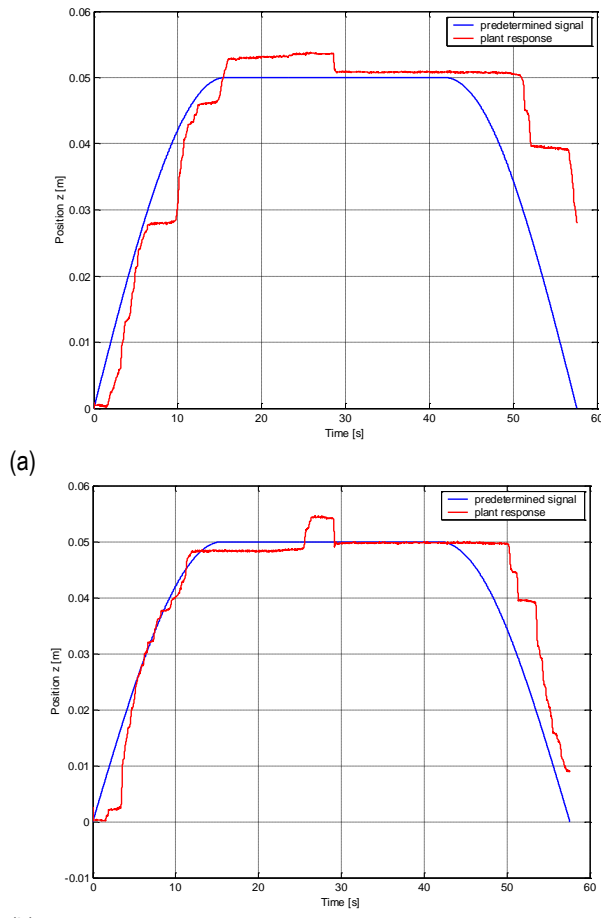
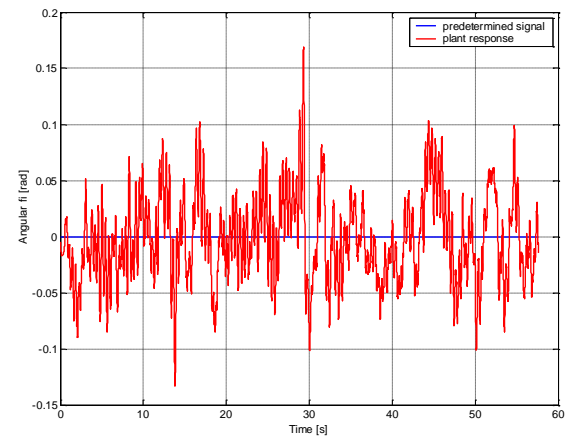
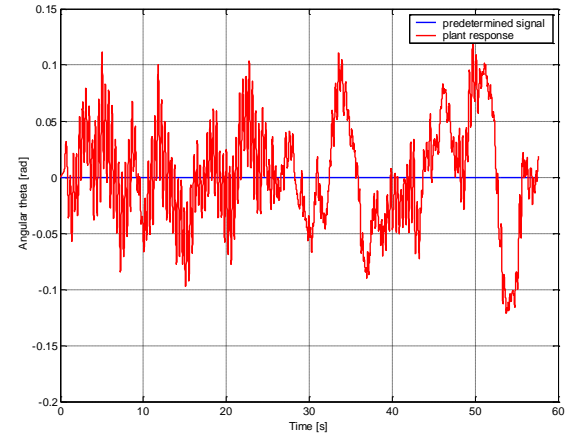


**Fig. 6.** Plant response for  $z$ : (a) PID controllers with fixed gains;  
 (b) adaptive PID controllers with gain scheduling.  
 PID, proportional integral derivative.

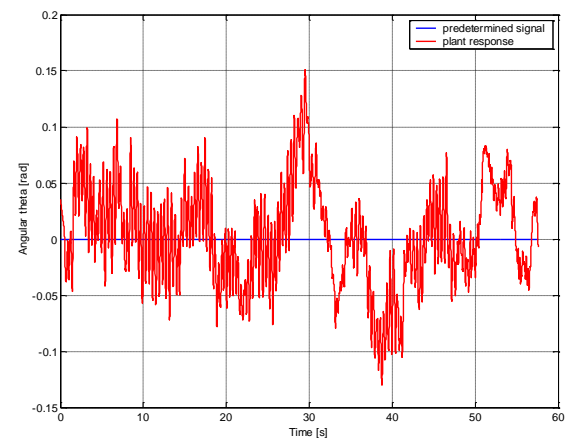


(b)

**Fig. 7.** Plant response for  $\phi$ : (a) PID controllers with fixed gains;  
 (b) adaptive PID controllers with gain scheduling.  
 PID, proportional integral derivative.

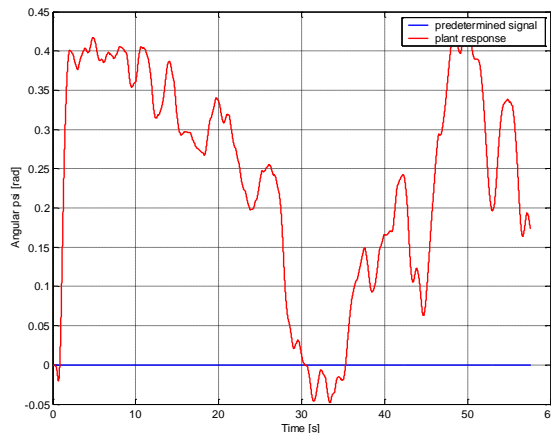


(a)

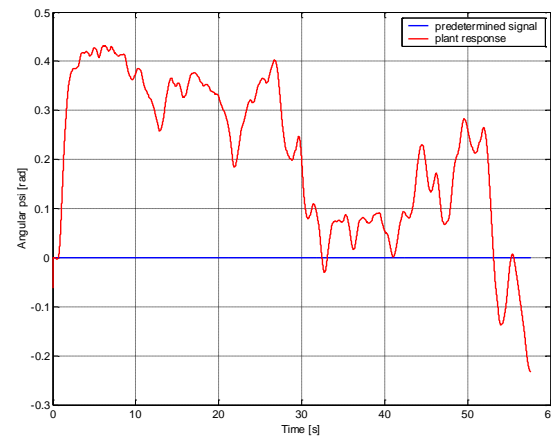


(b)

**Fig. 8.** Plant response for  $\theta$ : (a) PID controllers with fixed gains;  
 (b) adaptive PID controllers with gain scheduling.  
 PID, proportional integral derivative.



(a)



(b)

**Fig. 9.** Plant response for  $\psi$ : (a) PID controllers with fixed gains; (b) adaptive PID controllers with gain scheduling.  
PID, proportional integral derivative.

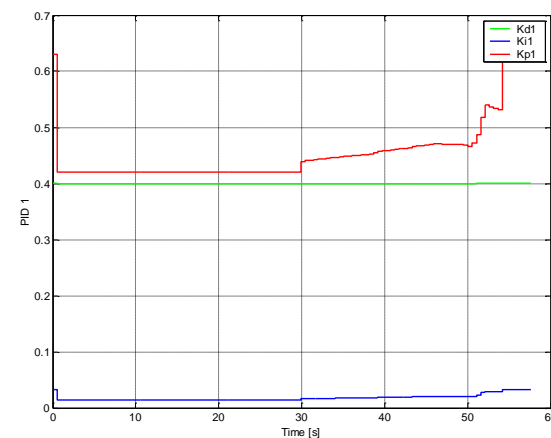


**Fig. 10.** Gains for adaptive PID 1 controllers with gain scheduling.  
PID, proportional integral derivative.

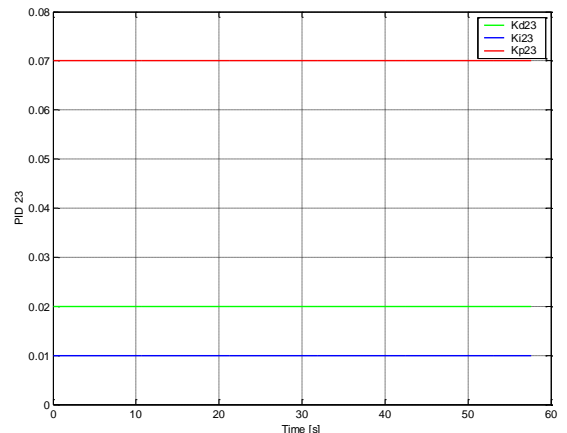


**Fig. 11.** Gains for adaptive PID 2 and PID 3 controllers with gain scheduling. PID, proportional integral derivative

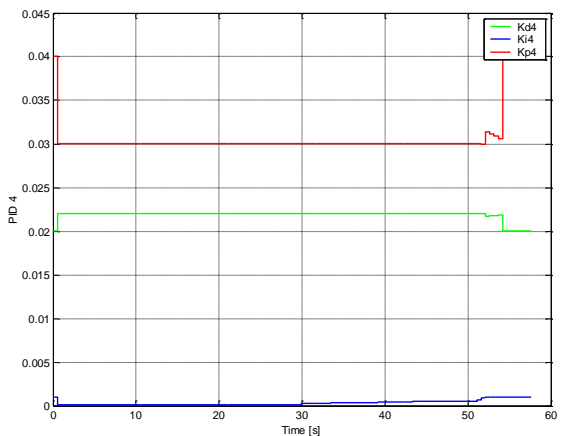


**Fig. 12.** Gains for adaptive PID 4 controllers with gain scheduling.  
PID, proportional integral derivative.

## 6. CONCLUSIONS

This article outlines quadcopter control experiments performed under laboratory conditions. The dynamic equations of motion derived for the plant were used to develop an accurate mass identification procedure; this required implementing the WRLS algorithm. The tests carried out for a real physical system confirmed that the use of low-pass and differential filters substantially improved the quality of the quadcopter control. The proposed adaptive PID control system with gain scheduling proved to be more suitable to control the response of a quadcopter with variable mass than classical PID controllers with fixed gains. The controllers with gain scheduling used setpoints determined through the optimisation procedure. The control system was stable irrespective of the quadcopter mass.

Despite significant measurement noise produced by the plant, the filter design process determines derivatives of signals with small errors. The use of PID controllers with fixed gains as well as low-pass and differential filters improved the plant response considerably. However, much higher control quality was observed for PID controllers with gain scheduling.

The identification procedure allows us to accurately estimate the quadcopter mass and, consequently, select the appropriate setpoints of the controllers (Fig. 5). The proposed control system

offers stable control of a quadcopter, it can be used with most commercially available controllers as it does not require high computational capacity.

The key advantage of the adaptation procedure with gain scheduling is that it allows the controller gains to vary depending on operating conditions (Figs. 10–12). This indicates that the controller can adapt to changes in plant dynamics and the operating environment. By adjusting the controller gains in RT, the controller can maintain stability and improve its tracking performance.

In contrast, other adaptation procedures, such as the adaptive control and model reference adaptive control, require controller gains to be adjusted based on the system's estimated parameters. This approach can be less effective as the estimated parameters may not accurately reflect plant dynamics or operating conditions.

Another advantage of gain scheduling is its ability to handle nonlinearities in plant dynamics (Figs. 6–9). Nonlinearities can cause the controller to behave unpredictably, leading to instability and poor performance. However, gain scheduling can account for these nonlinearities by adjusting the controller gains based on the specific operating conditions (Tab. 1).

Overall, the adaptation procedure with gain scheduling is a good method of control as it can adapt to changes in the plant dynamics and operating conditions, handle nonlinearities and provide excellent tracking performance.

The article discusses an adaptive PID control system developed to control a quadcopter. Based on the IAE index (Tab. 2), we can conclude that the developed gain scheduling control system achieves better results than the other tested control systems.

## REFERENCES

1. Hasseni SEI, Abdou L, Glida HE. Parameters tuning of a quadrotor PID controllers by using nature-inspired algorithms. *Evol Intel*. 2021 Mar 1;14(1):61–73.
2. Khatoon S, Nasiruddin I, Shahid M. Design and Simulation of a Hybrid PD-ANFIS Controller for Attitude Tracking Control of a Quadrotor UAV. *Arab J Sci Eng*. 2017 Dec 1;42(12):5211–29.
3. Kuantama E, Vesselenyi T, Dzitac S, Tarca R. PID and Fuzzy-PID Control Model for Quadcopter Attitude with Disturbance Parameter. *International Journal of Computers Communications & Control*. 2017 Jun 29;12(4):519–32.
4. Rinaldi M, Primatesta S, Guglieri G. A Comparative Study for Control of Quadrotor UAVs. *Applied Sciences*. 2023 Jan;13(6):3464.
5. Burggräf P, Pérez Martínez AR, Roth H, Wagner J. Quadrotors in factory applications: design and implementation of the quadrotor's P-PID cascade control system. *SN Appl Sci*. 2019 Jun 14;1(7):722.
6. Abdelhay S, Zakriti A. Modeling of a Quadcopter Trajectory Tracking System Using PID Controller. *Procedia Manufacturing*. 2019 Jan 1;32:564–71.
7. Miranda-Colorado R, Aguilar LT. Robust PID control of quadrotors with power reduction analysis. *ISA Transactions*. 2020 Mar 1;98: 47–62.
8. Okyere E, Bousbaine A, Poyi GT, Joseph AK, Andrade JM. LQR controller design for quad-rotor helicopters. *The Journal of Engineering*. 2019;2019(17):4003–7.
9. Martins L, Cardeira C, Oliveira P. Linear Quadratic Regulator for Trajectory Tracking of a Quadrotor. *IFAC-PapersOnLine*. 2019 Jan 1;52(12):176–81.
10. Jia Z, Yu J, Mei Y, Chen Y, Shen Y, Ai X. Integral backstepping sliding mode control for quadrotor helicopter under external uncertain disturbances. *Aerospace Science and Technology*. 2017 Sep 1;68:299–307.
11. Xiu C, Liu F, Xu G. General model and improved global sliding mode control of the four-rotor aircraft. *Proceedings of the Institution of Mechanical Engineers, Part I: Journal of Systems and Control Engineering*. 2018 Apr 1;232(4):383–9.
12. Mofid O, Mobayen S. Adaptive sliding mode control for finite-time stability of quad-rotor UAVs with parametric uncertainties. *ISA Transactions*. 2018 Jan 1;72:1–14.
13. Castillo-Zamora JJ, Camarillo-Gómez KA, Pérez-Soto GI, Rodríguez-Reséndiz J. Comparison of PD, PID and Sliding-Mode Position Controllers for V-Tail Quadcopter Stability. *IEEE Access*. 2018;6:38086–96.
14. Liu H, Tu H, Huang S, Zheng X. Adaptive Predefined-Time Sliding Mode Control for QUADROTOR Formation with Obstacle and Inter-Quadrotor Avoidance. *Sensors*. 2023 Jan;23(5):2392.
15. Jiang F, Pourpanah F, Hao Q. Design, Implementation, and Evaluation of a Neural-Network-Based Quadcopter UAV System. *IEEE Transactions on Industrial Electronics*. 2020 Mar;67(3):2076–85.
16. El Gmili N, Mjahed M, El Kari A, Ayad H. Particle Swarm Optimization and Cuckoo Search-Based Approaches for Quadrotor Control and Trajectory Tracking. *Applied Sciences*. 2019 Jan;9(8):1719.
17. Tanveer MH, Ahmed SF, Hazry D, Warsi FA, Joyo MK. Stabilized Controller Design for Attitude and Altitude Controlling of Quad-Rotor Under Disturbance and Noisy Conditions. *AJAS*. 2013 Jul 24;10(8):819–31.
18. Moreno-Valenzuela J, Pérez-Alcocer R, Guerrero-Medina M, Dzul A. Nonlinear PID-Type Controller for Quadrotor Trajectory Tracking. *IEEE/ASME Transactions on Mechatronics*. 2018 Oct;23(5):2436–47.
19. Wu Y, Hu K, Sun XM. Modeling and Control Design for Quadrotors: A Controlled Hamiltonian Systems Approach. *IEEE Transactions on Vehicular Technology*. 2018 Dec;67(12):11365–76.
20. Kidambi KB, Tiwari M, Ijoga EO, MacKunis W. Adaptive Modified RISE-based Quadrotor Trajectory Tracking with Actuator Uncertainty Compensation [Internet]. arXiv; 2023 [cited 2023 Dec 8]. Available from: <http://arxiv.org/abs/2303.10270>
21. Dong T, Zhang Y, Liu Y, Chen C. Quantitative Study of Load Stability of Quadrotor Based on Lyapunov Exponents. *International Journal of Antennas and Propagation*. 2023 Apr 19;2023:e9918890.
22. Tal E, Karaman S. Accurate Tracking of Aggressive Quadrotor Trajectories Using Incremental Nonlinear Dynamic Inversion and Differential Flatness. *IEEE Transactions on Control Systems Technology*. 2021 May;29(3):1203–18.
23. Hong JY, Chiu PJ, Pong CD, Lan CY. Attitude and Altitude Control Design and Implementation of Quadrotor Using NI myRIO. *Electronics*. 2023 Jan;12(7):1526.
24. Niedźliński A, Mościński J, Ogonowski Z. *AdaptiveControl*. PWN. Warsaw. 1995.
25. Audronis T. *Building Multicopter Video Drones*. Packt Publishing; 2014.
26. Bouabdallah S, Noth A, Siegwart R. PID vs LQ control techniques applied to an indoor micro quadrotor. In: 2004 IEEE/RSJ International Conference on Intelligent Robots and Systems (IROS) (IEEE Cat No04CH37566) [Internet]. 2004 [cited 2023 Dec 8]. p. 2451–6 vol.3.
27. Janecki D. Globally stable and exponentially convergent adaptive control. *International Journal of Control*. 1986 Feb 1;43(2):601–13.
28. Ammar NB, Gue SB, Ge JH. Modeling and Sliding Mode Control of a Quadrotor Unmanned Aerial Vehicle. *3rd International Conference on Automation, Control, Engineering and Computer Science*. 2016: 834–840.
29. Herrera M, Chamorro W, Gómez AP, Camacho O. Sliding Mode Control: An Approach to Control a Quadrotor. In: 2015 Asia-Pacific Conference on Computer Aided System Engineering [Internet]. 2015 [cited 2023 Dec 8]. p. 314–9.
30. Rabhi A, Chadli M, Pegard C. Robust fuzzy control for stabilization of a quadrotor. *15th International Conference on Advanced Robotics (ICAR)*. 2011 Jun 1: 471–475.
31. Szcześniak A, Szcześniak Z. Algorithmic Method for the Design of Sequential Circuits with the Use of Logic Elements. *Applied Sciences*. 2021 Jan;11(23):11100.

32. Jacobsen RH, Matlekovic L, Shi L, Malle N, Ayoub N, Hageman K, et al. Design of an Autonomous Cooperative Drone Swarm for Inspections of Safety Critical Infrastructure. *Applied Sciences*. 2023 Jan;13(3):1256.

33. Cheng LL, Liu HB. Examples of quadrocopter control on ROS. In: 2015 IEEE 9th International Conference on Anti-counterfeiting, Security, and Identification (ASID) [Internet]. 2015 [cited 2023 Dec 8]. p. 92–6.

34. Florek M, Huba M, Duchoň F, Šovčík J, Kajan M. Comparing approaches to quadrocopter control. In: 2014 23rd International Conference on Robotics in Alpe-Adria-Danube Region (RAAD) [Internet]. 2014 [cited 2023 Dec 8]. 1–6.

35. Holonec R, Copin Dean R, Dragan F, Rápolti L. Self-guided AR Drone using LabVIEW. 2016;57(5).

36. Gardecki S, Giernacki W, Goslinski J, Kasinski A. An adequate mathematical model of four-rotor flying robot in the context of control simulations. *Journal of Automation Mobile Robotics and Intelligent Systems* [Internet]. 2014 [cited 2023 Dec 8];Vol. 8, No. 2.

37. Koruba Z. Control and correction of a gyroscopic platform mounted in a flying object. *Journal of Theoretical and Applied Mechanics*. 2007. vol. 45, no. 1, p.41–51

38. Koruba Z, Dziopa Z, Krzysztofik I. Dynamics and control of a gyroscope-stabilized platform in a self-propelled anti-aircraft system. *Journal of Theoretical and Applied Mechanics*. 2010;48(1):5–26.

39. Astrom K, Wittenmark B. Adaptive control, Addison-Wesley Publishing Company, 1989.

40. Formánek I, Farana R. Experimental identification of mechanical properties of variable speed drives. In: 2017 18th International Carpathian Control Conference (ICCC) [Internet]. 2017 [cited 2023 Dec 8]. 117–22.

41. Formánek I, Farana R. Design and synthesis of control systems of material flow in industrial companies. In: 2017 18th International Carpathian Control Conference (ICCC) [Internet]. 2017 [cited 2023 Dec 8]. 112–6.

42. Viteckova M, Vitecek A, Janacova D. Robust stability and desired model method. In: 2018 Cybernetics & Informatics (K&I) [Internet]. 2018 [cited 2023 Dec 8]. 1–5.

43. Viteckova M, Vitecek A, Sladka K. Controller tuning by desired model method. In: 2017 18th International Carpathian Control Conference (ICCC) [Internet]. 2017 [cited 2023 Dec 8]. 171–6.

44. Viteckova M, Vitecek A. 2DOF PID controller tuning for integrating plants. In: 2016 17th International Carpathian Control Conference (ICCC) [Internet]. 2016 [cited 2023 Dec 8]. 793–7.

45. Janecki D. New recursive parameter estimation algorithms with varying but bounded gain matrix. *International Journal of Control*. 1988 Jan 1;47(1):75–84.

46. Basri A, Husain A, A. Danapalasingam K. Nonlinear Control of an Autonomous Quadrotor Unmanned Aerial Vehicle using Backstepping Controller Optimized by Particle Swarm Optimization. *Journal of Engineering Science and Technology Review*. 2015 Sep 1;8:39–45.

47. Erkol HO. Attitude controller optimization of four-rotor unmanned air vehicle. *International Journal of Micro Air Vehicles*. 2018 Mar 1;10(1):42–9.

48. Goldberg DE, Holland JH. Genetic Algorithms and Machine Learning. *Machine Learning*. 1988 Oct 1;3(2):95–9.

49. Chandra Mohan B, Baskaran R. A survey: Ant Colony Optimization based recent research and implementation on several engineering domain. *Expert Systems with Applications*. 2012 Mar 1;39(4): 4618–27.

50. Karaboga D, Gorkemli B, Ozturk C, Karaboga N. A comprehensive survey: artificial bee colony (ABC) algorithm and applications. *Artif Intell Rev*. 2014 Jun 1;42(1):21–57.

51. El Gmili N, Mjahed M, El Kari A, Ayad H. Particle Swarm Optimization and Cuckoo Search-Based Approaches for Quadrotor Control and Trajectory Tracking. *Applied Sciences*. 2019 Jan; 9(8):1719.

52. Joshi AS, Kulkarni O, Kakandikar GM, Nandedkar VM. Cuckoo Search Optimization- A Review. *Materials Today: Proceedings*. 2017 Jan 1;4(8):7262–9.

53. Imane S, Mostafa M, Hassan A, Abdeljalil EK. Control of a quadcopter using reference model and genetic algorithm methods. In: 2015 Third World Conference on Complex Systems (WCCS) [Internet]. 2015 [cited 2023 Dec 8]. p. 1–6.

54. LabVIEW™ . System Identification Toolkit Algorithm References. ni.com. June 2008.

55. Cedro L, Janecki D., Determining of Signal Derivatives in Identification Problems -FIR Differential Filters, *Acta Montanistica Slovaca*, R 16, ISSN 1335-1788, 47-54, 2011.

56. Cedro L, Filtry różniczujące w układach czasu rzeczywistego, *Przegląd Elektrotechniczny*, ISSN 0033-2097, R. 89 NR 7/2013. 137-141.

Leszek Cedro:  <https://orcid.org/0000-0002-2419-4044>

Krzysztof Wieczorkowski:  <https://orcid.org/0009-0008-8074-8284>

Adam Szcześniak:  <https://orcid.org/0000-0003-2411-9279>



This work is licensed under the Creative Commons BY-NC-ND 4.0 license.

## FATIGUE BEHAVIOUR OF MEDIUM CARBON STEEL ASSESSED BY THE BARKHAUSEN NOISE METHOD

Katarzyna MAKOWSKA\*, Tadeusz SZYMCZAK \*\*, Zbigniew L. KOWALEWSKI \*\*\*

\*Faculty of Mechatronics, Armament and Aerospace, Military University of Technology,  
ul. gen. Sylwester Kaliski 2, 00-908 Warsaw, Poland

\*\*Department of Vehicle Type-Approval & Testing, Motor Transport Institute, ul. Jagiellonska 80, 03-301 Warsaw, Poland

\*\*\*Department of Experimental Mechanics, Institute of Fundamental Technological Research of the Polish Academy of Sciences,  
ul. Pawinskiego 5B, 02-106 Warsaw, Poland

[katarzyna.makowska@wat.edu.pl](mailto:katarzyna.makowska@wat.edu.pl), [tadeusz.szymczak@its.waw.pl](mailto:tadeusz.szymczak@its.waw.pl), [zkowalew@ippt.pan.pl](mailto:zkowalew@ippt.pan.pl)

received 26 April 2023, revised 30 June 2023, accepted 6 July 2023

**Abstract:** In this paper, an attempt to estimate the stage of the fatigue process using the Barkhausen noise method is studied. First, microstructural and static tensile tests were carried out and, subsequently, fatigue tests up to failure were conducted. After determination of the material behaviour in the assumed static and dynamic conditions, the interrupted fatigue tests were performed. Each specimen was stressed up to a different number of cycles corresponding to 10%, 30%, 50%, 70% and 90% of fatigue lifetime for the loading conditions considered. In the next step of the experimental programme, the specimens were subjected to the Barkhausen magnetic noise measurements. Various magnetic parameters coming from the rms Barkhausen noise envelopes were determined. The linear relationship between the full-width at half-maximum (FWHM) of the Barkhausen noise envelope and the number of loading cycles to fracture was found. Specimens loaded up to a certain number of cycles were also subjected to a tensile test to assess an influence of fatigue on the fracture features.

**Keywords:** fatigue, Barkhausen noise, structural steel, fracture, mechanical properties, deformation

### 1. INTRODUCTION

It is well known that failures of 90% of working parts occur due to fatigue [1, 2]. The following components can be indicated as typical examples of such cases: crankshaft [4, 3], driveshaft [5], shaft [6] and idler gear [7]. They are usually investigated by means of different experimental techniques such as macrophotography [3, 6] or scanning electron microscopy (SEM) [4, 5]. These methods enable to identify quite easily a crack focus, fatigue lines and fringes, damage zone and crack orientation, and permanent deformation in micro-regions. It has to be emphasised however, that they represent destructive techniques, which involve specimen selections at the operational stage or after a specific technical incident. As a result, they lead to the solution of the inverse task, providing information about possible reasons for the crack or component separation only. From a practical point of view, an important issue is the influence of evaluation of fatigue cycles on material properties and technical condition assessment of the element without any physical interference in its geometry and properties. Therefore, non-destructive methods such as ultrasonic [8, 9], magnetic-particle [10] and Barkhausen noise [11, 12] can be relatively very helpful.

The ultrasonic method is the technique most often used in many branches of contemporary industry: automotive [13, 14], aviation [15-17], power engineering and building [18, 19]. However, it should be noted that conventional ultrasonic parameters such as the wave velocity and attenuation coefficient have some limits in applications. The non-homogeneity of the microstructure,

construction geometry and thickness assessment of the elements tested are the main difficulties in the wave velocity measurements. In the case of attenuation coefficient, a difficulty appears in elimination of the influence of material non-homogeneity and surface geometry [20]. In literature [21] the results at zero-to tension cycles on polycrystalline 99.99 mass % copper are discussed. Attenuation coefficient  $\alpha$ , and plate thickness resonant frequencies  $f_n$ , were measured using electromagnetic acoustic resonance (EMAR) [21].

The attenuation coefficient  $\alpha$  is known as follows:

$$\alpha = \left( \frac{16GBb^2}{\pi^4 C^2} \right) \Lambda L^4 f^2, \text{ represents} \quad (1)$$

where  $G$  is the shear modulus,  $\Lambda$  is the dislocation density,  $B$  is the damping constant,  $L$  is the dislocation loop length,  $b$  is the Burgers vector magnitude,  $C$  is the dislocation-line tension and  $f$  is the ultrasonic excitation frequency. The plate thickness resonant frequency can be calculated using the following expression:

$$f_n = nV / (2d), \quad (2)$$

where  $n$  is the integer identifying the mode,  $V$  is the shear wave velocity and  $d$  is the thickness of the plate.

Simultaneously, transmission electron microscopy (TEM) was used to follow the evolution of dislocation microstructure at the fatigue life. Three levels of stress: 105 MPa, 110 MPa and 115 MPa were used and the following values of the cycle number to fracture were obtained, respectively:  $N_f = 253\,800$ ,  $N_f = 116\,000$  and  $N_f = 41\,250$ .

The feature of ultrasonic parameter changes can be divided into four stages. In the first stage attenuation coefficient  $\alpha$  is constant and plate thickness values of frequency  $f_n$  slowly increase. Two processes occur in the material. There is an ongoing process of multiplication dislocation, which leads to an increase  $\Lambda$ , and the process of tangling causes a decrease in  $L$ . This keeps the dislocation damping nearly stable [21].

In the second stage, the coefficient  $\alpha$  increases markedly. Also, the value of  $f_n$  increases. Dislocation multiplication and movement beneath the specimen's surface occur through dislocation slips within the period representing 10% of the specimen fatigue life. The dislocation network is completely reorganised. Dislocations are released from heavy tangling and microstructural features and create stable cell structures [21]. According to Eq. (1) [21], dislocation loop length  $L$  increases, which leads to a significant increase in  $\alpha$  values due to the power relation  $\alpha \sim L^4$ . A slight drop in  $\alpha$  observed just before the maximum can be attributed to the reduced dislocation mobility caused by the heavy tangling and piling-up just before dislocation reorganisation [21].

In the third stage of the loading process, values of the  $\alpha$  coefficient  $\alpha$  decrease; however, its values are not lower than those obtained in the first stage of fatigue. Contrary to that, the  $f_n$  increases as the slip bands decrease. The dislocation mobility is suppressed because of the deceleration of increased slip-band density. As a consequence, dislocations become stationary even to the order of 0.1 nm or less values of ultrasonic amplitude [21]. Dislocations of cell structure have less mobility, and therefore, they are responsible for fatigue hardening [21].

Coefficient  $\alpha$  decreases slightly in the last stage, while  $f_n$  increases since the formation of cell walls is completed and only a very few free dislocations occur in the material considered [21].

Luo et al. [22] analysed an early stage of the pure iron damage due to fatigue carried out for  $R = -1$ ,  $f = 0.1$  Hz and constant stress amplitude equal to 160 MPa. A triangle waveform was applied. The fatigue was interrupted after 1, 2, 5, 10, 25, 100 and 1000 cycles. Each loading process was performed on the individual specimens separately. Two ultrasonic methods were applied. The first one was based on the measurements of longitudinal wave  $L_{CR}$  amplitude reflected at the first critical angle, then propagating beneath and parallelly to the surface [22]. The pulse-echo mode was the second ultrasonic method applied.

According to the first testing method, a new damage parameter was proposed in the following form:

$$A_{dif} = \frac{|A_N - A_0|}{A_{max}}, \quad (3)$$

where  $A_{dif}$  is the normalised amplitude difference,  $A_0$  is the amplitude of  $L_{CR}$  wave before loading,  $A_N$  is the amplitude of  $L_{CR}$  wave after damage and  $A_{MAX}$  is the maximal amplitude under all testing conditions [22].

Taking the pulse-echo mode method, the attenuation coefficient  $\alpha$  was calculated according to the following equation:

$$\mathcal{L} = \frac{20}{2d} \lg \left( \frac{A_1}{A_2} \right), \quad (4)$$

where  $d$  is the specimen thickness,  $A_1$  is the maximum value of amplitude for the first bottom echo and  $A_2$  is the maximum value of amplitude at the second bottom echo [22].

Initially, an amplitude of the  $L_{CR}$  wave was captured after different number of loading cycles. It was found that the amplitude values of the  $L_{CR}$  wave decrease monotonously with increasing cycles. Subsequently, the following parameters were calculated:  $A_{dif}$  of the  $L_{CR}$  method, and  $\alpha$  of the pulse-echo method. It was

found that both  $A_{dif}$  and  $\alpha$  increased first for the plastic strain to lower than  $\varepsilon_p = 3.2\%$ . If it reached  $\varepsilon_p = 3.2\%$ , the  $A_{dif}$  attained the stable stage, whereas the attenuation coefficient  $\alpha$  decreased, and subsequently increased slightly just before  $1 \times 10^3$  fatigue cycles were completed. It has to be mentioned, however, that amplitude difference stabilisation of  $A_{dif}$  can be a result of fatigue damage development and surface roughness  $R_q$  variation as well. The linear increase in  $R_q$  with the number of cycles was observed.

The early stage fatigue damage was considered also in the cast austenite stainless steel CAST by means of both the attenuation coefficient  $\alpha$  and electron backscatter diffraction (EBSD) method [23]. The fatigue process was conducted for the frequency  $f = 2$  Hz and cycle asymmetry coefficient  $R = 0.1$ . Three magnitudes of stress amplitude were considered: 230 MPa, 250 MPa and 270 MPa [23]. In order to evaluate fatigue damage, the  $M_L$  parameter coming from EBSD measurements was taken into account. This parameter was determined based on the analysis of orientation differences between selected points in a grain [24]. As shown in [25], the  $M_L$  parameter was important because the grain orientation affects the propagation of ultrasonic waves, and as a consequence, attenuation coefficient  $\alpha$ .

With respect to some limitations of the ultrasonic techniques, particularly in the damage assessments at the early stage of fatigue, another more powerful non-destructive method should be considered that would be able to potentially detect areas where damage appears.

It was decided that the magnetic Barkhausen noise (MBN) method would be suitable to give support in this matter due to its significant sensitivity to material damage, especially in the early stages of degradation. MBN emission is defined as a voltage signal that is generated by non-continuous domain wall movement in a magnetised material due to the discontinuous changes in the magnetic flux density [26]. The domain walls are pinned temporarily by microstructural barriers (voids, dislocations, precipitates, grain boundaries, non-metallic inclusions) to their motion and they are then released abruptly in the changing magnetic field [27]. A type of domain wall depends on the magnetocrystalline anisotropy coefficient [28]. In the case of steel, the domain walls are of  $180^\circ$  and  $90^\circ$  types [29]. There are some publications that describe some attempts for the Barkhausen noise method application in fatigue process monitoring [30–34]. The authors of [30] examined soft steel A48P2, which contains 0.15% C with a ferrite–pearlite microstructure. It is regarded as the most encountered in steam generator pipes. They also tested the alloyed steel 20CDV5 (0.20% C + Cr–Mo–V), which displays a martensitic microstructure. It is frequently used for steam turbine elements such as rotors or bolts. Both materials were subjected to tension/compression cycling under constant strain. In the case of A48P2 steel, the strain amplitudes of  $\varepsilon = \pm 0.2\%$  and  $\varepsilon = \pm 0.5\%$  were applied, whereas for the 20CDV5 steel, only one value of strain amplitude was taken into account,  $\varepsilon = \pm 1\%$ . Guyon and Mayos obtained the following results for the A48P2 steel: in the case of  $\varepsilon = \pm 0.2\%$  an increase in the maximum amplitude  $BN_{max}$  of the Barkhausen noise amplitude was observed, and moreover, a slight decrease in the position of the maximum amplitude  $HBN_{max}$ , was easily noticed. For a higher value of strain amplitude ( $\varepsilon = \pm 0.5\%$ ), a decrease in the  $BN_{max}$  parameter, and simultaneously, an increase in the  $HBN_{max}$  parameter were obtained. Moreover, a second peak appeared for negative values of the applied field [30], and the characteristic change in the shape of the Barkhausen noise envelope occurred continuously throughout the fatigue life of the material [30]. This behaviour can be attributed to

strain hardening due to growing hindrance of the domain wall movement, and as a consequence, an increase in dislocation density [29]. Unlike the soft ferrite-pearlitic A48P2 steel, the martensitic 20CDV5 steel exhibited fatigue softening during cyclic loading: an increase in the  $BN_{max}$  parameter with insignificant variations of the  $HBN_{max}$  parameter was observed. Moreover, the second peak does not appear [30].

Among the publications describing usage of the Barkhausen noise in evaluation of fatigue damage, the paper by Palit Sagar et al. [33] can be particularly mentioned. The authors examined a low-carbon steel with 0.15%C. The material was subjected to cyclic loading of the stress amplitude equal to 260 MPa and frequency of 10 Hz. It was observed that the maximum amplitude  $BN_{max}$  of the Barkhausen emission increased by up to 40% of the material fatigue lifetime and then started to decrease [33].

The measurements carried out by da Silva Junior et al. [32] on SAE8620 steel exhibited a strong sensitivity of the maximum amplitude  $BN_{max}$  of Barkhausen noise on the number of cycles in the early stage of damage process development (under a stress level of 259 MPa): a strong increase in the  $BN_{max}$  parameter with the number of cycles in the range from 0 to 60 000 cycles was clearly documented [32]. Palma et al. [35] calculated the values of the cumulative Barkhausen noise parameter ( $BN_{sum}$ ), according to the equation:

$$BN_{sum} = \sum_{n=0}^{n=n} \left( 1 - \frac{v_n}{v_0} \right), \quad (5)$$

where  $V_n$  is the root-mean-square (RMS) of Barkhausen voltage for the loaded specimen at the  $n$ -th fatigue cycle number, and  $V_0$  is the RMS voltage signal of steel in the as-received state. Similarly as in [32], SAE8620 steel was tested. It was subjected to three levels of stress amplitude: 217 MPa, 259 MPa and 427 MPa. The authors found that  $BN_{sum}$  increases as the number of cycles and stress amplitudes increases [30]. For the stress amplitude close to the fatigue limit of SAE8620 steel ( $S_e = 194 \pm 5$  MPa), the  $BN_{sum}$  parameter varies only slightly with the fatigue time [35]. Increasing the fatigue stress amplitude leads to an increase of the Barkhausen noise due to major changes in the material microstructure [35].

A shape of the Barkhausen noise envelopes for 14MoV6-3 (1.7715, 13HMF) and X10CrMoVNb9-1 (1.4903, P91) steels was studied in detail by Augustyniak et al. [34], after different levels of fatigue damage.

An innovation of this research is reflected by the fatigue effects analysis carried out simultaneously with the Barkhausen noise method usage. Thanks to such an approach, material damage can be monitored even in the early stages of exploitation, and moreover, the method provided information about the microstructural changes and strain/stress history as well.

## 2. MATERIAL, SPECIMENS AND EXPERIMENTAL PROCEDURE

The 42CrMo4 steel, also denoted as 1.7225, was selected for the experimental analysis due to its wide applicability, covering different branches of industry, that is motor transport, aviation, power engineering, building construction and so on [36]. One can indicate an application of the 42CrMo4 steel in the energy industry as hollow shafts for wind turbines [37]. Axles, shafts [37], crankshafts [38], connecting rods [39], chain wheels [40], motor cylin-

ders, ball pins and multi-spline shafts [41] can serve as typical examples of structural components where this kind of steel found widespread application. The mentioned application examples show that the material can be effectively used under various types of loading, from static to dynamic.

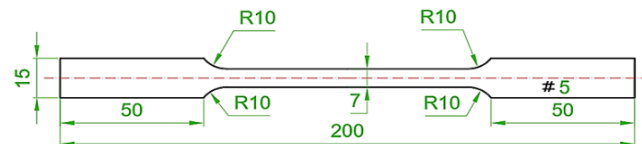


Fig. 1. Engineering drawing of flat specimen for tensile tests

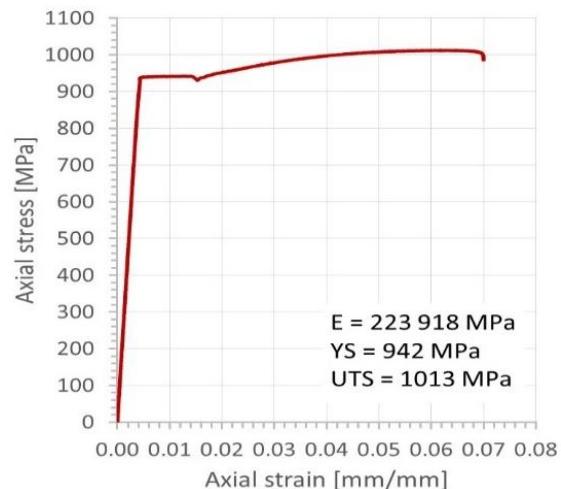


Fig. 2. Tensile characteristic and mechanical parameters of the 42CrMo4 steel in the as-received state: E – Young's modulus, YS – yield stress, UTS – ultimate tensile strength

Three main stages of the experimental procedure, represented by destructive and non-destructive tests and analysis of the relationships between results coming from fatigue and non-destructive magnetic investigation were performed. In the first stage, tensile tests were carried out in order to determine the mechanical parameters of the material in the as-received state. Hence, the flat specimens of geometry and the dimensions shown in Fig. 1 were employed. Standard tensile tests were carried out at room temperature using an 8802 INSTRON servo-hydraulic testing machine and flat specimens. The tests were executed under monotonically increasing loading with a displacement rate of 1 mm/min. Based on the tensile characteristic the following mechanical parameters were determined: Young's modulus (E), yield stress (YS) and ultimate tensile strength (UTS); see Fig. 2. Subsequently, the microstructural observations were performed on polished specimens using light microscopy technique; see Fig. 3. The specimens for microstructural inspections were etched using nital.

Fatigue tests were carried out in the second stage of the experiment. The specimens of the same geometry as for the static tensile tests were manufactured. An axial stress signal in the form of sinusoidal function was applied to control all fatigue tests. Cyclic loading in fatigue tests was characterised by the following parameters: cycle asymmetry coefficient  $R = 0.1$ , stress amplitude of 400 MPa and mean stress level of 500 MPa, while the minimum and maximum values of stress ranged from 100 MPa and 900 MPa, respectively; see Fig. 4. The value of maximum stress was

established based on the values of proportional and elastic limits determined from the tensile characteristic.

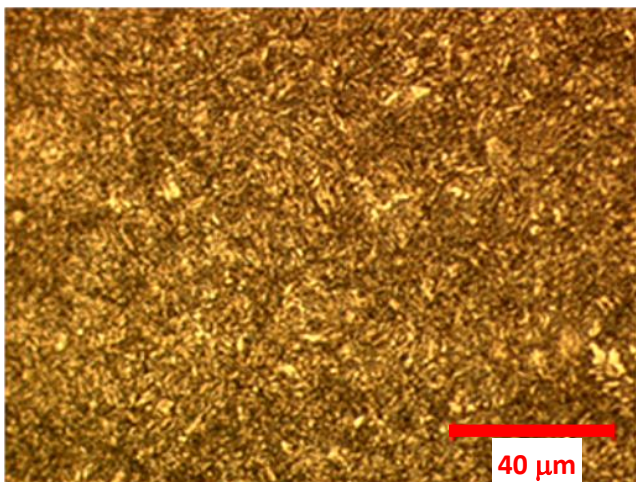


Fig. 3. Microstructure of the 42CrMo4 steel

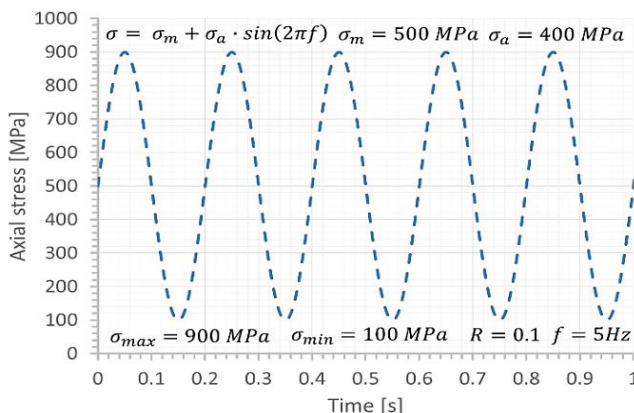


Fig. 4. A scheme of cyclic loading versus time with the main test parameters

The fatigue tests were stopped at defined values of cycle number: 2 510, 7 540, 12 566, 17 590 and 22 620. They correspond to the following lifetime percentage: 10%, 30%, 50%, 70% and 90%, respectively. For each portion of cycles considered, the material was unloaded, and subsequently, subjected to the Barkhausen noise measurements using an MEB-4C defectoscope.

The head of the measuring seat consisted of a U-shaped core of electromagnets wrapped in the wound excitation coil. The pick-up coil was built-in to the sensor. In the pick-up coil, a voltage signal was induced. A triangular waveform was used. The fast-variable component was separated by means of a high-pass filter  $f = (0-500)$  Hz. Analysis of this component provided information on the degree of simulated exploitation of the steel tested.

The envelopes of magnetic Barkhausen noise were calculated as rms value  $U_b$  according to the equation [29]:

$$U_b = \sqrt{\frac{1}{\tau} \int_0^\tau U_{tb1}^2(t) dt}, \quad (6)$$

where  $U_b$  [V] is the root mean square of the coil output voltage,  $U_{tb1}$  [V] is the fast-variable component defining voltage separated by means of the high-pass filter from the induced voltage in the pick-up coil and  $\tau$  [s] is the integration time.

Then, the amplitude of Barkhausen noise ( $Ub_{pp}$ ), defined as the voltage difference between the maximum peak value of the magnetic Barkhausen noise ( $U_b$ ) and the background noise ( $U_{tb}$ ), was determined.

In the next step the integral of the half-period voltage signal of MBN was calculated [29]:

$$Int(Ub) = \int_{-U_{gmax}}^{U_{gmax}} U_{sb} dU_g, \quad (7)$$

where  $U_{sb}$  [V] is the rms of the Barkhausen emission voltage after correction due to background noise,  $U_b$  [V] is the rms of the coil output voltage,  $U_{tb}$  [V] is the rms of background voltage and  $U_g$  [V] is the generator voltage.

Moreover, the full-width at half-maximum (FWHM) of rms envelope of the Barkhausen noise was determined.

In the next stage of the experimental programme, static tensile tests were performed on the specimens after fatigue in order to discover the nature of the material fracture.

### 3. RESULTS AND DISCUSSION

As it was discovered in this research, the 42CrMo4 steel exhibits very attractive mechanical parameters characterised by high values of yield stress and ultimate tensile strength: 942 MPa and 1013 MPa, respectively; see Fig. 2. This is due to the tempered martensite microstructure of the material in question (Fig. 3) and sufficient carbon content. It has to be emphasised that the proportional limit of this steel equal to 848 MPa is also very beneficial, taking into account a heavy loading of elements that require working conditions without permanent deformation. Thanks to this, 42CrMo4 steel can be treated as the engineering material of mechanical parameters fulfilling the requirements for high-strength steel grades.

Fracture regions of the fatigue pre-strained 42CrMo4 steel subjected to the tensile test, expressed differences in the material degradation, identifying an influence of the fatigue process on the steel response under monotonically increasing tensile force; see Fig. 5. It can be easily noticed that the fracture zones are represented by different sections. In the case of steel tested in the as-received state, two regions can be evidenced. In the middle of the fracture zone, the horizontal plane with longitudinal cracks was dominant, while the border area was represented by the angular plane; see Fig. 5a. This means that decohesion of the steel started under normal stress and was finalised thanks to the combination of shear and normal stress state components. In the case of pre-strained steel, due to fatigue loading history corresponding to 70% of the total fatigue lifetime, that is 17 590, the brittle region became more dominant; see Fig. 5b, and for the cycle numbers 22 620 (90% of the total fatigue lifetime) this region was completely covered by the damage zone; see Fig. 5c.

The shape of the Barkhausen noise envelope changed after the application of fatigue loading; see Fig. 6. RMS Barkhausen noise variations were attributed to the microstructural changes that occurred during the fatigue process. Since tempered martensite contained small cementite particles in the fine-grained ferritic martensite, only a slight increase in the effective voltage value  $U_b$  can be observed as the second maximum coming from cementite; see Fig. 6.

The magnetic parameters determined from the rms envelope of the Barkhausen noise were presented as a function of the number of cycles to failure. An increase in the  $Ub_{pp}$  parameter in the range from 0% to 10% of the fatigue damage lifetime was

clearly identified. This is because new dislocations appeared in the material due to dynamic loading. According to Moorthy et al. [42], the Barkhausen noise voltage increases when the microstructural features amount  $n$  and domain walls velocity  $v$  increase, but simultaneously, the time of flight  $t$  of domain walls movement between defects decreases. This can be described by the following expression:

$$U_b = \frac{nv}{t} \quad (8)$$

where:  $n$  is the amount of microstructural features,  $v$  is the velocity of domain walls and  $t$  is the time of flight of domain walls movement between defects.

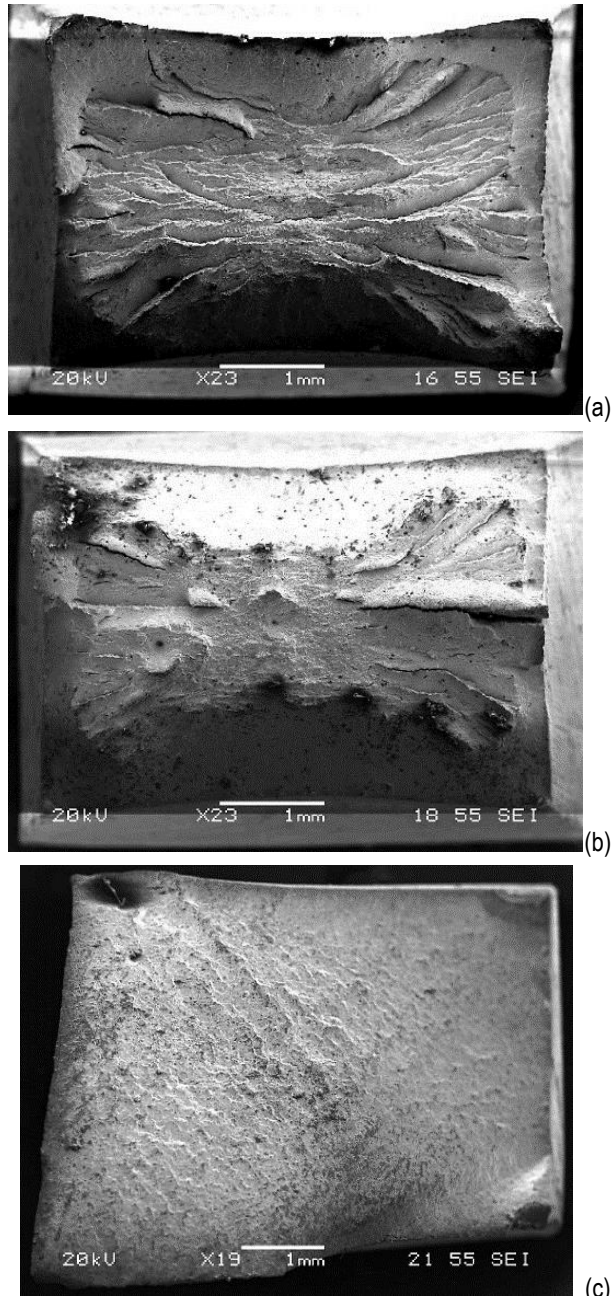


**Fig. 5.** Fracture zones after tensile tests in the 42CrMo4 steel preloaded due to fatigue for the following parts of the fatigue lifetime: (a) 0%, (b) 70% and (c) 90%

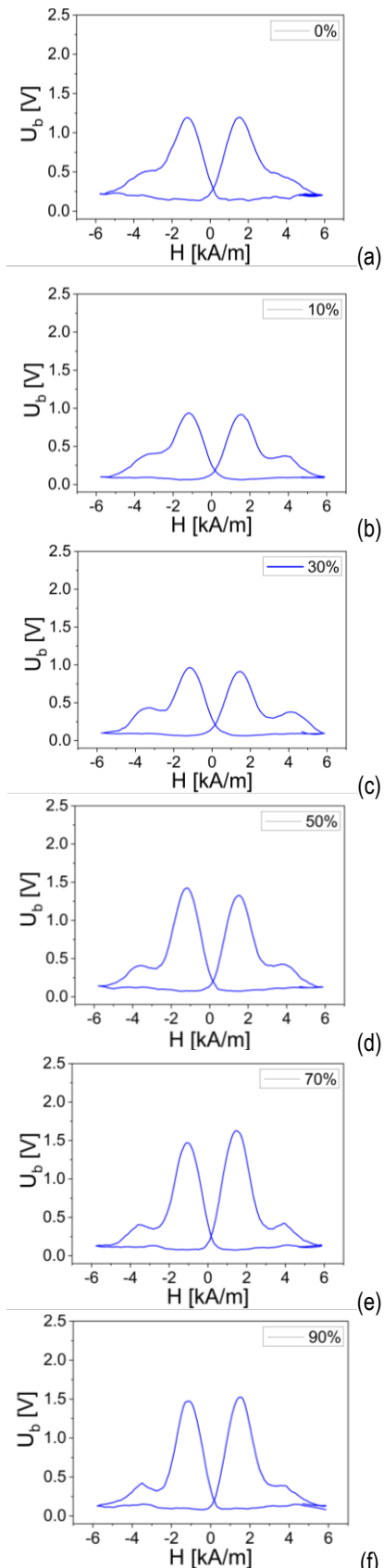


**Fig. 6.** Envelopes of the rms Barkhausen noise before and after fatigue loading: (a) as-received steel; (b), (c), (d), (e) and (f) steel tested under fatigue interrupted after 10%, 30%, 50%, 70% and 90% of the total lifetime of the material, respectively

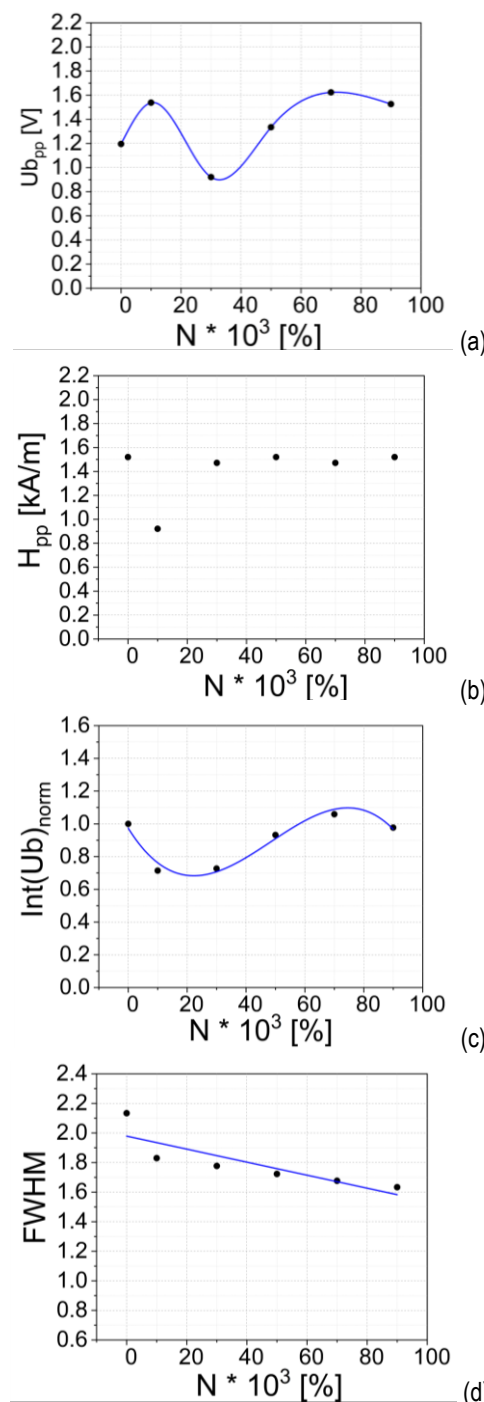


Fig. 7. Magnetic parameters determined from the rms Barkhausen noise envelope versus percentage of fatigue lifetime

As stated by Sagar et al. [33], the initial increase in Barkhausen noise amplitude can be attributed to the dislocation rearrangements and formation of cell structures. However, one can notice that these tests were carried out by this research team on low-carbon steel of the carbon content higher by weight of about 2.7 times in comparison to the steel tested in this research.

The results obtained for the fatigue pre-strained steel of up to 30% of the total fatigue lifetime show that the value of the  $Ub_{pp}$  parameter decreases. This effect can be attributed to the increase in dislocation density, which hinders the movement of the domain walls in the material [33]. As a consequence, a less number of the domain walls were able to move due to stronger pinning [33]. Sagar et al. [33] also observed a reduction in the dislocation cell

size in the low-carbon steel tested.

Another possible reason for the Barkhausen noise amplitude decrease is the persistent slip bands (PSBs) formation in the material due to dynamic loading [33]. The accumulation of deposited dislocations on the PSB–material matrix interfaces causes during fatigue three-dimensional residual compression stress in PSBs [43]. However, it is well known [27, 44, 45] that compressive stresses reduce the Barkhausen noise level in materials with a positive coefficient of magnetocrystalline anisotropy  $K$ . Steels belong to such materials.

Taking into account the results of the steel fatigue pre-strained for the higher number of loading cycles (exceeding 30% of the number of cycles to failure), the Barkhausen noise level, expressed as the  $Ub_{pp}$  parameter, increases. Under such testing conditions, the crack initiates, and then, the stress relaxation takes place, leading as a consequence to  $Ub_{pp}$  increase [33]. The trends in increase or decrease of the  $Ub_{pp}$  parameter of the medium carbon steel are very similar to those presented in the literature [32] for the SAE8620 steel.

Earlier publications did not pay attention to the magnetic parameters determined from the Barkhausen noise rms envelope, such as  $\text{Int}(Ub)$ ,  $H_{pp}$  and FWHM [32, 33, 46]. It turns out that changes in these parameters considered as a function of the number of loading cycles have a completely different character. For example, a linear decrease in the FWHM parameter versus the cycles to failure was observed.

#### 4. CONCLUSIONS

Magnetic Barkhausen effect was used to identify the damage degree of the 42CrMo4 medium carbon steel subjected to fatigue loading conditions. The rms Barkhausen noise envelope follows material degradation due to cyclic loading, and as a consequence evolution of dislocation structure.

Among the considered parameters, FWHM is the most suitable since it changes linearly with the increasing number of loading cycles, thus giving fast assessments of the material degradation. It decreases with the duration of the fatigue process and damage development.

The linear character of the relationship between the FWHM parameter and the number of loading cycles to fracture was discovered, providing the promising tool for early fatigue damage inspection. This means the method can support diagnostic and inspection processes of elements and structural metallic materials with the application of other non-destructive methods.

#### REFERENCES

1. Heyes AM. Automotive component failures. Eng Fail Anal. 1998;5(2):129–141. Available from: [https://doi.org/10.1016/S1350-6307\(98\)00010-7](https://doi.org/10.1016/S1350-6307(98)00010-7)
2. Meyers MA., Chawla KK. Mechanical behaviour of materials. Cambridge University Press, Cambridge, second edition, 2009.
3. Bhaumik SK. Fatigue fracture of crankshaft of an aircraft engine. Eng Fail Anal. 2002;9(3):255–263. Available from: [https://doi.org/10.1016/S1350-6307\(01\)00022-X](https://doi.org/10.1016/S1350-6307(01)00022-X)
4. Fonte M, Anes V, Duarte P, Reis L, Freitas M. Crankshaft failure analysis of a boxer diesel motor. Eng Fail Anal. 2015;5:109–115. Available from: <https://doi.org/10.1016/j.engfailanal.2015.03.014>
5. Godec M, Mandrino Dj, Jenko M. Investigation of the fracture of car's drive shaft. Eng Fail Anal. 2009;16(4):1252–1261. Available from: <https://doi.org/10.1016/j.engfailanal.2008.08.022>

6. Tjernberg A. Fatigue lives for induction hardened shafts with subsurface crack initiation. *Eng Fail Anal.* 2002; 9(1):45–61. Available from: [https://doi.org/10.1016/S1350-6307\(00\)00036-4](https://doi.org/10.1016/S1350-6307(00)00036-4)
7. Yu Z, Xu X. Failure analysis of an idler gear of diesel engine gearbox. *Eng Fail Anal.* 2006;13:1092–1100. Available from: <https://doi.org/10.1016/j.engfailanal.2005.07.015>
8. Chen B, Wang C, Wang P, Zheng S, Sun W. Research on fatigue damage in high-strength steel (FV520B) using nonlinear ultrasonic testing. *Shock and Vibration* 2020; 8(19):1–15. Available from: <https://doi.org/10.1155/2020/8847704>
9. Sarris G, Haslinger SG, Huthwaite P, Lowe MJS: Ultrasonic methods for the detection of near surface fatigue damage. *NDT & E Int.* 2023;135:1–13. Available from: <https://doi.org/10.1016/j.ndteint.2023.102790>
10. Kowalczyk D, Aniszewicz A. Experimental and simulation tests of 1MN screw coupling. *Problemy Kolejnictwa. Rail. Rep.* 2022;194: 97–102. Available from: <https://doi.org/10.36137/1943E>
11. Bjørheim F, Siriwardane SC, Pavlou D. A review of fatigue damage detection and measurement techniques. *Int. J. Fat.* 2022;154:1–16. Available from: <https://doi.org/10.1016/j.ijfatigue.2021.106556>
12. Wu H, Ziman JA, Raghuraman SR, Nebel J-E, Weber F, Starke P.: Short-time fatigue life estimation for heat treated low carbon steels by applying electrical resistance and magnetic Barkhausen noise. *Materials.* 2023;16:1–21. Available from: <https://doi.org/10.3390/ma16010032>
13. Roye W. Ultrasonic testing of spot welds in the automotive industry. *Krautkramer*, SD 298, 11/99, 6 pages.
14. Yuhas DE, Vorres CL, Remiasz JR, Gesch E, Yamane T. Non-destructive ultrasonic methods for quality assurance of brake pads. *EuroBrake*. 2012, April 16–18th 2012, Dresden Germany.
15. Lamarre A. Ultrasonic phased-array for aircraft maintenance, Amsterdam, November 2009, 76 slides. Available from: <https://ndt.aero/images/docs/UTPAfor%20maintenance.pdf>
16. Wronkowicz A, Dragan K. Damage evaluation based on ultrasonic testing of composite aircraft elements and image analysis methods. *MATEC Web of Conferences* 204, IMIEC 2018, 06003. Available from: <https://doi.org/10.1051/matecconf/201820406003>
17. Lubiński R, Ziemkiewicz J, Synaszko P, Zyluk A, Dragan KA. Comparison of composite specimens damage area measurements performed using pulsed thermography and ultrasonic NDT methods. *Fat. Air. Struc.* 2019; 2019(11): 68–77. Available from: <https://doi.org/10.2478/fas-2019-0007>
18. Drelich R, Rosiak M, Pakula M. Application of non-contact ultrasonic method in air to study fiber-cement corrugated boards, *Bull. Pol. Ac. Tech.*, 2021;69(2). Available from: <https://doi.org/10.24425/bpasts.2021.136740>
19. Callejas A, Palma R, Hernández-Figueirido D, Rus G. Damage detection using ultrasonic techniques in Concrete-Filled Steel Tubes (CFSTs) columns. *Sensors.* 2022;22,4400. Available from: <https://doi.org/10.3390/s2212440>
20. Mackiewicz S. Possibilities of ultrasonic evaluation of energetic steels as a result longterm exploitation (in Polish). *Materiały Konferencyjne VII Sympozjum Informacyjno-Szkoleniowe „Diagnostyka i remonty długookopłotowanych urządzeń energetycznych. Nowe problemy diagnostyczne na starych blokach energetycznych”*, 05–07 October 2005, Ustroń, Poland.
21. Hirao M, Ogi H, Suzuki N, Ohtani T. Ultrasonic attenuation peak during fatigue of polycrystalline copper. *Acta Mater.* 2000;48:517–524. Available from: [https://doi.org/10.1016/S1359-6454\(99\)00346-8](https://doi.org/10.1016/S1359-6454(99)00346-8)
22. Luo Z, Meng Y, Fan S, Lin L. Assessment of surface/subsurface damage in early-stage fatigue: A new attempt based on LCR wave. *Int. J. Fat.* 2023;170:107537. Available from: <https://doi.org/10.1016/j.ijfatigue.2023.107537>
23. Luo Z, Wang X, Ma Z, Zou L, Zhu X, Lin L. Combined quantitative evaluation on early-stage fatigue damage of coarse-grained austenite stainless steel based on EBSD and ultrasonic technique. *Ultrasonics* 2020;103:106090. Available from: <https://doi.org/10.1016/j.ultras.2020.106090>
24. Kamaya M, Kuroda M. Fatigue damage evaluation using backscatter diffraction. *Mater. Trans.* 2011;52:1168–1176. Available from: [https://doi.org/10.1016/S1359-6454\(99\)00346-810.2320/matertrans.M2011014](https://doi.org/10.1016/S1359-6454(99)00346-810.2320/matertrans.M2011014)
25. Luo Z, Dong H, Ma Z, Zou L, Zhu X, Lin L. Orientation relationship between ferrite and austenite and its influence on ultrasonic attenuation in cast austenitic stainless steel. *Acta Physica Sinica.* 2018;67: 238102. Available from: <https://doi.org/10.7498/aps.67.20181251>
26. Piotrowski L, Augustyniak B, Chmielewski M, Tomaś I. The influence of plastic deformation on magnetoelastic properties of the CSN12021 grade steel. *J Magn Magn Mater.* 2009;321(15):2331–2335. Available from: <https://doi.org/10.1016/j.jmmm.2009.02.028>
27. Blaow M, Evans JT, Shaw BA. The effect of microstructure and applied stress on magnetic Barkhausen emission in induction hardened steel. *J Mater Sci.* 2007;42(12):4364–4371. Available from: <https://doi.org/10.1007/s10853-006-0631-5>
28. Piech T. Magnetic research. Application of Barkhausen effect (in Polish). *Biuro Gamma*, Warsaw, 1998.
29. Jiles D. *Introduction to magnetism and magnetic materials*. CRC Press, Boca Raton. 1998.
30. Guyon M, Mayos M. Nondestructive evaluation of fatigue damage of steels using magnetic techniques. *Review of Progress in Quantitative Nondestructive Evaluation*. 14. Edited by D.O. Thompson and D.E. Chimenti, Plenum Press, New York, 1995, 1717–1724.
31. Palma ES, Mansur TR, Ferreira Silna Jr S, Alvarenga Jr A. Fatigue damage assessment in AISI 8620 steel using Barkhausen noise. *Int J Fat.* 2005;27(6):659–665. Available from: <https://doi.org/10.1016/j.ijfatigue.2004.11.005>
32. da Silva Junior SF, Mansur TR, Aguiar AE, Palma ES, Marques PV. Damage accumulation study in fatigue testing using Barkhausen noise. *Proceedings of COBEM 2003, 17th International Congress of Mechanical Engineering*, 10–14 November 2003, São Paulo, Brazil. Available from: <https://www.abcm.org.br/anais/cobem/2003/html/pdf/COB03-0558.pdf>
33. Sagar PS, Parida N, Das S, Dobmann G, Bhattacharya DK. Magnetic Barkhausen emission to evaluate fatigue damage in a low carbon structural steel. *International Journal of Fatigue.* 2005;27(3): 317–322. Available from: <https://doi.org/10.1016/j.ijfatigue.2004.06.015>
34. Augustyniak B, Piotrowski L, Chmielewski M, Kowalewski Z. Comparative study with magnetic techniques of P91 and 13HM steels properties subjected to fatigue tests. *J Elec Eng.* 2012;63(7):15–18. Available from: [http://iris.elf.stuba.sk/JEEEC/data/pdf/7s\\_112-04.pdf](http://iris.elf.stuba.sk/JEEEC/data/pdf/7s_112-04.pdf)
35. Palma ES, Junior AA, Mansur TR, Pinto JMA. Fatigue damage in AISI/SAE 8620 steel. *Proceedings of COBEM 2003, 17th International Congress of Mechanical Engineering*, 10–14 November 2003, São Paulo, Brazil. Available from: <https://www.abcm.org.br/anais/cobem/2003/html/pdf/COB03-0066.pdf>
36. Morsy MA, El-Kashif E. Repair welding reclamation of 42CrMo4 and C45 steels. *Proceedings of IIW 2017 International Conference*, June, 29–30 Shanghai, R.P. China.
37. Costa LL, Brito AMG., Rosiak A, Schaeffer L. Microstructure evolution of 42CrMo4 during hot forging process of hollow shafts for wind turbines. *Int. J. Adv. Man. Tech.* 2020; 106:511–517. Available from: <https://doi.org/10.1007/s00170-019-04642-w>
38. Fischer A, Scholtes B, Niendorf T. Influence of deep rolling and induction hardening on microstructure evolution of crankshaft sections made from 38MnSiVS5 and 42CrMo4. *HTM-J Heat Treat Mater.* 2021;76:175–179. Available from: <https://doi.org/10.1515/htm-2021-0002>
39. Basavaraj Y, Joshi R, Setty GR. FEA of NX-11 unigraphics modelled connecting rod using different materials. *Mater Today: Proc.* 2021;46:2807–2813. Available from: <https://doi.org/10.1016/j.matpr.2021.02.620>
40. Wieczorek AN. Studies on the combined impact of external dynamic forces and quartz abrasive on the wear of chain wheels made of 42CrMo4 steel which are used in conveyors [in Polish]. *Autobusy.* 2016;6:1207–1210.

41. Das S, Mukhopadhyay G, Bhattacharyya S. Failure analysis of axle shaft of a fork lift. *Case Studies in Eng Fail Anal.* 2015;3:46–51. Available from: <https://doi.org/10.1016/j.csefa.2015.01.003>
42. Moorthy V, Choudhury BK, Vaidyanathan S, Jayakumar T, Rao KBS, Raj B. An assessment of low cycle fatigue using magnetic Barkhausen emission in 9Cr-1Mo ferritic steel. *Int J Fat.* 1999;21(3):263–269. Available from: [https://doi.org/10.1016/S0142-1123\(98\)00079-6](https://doi.org/10.1016/S0142-1123(98)00079-6)
43. Polák J, Man J. Mechanisms of extrusion and intrusion formation in fatigue crystalline materials. *Mater Sci Eng A.* 2014;596:15–24. Available from: <https://doi.org/10.1016/j.msea.2013.12.005>
44. Anglada-Rivera J, Padovese LR, Capó-Sánchez J. Magnetic Barkhausen noise and hysteresis loop in commercial carbon steel: influence of applied tensile stress and grain size. *J Magn Magn Mater.* 2001;231(2-3):299–306. Available from: [https://doi.org/10.1016/S0304-8853\(01\)00066-X](https://doi.org/10.1016/S0304-8853(01)00066-X)
45. Stewart DM, Stevens KJ, Kaiser AB. Magnetic Barkhausen noise analysis of stress in steel. *Curr Appl Phys.* 2004;4(2-4):308–311. Available from: <https://doi.org/10.1016/j.cap.2003.11.035>
46. Tomita Y, Hashimoto K, Osawa N. Nondestructive estimation of fatigue damage for steel by Barkhausen noise analysis. *NDT & E Inter.* 1996;29(5):275–280. Available from: [https://doi.org/10.1016/S0963-8695\(96\)00030-8](https://doi.org/10.1016/S0963-8695(96)00030-8)

Katarzyna Makowska:  <https://orcid.org/0000-0002-7348-8700>

Tadeusz Szymczak:  <https://orcid.org/0000-0003-2533-7200>

Zbigniew L. Kowalewski:  <https://orcid.org/0000-0002-8128-0846>



This work is licensed under the Creative Commons  
BY-NC-ND 4.0 license.

## THE VARIATIONAL ITERATION METHOD FOR A PENDULUM WITH A COMBINED TRANSLATIONAL AND ROTATIONAL SYSTEM

Muhammad AMIR\*, Asifa ASHRAF \*\*, Jamil Abbas HAIDER\*

\*Abdus Salam School of Mathematical Sciences, Government College University, Lahore 54600, Pakistan

\*\*Department of Mathematics, University of Management and Technology, Lahore 54782, Pakistan

[muhammadamir282959@gmail.com](mailto:muhammadamir282959@gmail.com), [asifaashraf90@gmail.com](mailto:asifaashraf90@gmail.com), [jhaider@math.qau.edu.pk](mailto:jhaider@math.qau.edu.pk)

received 21 March 2023, revised 21 May 2023, accepted 17 June 2023

**Abstract:** The dynamic analysis of complex mechanical systems often requires the application of advanced mathematical techniques. In this study, we present a variation iteration-based solution for a pendulum system coupled with a rolling wheel, forming a combined translational and rotational system. Furthermore, the Lagrange multiplier is calculated using the Elzaki transform. The system under investigation consists of a pendulum attached to a wheel that rolls without slipping on a horizontal surface. The coupled motion of the pendulum and the rolling wheel creates a complex system with both translational and rotational degrees of freedom. To solve the governing equations of motion, we employ the variation iteration method, a powerful numerical technique that combines the advantages of both variational principles and iteration schemes. The Lagrange multiplier plays a crucial role in incorporating the constraints of the system into the equations of motion. In this study, we determine the Lagrange multiplier using the Elzaki transform, which provides an effective means to calculate Lagrange multipliers for constrained mechanical systems. The proposed solution technique is applied to analyse the dynamics of a pendulum with a rolling wheel system. The effects of various system parameters, such as the pendulum length, wheel radius and initial conditions, are investigated to understand their influence on the system dynamics. The results demonstrate the effectiveness of the variation iteration method combined with the Elzaki transform in capturing the complex behaviour of a combined translational and rotational system. The proposed approach serves as a valuable tool for analysing and understanding the dynamics of similar mechanical systems encountered in various engineering applications.

**Key words:** Elzaki transform, Variational iteration method, Combined translational and rotational system, Pendulum with rolling wheel

### 1. INTRODUCTION

A pendulum with a rolling wheel is a fascinating physical system that has numerous applications in engineering and physics. One of its most common applications is in the design of mechanical clocks, where the oscillation of the pendulum is used to regulate the motion of the clock's gears and maintain accurate time-keeping. The rolling wheel adds an extra dimension to the pendulum's motion, leading to new and interesting phenomena that can be studied and utilised in various applications. Another important application of a pendulum with a rolling wheel is in the study of dynamics and control systems. By analysing the system's motion and behaviour, engineers and scientists can gain valuable insights into how to control and stabilise complex mechanical systems. For example, this system can be used to design effective suspension systems for vehicles or to develop new control algorithms for robots and other automated machines [1-3]. Another interesting physical system is the combined translational and rotational system. This system is often encountered in many everyday devices, such as the wheels of a car or the rotor of a helicopter. By studying the motion of these systems, engineers can gain valuable insights into how to design more efficient and effective mechanical devices. Furthermore, the combined translational and rotational system has many applications in the field of robotics. By understanding how this system behaves and interacts with their environment, researchers can design more advanced and capable robots that can perform complex tasks and interact with the world in more natural ways.

F. Inada et al. [4] discussed the stability analysis of a two-degree-of-freedom system combined with a rotational and translational system. T. Koray Palazoğlu and Welat Miran [5] experimentally investigated the combined translational and rotational movement on radio frequency heating uniformity. The complex dynamics of a mechanical mechanism [6] can be solved both numerically and analytically by utilising the harmonic balance technique and RK fourth-order method. Two-dimensional numerical simulation [7] is used to investigate the mechanical activities on a moving invader into a granular material subject to a gravity field. The rotating pendulum system, three-degree-of-freedom auto-parametric system and spring-pendulum system have significant applications. The windmill and waterwheel aid in the development of energy harvesting. For many years, researchers have been striving to find a way to store the energy produced by heat and vibrations. The desire to power sensor networks and mobile devices without batteries that require external charging or maintenance is one of the driving forces behind the need for innovative energy-harvesting systems. Energy harvesting is also known as ambient power, or power harvesting is the process by which energy is derived from external sources such as solar electricity, wind, and thermal and kinetic energy; then stored for use by small, wireless autonomous devices such as wearable electronics devices, condition monitoring systems[8] and wireless networks of sensors [9]. Recently, pendulum energy harvesters have been used in ultra-low-frequency environments, including ocean waves, human motion and structural vibration.



Fig. 1. Classification of pendulum energy-harvesting technologies [10]

It is assumed that a rotational pendulum has a length and a lumped mass, and rotates at a constant speed. Wherever the pendulum's angular displacement in the vertical direction is, that is where the kinetic energy and potential energy exist. The Lagrange equation can be used to obtain the rotational pendulum equation. In many devices and structures, the vibrations that are excited generally have an improper and undesirable consequence. Currently, there are several various approaches to decrease or even stop the oscillating system's amplitude. A vibrating system coupled to an auxiliary mass using a spring is the most basic type of a dynamic vibration absorber. This kind is highly beneficial when the system becomes excited by a regularly changing force with a fixed frequency, particularly when the force's frequency is very close to the resonance frequency of the system under consideration [11]. The main system is coupled to an auto-parametric pendulum absorber as a secondary subsystem, which reduces the energy from the primary system [12]. Many constructed structures including clocks, percussion instruments, roller coasters and gravitational anomalies caused by earthquakes utilise pendulums from a practical perspective. Engineers are making an effort to comprehend the physics of the pendulum, centripetal force and inertia. A pendulum is used to improve the tempo of music. The oscillatory motion of a simple pendulum is one of the most investigated motions in applied physics and engineering. The motion of a pendulum plays a vital role in the historical background of physics and general topics in textbooks for undergraduate students. Thus, a simple pendulum is the most common mechanical example, and studying it eases the basics of classical mechanics. In many textbooks and engineering applications, the periodic motion is generated by reduced angle fluctuation using a simple pendulum [13]. The governing equation is non-linear if this restriction is not followed. However, this problem has an exact analytic solution within an integral formula [14]. Therefore, getting an exact, bounded approximated solution is helpful [15-16]. A simple pendulum has the most basic and comprehensive structure, which serves as the foundation for numerous complicated applications. Its significance in analysing the non-linear phenomena surrounding us is established in both engineering fields and fundamental areas such as physics and chemistry, and the lower dimensional compound system such as a swinging Atwood's machine [17], spring mass pendulum [18-19] and elastic pendulum [20-22] can demonstrate a wide variety of non-trivial phenomena including continuous processes and many types of resonance. A simple pendulum and another oscillating system, for example, a pendu-

lum rotating with a different trajectory of its pivots, are components of different machine parts. Auto-parametric resonance is significant for this type of mechanical system. Hence, to determine the significance of a simple pendulum problem, the present work focused on what happens when a simple pendulum is attached to a lightweight spring.

Ordinary and partial differential equations are significant in many fields of science, including biology, mathematics, chemistry and applied physics. The physical importance of the condition that qualitatively governs dynamic behaviours and uses of practical physics include population growth, potential fields, electrical circuits and tree biology. Differential equations are generated from physical conditions. The solution to a linear differential equation is quite easy, but finding an analytical solution of a non-linear differential equation can be challenging in many cases. Consequently, approximation and numerical techniques are frequently used because the majority of differential equations do not have an exact closed form solution. There are many methods to solve non-linear problems; for instance, the perturbation method [23] is used to find the approximate solution of a parametric pendulum. V.S. Sorokin [24] analysed the motion of an inverted pendulum using the method of direct separation of motion (MDSM). A.I. Ismail [25] investigated the motion of a solid pendulum by using a large parameter method (LPM). M.M Khan [26] determined the solution of an undamped pendulum and a harmonic oscillator by using the variational iteration method (VIM). J Freundlich and D Soda [27] applied the multi-scale method to analyse the mechanical system with a spherical pendulum. The multi-harmonic energy balance method [28] is used to identify the energy-dependent pattern of the synchronisation of coupled pendulums. An energy-harvesting instrument [47] is used to control the kinematics of a spring-pendulum system.

The natural decomposition method [29] is utilised to determine the inviscid Burgers' equation. The variational iteration technique [30] is used to find the solution of integro-differential equation. The analytic solution of the Duffing-van der Pol oscillator (DVdP) is obtained by using the multiple timescales technique [31]. The applications of thermal oscillation in a heat shock are discussed [32]. Many of these exact solution techniques cannot handle all types of non-linear problems. Numerous computational techniques are employed to solve problems involving non-linear dynamics [33-34]. However, analytical methods are preferable to numerical methods because they allow for easier understanding of the basic physics of the problem. The variational iteration technique was introduced in 1998 [35] and has been successfully used to solve a wide range of non-linear problems [36]. The main objective of this approach is to construct a correction function by utilising a general Lagrange multiplier that is carefully selected because its correctional solution is significant than the initial trial function. Numerous results depending on the variational iteration technique are unable to demonstrate in many problems, because the integral of the correctional function is convolution type then modification of Elzaki transform can be applied. The Lagrange multiplier plays a vital role in the variational iteration technique, and variational theory is used for this purpose. Furthermore, to find out the Lagrange multiplier using the Elzaki variational method is much better than using the variational theory [37].

The current work focuses on analysing the motion of a pendulum attached to a rolling wheel by a lightweight spring and a combined translational and rotational system by using the variational iteration method and Elzaki transform. Understanding the dynamics of a pendulum with a rolling wheel is important in mechanical

engineering, robotics, physics, etc. The system can be used to model a variety of real-world phenomena, such as the motion of a pendulum clock, the behaviour of a robotic arm or the dynamics of a vehicle with rolling wheels.

Overall, a pendulum with a rolling wheel is a fascinating example of a complex mechanical system that exhibits both translational motion and rotational motion, and it provides a rich area of research in various fields of science and engineering.

To perform the Elzaki transform based on the VIM, we follow the following four steps:

Apply the Elzaki transform to the non-linear differential equation, which involves converting the equation into a set of algebraic equations. This step can be accomplished using standard mathematical techniques.

Apply the inverse Elzaki transform to obtain an approximate solution to the differential equation.

Use the VIM to refine the approximate solution obtained in step 2. This involves iterating the solution until convergence is achieved.

Use the refined solution to obtain the final solution to the differential equation.

The combination of the Elzaki transform and the VIM provides an efficient and accurate method for solving a wide range of differential equations and has been applied in various fields of science and engineering.

The article is organised as follows: Section 2 discusses the identification of the Lagrange multiplier by using the Elzaki transform. Section 3 outlines the suitability and correctness of the purposed method for a pendulum with a rolling wheel and a combined translational and rotational system. Section 4 ends with the concluding remarks.

## 2. IDENTIFICATION OF VARIATION ITERATION METHOD'S LAGRANGE MULTIPLIER BY USING THE ELZAKI TRANSFORM

The identification of variation iteration method's Lagrange multiplier is a crucial step in solving optimisation problems. One approach to finding this multiplier is using the Elzaki transform. The Elzaki transform is a mathematical technique that transforms the Lagrangian function into a new function that involves only optimisation variables. This transform eliminates the need for the Lagrange multiplier, simplifying the problem and making it easier to solve.

To use the Elzaki transform, the original Lagrangian function is first expressed as a function of optimisation variables and the Lagrange multiplier. Then, the Elzaki transform is applied to this function, which results in a new function that only involves optimisation variables. The derivative of this new function is set to zero to find the optimal values of the optimisation variables, which can then be used to solve the original optimisation problem.

The use of the Elzaki transform in the identification of the Lagrange multiplier in the variation iteration method has proven to be an effective and efficient approach. It has been successfully applied in various fields, including engineering, economics and physics, to solve a range of optimisation problems. The technique is especially useful for complex problems with multiple constraints and variables, where traditional methods may not be suitable.

Consider a general non-linear oscillatory system:

$$v''(t) + f(v) = 0 \quad (2.1)$$

Initial conditions for this system can be written as follows:

$$v(0), v'(0) = 0$$

Equation (1) can be rewritten in the following form:

$$v'' + \Omega^2 v' + g(v) = 0, \quad (2.2)$$

where

$$g(v) = f(v) - \Omega^2 v$$

According to the VIM [38], we developed the correctional functional for equation (2) in the following manner:

$$\begin{aligned} v_{n+1}(t) = \\ v_n(t) + \int_0^t \lambda(t, \eta)[v_n''(\eta) + \Omega^2 v_n(\eta) \tilde{g}(v_n)] d\eta, \\ n = 0, 1, 2, \dots \end{aligned} \quad (2.3)$$

Here,  $\lambda$  represents the Lagrange multiplier,  $v_n$  denotes the approximate solution and  $\tilde{g}$  is the restricted variant. We then used another way of finding the Lagrange multiplier, which is a significant part of the variational technique. Generally, the Lagrange multiplier can be express as follows [39-40]:

$$\lambda = \lambda(t - \eta)$$

We applies the Elzaki transform [41] on both sides of equation (3), and using the properties of proposed transform, the correctional function can be written as follows:

$$\begin{aligned} E[v_{n+1}(t)] = E[v_n(t)] + E[\int_0^t \lambda(t - \eta)[v_n''(\eta) + \Omega^2 v_n(\eta) + \tilde{g}(v_n)] d\eta] = E[v_n(t)] + \\ E[\lambda(t) * (v_n''(\eta) + \Omega^2 v_n(\eta) + \tilde{g}(v_n))] = \\ E[v_n(t)] + \frac{1}{w} E[\lambda(t)] E[(v_n''(\eta) + \Omega^2 v_n(\eta) + \tilde{g}(v_n))] = \end{aligned} \quad (2.4)$$

$$E[v_n(t)] + \frac{1}{w} E[\lambda(t)] \left( \frac{1}{w^2} + \Omega^2 \right) E[v_n(t)] - s v_n(0) - v_n'(0) + E[\tilde{g}(v_n)] \quad (2.5)$$

By using the variation with respect to  $v_n$  for calculating the value  $\lambda$  in equation (2.5), the stationary condition can be express as follows:

$$E[\delta v_n] + \frac{1}{w} E[\lambda] \left( \frac{1}{w^2} + \Omega^2 \right) E[\delta v_n] = 0 \quad (2.6)$$

From equation (2.6), the following equation can be obtained:

$$E[\lambda(t)] = -\frac{w^3}{1+\Omega^2 w^2} \quad (2.7)$$

We assumed that

$$\frac{\delta}{\delta v_n} E[\tilde{g}(v_n)] = 0$$

We used the inverse Elzaki transform to determine the value of  $\lambda$ :

$$\lambda(t) = -\frac{1}{\Omega} \sin wt, \quad (2.8)$$

which is similar to that used by Anjum and He [42].

By utilising equation (4), we obtained the following recursive formula:

$$\begin{aligned} E[v_{n+1}(t)] = \\ E[v_n(t)] - \frac{1}{\Omega} E \left[ \int_0^t \sin w(t - \eta) [v_n''(\eta) + \Omega^2 v_n(\eta) + \tilde{g}(v_n)] d\eta \right] \end{aligned}$$

or

$$E[v_{n+1}(t)] = E[v_n(t)] - \frac{1}{\Omega} E[\sin \omega t] [v_n''(\eta) + \Omega^2 v_n(\eta) + \tilde{g}(v_n)] \quad (2.9)$$

Using the Elzaki transform properties, we can find higher order solutions by using the aforementioned recursive formula.

### 3. PENDULUM WITH ROLLING WHEEL

A pendulum with a rolling wheel is a classic physics problem that involves the motion of a wheel attached to a pendulum. The system consists of a wheel that is free to rotate and a pendulum that is free to swing back and forth. The wheel is attached to the pendulum at its centre of mass, and the entire system is free to move in a vertical plane.

As the pendulum swings, the wheel rolls along the ground, creating a complex motion that can be challenging to analyse. The motion of the wheel is affected by both its rotational motion and linear motion, making it difficult to predict its behaviour.

Despite its complexity, the pendulum with a rolling wheel is an important model for understanding the principles of mechanics and is often used to teach physics students the relationship between rotational motion and linear motion. It also has practical applications in areas such as robotics, where similar systems are used to control the movement of robotic arms and other devices.

Overall, the pendulum with a rolling wheel is a fascinating example of the interplay between rotational motion and linear motion and provides a valuable tool for understanding the principles of mechanics.

Fig.1 shows the movement of a pendulum connected to a rotating wheel and restrained by a lightweight spring [43]. Cartesian coordinates are utilised for a better fit, with the x-axis being parallel to the horizon and the y-axis being vertically upwards.

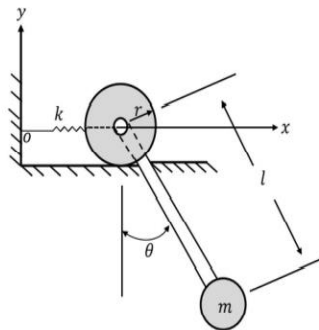


Fig. 2. Dynamic model

The given system's x-axis can be written as follows:

$$x = x_{wheel} + x_{pend} = r\theta + l_o \sin \theta \quad (3.1)$$

The supposed system's y-axis can be written as follows:

$$y = -l_o \cos \theta$$

As a result, the bob's location is specified as follows:

$$r = (r\theta + l_o \sin \theta, -l_o \cos \theta) \quad (3.2)$$

The kinetic energy of the system can be formulated as follows:

$$T = \frac{m}{2} (r^2 + l_o^2 + 2rl_o \cos \theta) \dot{\theta}^2$$

The potential energy is given as follows:

$$V = \frac{1}{2} kx_{wheel}^2 - mgl_o \cos \theta \quad (3.3)$$

The Lagrangian function of the system is given as follows:

$$L = \frac{m}{2} (r^2 + l_o^2 + 2rl_o \cos \theta) \dot{\theta}^2 - \frac{1}{2} kr^2 \theta^2 - mgl_o \cos \theta$$

The organisation thus takes one degree of freedom.

Consequently, the motion equation becomes as follows:

$$\frac{d}{dt} \left( \frac{\partial L}{\partial \dot{\theta}} \right) - \frac{\partial L}{\partial \theta} = 0$$

or

$$m(r^2 + l_o^2 + 2rl_o \cos \theta) \ddot{\theta} - mr\dot{\theta}^2 \sin \theta + kr^2 \dot{\theta}^2 + mgl_o \sin \theta = 0 \quad (3.4)$$

Nayfeh [44] provided similar derivations of Eq. (3.4) in different cases for numerous mechanical problems, and El-Dib and Moatimid [45] provided derivations for a rigid rod that rocks across a circular surface. To simplify the governing equation of motion and minimise the scaling effects, the following non-dimensional parameters are modified.

Consider  $l$ ,  $m$  and  $\sqrt{\frac{l}{g}}$  to be the characteristic length, mass, and time respectively; as a result, Eq. (3.4) can be written as follows:

$$(r^2 + l_o^2 + 2rl_o \cos \theta) \ddot{\theta} - r\dot{\theta}^2 \sin \theta + kr^2 \dot{\theta}^2 + \sin \theta \quad (3.5)$$

For small values of  $\theta$ , the Taylor expansion is expanded, assuming  $\sin \theta \cong \theta - \frac{\theta^3}{3!}$  and  $\cos \theta \cong 1 - \frac{\theta^2}{2!}$ .

Then, Equation (3.5) is formulated as follows:

$$(1 - \alpha \theta^2) \ddot{\theta} + \omega^2 \dot{\theta}^2 - \alpha \theta \dot{\theta}^2 + \frac{\alpha}{6} \theta^3 \dot{\theta}^2 - \beta \theta^3 = 0 \quad (3.6)$$

where

$$= \frac{r}{(r+1)^2}, \omega^2 = \frac{kr^2+1}{(r+1)^2} \text{ and } \beta = \frac{1}{6(r+1)^2}$$

Equation (3.6) can be rewritten as follows:

$$(1 - \alpha v^2) \ddot{v} + \Omega^2 v - \alpha v \dot{v}^2 + \frac{\alpha}{6} v^3 \dot{v}^2 - \beta v^3 = 0 \quad (3.7)$$

Initial conditions are given as follows:

$$v(0) = 1, v'(0) = 0$$

The correctional functional is written as follows:

$$E[v_{n+1}(t)] = E[v_n(t)] - \frac{1}{\Omega} E[\sin \Omega t] E[(1 - \alpha v_n^2) \ddot{v}_n + \Omega^2 v_n - \alpha v_n \dot{v}_n^2 + \frac{\alpha}{6} v_n^3 \dot{v}_n^2 - \beta v_n^3] \quad (3.8)$$

Substituting  $n = 0$ , we have

$$E[v_1(t)] = E[v_0(t)] - \frac{1}{\Omega} E[\sin \Omega t] E[(1 - \alpha v_0^2) \ddot{v}_0 + \Omega^2 v_0 - \alpha v_0 \dot{v}_0^2 + \frac{\alpha}{6} v_0^3 \dot{v}_0^2 - \beta v_0^3]$$

Assuming the initial solution is  $v_0(t) = A \cos \Omega t$ , we have

$$E[v_1(t)] = E[v_0(t)] - \frac{1}{\Omega} E[\sin \Omega t] E[-A \omega^2 \cos \Omega t - \alpha A^2 \cos^2 \Omega t (-\alpha \Omega^2 \cos \Omega t) + \Omega^2 A \cos \Omega t - \alpha A \cos \Omega t (-\alpha \Omega \sin \Omega t)^2 + \frac{\alpha}{6} A^3 \cos^3 \Omega t (-\alpha \Omega \sin \Omega t)^2 - \beta A^3 \cos^3 \Omega t] = 0$$

After some calculations, the previous expression becomes as follows:

$$E[v_1(t)] = E[A \cos \Omega t] - \frac{1}{\Omega} \left[ \left( -A \Omega^2 + \frac{3A^3 a \Omega^2}{4} + A \Omega^2 \cdot \alpha A^3 \Omega^2 + \frac{3A^3 a \Omega^2}{4} + \frac{A^5 a \Omega^2}{8} - \frac{5A^5 a \Omega^2}{48} \right) E[\cos \Omega t] E[\sin \Omega t] + \left( \frac{A^3 a \Omega^2}{4} - \frac{A^3 a \Omega^2}{4} + \frac{A^5 a \Omega^2}{24} - \frac{5A^5 a \Omega^2}{6} - \frac{A^3 \beta}{4} \right) E[\cos 3\Omega t] E[\sin \Omega t] - \frac{A^5 a \Omega^2}{96} E[\cos 5\Omega t] E[\sin \Omega t] \right] \quad (3.9)$$

Taking the inverse Elzaki transform of equation (3.9), we get the first-order approximate results as follows:

$$-\frac{1}{\Omega} \left[ \left( -A \Omega^2 + \frac{3A^3 a \Omega^2}{4} + A \Omega^2 - \alpha A^3 \Omega^2 + \frac{3A^3 a \Omega^2}{4} + \frac{A^5 a \Omega^2}{8} - \frac{5A^5 a \Omega^2}{48} - \frac{3A^3 \beta}{4} \right) \right]$$

This results in the expression for the system's angular frequency.

$$\Omega = \sqrt{\frac{\frac{9}{7} \beta A^3}{\frac{3}{4} \alpha A^5 - \alpha A^2 - \frac{a^3}{12}}}$$

#### 4. COMBINED TRANSLATIONAL AND ROTATIONAL SYSTEM

A combined translational and rotational system is a physical system that involves both translational motion (motion in a straight line) and rotational motion (motion around an axis). This system can be found in a wide range of mechanical devices, from car engines to amusement park rides. In a combined system, both translational motion and rotational motion are interconnected and affect each other. For example, in a car engine, the pistons move in a straight line to create rotational motion in the crankshaft, which in turn drives the wheels to create translational motion of the vehicle. Analysing a combined translational and rotational system can be complex as the motion of each component is interdependent. This requires an understanding of the physics of both translational motion and rotational motion, as well as the principles of torque and energy transfer. Despite their complexity, a combined translational and rotational system is vital to many everyday devices and are crucial to the functioning of modern technology. Studying these systems can lead to advancements in engineering and physics and can help us better understand the world around us. The idealised description of a mechanical device is a homogenous, uniform wheel rolling smoothly over a horizontal surface. A combined translational and rotational system is shown geometrically [36,46] in Figure 2.

The device's frame is secured to the centre of the wheel by a linear spring and a force. At the top of the wheel, the force  $F = \cos \Omega t$  is used.

$$\tilde{v}'' + \frac{2k}{3m} \tilde{v} - \frac{2}{3m} \cos^2 \Omega t = 0 \quad (4.1)$$

Initial conditions of equation (4.1) are as follows:

$$\tilde{v}'(0) = A, \quad \tilde{v}(0) = 0 \quad (4.2)$$

To simplify this model,  $\alpha$  and  $\beta$  are taken as follows:

$$\alpha = \frac{2k}{3m}, \quad \beta = \frac{2}{3m}$$

Equation (4.2) can be rewritten as follows:

$$\tilde{v}'' + \alpha \tilde{v} - \beta \cos \Omega t = 0 \quad (4.3)$$

Now, we rewrite the equation according to the solution of the variational iterative technique with the Elzaki transform:

$$\tilde{v}'' + \Omega^2 \tilde{v} + g(\tilde{v}) = 0 \quad (4.4)$$

where

$$g(\tilde{v}) = (\alpha - \Omega^2) \tilde{v} - \beta \cos^2 \Omega t$$

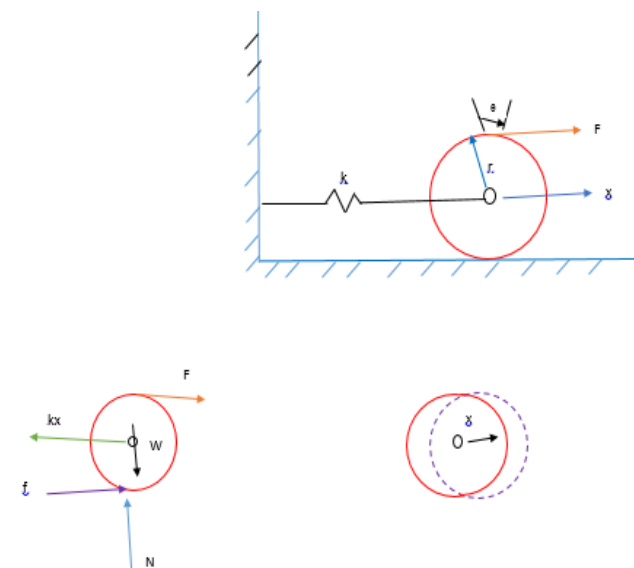


Fig. 3. Combined translational and rotational system

The iterative formula of the aforementioned model can be written as follows:

$$\begin{aligned} E[\tilde{v}_{n+1}(t)] &= E[\tilde{v}_n(t)] - E[\int_0^t \frac{1}{\Omega} \sin \Omega(t-\eta) [\tilde{v}_n''(\eta) + \Omega^2 \tilde{v}_n(\xi) + g(\tilde{v}_n)] d\eta] \\ E[\tilde{v}_{n+1}(t)] &= E[\tilde{v}_n(t)] - \frac{1}{\Omega} E[\sin \Omega t] E[\tilde{v}_n''(t) + \Omega^2 \tilde{v}_n(t) + g(\tilde{v}_n)] \\ &= E[\tilde{v}_n] - \frac{1}{\Omega} E[\sin \Omega t] E[\tilde{v}_n'' + \alpha \tilde{v}_n(t) - \beta \cos^2 \Omega t] \quad (4.5) \end{aligned}$$

We assume the initial solution as

$$\tilde{v}_0(t) = A \cos \Omega t \quad (4.6)$$

By utilising equation (4.6) to find the solution of equation, we substitute  $n = 0$ :

$$E[\tilde{v}_1(t)] = E[A \cos \Omega t] - \frac{1}{\Omega} E[\sin \Omega t] E[-A \Omega^2 \cos \Omega t + \alpha A \cos \Omega t - \beta \cos \Omega t] \quad (4.7)$$

We apply the inverse Elzaki transform to equation (4.7) to obtain the first approximate solution:

$$\begin{aligned} \tilde{v}_1(t) &= \\ &A \cos \Omega t - \frac{1}{\Omega} (-4A \Omega^2 + \alpha A - 3\beta) \left( \frac{1}{2\Omega^2} \sin \Omega t - \frac{1}{2\Omega} t \cos \Omega t \right) \quad (4.8) \end{aligned}$$

The second term expressed the secular term, so amplitude increases with time. To ensure convergence, we must eliminate the secular term to obtain the approximate solution:

$$(-4A\Omega^2 + \alpha A - 3\beta) = 0 \quad (4.9)$$

Simplify equation (4.9), the angular frequency is expressed as follows:

$$\Omega = \sqrt{\alpha - \frac{3\beta}{4A}}$$

$$\tilde{v}_1(t) = A \cos(\sqrt{\alpha - \frac{3\beta}{4A}})t,$$

which is similar to that obtained by using the Laplace-based variational iteration method [46].

## 5. CONCLUDING REMARKS

The objective of most researchers working on non-linear differential equations is to find analytical and numerical solutions. The current research emphasised on the basic pendulum problem when it was connected with a lightweight spring because it is significant in several fields. So, the purpose of this study was to analyse a pendulum with a spinning wheel, which is connected by a lightweight spring. The conserved equation generates a non-linear equation under some particular situations. Unfortunately, we failed to completely remove the secular terms when utilising the existing traditional techniques. As a result, the approximate solution that was obtained shows increased amplitude with time. A combination of variational iteration and Laplace transforms is used to find the solution of a translational and rotational system and a basic pendulum attached to a wheel and lightweight spring. A pendulum with a rolling wheel, also known as a rolling pendulum, is a system that consists of a pendulum attached to a wheel that rolls along a track. A combined translational and rotational system is a system in which an object moves both in a straight line and rotates about an axis simultaneously. This system has several interesting applications in physics and engineering listed as follows:

- Demonstrating conservation of energy: A rolling pendulum is an excellent demonstration of the conservation of energy. As the pendulum swings back and forth, the energy is transferred between potential energy (when the pendulum is at its highest point) and kinetic energy (when the pendulum is at its lowest point).
- Studying non-linear dynamics: The motion of a rolling pendulum is highly non-linear and chaotic. It is an interesting system for studying non-linear dynamics and chaos theory.
- Developing mechanical systems: A rolling pendulum can be used to develop mechanical systems that convert linear motion into rotational motion. This can be useful in designing various machines and devices.
- Measuring gravitational acceleration: The period of a rolling pendulum is dependent on the gravitational acceleration. Therefore, it can be used as a tool to measure gravitational acceleration accurately.
- Understanding motion and stability: A rolling pendulum is a great example of how motion and stability are interconnected. As the pendulum swings back and forth, the wheel rolls along the track, and the system's stability changes.

- Automotive engineering: Cars, trucks and other vehicles are examples of combined translational and rotational systems. The wheels of a vehicle move in a straight line while rotating about an axis, and the engine generates a rotational force to propel the vehicle forward.
- Robotics: Robotics is another field where combined translational and rotational systems are used. Robots with rotating arms can move in a straight line while rotating about an axis, making them useful in applications such as assembly lines and manufacturing.
- Mechanical engineering: Many mechanical systems, such as gears, pulleys and belts, involve combined translational and rotational motion. These systems are used in machines such as engines, motors and turbines.
- Sports equipment: Sports equipment such as baseballs, footballs and golf balls all involve combined translational and rotational motion. This motion affects the ball's trajectory and can be optimised for maximum distance or accuracy.
- Physics education: Combined translational and rotational systems can be used as teaching tools in physics classrooms. Simple examples such as rolling balls and wheels can be used to illustrate concepts such as angular momentum, torque and conservation of energy.

## REFERENCES

1. Moatimid GM, Amer TS. Analytical solution for the motion of a pendulum with rolling wheel: stability analysis. *Scientific Reports*. 2022 Jul 24;12(1):12628.
2. Haider JA, Muhammad N, Nadeem S, Asghar S. Analytical analysis of the fourth-order Boussinesq equation by traveling wave solutions. *International Journal of Modern Physics B*. 2023 Jul 10;37(17):22350170.
3. Matrosov I, Morozov Y, Pesterev A. Control of the robot-wheel with a pendulum. In: 2020 15th International Conference on Stability and Oscillations of Nonlinear Control Systems (Pyatnitskiy's Conference)(STAB) 2020 Jun 3 (1-4). IEEE.
4. Haider JA, Zaman FD, Lone SA, Anwar S, Almutlak SA, Elseesy IE. Exact solutions of Euler–Bernoulli beams. *Modern Physics Letters B*. 2023 Jul 12:2350161.
5. Palazoğlu TK, Miran W. Experimental investigation of the combined translational and rotational movement on an inclined conveyor on radio frequency heating uniformity. *Innovative Food Science & Emerging Technologies*. 2018 Jun 1;47:16-23.
6. Tanly NN, Fotsa RT, Woafao P. Complex Dynamics of a Mechanical Mechanism Combining Translational and Rotational Motions. *Journal of Vibration Engineering & Technologies*. 2022 Jul;10(5):1753-64.
7. Raza MY, Haider JA, Ahammad NA, Guedri K, Galal AM. Insightful study of the characterization of the Cobalt oxide nanomaterials and hydrothermal synthesis. *International Journal of Modern Physics B*. 2023 Apr 30;37(11):2350101.
8. Panayanthatta N, Clementi G, Ouhabaz M, Costanza M, Margueron S, Bartasyte A, Basrour S, Bano E, Montes L, Dehollaïn C, La Rosa R. A self-powered and battery-free vibrational energy to time converter for wireless vibration monitoring. *Sensors*. 2021 Nov 11;21(22):7503.
9. Guler U, Sendi MS, Ghovanloo M. A dual-mode passive rectifier for wide-range input power flow. In: 2017 IEEE 60th International Midwest Symposium on Circuits and Systems (MWSCAS) 2017 Aug 6 (pp. 1376-1379). IEEE.
10. Chen J, Bao B, Liu J, Wu Y, Wang Q. Pendulum Energy Harvesters: A Review. *Energies*. 2022 Nov 18;15(22):8674.
11. Hunt JB. Dynamic vibration absorbers. 1979.

12. Nadeem S, Haider JA, Akhtar S, Ali S. Numerical simulations of convective heat transfer of a viscous fluid inside a rectangular cavity with heated rotating obstacles. *International Journal of Modern Physics B*. 2022 Nov 10;36(28):2250200.
13. Serway RA, Beichner RJ. *Physics for Scientists and Engineers* 5th edn (Forth Worth, TX: Saunders).
14. Beléndez A, Pascual C, Méndez DI, Beléndez T, Neipp C. Exact solution for the nonlinear pendulum. *Revista brasileira de ensino de física*. 2007;29:645-8.
15. Parwani RR. An approximate expression for the large angle period of a simple pendulum. *European journal of physics*. 2003 Oct 10;25(1):37.
16. Haider JA, Rahman JU, Zaman FD, Gul S. Travelling wave solutions of the non-linear wave equations. *Acta mechanica et automatica*. 2023;17(2).
17. Elmandouh AA. On the integrability of the motion of 3D-Swinging Atwood machine and related problems. *Physics Letters A*. 2016 Mar 6;380(9-10):989-91.
18. Wang F, Bajaj AK, Kamiya K. Nonlinear normal modes and their bifurcations for an inertially coupled nonlinear conservative system. *Nonlinear Dynamics*. 2005 Nov;42:233-65.
19. El-Sabaa FM, Amer TS, Gad HM, Bek MA. On the motion of a damped rigid body near resonances under the influence of harmonically external force and moments. *Results in Physics*. 2020 Dec 1;19:103352.
20. Anurag, Mondal B, Shah T, Chakraborty S. Chaos and order in librating quantum planar elastic pendulum. *Nonlinear Dynamics*. 2021 Feb;103:2841-53.
21. Haider JA, Asghar S, Nadeem S. Travelling wave solutions of the third-order KdV equation using Jacobi elliptic function method. *International Journal of Modern Physics B*. 2023 May 10;37(12):2350117.
22. Amer TS, Bek MA, Abohamer MK. On the motion of a harmonically excited damped spring pendulum in an elliptic path. *Mechanics Research Communications*. 2019 Jan 1;95:23-34.
23. Xu X, Wiercigroch M. Approximate analytical solutions for oscillatory and rotational motion of a parametric pendulum. *Nonlinear Dynamics*. 2007 Jan;47:311-20.
24. Sorokin VS. Analysis of motion of inverted pendulum with vibrating suspension axis at low-frequency excitation as an illustration of a new approach for solving equations without explicit small parameter. *International Journal of Non-Linear Mechanics*. 2014 Jul 1; 63:1-9.
25. Haider JA, Ahammad NA, Khan MN, Guedri K, Galal AM. Insight into the study of natural convection heat transfer mechanisms in a square cavity via finite volume method. *International Journal of Modern Physics B*. 2023 Feb 10;37(04):2350038.
26. Khan MM. Variational Iteration Method for the Solution of Differential Equation of Motion of the Mathematical Pendulum and Duffing-Harmonic Oscillator. *Earthline Journal of Mathematical Sciences*. 2019 May 2;2(1):101-9.
27. Amir M, Haider JA, Ahmad S, Ashraf A, Gul S. Approximate solution of painlevé equation i by natural decomposition method and laplace decomposition method. *acta mechanica et automatica*. 2023;17(3).
28. Ozis T, Yildirim A. Determination of the frequency-amplitude relation for a Duffing-harmonic oscillator by the energy balance method. *Computers and Mathematics with Applications*. 2007 Oct 1;54(7):1184-7.
29. Amir M, Awais M, Ashraf A, Ali R, Ali Shah SA. Analytical Method for Solving Inviscid Burger Equation. *Punjab University Journal of Mathematics*. 2023 Dec 3;55(1).
30. Wang SQ, He JH. Variational iteration method for solving integro-differential equations. *Physics letters A*. 2007 Jul 23;367(3):188-91
31. Haider JA, Ahmad S. Dynamics of the Rabinowitsch fluid in a reduced form of elliptic duct using finite volume method. *International Journal of Modern Physics B*. 2022 Dec 10;36(30):2250217.
32. Liu F, Zhang T, He CH, Tian D. Thermal oscillation arising in a heat shock of a porous hierarchy and its application. *Facta Universitatis, Series: Mechanical Engineering*. 2022 Nov 30;20(3):633-45.
33. Haider JA, Muhammad N. Computation of thermal energy in a rectangular cavity with a heated top wall. *International Journal of Modern Physics B*. 2022 Nov 20;36(29):2250212.
34. Haider JA, Muhammad N. Computation of thermal energy in a rectangular cavity with a heated top wall. *International Journal of Modern Physics B*. 2022 Nov 20;36(29):2250212.
35. He JH. Variational iteration method—a kind of non-linear analytical technique: some examples. *International journal of non-linear mechanics*. 1999 Jul 1;34(4):699-708.
36. Rahman JU, Mannan A, Ghoneim ME, Yassen MF, Haider JA. Insight into the study of some nonlinear evolution problems: Applications based on Variation Iteration Method with Laplace. *International Journal of Modern Physics B*. 2023 Jan 30;37(03):2350030.
37. He JH, Latifizadeh H. A general numerical algorithm for nonlinear differential equations by the variational iteration method. *International Journal of Numerical Methods for Heat & Fluid Flow*. 2020 Oct 15;30(11):4797-810.
38. He JH. Variational iteration method—a kind of non-linear analytical technique: some examples. *International journal of non-linear mechanics*. 1999 Jul 1;34(4):699-708.
39. He JH. Approximate analytical solution for seepage flow with fractional derivatives in porous media. *Computer Methods in Applied Mechanics and Engineering*. 1998 Dec 1;167(1-2):57-68.
40. He JH. Variational iteration method—some recent results and new interpretations. *Journal of computational and applied mathematics*. 2007 Oct 1;207(1): 3-17.
41. Elzaki TM. Application of new transform “Elzaki transform” to partial differential equations. *Global Journal of pure and applied Mathematics*. 2011;7(1):65-70.
42. Anjum N, He JH. Laplace transform: making the variational iteration method easier. *Applied Mathematics Letters*. 2019 Jun 1;92:134-8
43. Moatimid GM, Amer TS. Analytical solution for the motion of a pendulum with rolling wheel: stability analysis. *Scientific Reports*. 2022 Jul 24;12(1):12628.
44. Nayfeh AH. *Introduction to perturbation techniques*. John Wiley & Sons; 2011 Apr 8.
45. Ghaleb AF, Abou-Dina MS, Moatimid GM, Zekry MH. Analytic approximate solutions of the cubic-quintic Duffing–van der Pol equation with two-external periodic forcing terms: Stability analysis. *Mathematics and Computers in Simulation*. 2021 Feb 1;180:129-51.
46. Asghar S, Haider JA, Muhammad N. The modified KdV equation for a nonlinear evolution problem with perturbation technique. *International Journal of Modern Physics B*. 2022 Sep 30;36(24):2250160.
47. He CH, Amer TS, Tian D, Abolila AF, Galal AA. Controlling the kinematics of a spring-pendulum system using an energy harvesting device. *Journal of Low Frequency Noise, Vibration and Active Control*. 2022 Sep;41(3):1234-57.

**Acknowledgments:** The Higher Education Commission of Pakistan (HEC) is pleased to acknowledge the support provided through the Researchers Supporting Project with the identification number PQRWZK2023P9. Gratitude is extended by the third author, Jamil Abbas Haider, for the invaluable support received during the research program.

Muhammad Amir:  <https://orcid.org/0009-0002-4871-4312>

Jamil Abbas Haider:  <https://orcid.org/0000-0002-7008-8576>

Asifa Ashraf:  <https://orcid.org/0009-0005-4786-7757>



This work is licensed under the Creative Commons BY-NC-ND 4.0 license.

# MACHINING OF TiAl6V4 USING LUBRICANTS CONTAINING RENEWABLE MICROALGAE-BORN PERFORMANCE ADDITIVES

Thomas KOCH\*, Dominik WENZEL\*\*, Ralf GLÄBE\*\*

\*Industrie Beratung, Isarstraße 95, Bremen, 28199, Germany

\*\*Hochschule Bremen, Fakultät 5 Natur und Technik, Neustadtswall 30, 28199 Bremen, Germany

[tkoch@uni-bremen.de](mailto:tkoch@uni-bremen.de), [Dominik.Wenzel@hs-bremen.de](mailto:Dominik.Wenzel@hs-bremen.de), [ralf.glaebe@hs-bremen.de](mailto:ralf.glaebe@hs-bremen.de)

received 21 October 2022, revised 17 June 2023, accepted 19 June 2023

**Abstract:** Titanium and its alloys represent a special class of materials. A density of 4.81 g/cm<sup>3</sup>, a tensile strength of over 1,200 MPa, a fatigue strength greater than that of steel, a low modulus of elasticity and its self-passivating, inert surface make titanium an ideal material for lightweight structures in aerospace, marine applications, the chemical industry and medical implants. Although titanium is inert in its oxidised state, its nascent surface created in machining reacts with almost everything in its environment, including the tool. Moreover, its poor thermal conductivity results in high thermal stress on the tools. Overall, these properties lead to high wear rates and result in the requirement for finding a particularised solution for processes such as milling that involve the need to overcome such challenges. Such processes therefore require lubricants with well-selected performance additives. However, most of these performance additives are based on mineral oil and thus come from a non-renewable resource. In the presented work, environmental-friendly alternatives to conventional mineral oil-based performance additives were investigated. Due to the working mechanisms of performance additives in machining, this work focusses on sulphur- and phosphorus-containing polysaccharides and proteins from microalgae. It has been successfully shown that lubricants using extracts from microalgae as performance additives can be used for high-speed milling (HSC) of TiAl6V4. The investigated extracts were able to reach the performance level of conventional additives in terms of tool lifetime and wear. The results obtained show that appropriate alternatives to mineral oil-based additives exist from renewable raw-material sources.

**Key words:** titanium, TiAl6V4, high-speed milling, metalworking fluid, additives

## 1. INTRODUCTION

In metalworking processes, metalworking fluids (MWF) are used in various applications. In machining or forming processes, MWF are used to cool the process and enhance the tribological conditions between the workpiece and the tool. In general, MWF are based on mineral oils, synthetic base fluids, vegetable oils or even water and supplemented with specific additives. The additives improve and adjust, e.g. performance in machining and protection against wear and corrosion. Sulphur- and phosphorus-containing, esterified or ethoxylated hydrocarbons, fatty alcohols and fatty acid esters are typically used as performance additives. These performance additives interact electrochemically with the workpiece surface and provide the desired technical properties (Fig. 1). The type and strength of the interaction depend in particular on the kind of application, the workpiece material (quantity and type of alloying constituents and oxide structure of the metal surface) and the chemical-structural characteristics of the additives. The effects of additives occur in its adjacent surfaces and within the workpiece material itself and are caused by physical and chemical mechanisms in the MWF (Fig. 2). A substantial proportion of additives is made up of mineral oils and is therefore unsustainable. Manufacturers of lubricants and MWF are challenged to find suitable alternatives to offer to their customers, due to the increasing legal requirements, and the demand from civil society and industry to act more sustainably [1–3]. The research project ALBINA presented here has focused on the development of alternative performance additives based on microalgae as a resource for a new class of sustainable additives. Several microalgae produce substances that, due to their chemical structure,

can be used as analogues to conventional additives in metal working processes. The results obtained in HSC milling of TiAl6V4 show the potential of algae-born substance to supplement conventional performance additives [4–5].

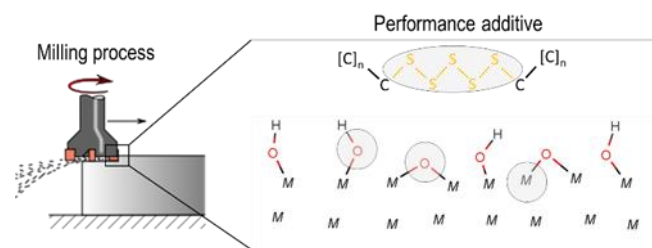


Fig. 1. Milling process as an example for metal cutting and working site of metalworking fluids. Scheme of a conventional performance additive and metal surface. The areas relevant to a potential interaction are highlighted in grey

Working mechanism	Working site		
	Surface/interface	Bulk fluid	
Chemically	EP-Additive AW-Additive Friction modifier	Corrosion inhib.	Anti-oxidant Detergent
Physically	Dispersant Anti-foam Demulsifier		Pour-point depr. Viscosity modifier
Function	Performance additives	Maintainers	Rheo improvers

Fig. 2. Working sites and mechanisms of action for exemplary groups of additives (acc. [3], modified). AW, anti-wear; EP, extreme pressure

## 2. OBJECTIVE

The overall objective of the work presented is to replace conventional MWF additives with components from microalgae. Many algae species are capable of synthesising substances that can work as equivalents to the common additives used in MWF. These include, in particular, sulphur- and phosphorus-containing polysaccharides and protein components. It is known that several polysaccharides and protein structures have naturally incorporated sulphur or phosphorus atoms. Therefore, they represent an ideal partner for interactions with the metal surface. These structural analogues are intended to replace conventional additives in tribological applications and ideally surpass them in their technical impact.

### 2.1. Titanium

Titanium is one of the most common elements in the Earth's crust. Alloys of titanium represent a special class of materials. Titanium has a density of  $4.81 \text{ g/cm}^3$ , a tensile strength of over  $1,200 \text{ MPa}$ , a fatigue strength greater than the one of steel and a low modulus of elasticity. In addition to its specific mechanical properties, titanium is extremely corrosion-resistant due to the self-passivation of the surface with an oxide layer. Therefore, it is an ideal material for lightweight structures in aerospace and marine applications, the chemical industry and medical implants. In machining processes, the high strength and low thermal conductivity lead to a high thermal load and thus wear on the tool. Furthermore, the increasing spring-back effect with increasing cutting speed leads to a larger contact zone at the flank face of the tool, which also manifests itself in increased wear rates. Nascent titanium surfaces have a high affinity for oxygen, carbon and nitrogen. The surface created in machining processes can react with the tool and the components of the MWF. Due to this, specific additives are required for an efficient machining process [6–8].

### 2.2. Why microalgae

Microalgae are microscopic, mostly unicellular, phototrophic organisms. They colonise marine as well as limnic and terrestrial habitats. Numerous species have adapted to particularly extreme conditions. The estimated approximately 100,000 species of algae offer a high potential for substances of interest [9]. Applications can be found in biotechnology and the food and feed industry, as well as in technical industries. Due to their high surface-to-volume ratio, microalgae are highly productive and therefore suitable candidates for the production of renewable bio-based resources. So far, microalgal biomass production is being researched and commercialised, especially for food technology (pigments, lipids) and biofuel industries [10, 11].

The cultivation and harvesting of about 20 industrially used microalgae species are technically mastered. This creates an important prerequisite for the sustainable production of algae biomass for the development of new areas of application. The cultivation of microalgae is not tied to the use of agricultural land. Therefore, the need to consider the tank-plate conflict, which would require discussion in the case of other energy crops, is negligible.

### 2.3. Process data and material

The tests were carried out as a counter-face milling process on a five-axis high-speed milling machine shop Röders RXP 601 DS from Röders GmbH, Soltau. A sensory tool holder Spike V1.2 HSKE50 PG25 L100 C from pro-micron GmbH, Kaufbeuren, was applied for the recording of the resulting bending moment  $M$ , calculated from the individual moments  $M_x$  and  $M_y$ , the torsion  $T$  and the tensile/compressive force  $F$  during machining. Data analysis was performed post-process. The used cutting tool was a modular milling cutter equipped with two uncoated, round indexable inserts RDHT10T3M0-8-E04 H25 from Seco Tools GmbH, Erkrath, Germany. For tool wear measurements, the machine-integrated LTS35.60-40 laser-tool-measuring system from m&h Inprocess Messtechnik GmbH, Waldburg was applied. It enables automatic length correction, diameter and contour measurement, wear monitoring and breakage control of the milling tools. The accuracy is  $\pm 1.0 \mu\text{m}$ . The cutting-edge offset is integrated at  $5^\circ$  sections over a projected  $50^\circ$  arc on the insert and the worn area of the tool is calculated (Fig. 3).

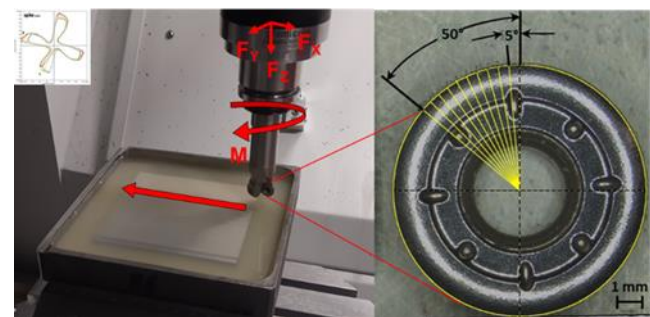


**Fig. 3.** Left: Work area of the five-axis high-speed milling machine Röders RXP 601 DS with tool and workpiece. Right: Top view of an indexable insert with segmentation of the  $5^\circ$  measuring locations where the deviation from the pristine tool geometry was measured by a laser-tool-measuring system of the machine

The workpiece was titanium grade 5 (TiAl6V4, 3.71649) with the following content of alloys:

- Al = 5.5%–6.75%,
- V = 3.5%–4.5%,
- Fe =  $\leq 0.3\%$ ,
- O =  $\leq 0.2\%$ .

TiAl6V4 is the most common titanium alloy and is used in aerospace and medical applications. Tab. 1 documents the material and process data of the milling process.

A mineral oil-free water-miscible MWF concentrate (internal abbreviation: DBG\_ohne) was used as the base fluid for the experiments. It was formulated without performance additives so as not to cover the effect of the tested substances in the milling process. The concentration of the MWF emulsion used was set up to 5% (v/v), and that of the reference substances and algae extracts was 0.05% (w/v) in the mixtures. As references, the following substances were incorporated into the MWF emulsion:

- Iota-carrageenan (CAS 9062-07-1) as a reference for sulphated polysaccharide,
- Gelita Novotec CL800 (CAS 68410-45-7), a gelatine hydrolysate as a reference for proteins,

- TPS20 and TPS32 (CAS 68425-15-0), a tertiary dodecyl polysulphide, as reference for commercial performance additives, and
- RC 2526, a sulphurised vegetable fatty acid ester, as a reference for commercial performance additives.

**Tab. 1.** Material and process data of the HSC milling process

Process	HSC face milling
Workpiece	TiAl6V4
Hardness (HRC)	33 ± 2
Tensile strength (N/mm <sup>2</sup> )	>895
Diam. tool (mm)	20/eff. 16
No. of cutting edges	2
Diam. insert (mm)	10
Cutting microstructure	Fine grain
Grain size (µm)	<1
Cobalt (%)	~5
Microstructure hardness (HV10)	1,750
Rake angle (°)	20
Coating	None
Rotational speed, <i>n</i> (min <sup>-1</sup> )	7,958
Cutting speed, <i>v<sub>c</sub></i> (m/min)	400
Feed/tooth, <i>f<sub>th</sub></i> (mm/th)	0.025
Feed rate, <i>v<sub>f</sub></i> (mm/min)	398
Depth of cut, <i>a<sub>p</sub></i> (mm)	1.0
Width of cut, <i>a<sub>e</sub></i> (mm)	6.0
MWF concentration (%)	5.0
Additive concentration (%)	0.05

HSC, high-speed milling; MWF, metalworking fluid

The reviewed algae extracts are lyophilised biomass of the commercially available microalgae strains *Nannochloropsis salina* and *Porphyridium purpureum*. The lyophilizates were rehydrated at a concentration of 0.05% (w/v) in warm tap water for 15 min. Two batches were prepared from this stock solution:

- To the first batch 5% (v/v) of the above-described MWF, concentrate was added to obtain the emulsions Nanno BBT and Porph BBT (both internal abbreviations).
- In the second batch, the fluid was homogenised using a CAT X1740 homogeniser at 17,000 min<sup>-1</sup> for 2 min. After resting it for 2 min, a second homogenisation step was performed at 17,000 min<sup>-1</sup> for 2 min. Afterwards, 5% (v/v) of the above-described MWF concentrate was added to obtain the emulsions Nanno hom (abbr.) and Porph hom (abbr.). This processing approach was used to release the target substances' polysaccharides and proteins from the inner cellular material.

The HSC milling process was performed in triplicate for each of the described MWF compositions. The deviation bars reflect the minimum, mean and maximum of the respective values.

### 3. RESEARCH RESULTS

While comparing the performance of the respective MWF formulations, the HSC milling process of TiAl6V4 was stopped after a milling distance time of 1,000 mm. The addition of the reference substances, as well as the microalgae extracts, led to a significant

reduction in tool wear, ranging about 50%, compared to the basic MWF without performance additives. However, the wear reduction effect is related to the individual additives. In particular, the addition of the extracts obtained from the microalgae *N. salina* shows a noticeable reduction in tool wear. The worn area is even less compared to one of the commercial additives. The homogenised extract of the microalgae *P. purpureum* led to a less pronounced reduction in tool wear, accompanied by a large scattering. Its positive effect on tool wear is smaller compared to the reference substances. Of the commercially available additives, the best results were obtained with the addition of TPS32 (Fig. 4).

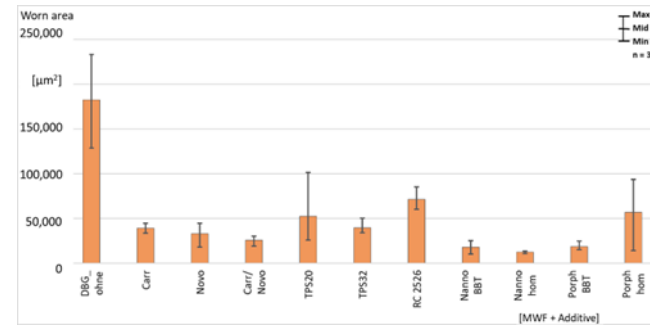


**Fig. 4.** Tool wear displayed as a worn area after a tool lifetime of 1,000 mm in the HSC milling process. HSC, high-speed milling; MWF, metalworking fluid

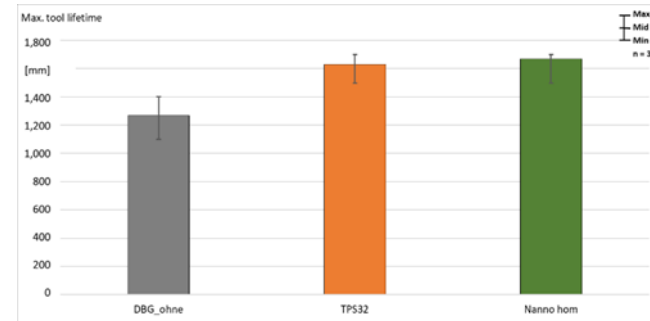


**Fig. 5.** Maximum tool lifetime of the MWF without performance additives and the MWF formulated with each 0.05% TPS32 and the homogenised *N. salina* biomass, respectively. MWF, metalworking fluid

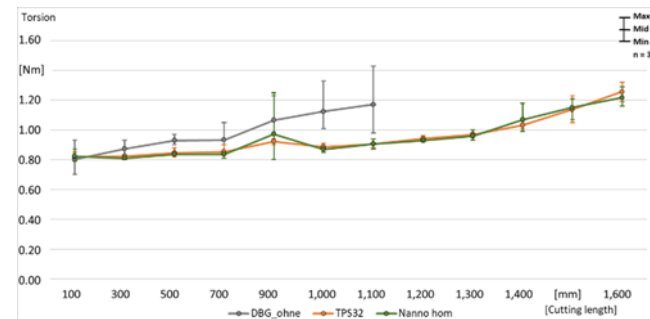


**Fig. 6.** Measured resulting bending moment in the tool during milling using the MWF without performance additives and the MWF formulated with each 0.05% TPS32 and the homogenised *N. salina* biomass, respectively. MWF, metalworking fluid

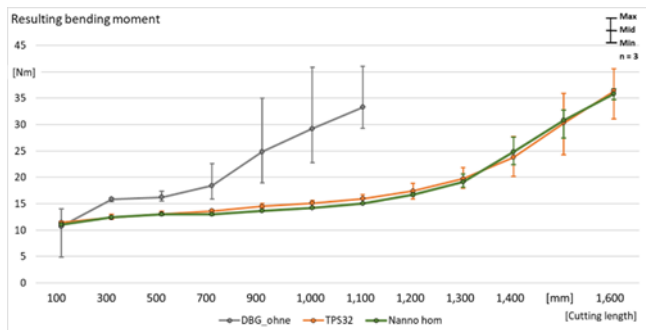


**Fig. 7.** Measured torsion in the tool during milling using the MWF without performance additives and the MWF formulated with each 0.05% TPS32 and the homogenised *N. salina* biomass, respectively.  
MWF, metalworking fluid

To determine the maximum tool lifetime, the homogenised extract of the microalgae *N. salina* was compared with the commercial performance additive TPS32. The non-additive MWF served as a reference. The results of the maximum tool lifetime determination in the milling of TiAl6V4 show that the homogenised extract of the microalgae *N. salina* has the same performance as the additive TPS32. The maximum achievable tool lifetime (Fig. 5), the measured resulting bending moment (Fig. 6) and torsion (Fig. 7) suffered by the tool, while working with the microalgae extract, are similar to those observed corresponding to the use of the conventional additive TPS32.

#### 4. DISCUSSION

The subject of the investigations presented is to prove the potential of algae-based substances to work as a performance additive for MWF in a milling process of TiAl6V4. These are intended to replace the mineral oil-based conventional additives as sustainable active substances. The results obtained can be summarised as follows. Considering the values of the reference substances and commercial additives, TPS32 led to the best results regarding the worn area after a milling distance of 1,000 mm compared to the non-additive MWF. The tool wear of the algae substances was the lowest of all tested additives except for the homogenised *P. purpureum*. Compared to the conventional additive TPS32, the substances of the algae *N. salina* reached the same level regarding the anti-wear and performance properties. Concerning the process criteria maximum tool lifetime, the resulting bending moment and the measured torsion, it reached values similar to those involved in usage of the conventional additive TPS32.

The reason underlying the remarkable results obtained resultant to using the *N. salina* extract can be explained in terms of the chemical composition of the algae material. The protein fraction contains, among others, the amino acid hydroxyproline, for which a high affinity to metallic surfaces has been demonstrated. Similarly, the oximes from the polysaccharides, which also have a high intramolecular local charge density, can cause these interactions between the metal surface and the additive molecules. In milling, the cutting process is periodically interrupted, whereupon the influence of the MWF is obtaining a higher significance. During one revolution in face milling as conducted here, the cutting edge is wetted by the MWF for most of the time. The hot edge leaving the workpiece readily reacts with MWF constituents, which can

lead to the formation of a protective film on its surface. The above-mentioned molecules can build up a tribological active surface layer on the tool and thus led to the reduction in wear observed in the milling experiments of titanium [4–6, 12, 13].

The anti-wear behaviour of the algae-born additives observed here is related to the high cutting speed in the HSC milling process. Titanium is a weak heat conductor [6, 14]. As a result, at lower cutting speeds, the temperatures at the cutting edge are not high enough to allow a chemical reaction between the tool surface and the additive molecules. This dependence was also observed by Ma et al. [15] whilst performing drilling processes under different process parameters.

Benedicto et al. [16] used the Tapping Torque Test for their tribological experiments. They assessed the surfactant's charge, the hydrocarbon chain length and the ethoxylation degree on machining TiAl6V4. One result they found is the context between the molecular structure of surfactants and the tool wear: the wear rate decreased with increasing chain length of the tested surfactants, independent of their ionic character. In addition, they found that the higher the number of ethoxylation on the hydrocarbon chain, the more significant was the observed increase in lubricity [16].

The subject of the research of Ma et al. [15] was to investigate the effect of polyalkylene glycol polymer-ester-based additives and phosphorus-based additives on the machining performance during the drilling of TiAl6V4. The tool wear and energy-dispersive spectrometry (EDS) were evaluated to assess the performance of the additives in the process. The drilling process was carried out with a constant material removal rate under varying feed rates and spindle speeds. The performance of the additives was dependent on the conditions of the drilling process. The MWF containing phosphorus led to a higher lubricity at lower spindle speeds compared to the polymer-based MWF. In addition, at higher spindle speeds, both phosphorus-rich and carbon-rich tribological layers were observed on the flank surface, depending on the MWF used [15].

Research dealing with the effect of additives in titanium machining in more detail is rare. The papers cited here support the approach that additives with a local charge density can improve the machining process of titanium. As mentioned above, additives with charge carriers such as phosphates and ethoxylates can lead to reduced wear and better performance.

#### 5. SUMMARY AND OUTLOOK

The presented investigation focusses on algae-based substances as a sustainable substitute for conventional mineral oil-based performance additives in metalworking processes. The obtained results show the potential of the microalgae extracts to work as anti-wear additives in high-speed milling of TiAl6V4. Compared to the commercial additive TPS32, the extracts of the microalgae *N. salina* reached the same performance level regarding the tool wear and lifetime as well as the torsion and the resulting bending moment. The findings reveal that microalgae-based additives will be a first step to a new type of MWF additive. In combination with plant-based base oil, a fully sustainable and CO<sub>2</sub> neutral MWF will be achieved.

## REFERENCES

1. Byers JP. Metalworking Fluids. Third Edition, Boca Raton, Taylor & Francis, CRC Press. 2017.
2. Czichos H, Habig KH. Tribologie-Handbuch, Springer Vieweg, Wiesbaden. 4. Edition. 2015.
3. Minami I. Molecular Science of Lubricant Additives. Applied Sciences, 2017, 7(5): 445. <https://doi.org/10.3390/app7050445>
4. Koch T, Gläbe R, Wenzel D, Siol A, Köser J, Thoeming J, Mesing S, Larek R, Gavalás-Olea A, Lang I. Nachhaltige Schmierstoff-Additive auf Basis von Mikroalgen in der Umformung und Zerspanung. Teil 1. Tribologie und Schmierungstechnik. 2022; 69(3): 18-26. DOI:10.24053/TuS-2022-0014
5. Koch T, Gläbe R, Wenzel D, Mesing S, Wilke K, Larek R. Nachhaltige Schmierstoff-Additive auf Basis von Mikroalgen in der Umformung und Zerspanung. Teil 2. Tribologie und Schmierungstechnik. 2022; 69(3): 18-26. DOI:10.24053/TuS-2022-0015
6. Meier L. Developing Metalworking Fluids for Titanium Cutting. ETH Zürich, PhD-Thesis. 2020. <https://doi.org/10.3929/ethz-b-000413413>
7. Schaal N, Kustera F, Wegener K. Springback in metal cutting with high cutting speeds. Procedia CIRP. 2015, 31: 24-28. <https://doi.org/10.1016/j.procir.2015.03.065>
8. Thieme Römpf Lexikon: Titan - RÖMPP, Thieme Gruppe (cited 2022 Apr 08).
9. www.algaebase.org. (cited 2022 Apr 08).
10. D'Alessandro EB, Nelson RAF. Concepts and studies on lipid and pigments of microalgae: A review. Renewable and Sustainable Energy Reviews. 2016; 58: 832-841. <https://doi.org/10.1016/j.rser.2015.12.162>
11. Roux JM, Lamotte H, Achard JL. An Overview of Microalgae Lipid Extraction in a Biorefinery Framework. Energy Procedia. 2017; 112: 680-688. <https://doi.org/10.1016/j.egypro.2017.03.1137>
12. Murmu M, Sengupta S, Pal R, Mandal S, Murmu N.C. Banerjee P. Efficient tribological properties of azomethine functionalized chitosan as a bio-lubricant additive in paraffin oil: experimental and theoretical analysis. RSC Advances. 2020; 10(55): 33401-33416. DOI:10.1039/D0RA07011D
13. Reihmann M, Köhler B, Ritterreiser N, Yüce C. New Properties of Metalworking Fluids by Introducing Hydrophilic Protein Protection Layers. OilDoc Conference & Exhibition Nov. 17<sup>th</sup>-19<sup>th</sup> 2021.
14. Krishnaraj V, Samsudeensadham S, Sindhummithi R, Kuppan PA. Study on high speed end milling of titanium alloy. Procedia Engineering. 2014, 97: 251-257.
15. Ma J, Mohammadi J, Zhou Y, Larsh J, Januszkiewicz K, Ewans R, Zhao Y, Gali OA, Riahi RA. An investigation into cutting fluid additives performance during machining processing of Ti-Al6-V4. Int J Adv Manuf Technol. 2021; 112: 977-987. [doi.org/10.1007/s00170-020-06403-6](https://doi.org/10.1007/s00170-020-06403-6)
16. Benedicto E, Rubio EM, Carou D, Santacruz C. The Role of Surfactant Structure on the Development of a Sustainable and Effective Cutting Fluid for Machining Titanium Alloys. Metals. 2020; 10(10): 1388. <https://doi.org/10.3390/met10101388>

Acknowledgement: The members of the ALBINA research project thank the Agency for Renewable Resources (FNR) and the German Federal Ministry of Food and Agriculture (BMEL), which is funding this project through a resolution of the German Bundestag.

Gefördert durch:



aufgrund eines Beschlusses  
des Deutschen Bundestages



Thomas Koch: <https://orcid.org/0000-0002-5649-9328>

Ralf Gläbe: <https://orcid.org/0000-0001-9732-7496>



This work is licensed under the Creative Commons  
BY-NC-ND 4.0 license.

## THERMAL AND VISUALISATION STUDY OF THE HFE7100 REFRIGERANT CONDENSATION PROCESS

Tadeusz BOHDAL<sup>✉</sup>, Małgorzata SIKORA<sup>✉</sup>, Karolina FORMELA<sup>✉</sup>

\* Faculty of Mechanical Engineering, Department of Energy Engineering, Koszalin University of Technology,  
ul. Racławicka 15-17, 75-620 Koszalin, Poland

[tadeusz.bohdal@tu.koszalin.pl](mailto:tadeusz.bohdal@tu.koszalin.pl), [malgorzata.sikora@tu.koszalin.pl](mailto:malgorzata.sikora@tu.koszalin.pl), [karolina.formela@s.tu.koszalin.pl](mailto:karolina.formela@s.tu.koszalin.pl)

received 27 February 2023, revised 5 June 2023, accepted 27 June 2023

**Abstract:** Technological advances are contributing to the search for highly efficient energy designs, and increasing interest in compact heat exchangers. Indeed, small channel diameters determine large heat transfer coefficients and condition a significant heat transfer area about the overall volume of the heat exchanger, as well as a smaller amount of refrigerant flowing in the system. Nevertheless, the operating stability and energy efficiency of compact heat exchangers are influenced by two-phase flow structures, which depend on thermal flow parameters. Knowledge of the structures formed during the condensation process is therefore essential for optimising the operation of refrigeration and air-conditioning equipment. This article presents the results from experimental studies of the HFE7100 refrigerant, from the hydrofluorocarbon group, condensation process in mini-channels with hydraulic diameters  $d_h = 2.0$  mm, 1.2 mm, 0.8 mm and 0.5 mm. Thermal flow characteristics were determined, and the forming structures of two-phase flow were recorded. The results of visualisation were subjected to morphological image analysis, based on a special algorithm written in MATLAB software. The algorithm makes it possible to determine the void fraction, which is necessary for calculating the vapour quality, as well as the area of vapour bubbles and their number, directionality and length along the x- and y-axes.

**Key words:** condensation, mini-channels, flow structures, HFE7100

### 1. INTRODUCTION

The condensation process is one of the frequently used phase transformations in heat pumps, refrigeration systems, air-conditioning systems, thermal power plants and heat recovery systems. The performance of these devices is significantly affected by the physical and chemical parameters of refrigerants [1]. The mutual configurations of the gas and liquid phases in radial and axial directions that form during the condensation process also affect the stability and efficiency of thermal machines [2]. However, their formation is interdependent on momentum and energy exchange mechanisms, which are directly shaped by changes in the conditions of the condensation process. Accordingly, thermal flow effects depend on flow structures. It should be noted that the diameter of the channel significantly affects the resulting flow structures of two-phase condensation, which are subject to changes in the length and cross-section of the channel [3, 4]. These changes are related to the type and nature of the flow, as well as the cross-section shape and spatial orientation of the channel. In addition, the formation of two-phase flow structures during condensation is affected by mechanisms of reciprocal relationships of internal forces that are formed in the area of the interfacial surface [5, 6]. It is worth noting that some structures intensify heat transfer, while others inhibit it. In terms of horizontal axis mini-channels, four main groups of structures can be distinguished, i.e. intermittent, dispersed, stratified and annular. Intermittent structures include slug and plug substructures. In the group of dispersed structures, which occur in the form of bubbles, droplets or particles suspended in the continuous phase, the

bubble and mist substructures are distinguished. Stratified structures include wave substructures. There are also transitional structures, such as the annular-wave flow. The most commonly observed structure in mini-channels is the annular flow. In micro-channels, a common structure is bubbly flow; dispersed, stratified and intermittent structures are observed much less frequently [7, 8]. The characteristics of the basic structures are described below (Fig. 1).

1. Mist flow—a structure in which the heat transfer process occurs with the highest intensity, while the pressure drops are the highest. With the increase in inertia forces, liquid droplets are entrained from the condensate film; hence, the liquid film disappears, and gas, in which there are fine liquid droplets, flows through the entire cross-section of the channel.
2. Bubble flow—a phase structure in which gas bubbles occupy a small part of the cross-section of the channel flow in the liquid phase.
3. Wave flow—liquid and gas flow through the channel concurrently, separated by strong gravitational force. Higher velocities of the gas phase determine the formation of disturbances at the boundary layer, resulting in the formation of waves on its surface. This contributes to an increase in the intensity of heat transfer.
4. Plug flow—gas bubbles of size comparable to the dimension of the channel diameter moving mainly in the upper part of the cross-section of the channel.
5. Slug flow—as a result of an increasing flow rate, shear stresses contribute to an increase in the range of waves responsible for the formation of gas bubbles according to the direction of

flow in the channel. As a result, large gas bubbles and some amount of liquid phase with small bubbles suspended alternately flow through the channel [9–11].

To recognize the conditions for the formation of two-phase condensation flow structures, it is necessary to conduct visualization studies [12]. The recorded image of the refrigerant flow, together with the thermal flow tests conducted, forms the basis for the development of maps of two-phase flow. These maps graphically depict the transition boundaries of the flow structures based on the characteristic parameters of phase transformation. They are usually two-dimensional drawings described by two quantities characteristic of the phenomenon [11].

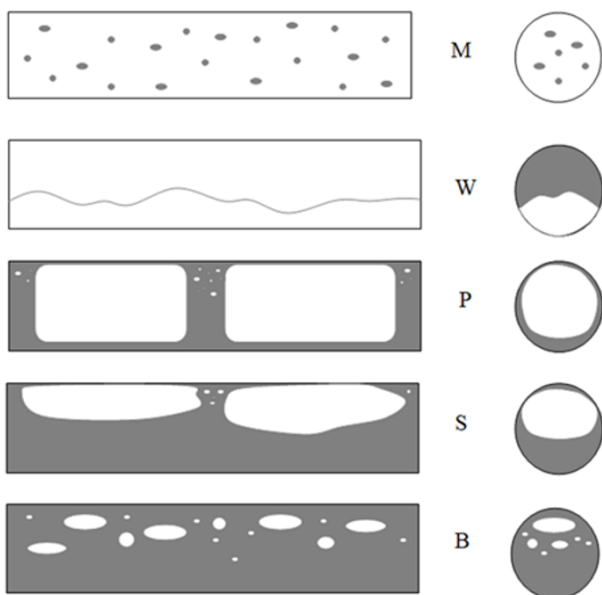


**Fig. 1.** Schematic view of described two-phase flow structures: M – mist flow, W – wave flow, S – slug flow, P – plug flow, B – bubbly flow

In nonadiabatic flows, the transition boundaries of structures are most often described by the vapour quality  $x$  and mass flux density  $G$ . These quantities, in addition to the flow parameters, also make it possible to consider parameters that describe heat transfer. Flow maps are important due to the increased interest in compact heat exchangers in air-conditioning and refrigeration solutions. Therefore, it is important to develop visualisation studies during the condensation process in mini-channels, which, due to the difficulty in the implementation of the condensation transformation itself, as well as in the measurement of its parameters, is much less frequently described compared to boiling or adiabatic two-phase processes [13].

Coleman and Garimella (1999, 2003) [7, 14] conducted an extensive study of two-phase condensation transformation during the flow of the R134a refrigerant in nine air-cooled mini-channels with circular, square and rectangular cross-sections in the range of hydraulic diameter  $dh = 1\text{--}4.91$  mm and mass flux density  $G = 50\text{--}150$  kg/(m<sup>2</sup>s). They conducted flow visualisation studies and observed intermittent, dispersed, annular and wave structures. In addition, they demonstrated the effect of vapour quality, flow rate and channel diameter dimension on the flow structures formed. They also showed the effects of gravity, inertia and interfacial interactions on the formed structures.

Sikora (2015) [15] carried out visualisation studies during the condensation process of the HFE7100 refrigerant in a mini-

channel with a hydraulic diameter of  $dh = 2.0$  mm in the mass flux density range below 200 kg/(m<sup>2</sup>s). Wave, plug, bubble and annular-wave structures were observed in the flow. This study reported that systematic studies of the condensation process of various low-pressure refrigerants may make it possible in the future to create a general structure map for refrigerants.

Al-Zaidi et al. (2018) [16] conducted a study of flow structures during the two-phase condensation flow of the HFE7100 refrigerant in a multiport, which was made in rectangular mini-channels with a hydraulic diameter of  $dh = 0.57$  mm in the mass flux density range  $G = 48\text{--}126$  kg/(m<sup>2</sup>s). They observed that at high mass flux densities, a ring structure was most often formed in the flow, while at lower values, a slug and bubble structure was observed.

Xiao and Hrnjak (2019) [17] presented the condensation results of the following refrigerants: R134a, R1234ze, R32, R245fa and R1233zd. These tests were performed in channels with a hydraulic diameter  $dh = 1.4\text{--}6.0$  mm. They described the exact conditions under which transitions between structures occur. According to this, in the annular flow, the influence of surface tension and shear forces prevails over gravity. The increase in the condensate film thickness affects the increase in the gravitational force impact. When its value exceeds the force of surface tension and shear stress, a stratified structure is formed in the flow. The formation of Kelvin–Helmholtz instability determines the transition between stratified and wave structures. Wave heights depend on the velocity difference of both, liquid and gas phases. At wave heights close to the inner diameter of the channel, the transition to an intermittent structure occurs. Indeed, low values of mass flux density determine low wave heights; hence, the discontinuous structure is not formed although there is an increase in the condensate film thickness.

Sikora (2020) [11] carried out visualisation studies of HFE7100, HFE7000 and Novec649 refrigerants under condensation conditions in mini-channels in the range of hydraulic diameter  $dh = 0.5\text{--}2.0$  mm, which were subjected to image analysis. As a result, the geometric dimensions of the structures, the vapour quality, the void fraction and the velocities of various phases were determined. The author analysed the results of modelling the heat transfer process and flow resistance; hence, it was shown that there are correlations between the flow resistance and the heat transfer coefficient with the type of two-phase flow structures. This paper mapped the flow structures considering the three factors studied and presented the conditions under which the transitions between the structures occur based on the magnitude of mass flux density and the void fraction.

## 2. RESEARCH STAND

Fig. 2 schematically illustrates the research stand for conducting thermal flow and visualisation tests during the condensation process of the HFE7100 refrigerant. From the analysis of this scheme, it can be observed that liquid refrigerant flows through the pump, and is successively pumped to the evaporator. An Endress + Hauser Coriolis mass flow meter 34XIP67 (accuracy class 0.5) is placed on the inlet to the evaporator. Then, using an electric heater system, heat flux is supplied to the refrigerant until it evaporates. The vapour of the refrigerant, at a constant temperature that is maintained by a thermostat, reaches the heat exchanger. This heat exchanger takes away the heat of vapour superheating to regulate the inlet vapour quality of the refrigerant. The next element is the measuring part of the research stand,

which includes a stainless steel mini-channel placed in the water channel. The refrigerant also flows through a glass mini-channel, where its flow is recorded with an Olympus i-speed 3 (CMOS) time-lapse camera (with a maximum recording speed of 10,000 fps and a maximum resolution of  $1280 \times 1024$  pixels). The measuring section of the stand includes K-type thermocouples (with a thermocouple diameter of 0.1 mm), which are distributed along the length of the mini-channels and the water channel. A piezoresistive pressure sensor (with a measuring range of 0–40 MPa and a class of 0.5) and differential pressure transducer (Endress + Hauser Deltabar SPMP, with a measuring range of 0–1.5 MPa and a class of 0.075) are also mounted. After leaving the measuring section, the refrigerant flows into a water-cooled heat exchanger, which is responsible for its subcooling. Then, the refrigerant is directed to the liquid refrigerant tank. As a result, a series

of phase transformations begins again.

The research stand was subjected to tests to evaluate the correctness of its operation and zeroing of the measuring sensors. The test results are shown in Fig. 3. Testing of the stand consisted of passing only the liquid of the refrigerant through the measuring section and comparing the frictional coefficient of flow resistance with the results of theoretical calculations under the same conditions. For this purpose, the Blasius equation (Eq. [1]) and Hagen–Poiseuille equation (Eq. [2]) were used.

$$\lambda = 0.3164/Re^{0.25} \quad (1)$$

$$\lambda = 64/Re \quad (2)$$

As can be seen, the discrepancy between theoretical and experimental results is about  $\pm 20\%$ .

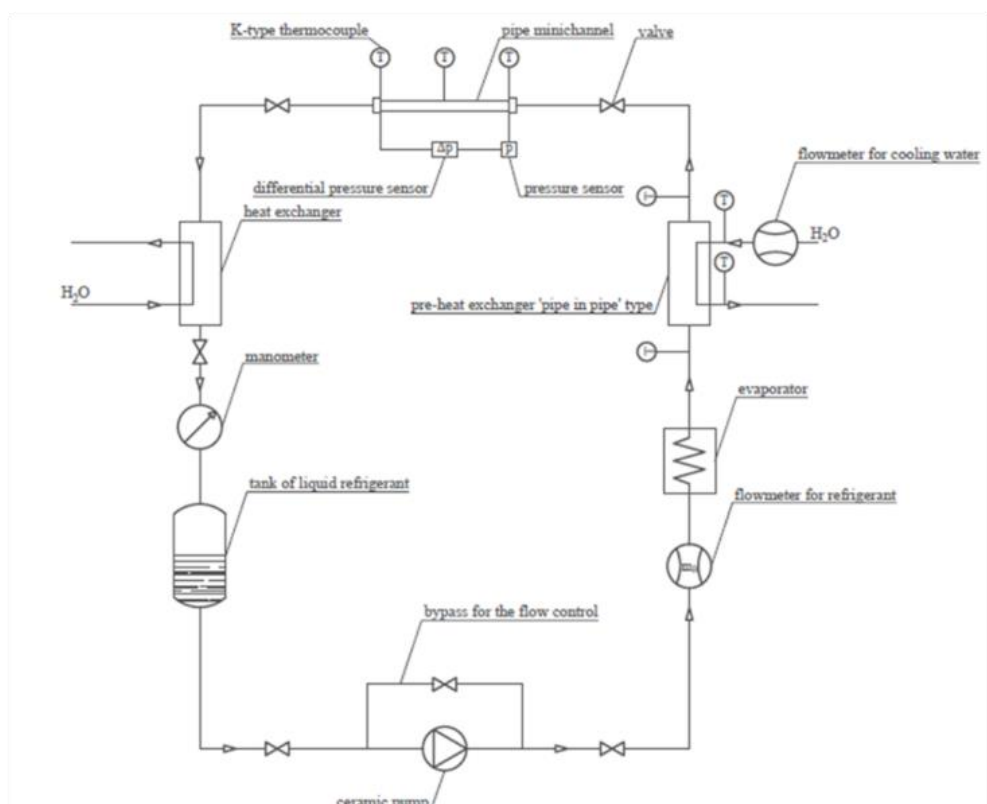


Fig. 2. Scheme of the test stand

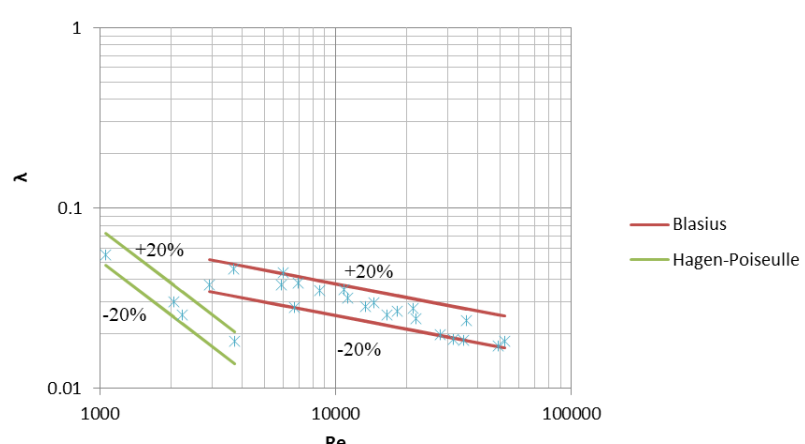


Fig. 3. Comparison of experimental and theoretical frictional coefficient of flow resistance  $\lambda$  versus Reynolds number  $Re$  for the HFE7100 agent in tubular mini-channels with internal diameter  $d_h = 0.5\text{--}2.0$  mm

### 3. RESEARCH METHODS

Determination of thermal flow characteristics of the condensation process and visualisation studies of two-phase flow structures were carried out simultaneously, which is innovative since previous studies have first performed thermal and then visualisation studies, such as Bohdal et al. (2015) and Sikora and Bohdal (2020) [15, 18]. In the thermal tests, the following parameters were measured using control and measurement equipment: the temperature of the wall surface and cooling water, as well as the mass flow rate of the cooling water and the refrigerant. The overpressure of the refrigerant on the inlet and the pressure difference along the length of the mini-channel were also measured directly. Appropriate instrumentation of the heat exchanger made it possible to record temperature measurements of the refrigerant and the cooling water, which in turn made it possible to determine the vapour quality of the refrigerant on the mini-channel, according to the equation:

$$\dot{Q} = \dot{m}_R \cdot c_R \cdot (T_R - T_S) + \dot{m}_R \cdot r \cdot (1 - x), \quad (3)$$

where  $\dot{m}_R$  is mass flux density of refrigerant,  $c_R$  is the specific heat of the refrigerant,  $T_R$  is the temperature of the refrigerant and  $T_S$  is the saturation temperature under given conditions and  $r$  is the unit heat of the phase transformation of condensation.

In the thermal study, the local value of the vapour quality  $x_i$  along the mini-channel during condensation was calculated by using the following equation:

$$x_i = x_{i-1} - \frac{[\dot{m}_w \cdot c_w \cdot (T_{wi-1} - T_{wi})]}{\dot{m}_r \cdot r}, \quad (4)$$

where  $x_{i-1}$  is vapour quality from the previous section,  $\dot{m}_w$  is mass flux density of the cooling water,  $c_w$  is the specific heat of the water,  $T_{wi-1}$  is the channel wall temperature in the previous section and  $T_{wi}$  is the channel wall temperature in this section.

Both the vapour quality and the heat flux density were determined indirectly, the values of which at individual cross-sections of the mini-channel made it possible to determine the heat transfer coefficient during the equation:

$$\alpha_i = \frac{q_i}{\Delta T_i}, \quad (5)$$

where  $\Delta T_i$  is the difference between the saturation temperature of refrigerant  $T_S$  and the temperature of the channel wall in a given cross-section  $T_{ci}$  under the given conditions.

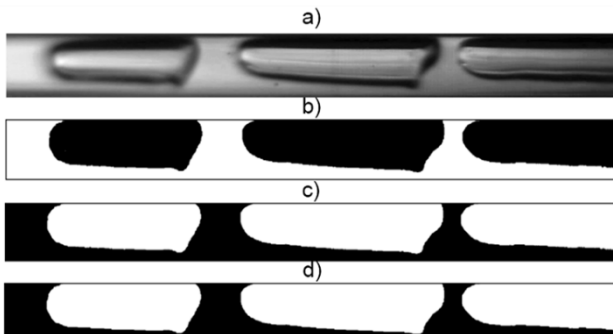


Fig. 4. Interpretation of image processing and analysis steps: a) image after cutting out the inside of the channel, b) binary image, c) image after inversion, d) image after noise removal

The computational method was also used to determine the mass flux density. To visualise the two-phase flow structures, a time-lapse camera was used to record images of the refrigerant flow. Frames were generated from the recorded image, from which the image of the inside of the mini-channel was sequentially cut out (Fig. 4a). In the next step, the phase separation line was closed. The image thus prepared was subject to morphological analysis by a special algorithm written in MATLAB R2019a. The algorithm performed binarisation (Fig. 4b), as a result of which black pixels occupied fields filled with the gas phase, while white pixels occupied those filled with the liquid phase. The next step was to perform inversion (Fig. 4c) and remove the "noise" (Fig. 4d). After this step, the gas phase was described by the white pixels, while the liquid phase was described by the black pixels. Based on the given image dimensions and the black and white pixels counted by the algorithm, the area occupied in the image by each phase was determined. The ratio of the area of the white pixels to the total area of the image is the void fraction  $\phi$ , and based on this, it is possible to determine the vapour quality  $x$  [19]:

$$x = \frac{\rho_v}{\left(\frac{\rho_l}{\phi} - \rho_l + \rho_v\right)}, \quad (6)$$

where  $\rho_l$  is the density of the liquid phase and  $\rho_v$  is the density of the vapour phase. A full description of the investigation methodology and accuracy of the measurement equipment is provided in the studies of Sikora et al. [18] and Sikora [19]. The heat transfer coefficient was determined with an accuracy of 10%, and the accuracy of pressure drop measurement was 8%. The vapour quality in visualisation studies was determined based on a two-dimensional image, and accordingly the accuracy of its determination is at the level of 12%.

### 4. PROPERTIES OF THE HFE7100 REFRIGERANT

A non-flammable, low-toxicity and thermally stable refrigerant from the hydrofluoroether group was used to perform thermal flow and visualisation studies. Selected physical properties of this odourless and almost colourless substance are shown in Table 1. The HFE7100 refrigerant is distinguished by its zero ozone depletion potential (ODP) and low global warming potential (GWP) parameter of 320. Its lifetime in the atmosphere is less than 5 years.

Tab. 1. Physical properties of the HFE7100 refrigerant for a temperature of 25°C and normal pressure

Chemical Formula	$C_4F_9OCH_3$
Molar Mass [Kg/Kmol]	250
Boiling Point [°C]	61
Freezing Point [°C]	-135
Liquid Density [Kg/M³]	1510
Critical Pressure [Mpa]	2.23
Critical Temperature [°C]	195
Dielectric Constant	7.4
Latent Heat [KJ/Kg]	112
Specific Heat [J/(Kg·K)]	1170
Heat Conductivity [W/(M·K)]	0.0069
Vapour Pressure [Kpa]	26.9

Therefore, its environmental safety profile is excellent. In addition, its good dielectric properties mean that there is no risk of damage to electrical equipment during operation due to a leak or other failure. Most metals (aluminium, copper, brass, stainless steel) and hard polymers (polycarbonate, polypropylene, polyethylene, acrylic) offer a good compatibility as candidates for material to be used in the installation of the refrigeration circuit through

which the HFE7100 refrigerant flows. Based on the specified thermodynamic properties of the HFE7100 refrigerant, significant relationships were developed and used in the study. Fig. 5 illustrates some of them. A plot of the dependence of saturation temperature on saturation pressure was made. Characterisations of density, dynamic viscosity and specific heat of the liquid phase as a function of saturation temperature were also made.

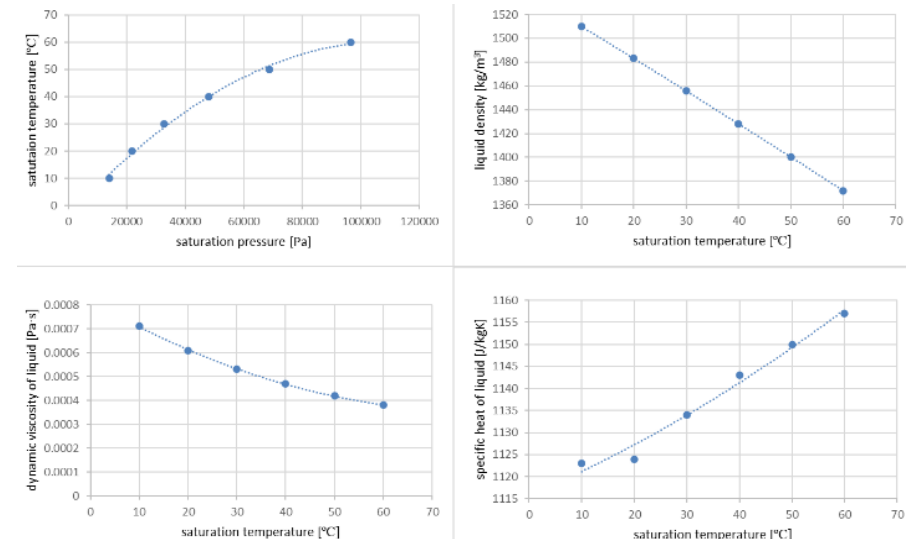


Fig. 5. Selected physicochemical relationships of the HFE7100 refrigerant

## 5. EXPERIMENTAL THERMAL FLOW CHARACTERISTICS

The basic thermal characteristic, which is the dependence of the heat transfer coefficient  $\alpha$  on the vapour quality  $x$ , is illustrated in Fig. 6. From its course in  $\alpha = f(x)$ , it can be observed that heat transfer intensifies as a result of the increase in the vapour quality and the density of the mass flow. One reason for this is the increase in turbulence due to higher refrigerant flow velocity, which results in more efficient heat transfer. In addition, increasing the

amount of the gas phase in the system also intensifies heat transfer, since gas has a higher thermal conductivity coefficient than liquids, and the condensate layer is similar to an insulator. From an analysis of the graphical summaries in Fig. 6, it can also be observed that a decrease in the dimension of the hydraulic diameter determines the increase in the value of the heat transfer coefficient. Indeed, increasing the energy efficiency of heat transfer has a beneficial effect on the two-phase transformation of condensation.

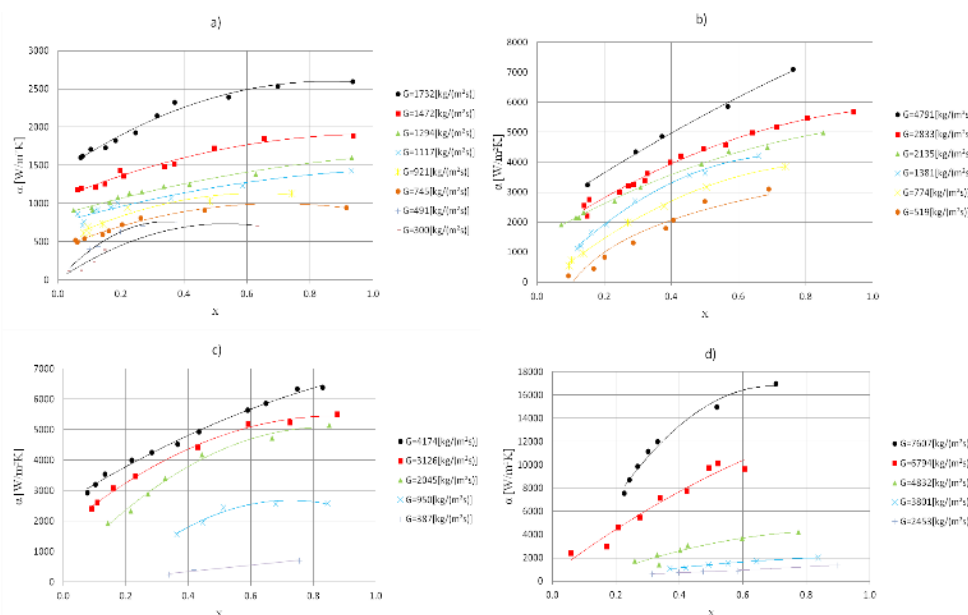
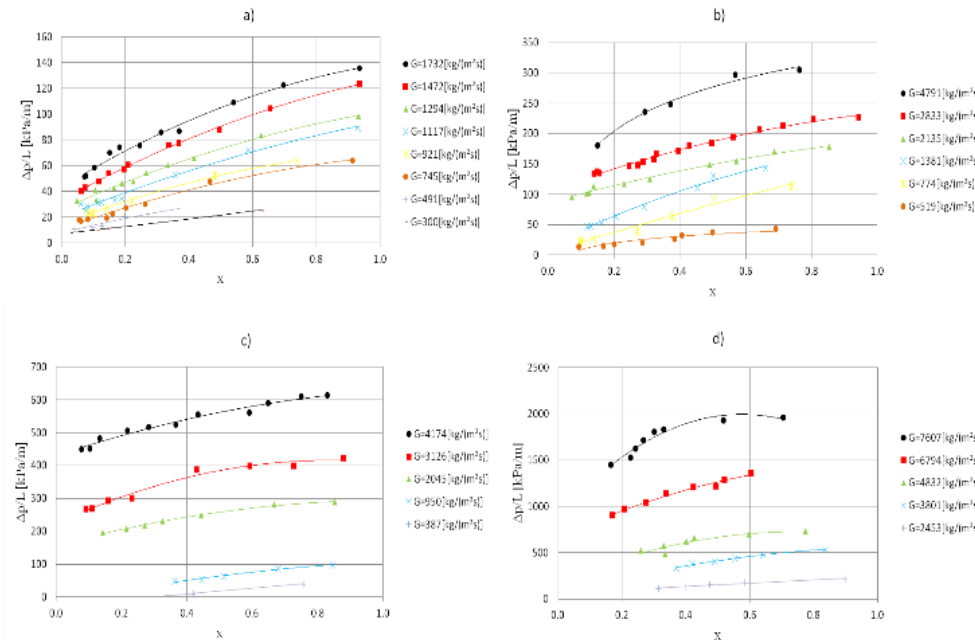


Fig. 6. Dependence of the heat transfer coefficient  $\alpha$  as a function of the vapor quality  $x$  for different mass flux densities  $G$  during the condensation process of the HFE7100 agent in a mini-channel with a diameter: a)  $dh = 2.0$  mm, b)  $dh = 1.2$  mm, c)  $dh = 0.8$  mm, d)  $dh = 0.5$  mm

Fig. 7 illustrates the dependence of flow resistance  $\Delta p/L$  as a function of vapour quality  $x$  for different values of mass flux density  $G$ . From the analysis of the characteristics presented in the graphical form, it is noticeable that the flow resistance increases with an increase of the vapour quality. Undoubtedly, the increasing

flow velocity of the refrigerant determines the increased pressure drop along the length of the mini-channel. The hydraulic diameter of the channel also has a significant impact on flow resistance. A decrease in its dimension contributes to an increase in flow resistance.



**Fig. 7.** Dependence of flow resistance  $\Delta p/L$  on the degree of dryness  $x$  for different mass flux densities  $G$  during the condensation process of the HFE7100 refrigerant in a mini-channel with diameter: a)  $dh = 2.0$  mm, b)  $dh = 1.2$  mm, c)  $dh = 0.8$  mm, d)  $dh = 0.5$  mm

## 6. RESULTS OF VISUALISATION STUDIES OF TWO-PHASE FLOW STRUCTURES

Example results of visualisation of two-phase condensation flow structures of the HFE7100 refrigerant in a mini-channel with a diameter of 2.0 mm are shown in Fig. 8. The following structures were observed: plug (Fig. 8a), bubble (Fig. 8b), annular-wave (Fig. 8c) and slug (Fig. 8d).

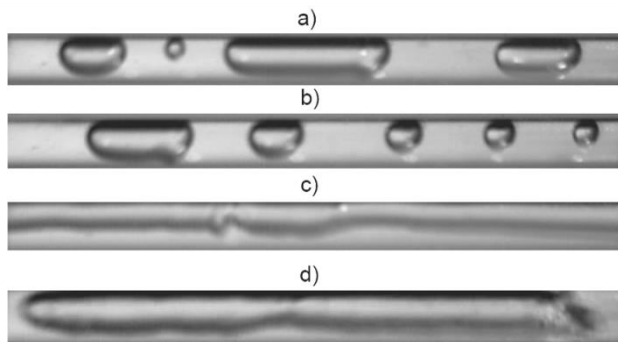


**Fig. 8.** Experimental results of visualization studies during the condensation process of the HFE7100 refrigerant in a mini-channel with a diameter of  $dh = 2.0$  mm: (a) plug structure,  $G = 150$  kg/m $^2$ s,  $T_s = 67.4^\circ\text{C}$ ,  $\varphi = 0.36$ , (b) bubble structure  $G = 300$  kg/m $^2$ s,  $T_s = 67.1^\circ\text{C}$ ,  $\varphi = 0.23$ , (c) annular-wave structure  $G = 309$  kg/m $^2$ s,  $T_s = 67.6^\circ\text{C}$ ,  $\varphi = 0.56$ , (d) slug structure  $G = 504$  kg/m $^2$ s,  $T_s = 70.9^\circ\text{C}$ ,  $\varphi = 0.63$

Fig. 9 shows images of the structures that were observed during the testing of the condensation process of the HFE7100 refrigerant in a mini-channel with a diameter of 1.2 mm. In this case, bubble (Fig. 9a), plug (Fig. 9b), annular (Fig. 9c) and annular-wave (Fig. 9d) structures were observed. Example results of two-phase flow structures visualisation during condensation of the HFE7100 refrigerant in a mini-channel with a diameter of 0.8 mm are shown in Fig. 10. The following structures were observed: annular-wave (Fig. 10a), bubble (Fig. 10b), slug (Fig. 10c) and annular (Fig. 10d).

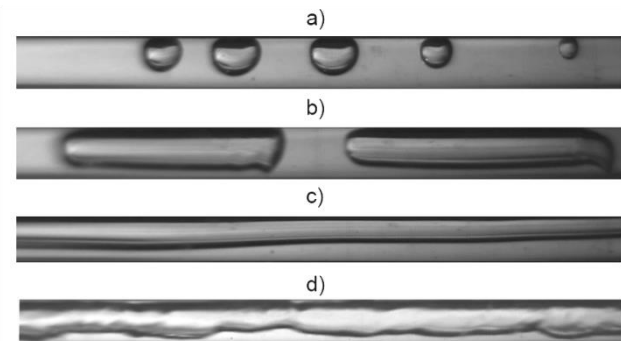


**Fig. 9.** Experimental results of visualization studies during the condensation process of the HFE7100 refrigerant in a mini-channel with a diameter of  $dh = 1.2$  mm: (a) bubble structure  $G = 270$  kg/m $^2$ s,  $T_s = 70.7^\circ\text{C}$ ,  $\varphi = 0.17$ , (b) plug structure  $G = 491$  kg/m $^2$ s,  $T_s = 70.8^\circ\text{C}$ ,  $\varphi = 0.63$ , (c) annular structure  $G = 786$  kg/m $^2$ s,  $T_s = 71.1^\circ\text{C}$ ,  $\varphi = 0.62$ , (d) annular-wave structure  $G = 2801$  kg/m $^2$ s,  $T_s = 74.6^\circ\text{C}$ ,  $\varphi = 0.54$

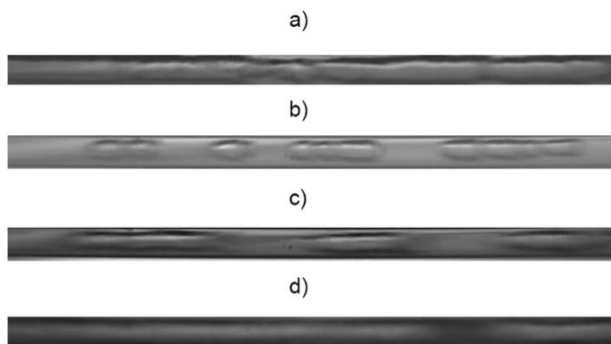


**Fig. 10.** Experimental results of visualization studies during the condensation process of the HFE7100 refrigerant in a mini-channel with a diameter of  $d_h = 0.8$  mm:  
(a) annular-wave structure  $G = 884 \text{ kg/m}^2\text{s}$ ,  $T_s = 70.6^\circ\text{C}$ ,  $\varphi = 0.70$ , (b) bubble structure  $G = 884 \text{ kg/m}^2\text{s}$ ,  $T_s = 70.7^\circ\text{C}$ ,  $\varphi = 0.38$ , (c) slug structure  $G = 2045 \text{ kg/m}^2\text{s}$ ,  $T_s = 68.5^\circ\text{C}$ ,  $\varphi = 0.37$ , (d) annular structure  $G = 4257 \text{ kg/m}^2\text{s}$ ,  $T_s = 82.7^\circ\text{C}$ ,  $\varphi = 0.79$

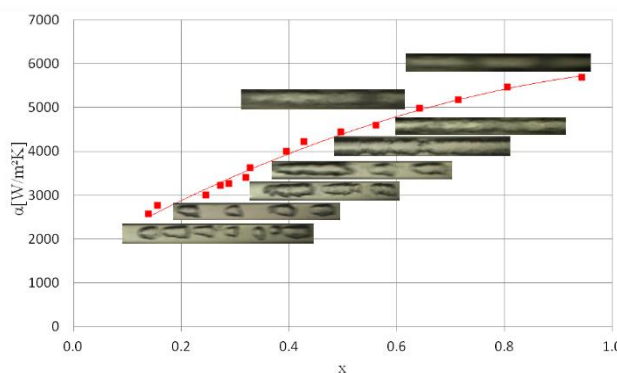


**Fig. 11.** Two-phase flow structures in a mini-channel with diameter  $d_h = 1.2$  mm for mass flux density  $G = 2833 \text{ kg/m}^2\text{s}$ ,  $T_s = 74-78^\circ\text{C}$  during condensation of the HFE7100 refrigerant

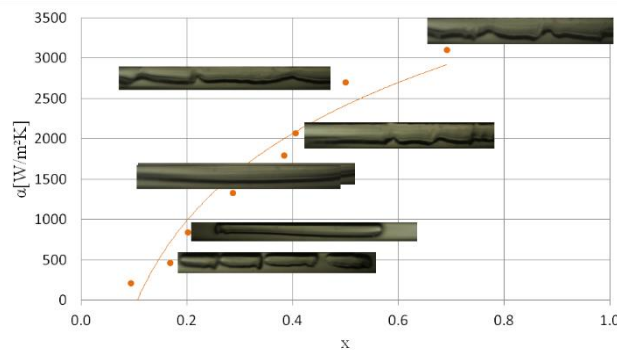


**Fig. 12.** Two-phase flow structures in a mini-channel with diameter  $d_h = 1.2$  mm for mass flux density  $G = 519 \text{ kg/(m}^2\text{s)}$ ,  $T_s = 71-74^\circ\text{C}$  during condensation of the HFE7100 refrigerant

The type of structure formed is mainly influenced by flow parameters [20]. Among these are the mass flux density  $G$  and the liquid and vapour phase velocities, as well as the vapour quality  $x$  and the void fraction  $\varphi$ . As can be seen in Figs. 11 and 12, a change in the vapour quality  $x$  and mass flux density changes the flow structure that occurs, and these structures closely affect the intensity of heat transfer, i.e. an increase in the liquid phase

amount causes a decrease in the heat transfer coefficient. However, the shape of the phase separation surface is not insignificant. The more developed the phase separation surface, the higher the heat transfer coefficient resultantly obtained. The development of the phase separation surface is closely related to the flow velocity of the gas phase since a high value of it disturbs the interfacial surface.

## 7. CONCLUSIONS

Heat transfer and visualisation studies were carried out during the condensation process of a substance from the hydrofluoro-ether group, HFE7100, in horizontal mini-channels. Based on the obtained results, the dependence of the heat transfer coefficient and flow resistance as a function of the vapour quality was shown in a graphical form. An analysis of the effect of mass flux density and the dimension of the hydraulic diameter of the mini-channel on the energy efficiency of heat transfer and pressure drop along the length of the channel was carried out. The observed structures of two-phase flow during condensation of the HFE7100 refrigerant were presented. The following conclusions can be drawn from the experimental results obtained:

- A significant effect on the heat transfer coefficient  $\alpha$  is determined by the vapour quality  $x$  and the mass flux density  $G$ . Increasing the values of these parameters leads to an intensification of heat transfer. An increase in the heat transfer coefficient is also observed following a decrease in the dimension of the hydraulic diameter  $d_h$  of a single-pipe mini-channel.
- The value of flow resistance  $\Delta p/L$  is determined not only by the vapour quality  $x$  but also by the mass flux density  $G$ . Therefore, an increase in the vapour quality and mass flux density contributes to an increase in flow resistance. The dimension of the hydraulic diameter of the mini-channel also has a significant effect on flow resistance. Under the same conditions of the condensation process, an increase in the hydraulic diameter of the mini-channel is accompanied by a decrease in flow resistance.
- The type of structure formed is mainly influenced by the following flow parameters: mass flux density  $G$  and liquid and vapour phase velocity, as well as the vapour quality  $x$  and the void fraction  $\varphi$ .
- The thermal flow effects of two-phase condensation depend on the flow structure. On the other hand, some two-phase flow structures intensify heat transfer, whereas others limit the energy efficiency of heat transport (annular, annular-wave, slug and plug structures). Unfortunately, these structures with given higher heat transfer coefficients are given high pressure drops too.

## REFERENCES

1. Wang Z, Xu Z, Luo L, Xia X, Peng D, Li X. Experimental investigation of condensation pressure drop of zeotropic refrigerant/oil mixtures in plate heat exchanger. International Journal of Refrigeration 2023; 149: 192-203. <https://doi.org/10.1016/j.ijrefrig.2022.12.026>
2. Mikielewicz D, Andrzejczyk R, Jakubowska B, Mikielewicz J. Comparative study of heat transfer and pressure drop during flow boiling and flow condensation in minichannels. Archives of Thermodynamics. 2014; 35: 17-37. <https://doi.org/10.2478/atom-2014-0019>

3. Jige D, Kikuchi S, Eda H, Inoue N, Koyama S. Two-phase flow characteristics of R32 in horizontal multiport minichannels. Flow visualization and development of flow regime map. *International Journal of Refrigeration* 2018; 95: 156–164. <https://doi.org/10.1016/j.ijrefrig.2018.09.005>
4. Doretti L, Zilio C, Mancin S, Cavallini A. Condensation flow patterns inside plain and microfin tubes: A review. *International Journal of Refrigeration*. 2013; 36: 567–587. <https://doi.org/10.1016/j.ijrefrig.2012.10.021>
5. Xiao J, Hrnjak P. A flow regime map for condensation in macro and micro tubes with non-equilibrium effects taken into account. *Int J Heat Mass Transf.* 2019; 130: 893–900. <https://doi.org/10.1016/j.ijheatmasstransfer.2018.10.081>
6. Soligo G, Roccon A., Soldati A. Mass-conservation-improved phase field methods for turbulent multiphase flow simulation. *Acta Mech.* 2019; 230: 683–696. <https://doi.org/10.1007/s00707-018-2304-2>
7. Coleman JW, Garimella S. Two-phase flow regimes in round, square and rectangular tubes during condensation of refrigerant R134a. *International Journal of Refrigeration* 2003; 26: 117–128. [https://doi.org/10.1016/S0140-7007\(02\)00013-0](https://doi.org/10.1016/S0140-7007(02)00013-0)
8. Fronk BM, Garimella S. In-tube condensation of zeotropic fluid mixtures: A review. *International Journal of Refrigeration* 2013; 36: 534–561. <https://doi.org/10.1016/j.ijrefrig.2012.11.030>
9. Garimella Srinivas FBM. Encyclopedia of two-phase heat transfer and flow I. Fundamentals and Methods II. Condensation heat transfer. World Scientific 2016
10. Dziubiński M, Prywer J. Mechanika plynów dwufazowych. Wydawnictwo Naukowo Techniczne, Warszawa 2009
11. Sikora M. Modelowanie struktur przepływu dwufazowego podczas skraplania w minikanałach 2020
12. Ligus G, Zajac D, Masiukiewicz M, Anweiler S. A New Method of Selecting the Airlift Pump Optimum Efficiency at Low Submergence Ratios with the Use of Image Analysis. *Energies (Basel)* 2019; 12: 735. <https://doi.org/10.3390/en12040735>
13. El Hajal J, Thome JR, Cavallini A. Condensation in horizontal tubes, part 1: two-phase flow pattern map. *Int J Heat Mass Transf.* 2003; 46: 3349–3363. [https://doi.org/10.1016/S0017-9310\(03\)00139-X](https://doi.org/10.1016/S0017-9310(03)00139-X)
14. Coleman JW, Garimella S. Characterization of two-phase flow patterns in small diameter round and rectangular tubes. *Int J Heat Mass Transf.* 1999; 42: 2869–2881. [https://doi.org/10.1016/S0017-9310\(98\)00362-7](https://doi.org/10.1016/S0017-9310(98)00362-7)
15. Bohdal T, Sikora M, Widomska K, Radchenko AM. Investigation of flow structures during HFE-7100 refrigerant condensation. *Archives of Thermodynamics* 2016; 36: 25–34. <https://doi.org/10.1515/aoter-2015-0030>
16. Al-Zaidi AH, Mahmoud MM., Karayiannis TG. Condensation flow patterns and heat transfer in horizontal microchannels. *Exp Therm Fluid Sci.* 2018; 90:153–173. <https://doi.org/10.1016/j.expthermflusci.2017.09.009>
17. Xiao J, Hrnjak P. A flow regime map for condensation in macro and microtubes with non-equilibrium effects taken into account. *Int J Heat Mass Transf.* 2019. <https://doi.org/10.1016/j.ijheatmasstransfer.2018.10.081>
18. Sikora M, Bohdal T. Heat and flow investigation of NOVEC649 refrigerant condensation in pipe minichannels. *Energy* 2020. <https://doi.org/10.1016/j.energy.2020.118447>
19. Sikora M, Bohdal T, Formela K. Experimental Study of HFE 7000 Refrigerant Condensation in Horizontal Pipe Minichannels. *Materials*. 2021; 14: 6886. <https://doi.org/10.3390/ma14226886>
20. Chen Y, Gao H, Liu H, Chen D, Jiang J., Ma Z. Experimental investigation on condensation regimes and transition boundary during bubble condensation in narrow rectangular channel. *International Journal of Thermal Sciences* 2023; 188: 108212. <https://doi.org/10.1016/j.ijthermalsci.2023.108212>

Tadeusz Bohdal:  <https://orcid.org/0000-0002-0621-2894>

Małgorzata Sikora:  <https://orcid.org/0000-0001-8373-3573>

Karolina Formela:  <https://orcid.org/0000-0002-8289-652X>



This work is licensed under the Creative Commons BY-NC-ND 4.0 license.

## FUZZY BASED SUPERVISION APPROACH IN THE EVENT OF ROTATIONAL SPEED INVERSION IN AN INDUCTION MOTOR

Noura Rezika HATEM BELLAHSENE\*<sup>✉</sup>

\*LTII Laboratory, Department of Automatic, Telecommunications and Electronic, University A. Mira of Bejaia, Bejaia, Algeria

[bellahsenehatem@gmail.com](mailto:bellahsenehatem@gmail.com)

received 12 December 2022, revised 22 July 2023, accepted 23 July 2023

**Abstract:** This article aims to implement the fuzzy control for an asynchronous motor after a general representation of the vector control. We develop MAMDANI type fuzzy algorithm for MAS speed regulation; its purpose is to cancel static error, decrease overshoot, decrease response time, and rise time to obtain an adequate response of the process and regulation and to have a precise, fast, stable and robust system. This paper investigates the design of a fuzzy-based approach for monitoring the inversion of the rotational speed of an induction motor. We will indeed present a robust vector control technique extended to blur in the event of a fault. Direct torque control is known to produce fast and robust response in the AC drive system. However, in a steady state, a rapid and unexpected change in speed can occur which could be dangerous. The performance of the conventional PID controller can be improved by implementing fuzzy logic techniques. The first step is the modelling of the whole system, including the capacitors, the induction generator and the loads. The model is obtained using the Park transformation. The results are thus compared with those of the standard PID control. This approach is applied to a three-phase asynchronous motor (LS90LZ). The presented study improves the transient response time and the precision of the servo system. An inversion of the reference speed of rotation is considered, and the results are very convincing.

**Key words:** fuzzy control, PID control, Park transformation, speed reversal, vector control, induction motor

### 1. INTRODUCTION

The use of conventional control techniques requires modeling of the process to be controlled. This is not always easy to achieve, especially when it comes to a nonlinear system for which conventional controllers are poorly suited.

To solve this problem, new control strategies, based on the expertise of the operator, have been developed. Among these, the fuzzy control (or regulator) occupies a privileged place. It is characterized by its aptitude to apprehend the problem of nonlinearity.

The fuzzy regulator provides an algorithm that can convert linguistic control strategy based on expert knowledge into an automatic control strategy. Experience has shown that fuzzy logic control gives better results than those obtained by classical control algorithms.

Among many types of machines, three-phase induction motors (IMs) benefit from a large popularity. In industry, almost all drive systems use IMs. The adjustable speed IM drives from power electronic converters, which are increasing, phasing out DC drives [1].

The results of conventional supervision methods have been demonstrated in many works for the resolution of practical problems related to the asynchronous motor, such in the industry. Nevertheless, it has been proven that there are still unanswered questions, which can probably be solved by the fuzzy system approach [2-4].

Thus, the advanced supervision methods developed by theorists are only partially able to satisfy the requirements. To overcome these shortcomings, fuzzy modelling can play an important role.

A conventional PID controller is effectively utilized in AC motor electrical drives. The design of conventional PID controllers is more complex when this controller is used in the high rating electrical drives, hence increasing the cost. Soft computing techniques are used in the closed loop control of an electrical system, and it is known as advanced intelligent control.

Nowadays, the intelligent control is playing an essential role in industries control. Intelligent control techniques can be implemented using microprocessors and microcontrollers which have high computation ability, and which operate at high speed [5, 6].

The asynchronous motor is modelled by Park's equations to facilitate calculations and simplify representations [7-12]. The modelling of the asynchronous motor requires certain simplifying assumptions to obtain simple relations.

It will thus be assumed that the self-inductances are constant [12-19], the mutual inductances are considered according to the position of their magnetic axes and the rotor resistances are constant with respect to the rotational speed axes and the rotor resistances are constant with respect to the rotational velocity [20-25].

### 2. THREE PHASES AM MODELING

The rotor can be modelled by three identical windings staggered in space by  $120^\circ$ . These windings are short-circuited, and the voltage across them is zero. We pose " $\theta$ " the electrical angle between the phase 'A' stator and the phase 'a' rotor as shown in Fig. 1.

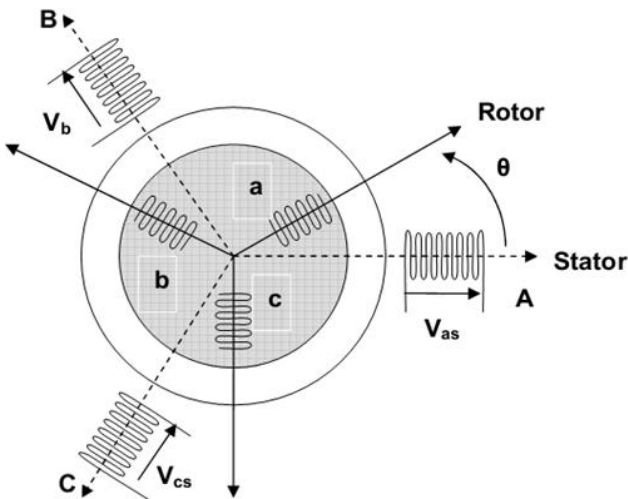


Fig. 1. Schematic representation of three-phases AM

The modelling of the asynchronous machine requires certain simplifying assumptions in order to obtain simple relations; this it will be assumed that the self-inductances are constant, the mutual inductances are a function of the position of their magnetic axes and the rotor resistances are constant with respect to the speed of rotation.

– Electrical equations

By applying Ohm's law and Faraday's law to the windings of the stator and the rotor, we find a writing in the matrix form:

$$\begin{aligned} [V_s] &= [R_s][I_s] + \frac{d}{dt}[\Phi_s] \\ [V_r] &= [0] = [R_r][I_r] + \frac{d}{dt}[\Phi_r] \end{aligned}$$

– Magnetic equations (of flows)

The totalized fluxes coupled between the stator and rotor phases are expressed in the form:

$$[\Phi_s] = [L_{ss}][I_s] + [M_{sr}][I_r]$$

$$[\Phi_r] = [L_{rr}][I_r] + [M_{sr}]^t[I_s]$$

By replacing the magnetic equations in electrical equations, we obtain the two expressions of the stator and rotor voltages:

$$[V_s] = [R_s][I_s] + [L_{ss}] \frac{d}{dt}[I_s] + \frac{d}{dt}\{[M_{sr}][I_r]\}$$

$$[V_r] = [R_r][I_r] + [L_{rr}] \frac{d}{dt}[I_r] + \frac{d}{dt}\{[M_{sr}]^t[I_s]\}$$

– Mechanical equations

The torque  $C_e \frac{1}{2}$

Movement (speed)  $J \frac{d\Omega}{dt} + F\Omega = C_e - C_r$

$m_s, m_r$ : Mutual inductances between phases, stator and rotor.

$l_s, l_r$ : Proper, stator and rotor inductances of a phase.

$L_{ss}, L_{rr}$ : Stator and rotor induction matrix.

$M_{sr}, M_{sr}$ : Matrix of mutual inductances stator\_rotor and rotor\_stator.

$\theta$ : Angle between the rotor axis and the stator axis.

$C_r = F \cdot \Omega$ : Resistant torque.

$\Omega = \frac{\omega_r}{p}$ : mechanical angular speed of the rotor.

$J$ : moment of inertia.

$F$ : Coefficient of friction.

### 3. PARK MODEL

The machine equations can be further simplified by choosing a particular frame of reference for dq. The choice of benchmark is made according to the purpose of the application. Three types of benchmarks can be considered, namely:

- Referencial linked to the stator ( $\alpha, \beta$ ): It is interesting during the study of significant variation of the speed of rotation seen that appears in the equation.
- Referencial linked to the rotor ( $x, y$ ): It is interesting when studying transient regimes where the speed is considered constant.
- Referencial linked to in the rotating field (d, q): It eliminates the influence of rotor and stator leakage reactances.

The referencial linked to in the rotating field (d, q) is the repository which is chosen during our study (Fig. 2), because it has advantages when studying the loads around a given point. The advantage of using this model is to have constant quantities in steady state. It is then easier to regulate it.

The temporal simulation of instantaneous electrical and mechanical quantities, considering the diffusive character of the skin effect in the rotor, requires adapting the model of Park in order to isolate the non-integer order transfer function representing the rotor. To simplify the representation of the previous equations, we introduce the transformation of Park, obtained using the matrix  $P$ , which consists in moving from a three-phase winding to a bi-phase winding and vice versa [3].

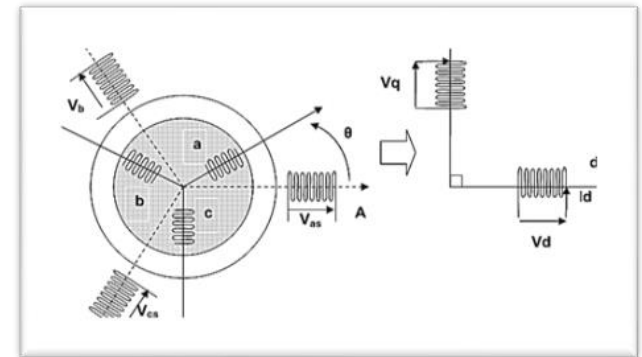


Fig. 2. Asynchronous machine Park model

The change of variables relating to currents, voltages and fluxes is given by the transformation:

$$\begin{bmatrix} X_d \\ X_q \\ X_0 \end{bmatrix} = P(\theta) \begin{bmatrix} X_a \\ X_b \\ X_c \end{bmatrix}, \begin{bmatrix} X_a \\ X_b \\ X_c \end{bmatrix} = P(\theta)^{-1} \begin{bmatrix} X_d \\ X_q \\ X_0 \end{bmatrix}$$

With  $[X]$  is tension, courant or flux and the matrixes  $P(\theta)$  and  $P(\theta)^{-1}$  are given as follows:

$$P(\theta) = \sqrt{\frac{2}{3}} \begin{bmatrix} \cos(\theta) & \cos\left(\theta - \frac{2\pi}{3}\right) & \cos\left(\theta + \frac{2\pi}{3}\right) \\ -\sin(\theta) & -\sin\left(\theta - \frac{2\pi}{3}\right) & -\sin\left(\theta + \frac{2\pi}{3}\right) \\ \sqrt{\frac{1}{2}} & \sqrt{\frac{1}{2}} & \sqrt{\frac{1}{2}} \end{bmatrix}$$

$$P(\theta)^{-1} = \begin{bmatrix} \cos(\theta) & -\sin(\theta) & \sqrt{\frac{1}{2}} \\ \sqrt{\frac{2}{3}} \cos\left(\theta - \frac{2\pi}{3}\right) & -\sin\left(\theta - \frac{2\pi}{3}\right) & \sqrt{\frac{1}{2}} \\ \sqrt{\frac{2}{3}} \cos\left(\theta + \frac{2\pi}{3}\right) & -\sin\left(\theta + \frac{2\pi}{3}\right) & \sqrt{\frac{1}{2}} \end{bmatrix}$$

Where  $\theta$  is the electrical angle between the stator phase 'A' and the rotor phase 'a'.

The application of the Park transform gives rise to the equations:

$$\begin{aligned} \begin{bmatrix} V_{ds} \\ V_{qs} \end{bmatrix} &= \begin{bmatrix} R_s & 0 \\ 0 & R_s \end{bmatrix} \begin{bmatrix} I_{ds} \\ I_{qs} \end{bmatrix} + \frac{d}{dt} \begin{bmatrix} \Phi_{ds} \\ \Phi_{qs} \end{bmatrix} + \begin{bmatrix} 0 & -w_s \\ w_s & 0 \end{bmatrix} \begin{bmatrix} \Phi_{ds} \\ \Phi_{qs} \end{bmatrix} \\ \begin{bmatrix} V_{dr} \\ V_{qr} \end{bmatrix} &= \begin{bmatrix} R_r & 0 \\ 0 & R_r \end{bmatrix} \begin{bmatrix} I_{dr} \\ I_{qr} \end{bmatrix} + \frac{d}{dt} \begin{bmatrix} \Phi_{dr} \\ \Phi_{qr} \end{bmatrix} + \begin{bmatrix} 0 & -w_r \\ w_r & 0 \end{bmatrix} \begin{bmatrix} \Phi_{dr} \\ \Phi_{qr} \end{bmatrix} \\ \begin{bmatrix} \Phi_{ds} \\ \Phi_{qs} \end{bmatrix} &= \begin{bmatrix} L_s & 0 \\ 0 & L_s \end{bmatrix} \begin{bmatrix} I_{ds} \\ I_{qs} \end{bmatrix} + \begin{bmatrix} M & 0 \\ 0 & M \end{bmatrix} \begin{bmatrix} I_{dr} \\ I_{qr} \end{bmatrix} \\ \begin{bmatrix} \Phi_{dr} \\ \Phi_{qr} \end{bmatrix} &= \begin{bmatrix} L_r & 0 \\ 0 & L_r \end{bmatrix} \begin{bmatrix} I_{dr} \\ I_{qr} \end{bmatrix} + \begin{bmatrix} M & 0 \\ 0 & M \end{bmatrix} \begin{bmatrix} I_{ds} \\ I_{qs} \end{bmatrix} \end{aligned}$$

After calculations, writing in the matrix form, the electric and magnetic equations are given as follows:

$$\begin{bmatrix} V_{ds} \\ V_{qs} \\ 0 \\ 0 \end{bmatrix} = \begin{bmatrix} (R_s + L_s S) & -L_s \omega_s & MS & -M \omega_s \\ L_s \omega_s & (R_s + L_s S) & M \omega_s & MS \\ MS & -\omega_{gl} M & (R_s + L_s S) & -\omega_{gl} L_r \\ \omega_{gl} M & MS & \omega_{gl} L_r & (R_r + L_r S) \end{bmatrix} \begin{bmatrix} I_{ds} \\ I_{qs} \\ I_{dr} \\ I_{qr} \end{bmatrix}$$

The courant equations are given:

$$\begin{aligned} I_{ds} &= \frac{L_r}{L_s L_r - M^2} \Phi_{ds} - \frac{M}{L_s L_r - M^2} \Phi_{dr} \\ I_{qs} &= \frac{L_r}{L_s L_r - M^2} \Phi_{qs} - \frac{M}{L_s L_r - M^2} \Phi_{qr} \\ I_{dr} &= \frac{L_s}{L_s L_r - M^2} \Phi_{dr} - \frac{M}{L_s L_r - M^2} \Phi_{ds} \\ I_{qr} &= \frac{L_s}{L_s L_r - M^2} \Phi_{qr} - \frac{M}{L_s L_r - M^2} \Phi_{qs} \end{aligned}$$

The determination of the instantaneous electromagnetic torque in a machine can be carried out in two ways: by an instantaneous power balance or by the so-called "virtual work" method.

We will use the first method. The instantaneous electrical power supplied to the stator and rotor windings as a function of the axis sizes d,q is given by the following expression:

$$P_e = V_{ds} I_{ds} + V_{qs} I_{qs} + V_{dr} I_{dr} + V_{qr} I_{qr}$$

However, the electromechanical power is related to the electromagnetic torque by the following expression:

$$C_e = \frac{P_{em}}{\Omega} = p \cdot \frac{P_{em}}{\omega}$$

However, the electromechanical power is related to the electromagnetic torque by the following expression:

$$C_e = p \frac{M}{L_r} (\Phi_{dr} I_{qs} - \Phi_{qr} I_{ds})$$

It can be seen that the electromagnetic torque equation is not linear, due to the cross product of the current and flux components (coupling).

The principle of vector control (Fig. 3) is to have an operation similar to that of a DC motor with independent excitation, where there is a natural decoupling process between the quantity controlling the flux (the excitation current) and that linked to the torque (the armature current). This decoupling makes it possible to obtain a very fast torque response.

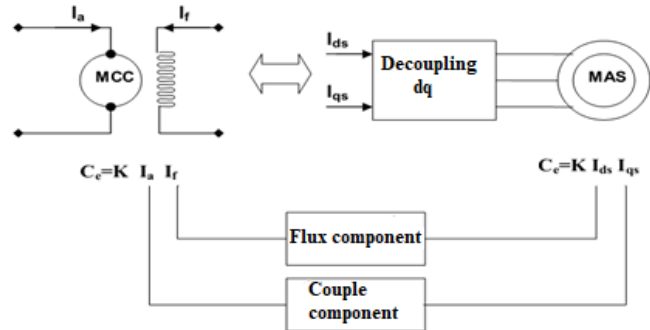


Fig. 3. Diagram of the decoupling principle for AM by analogy with MCC

Several strategies are possible such as:

1. Orientation of the stator flux:  $\Phi_{ds} = \Phi_s$  and  $\Phi_{qs} = 0$
2. Orientation of the rotor:  $\Phi_{dr} = \Phi_r$  and  $\Phi_{qr} = 0$
3. Orientation of the air gap:  $\Phi_{de} = \Phi_e$  and  $\Phi_{qe} = 0$

We will limit ourselves to exposing the command with oriented rotor flux ( $\Phi_{dr} = \Phi_r$  and  $\Phi_{qr} = 0$ ) (Fig. 4), whose principle is to cancel the flux  $\Phi_{qr}$ ; it is based on:

- Maintaining the flux  $\Phi_{dr}$  constant and aligned on the axis d of the reference d - q by action on current  $I_{ds}$ .
- Electromagnetic torque control by action on the current  $I_{qs}$ .

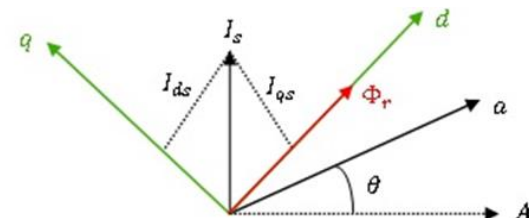


Fig. 4. Command with oriented rotor flux

$$\text{The torque is given then by } C_e = P \frac{M}{L_r} (\Phi_{dr} I_{qs})$$

The equations of tensions on the reference (d,q) are given as follows:

$$V_{ds} = R_s I_{ds} + L_s \frac{dI_{ds}}{dt} - \omega_s L_s I_{qs} + M \frac{dI_{dr}}{dt} - \omega_s M I_{qr}$$

$$V_{qs} = R_s I_{qs} + L_s \frac{dI_{qs}}{dt} - \omega_s L_s I_{ds} + M \frac{dI_{qr}}{dt} + \omega_s M I_{dr}$$

$$0 = M \frac{dI_{ds}}{dt} - (\omega_s - \omega_m) M I_{qs} + L_r \frac{dI_{dr}}{dt} + R_r I_{dr} - (\omega_s - \omega_m) L_r I_{qr}$$

$$0 = M \frac{dI_{qs}}{dt} - (\omega_s - \omega_m) M I_{ds} + L_r \frac{dI_{qr}}{dt} + R_r I_{qr} + (\omega_s - \omega_m) L_r I_{dr}$$

$$\text{With } \omega_s = \omega_m + \frac{M R_r}{L_r \Phi_{rd}} I_{qs}$$

The rotor current equations are given:

$$V_{ds} = R_s I_{ds} + \sigma L_s \frac{dI_{ds}}{dt} + \frac{M}{L_r} \frac{\Phi_{dr}}{dt} - \omega_s \sigma L_s I_{qs}$$

$$V_{qs} = R_s I_{qs} + \sigma L_s \frac{dI_{qs}}{dt} + \omega_s \frac{M}{L_r} \Phi_{dr} + \omega_s \sigma L_s I_{ds}$$

$$MI_{ds} = \Phi_{dr} + \frac{L_r}{R_r} \frac{d\Phi_{dr}}{dt}$$

The classical PID diagram is given in Fig.5.

The PID parameters, according to Fig.5, are given as follows

$$K_d = P \cdot \frac{M}{L_r}, \Omega_r, K_p = \frac{2 \cdot \varepsilon \cdot \omega_n \cdot J + F}{K_e}, K_i = \frac{\omega_n^2 \cdot J}{K_p \cdot K_e}$$

$K_p = 9.25, K_d = 0$  and  $K_i = 6.25$  ( $\omega_n = 16 \text{ rad/s}$  : proper pulsation,  $\varepsilon = 0.7$ : damping factor).

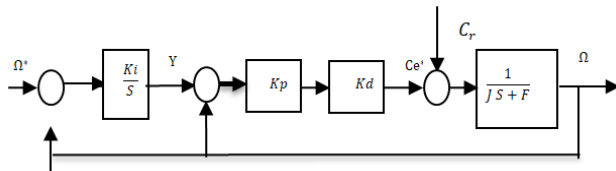


Fig. 5. PID control topology

## 5. FUZZY LOGIC CONTROL DESIGN

The fuzzy logic regulator (FLR) takes its place in the control chain as shown in (Fig. 6).

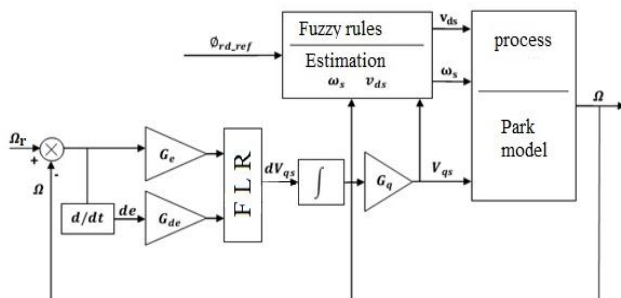


Fig. 6. Fuzzy-logic control design

Input variables are mostly error 'e' and the change-of-error 'de' regardless of complexity of controlled plants. Alternatively, the change of control input is used as its output variable. The parameters of the motor are calculated: the rotor time constant ( $T_r = 0.0720 \text{ s}$ ) and the Blondel dispersion coefficient ( $\sigma = 0.1134$ ). Fig. 7 provides the fuzzy regulator chain.

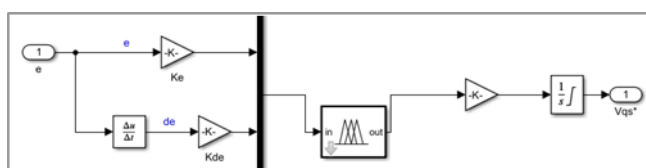


Fig. 7. The fuzzy regulator

A table of fuzzy rules (Table I) is then constructed on a two-dimensional (2-D) space. The output is calibrated to allow it to vary in the domain accepted by the system. For reasons of simplification during the simulation, we adopt as membership functions, those having the triangular form distributed in a uniform and equi-

distant manner with symmetrical forms. The interval of interest for each input variable, namely the error e and the variation in the error, is subdivided into three classes (subsets). Regarding the variation of the order, it is subdivided into seven classes as well. Each of these classes is associated with a membership function. The distribution of membership functions in their respective universes of discourse is given in Fig. 8, Fig. 9, and Fig. 10. The adjustment strategy mainly depends on the inferences adopted. The fuzzy input-based inference engine uses the "If...Then" property of rules in the knowledge base to make decisions.

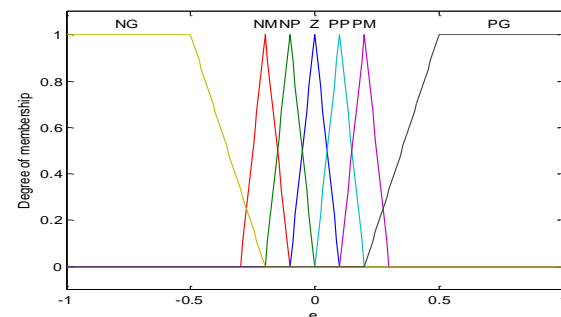


Fig. 8. Input 'e' membership functions

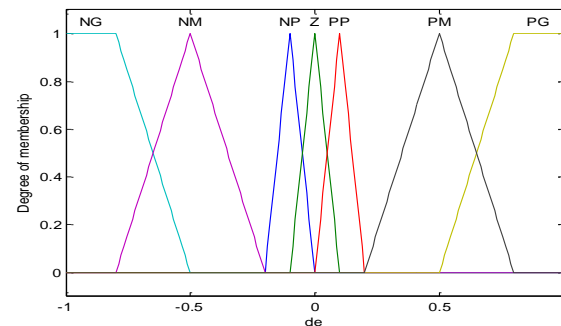


Fig. 9. Input 'de' membership functions

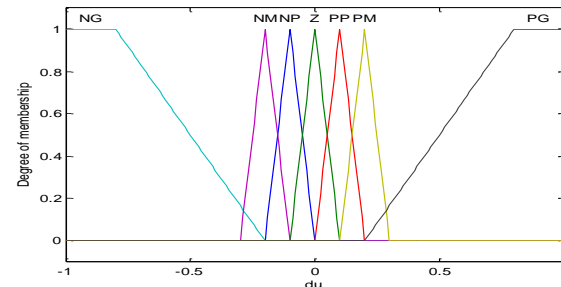


Fig. 10. Output 'du' membership functions

Tab. 1. Table of fuzzy control rules

e \ de	NG	NM	NP	Z	PP	PM	PG
NG	NG	NG	NG	NG	NG	NG	Z
NM	NG	NG	NM	NP	NP	Z	PG
NP	NM	NM	NP	NP	Z	PP	PP
Z	NG	NG	NP	Z	PP	PG	PG
PP	NP	NP	Z	PP	PP	PM	PM
PM	NP	Z	PP	PP	PM	PM	PG
PG	Z	PP	PP	PM	PM	PG	PG

In our case, the inferences specify how the linguistic value of the variable of the command  $du$  is calculated according to the linguistic values of  $e$  and  $de$ . Given the advantages it offers, MAMDANI's Max-Min inference method is chosen in our application. The decision rules consist of situation/action pairs of the form:

If  $e$  is  $A$  AND  $de$  is  $B$ , then  $du$  is  $C$ .

This set of rules should regroup all the possible situations of the system evaluated for the different values assigned to  $e$  and  $de$  and all the corresponding values of  $du$ .

The decision table that we have chosen in our work is the famous MAC VICAR-WHELAN rule base (Table I) with inputs ( $e$ : error,  $de$ : derivative of error) and the output ( $du$ ).

This rule base is organized in the form of a symmetrical diagonal inference table; it can be deduced for example according to a temporal analysis which consists in comparing the response of the system to the instruction according to the objectives fixed in closed loop.

( $e = \Omega_r - \Omega$ ) with ( $\Omega_r$  : reference speed) is the derivative of the error and sometimes of the integral of the error. The output "du" of the regulator can be the torque variation ( $dCe$ ), either the variation of the current ( $dlqs$ ) or the variation of the voltage ( $dVqs$ ).

(FLR parameters are  $Gq=3000$ ;  $Ke=1/12$  and  $Kde=1/600$ ). Defuzzification is the last stage of the regulator; it converts the linguistic value of  $du$  (variation of the action) into a numerical value. Our choice fell on the method of defuzzification of the center of gravity for its simplicity and its performance.

## 6. APPLICATION

The characteristics of the asynchronous machine are shown in Tab. 2- 5.

**Tab. 2.** Mechanical parameters

Nominal power	$P_n = 1500$	$W$
Synchronism speed	$N = 1420$	$tr / min$
Rated load torque	$C_r = 10$	$N.m$
Tension	$V = 220/380$	$V$
Nominal current	$I = 6.31/3.64$	$A$
Synchronism frequency	$f_s = 50$	$Hz$
Yield	$\eta = 0.78$	%
Flux	$\Phi = 0.7$	$Wb$

**Tab. 3.** Controller settings

$K_e = 1 / 150$	$Kp = 9.25$
$K_{de} = 1 / 1500$	$Ki = 6.25$
$G_q = 300000$	

**Tab. 4.** Machine electrical characteristics

Stator resistance	$R_s = 4.85$	$\Omega$
Rotor resistance	$R_r = 3.805$	$\Omega$
Stator duty cycle inductance	$L_s = 0.274$	$H$
Rotor cyclic inductance	$L_r = 0.274$	$H$
Mutual cyclic inductance	$M = 0.258$	$H$
Rotor time constant.	$T_r = L_r / R_r$	
Blondel dispersion coefficient	$\sigma = 1 - (M^2 / L_s L_r)$	

**Tab. 5.** Nominal parameters

Moment of inertia	$J = 0.031$	$Kg.m^2$
Friction coefficient	$F = 0.0081$	$N.m.s / rad$

## 7. RESULTS AND DISCUSSION

Vector control has been applied to the asynchronous machine. The figures Fig.11, Fig.12, Fig.13 and Fig.14 give graphs of the response of each parameter (Fluxdr, Fluxqr, stator current component  $lqs$  and stator current) of the motor at no load.

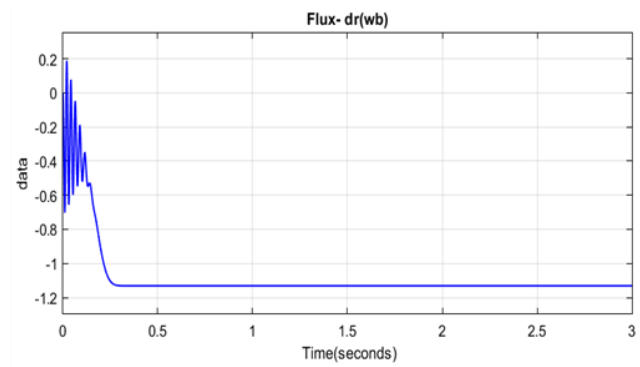


Fig. 11. Flux-dr response at no load

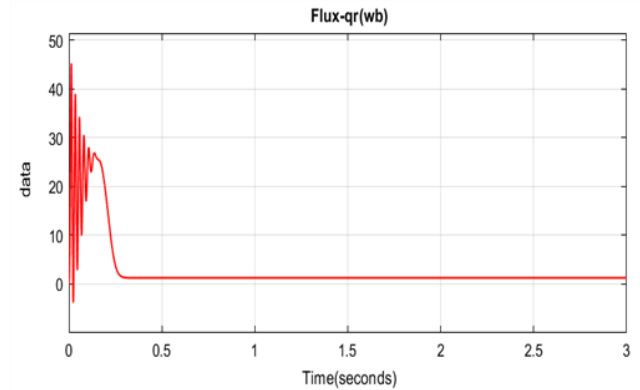


Fig. 12. Flux-qr response at no load

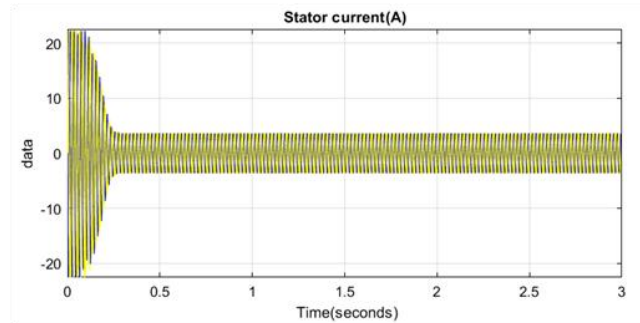


Fig. 13. Stator current response at no load

The responses of the IM model, for a reference speed of 150 rad/s, are given below.

The curves in figures (Fig. 15-19) detail separately the evolution of the characteristics of the MAS in load of 10 N.m applied

from 0.75 for 1s. The results show that when the motor is acted upon by resistive torque  $Cr = 10N \cdot m$ , the velocity exceeds the reference value and then decreases to 148 rad/s (Fig. 15).

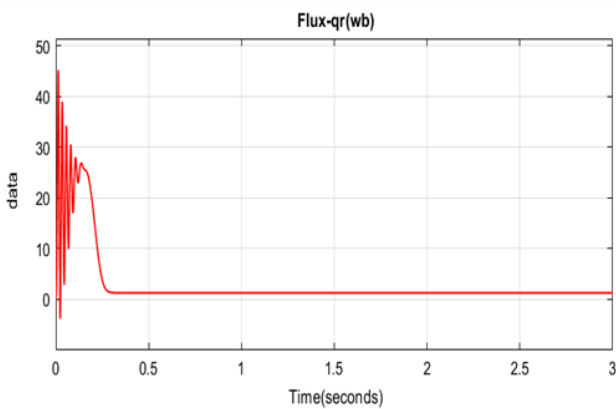


Fig. 14. Stator current component  $I_{qs}$  response at no load

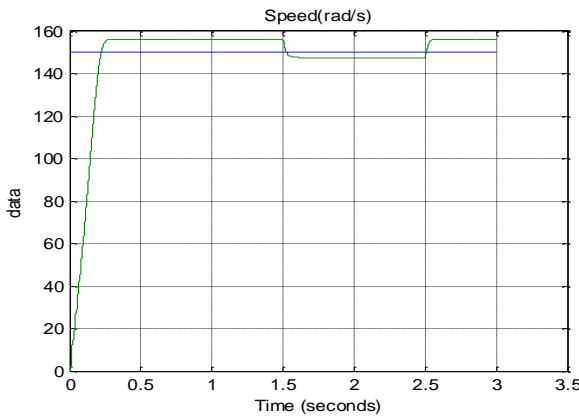


Fig. 15. Velocity response

The stator current increases to its nominal value and the stator current (Fig. 16) following axis  $I_{qs}$  decreases and stabilizes at -5.2 A.

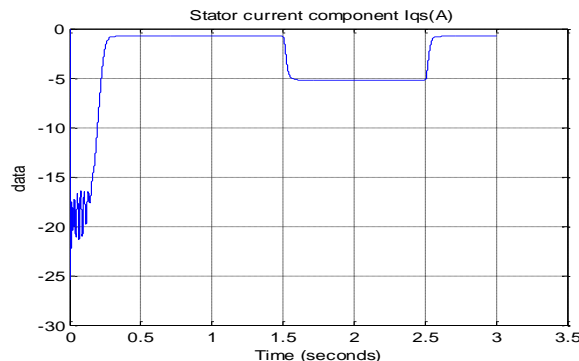


Fig. 16. Stator current component  $I_{qs}$  response

The torque (Fig. 17) also increases until it reaches the value to drive the load and the rotor fluxes (Fig. 18) and (Fig. 19) increase and stabilize, respectively, at -0.15 Wb and 0.1 Wb.

Regarding to the PID controller and taking in account the AM characteristics, the parameters considered are  $K_p=9.25$ ,  $K_d=0$  and  $K_i=6.25$ . The fuzzy responses of the regulator are compared

with those given by the PID regulator. The results are shown in the figures below.

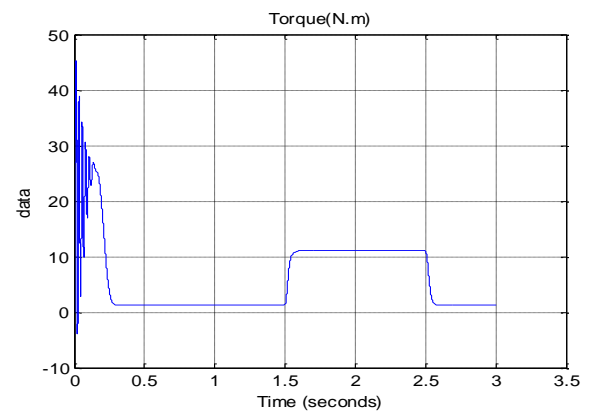


Fig. 17. Torque response

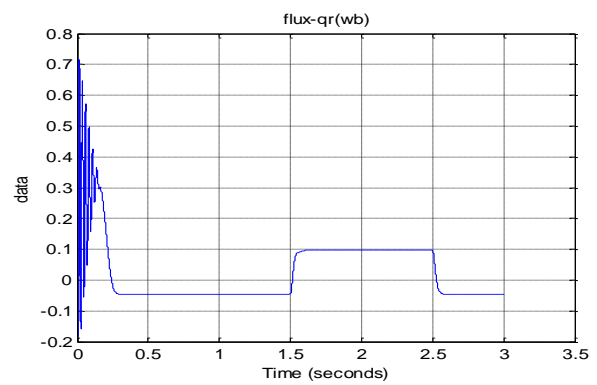


Fig. 18. Flux-qr response

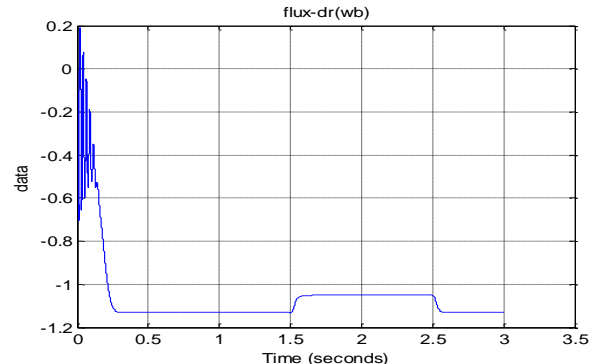
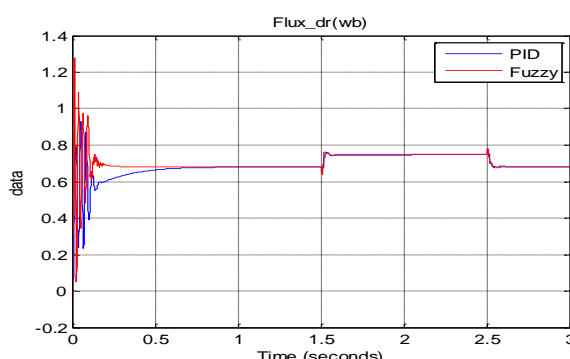
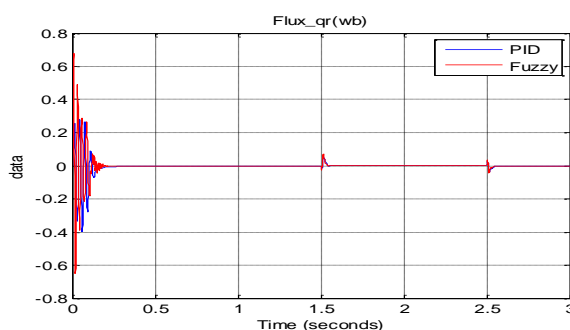
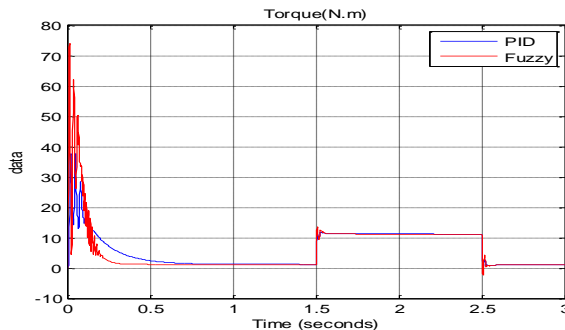


Fig. 19. Flux-dr response

The torque oscillation (Fig. 20) reaches the maximum value of the order of 4.5 times the nominal torque (rises to more than 45.27 N · m).

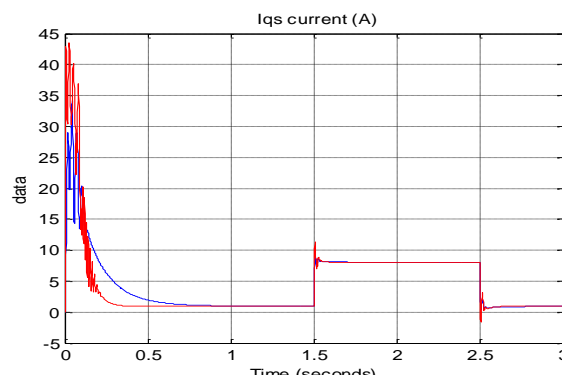
This is due to noises generated by mechanical parts. After the disappearance of the transient regime which lasts 0.16s, the torque decreases almost linearly from 26.9 N · m and tends towards zero.

The minimum value is 0.314 N · m; it is due to friction. These results show that the two types of control demonstrate good performance for Flux $q_r$  (Fig. 21) and Flux $dr$  (Fig. 22) and stator current component  $I_{qs}$  (Fig. 22).



We find almost the same situation with the only difference in response time of speed; the response time of the PI controller is always the same under all conditions, but that of the fuzzy controller depends on the set point.

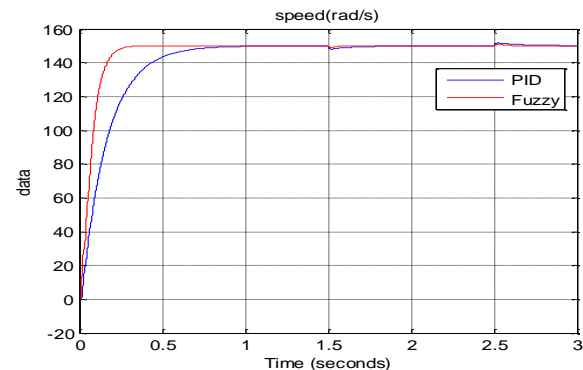
In transient mode, mains supply shows a high current demand of 27.06 A (Fig. 23). After its disappearance, the steady state is reached.



During start-up and in the transient state, the rotational speed increases and evolves with a rise time of 0.2 s, at  $t = 0.3$  s (start of the steady state); it stabilizes at a value close to the set point velocity (156.7 rad/s) (Fig. 24).

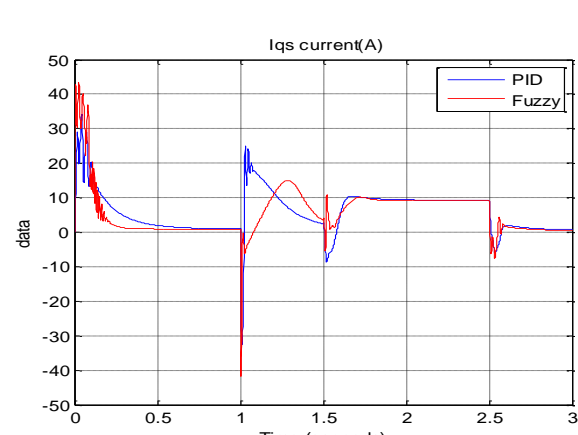
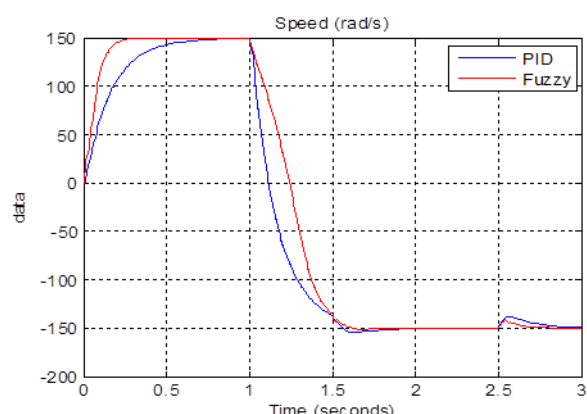
We observe a perfect continuation of the reference velocity, an insensitivity and rapid rejection of the load (0.88%).

Let us now consider the case where the motor is in the final position and an unknown load at some frequency is applied to the motor shaft.



An inversion of the reference rotational speed (Fig. 25) occurs after 1 s and a load of 10 N·m at 2 s from the start.

The output (Fig. 26) has a good follow-up of the set point; the current  $I_{qs}$  does not have an overshoot during this inversion.



This difference is due to the fact that the response time of the PI regulator is determined by its design ; it always manages on its first rise to catch up with 95% of its reference value within the regulation time ; if this time is fast compared with the machine, we notice an overshoot.

The fuzzy controller, on the other hand, finds a different response time each time because this time is not determined in its design, and overshoot is always acceptable.

Therefore, these results show that the two types of control give good performance ; we find almost the same with the only difference in terms of the speed response time; the response time of the PI regulator is always the same under all conditions ; on the other hand, that of the fuzzy regulator depends on the set point value ; the closer this value is to the initial value, the faster the response.

The control strategy with the fuzzy logic has been applied to the AM, and the results of simulation have proved the efficiency of control of the system whose required performance indicators were fully met, namely:

- An appreciable rise time.
- A negligible excess.
- A good pursuit of the set-point.
- Rejection of the disturbance.
- The speed of reversal of the direction of rotation.

The fuzzy control greatly improves the behavior and the efficiency of the vector control and thus allows obtaining a high-performance variable speed drive which is justified by the results obtained by comparing the vector control with conventional PI regulators and by fuzzy logic controllers. The fuzzy controller improves the robustness of the vector control; the simulations show that the errors converge towards negligible static values which give good control results.

The results of this approach based on field-oriented control and fuzzy logic regulator are very conclusive as long as they do not differ too much from the results already seen with the same regulator in the event that the engine parameters do not vary. However, we see a slightly higher response time.

## 8. CONCLUSION

The PID control often displays low performance. Overshoot and rise times are tightly coupled, making gain adjustments difficult. In this article, we have presented the results obtained by applying the fuzzy control, which considerably improves the behavior and the efficiency of the vector control.

Fuzzy logic extended vector control provides a diagnostic approach to significantly decouple overshoot and rise time, allowing for easy setup and very high load rejection characteristics.

The presented study improves the transient response time and the precision of the servo system. An inversion of the reference rotational speed is considered, and the results are very consistent.

Considering these results, we find a perfect tracking reference speed, insensitivity, and rapid rejection of loads, as well as a decoupling of the d-q axes which is not influenced by the regime applied to the machine.

The fuzzy control improves the behavior and efficiency of the vector control and thus makes it possible to obtain a variable speed drive that is more stable and robust to faults.

Analysis of variations in machine parameters such as electromagnetic torque, stator and rotor currents in the Park's mark is

used to detect the presence of defects.

The control developed adapts to the sudden change in behavior such as a speed reversal.

Time will show whether these theoretical concepts represent a sufficient degree of improvement over the existing techniques to enter the domain of commercial drives.

However, and through this study, it appears that the major shortcoming of fuzzy logic control is that it depends on human expertise. The rules of a fuzzy logic control system must be regularly updated.

As, perspectives, the artificial neuronal networks (ANNs) can be combined with fuzzy logic to improve the control, extending the IM driver life, and achieving proper motor operation and performance is significant. In this case, artificial intelligence (AI) is a helpful tool to match the motor parameter values and the data needed by the controller.

## REFERENCES

1. Trzynadlowski AM. Control of Induction Motors. Academic Press. 2001; ISBN 9780127015101; Nevada. <https://doi.org/10.1016/B978-012701510-1/50000-3>
2. PREMKUMAR K, THAMIZHSELVAN T, PRIY M, Vishnu et al. Fuzzy anti-windup pid controlled induction motor. International Journal of Engineering and Advanced Technology. 2019; 9(1): 184-189.
3. Korbut M, Szpica D. A Review of Compressed Air Engine in the Vehicle Propulsion System. Acta Mechanica et Automatica. 2021;15(4): 215-226. <https://doi.org/10.2478/ama-2021-0028>
4. [https://www.researchgate.net/profile/Drkmkumar/publication/337285022\\_Fuzzy\\_Anti-indup\\_PID\\_Controlled\\_Induction\\_Motor/](https://www.researchgate.net/profile/Drkmkumar/publication/337285022_Fuzzy_Anti-indup_PID_Controlled_Induction_Motor/)
5. Mehidi IM, SAAD N, MAGZOUB M and al. Simulation analysis and experimental evaluation of improved field-oriented controlled induction motors incorporating intelligent controllers. IEEE Access. 2022;10: 18380-18394 Design and Simulation of Neuro-Fuzzy Controller for Indirect Vector-Controlled Induction Motor Drive SpringerLink.
6. Roose A, Yahya S, and Al-Rizzo H Fuzzy-logic control of an inverted pendulum on a cart. Computers & Electrical Engineering, Elsevier. 2017.
7. Badr B, Eltamaly A M, and Alolah. Fuzzy controller for three phases induction motor drives. IEEE Vehicle Power and Propulsion Conference, Sept. 2010. <https://doi.org/10.1109/VPPC.2010.5729080>
8. Achbi M, Kehida S, Mhamd Lan and Hedi D A Neural-Fuzzy Approach for Fault Diagnosis of Hybrid Dynamical Systems: Demonstration on Three-Tank System" Acta Mechanica et Automatica. 2021; 15 (1): 1-8. <https://doi.org/10.2478/ama-2021-0001>
9. Khan F, Sulaimanandani and Ahmad Z Review of Switched Flux Wound-Field Machines Technology. IETE Technical Review, 2016.
10. Zerdali E, Met A, Barkak A and Erkan M Computationally efficient predictive torque control strategies without weighting factors Turkish Journal of Electrical Engineering and Computer Sciences.2022; 30 (6). <https://doi.org/10.55730/1300-0632.3955>
11. Ananthamoorthy N and Baskaran K. Velocity and torque control of permanent magnet synchronous motor using hybrid fuzzy proportional plus integral controller. Journal of Vibration and Control, SAGE Publications. 2013; 20-29.
12. Aissaoui A, Abid M. A fuzzy logic controller for synchronous machine. Journal of Electrical Engineering. 2007; 285-290.
13. Bharathi Y and. al., "Multi-input fuzzy logic controller for brushless DC motor drives", Defence Science Journal. 2008; 58 (1): 147-158. <https://doi.org/10.14429/dsj.58.1632>
14. Faiz J, Manoochehri M, Shahgholia G. Performance improvement of a linear permanent magnet synchronous drive using fuzzy logic controller. Proceedings of IEEE International Conference on Power System Technology, Oct. 2010. <https://doi.org/10.1109/POWERCON.2010.5666041>

15. Soundarajan A, Sumathi A. Fuzzy based intelligent controller for power generating stations. *Journal of Vibration and Control*. 2011; 17(2): 214–227. <https://doi.org/10.1177/1077546310371347>
16. Ozturk N. Celik Educational Tool for the Genetic Algorithm-Based Fuzzy Logic Controller of a Permanent Magnet Synchronous Motor Drive. *International Journal of Electrical Engineering Education*. SAGE Publications. 2014. <https://doi.org/10.7227/IJEEE.51.3.4>
17. Bharathi Y and al. Multi-input fuzzy logic controller for brushless DC motor drives. *Defence Science Journal*. 2008; 58 (1): 147–158. <https://doi.org/10.14429/dsj.58.1632>
18. Ruiz J, Espinosa A, Romeral L. An introduction to fault diagnosis of permanent magnet synchronous machines in master's degree courses. *Comput. Appl. Eng. Educ.* 2010; published online.
19. Siavashi E, Pahlavanhoseini R, Pejmanfar A. Using Clonal Selection Algorithm to optimize the Induction Motor Performance. *Canadian Journal on Electrical and Electronics Engineering*. 2011; 2 (9).
20. Zidani F, Nait Said R. Direct Torque Control of Induction Motor with Fuzzy Minimization Torque Ripple. *Journal of Electrical Engineering*. 2005; 56 (7–8): 183–188.
21. Ameur F. Application of Fuzzy Logic for a Ripple Reduction Strategy in DTC Scheme of a PWM Inverter fed Induction Motor Drives. *Journal of Electrical Systems*. 2009; 1: 13–17.
22. Gadoue S, Giaouris D and Finch J. Artificial intelligence-based speed control of DTC induction motor drives: A comparative study. *Electric Power Systems Research*. 2009; 79 (1): 210–219. <https://doi.org/10.1016/j.epsr.2008.05.024>
23. Liu S, Wang M, Chen Y and Li. SA Novel Fuzzy Direct Torque Control System for Three-level Inverter-fed Induction Machine. *International Journal of Automation and Computing*. 2020; 7 (1): 78–85. <https://doi.org/10.1007/s11633-010-0078-7>
24. Pasamontes M and al. Learning switching control: A tank level-control exercise." *IEEE Trans. Educ.* 2012; 55 (2): 226–232. <https://doi.org/10.1109/TE.2011.2162239>
25. Guven U, Sonmez Y and Birolgul SA. Computer based educational tool for fuzzy logic-controlled DC-DC converters. *J. Polyt.* 2007; 10: 339–346.

Noura Rezika H. Bellahsene:  <https://orcid.org/0000-0002-6644-9930>



This work is licensed under the Creative Commons BY-NC-ND 4.0 license.

# ANALYSIS OF FRACTIONAL ELECTRICAL CIRCUIT CONTAINING TWO RC LADDER ELEMENTS OF DIFFERENT FRACTIONAL ORDERS

Ewa PIOTROWSKA\*<sup>✉</sup>, Rafał MELNIK\*<sup>✉</sup>

\*Faculty of Computer Science and Technology, Department of Automation and Robotics,  
University of Lomza, Akademicka 1, 18-400 Łomża, Poland

[epiotrowska@al.edu.pl](mailto:epiotrowska@al.edu.pl), [rmelnik@al.edu.pl](mailto:rmelnik@al.edu.pl)

received 20 April 2023, revised 12 June 2023, accepted 7 July 2023

**Abstract:** The study addresses the topic of different fractional orders in the context of simulation as well as experiments using real electrical elements of fractional-order circuit. In studying the two solutions of the resistance-capacitance (RC) ladder circuit of appropriate parameters, different fractional orders of the electrical circuit are considered. Two fractional-order (non-integer) elements were designed based on the Continued Fraction Expansion (CFE) approximation method. The CFE method itself was modified to allow free choice of centre pulsation. It was also proposed that when making individual ladder circuits, in the absence of elements with the parameters specified by the program, they should be obtained by connecting commercially available elements in series or parallel. Finally, the theoretical analysis of such a circuit is presented using state-space method and verified experimentally.

**Key words:** fractional-order circuit, RC ladder, Continued Fraction Expansion

## 1. INTRODUCTION

Fractional calculus is a generalisation of classical calculus where the order can be a real or complex number. For integer orders, classical derivative is obtained. Fractional calculus has been gaining significant interest in the field of dynamical systems due to its potential for the development of mathematical models that reflect various phenomena, in the field of science and engineering [6], with higher fidelity than the models based on classical differential calculus. Moreover, its vital feature is the capability to describe the memory effect in the system [8]. For instance, the improved models of the RC, RL and RLC electrical circuits as well as supercapacitors and batteries have been successfully developed using fractional calculus [6, 9, 21].

The RC ladder network is a form of realisation of elements described as a fractional derivative, which can be used for modeling, e.g. supercapacitors or transmission lines [8, 14]. The ladder circuit is characterised by an electrical circuit configured based on series and parallel connections. Unlike supercapacitors, ladder elements have a fixed pseudocapacitance and the order of derivative has no nonlinear effects. The theory predicts that a ladder system can behave in a way that is analogous to the behaviour of fractional-order elements only if it has infinitely many components. In practice, this number is finite, which is associated with a limited use of this system as an element of the fractional order. The main problem in using a ladder circuit is the equivalent resistance, which can be derived by successively applying the series and parallel reduction formulae using the appropriate approximation. For this reason, the choice of resistance and capacitance is important. In addition, the designed ladder network should behave with the greatest possible accuracy and in a wide frequency range as an element of a fractional derivative [14, 23, 24, 26].

An example is the paper by Petras et al. [16] that proposes a relatively simple way of selecting resistance and capacitance, requiring, however, the use of a large number of passive components. In order to achieve phase compatibility (over three decades), the authors built a ladder network consisting of up to 130 meshes. The method they propose is limited to an order of 0.5.

There are other, more sophisticated, methods of selecting parameters of components such as resistance and capacitance ladder circuit in order to obtain the desired frequency range in which the ladder acts with good accuracy as a fractional with a much smaller mesh. These methods are based on the approximation of the function ( $s$  to the power of  $\alpha$ ) by the ratios of polynomials of the same degree, which also allows the selection of the required order of the derivative [5, 19, 20, 23].

Although fractional calculus was first used in 1695 by Leibniz and L'Hospital, the theory and applications of fractional calculus developed greatly in the 19th and 20th centuries, and many authors gave different definitions of fraction derivatives and integrals. Subsequently, many general calculus solutions have been developed, for example, the Riemann-Liouville fractional derivative definition, the Grünwald-Letnikov derivative definition and the Caputo fractional derivative definition [2, 3, 4, 7, 15, 22, 25, 26].

The present study is one of the first to address the topic of different fractional orders in the context of simulation as well as experiments using real elements of fractional-order RC circuit. An attempt was made to implement RC ladder networks based on Continued Fraction Expansion (CFE) development using Caputo's fractional derivative definition. For the purpose of the project, an algorithm was developed to select the parameters of passive elements included in the ladder circuits acting as physical elements of incomplete orders. Two ladder circuits of fractional orders of 0.5 and 0.7 were made. Subsequently, an electrical circuit was assembled that included both incomplete-order elements and

resistors and then tested in the time and frequency domain. Theoretical predictions were compared with the experimental data.

## 2. MATHEMATICAL PRELIMINARIES

Definition 1. The Caputo derivative of the fractional order  $\alpha \in (0, 1)$  of differentiable function  $f(t)$  is defined by Eq. (1):

$$D_t^\alpha f(t) = \frac{1}{\Gamma(1-\alpha)} \int_0^t (t-\tau)^{-\alpha} \dot{f}(\tau) d\tau \quad (1)$$

where  $\Gamma(x)$  is the Euler gamma function.

The one-sided Laplace transform of the fractional operator (Eq. [1]) is given by the following expression (Eq. [2]):

$$L[D_t^\alpha f(t)] = s^\alpha F(s) - s^{\alpha-1} f(0) \quad (2)$$

where  $F(s) = L[f(t)]$ .

Let us consider a fractional electrical element in which the current  $i(t)$  and voltage  $u(t)$  relation is described by Eq. (3):

$$i(t) = C_\alpha D_t^\alpha u(t) \quad (3)$$

where  $C_\alpha$  is called a pseudocapacitance and  $0 < \alpha \leq 1$  is the order of the element.

The impedance in  $s$ -domain of this element is represented by Eq. (4):

$$Z(s) = \frac{U(s)}{I(s)} = \frac{1}{C_\alpha s^\alpha} \quad (4)$$

and the spectral impedance is given by Eq. (5):

$$Z(j\omega) = \frac{1}{C_\alpha j^\alpha \omega^\alpha} = \frac{1}{C_\alpha [\cos(\frac{\pi\alpha}{2}) + j \sin(\frac{\pi\alpha}{2})] \omega^\alpha} \quad (5)$$

Computing the magnitude of the spectral impedance (Eq. [5]) yields the following expression (Eq. [6]):

$$A(\omega) = |Z(j\omega)| = \frac{1}{C_\alpha \omega^\alpha} \quad (6)$$

and in the logarithmic scale, we obtain the following (Eq. [7]):

$$M(\omega) = 20 \log A(\omega) = -20\alpha \log \omega - 20 \log C_\alpha \quad (7)$$

while the phase shift has the following form (Eq. [8]):

$$\varphi(\omega) = \arg Z(j\omega) = -\frac{\pi}{2} \alpha \quad (8)$$

## 3. FRACTIONAL-ORDER ELECTRIC ELEMENT

There are many different methods reported in the literature for designing electrical components of a fractional order [1, 10, 11, 17, 18, 23]. They require the selection of a certain type of electrical circuit consisting of passive elements and determining the method of selecting their parameters. A commonly used approach is to choose a circuit in the form of a ladder network consisting of  $n$  capacitors and  $n+1$  resistors, as depicted in Fig. 1.

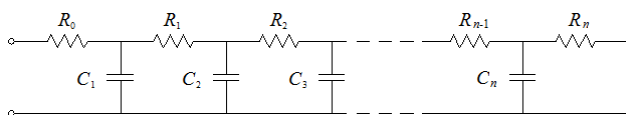


Fig. 1. Internal structure of the fractional-order element

The method of selecting parameters of an RC ladder model implementing the element described by a fractional derivative of the parameter  $\alpha$  is based on the development of the CFE [12, 13, 19, 23], as expressed by Eq. (9).

$$(1+x)^{-\alpha} = 1 - \frac{\alpha x}{1 + \frac{(1-\alpha)x}{2 + \frac{(2+\alpha)x}{3 + \frac{(2-\alpha)x}{2 + \frac{(3+\alpha)x}{5 + \frac{(3-\alpha)x}{2 + \frac{(4+\alpha)x}{7 + \frac{(4-\alpha)x}{2 + \dots}}}}}}}} \quad (9)$$

Due to the finite number of elements of the ladder network, amounting to  $2n + 1$ , the expansion of Eq. (9) should be finished at a certain step, allowing approximation of the  $n$ -th order of  $(1+x)^{-\alpha}$ , as presented in Eq. (10).

$$A_n^\alpha(x) = 1 - \frac{\alpha x}{1 + \frac{(1-\alpha)x}{2 + \frac{(n-1+\alpha)x}{2n-1 + \frac{(n+\alpha)x}{2 + \dots}}}} \quad (10)$$

Substituting  $x = \frac{s}{\omega_0} - 1$  within Eq. (10), where  $\omega_0$  is the centre frequency, yields the following function (Eq. [11]):

$$a_n^\alpha(s) = A_n^\alpha\left(\frac{s}{\omega_0} - 1\right) \quad (11)$$

while the approximating expression is:

$$(1+x)^{-\alpha} = \omega_0^\alpha s^{-\alpha} \quad (12)$$

This is a modification of the commonly used method that assumes  $\omega_0 = 1$  rad/s. The approximation of Eq. (11) is accurate when  $s = \omega_0$  is substituted, as indicated in Eq. (13):

$$a_n^\alpha(\omega_0) = A_n^\alpha\left(\frac{\omega_0}{\omega_0} - 1\right) = A_n^\alpha(0) = 1 \quad (13)$$

The simplification of the continued fraction (Eq. [11]) provides the rational function of the variable  $s$  (Eq. [14]):

$$a_n^\alpha(s) = \frac{l_n s^n + l_{n-1} s^{n-1} + \dots + l_1 s + l_0}{m_n s^n + m_{n-1} s^{n-1} + \dots + m_1 s + m_0} \quad (14)$$

Implementation of the fractional element with an impedance operator as in Eq. (3) is possible based on the approximation (Eq. [14]) that yields the following expression (Eq. [15]):

$$Z(s) = \frac{\omega_0^\alpha s^{-\alpha}}{C_\alpha \omega_0^\alpha} \approx K \frac{l_n s^n + l_{n-1} s^{n-1} + \dots + l_1 s + l_0}{m_n s^n + m_{n-1} s^{n-1} + \dots + m_1 s + m_0} \quad (15)$$

Constant  $K$  is as defined in Eq. (16):

$$K = \frac{1}{C_\alpha \omega_0^\alpha} \quad (16)$$

It is a scaling constant expressed in Ohms, allowing the selection of resistance and capacitance in such a way that the currents flowing into the electrical circuit have an appropriate order of magnitude.

The diagram of the RC ladder network depicted in Fig. 1 has an impedance operator that can be expressed in terms of the following (Eq. [17]):

$$Z_n(s) = R_0 + \frac{1}{C_1 s + \frac{1}{R_1 + \frac{1}{C_2 s + \frac{1}{R_2 + \dots + \frac{1}{C_n s + \frac{1}{R_n}}}}}} \quad (17)$$

The results that we obtain by developing a rational function  $Z_n(s)$  in a continued fraction with individual resistances  $R_k$  and capacitances  $C_k$  would be as in Eq. (17).

The above procedure makes it possible to design a ladder network of fractional order  $\alpha$  based on the scaling constant  $K$ , the center pulsation  $\omega_0$  and the number of capacitors  $n$ . The algorithm consists of the following steps:

1. Input of a set of ladder network parameters:
  - a. order of derivative  $\alpha$ ,
  - b. number of capacitors  $n$ ,
  - c. scaling constant  $K$ ,
  - d. centre pulsation  $\omega_0$ .
2. Calculation of coefficients  $l_k$  and  $m_k$  of polynomials being the numerator and denominator of the right side of Eq. (15).
3. Determination of the coefficients  $R_k$  and  $C_k$  of the expansion provided in Eq. (17), based on knowledge of  $l_k$  and  $m_k$  and the constant  $K$ .

#### 4. USING THE TEMPLATE RC LADDER MODEL BASED ON CFE DEVELOPMENT

The CFE method was used to design an RC ladder circuit according to the diagram in Fig. 1. Adoption of the assumed input parameters was as the following: order of the derivative  $\alpha_1 = 0.5$ , constant  $K_1 = 2087.67 \Omega$ , centre frequency  $f_0 = 100$  Hz and the number of meshes of the ladder network  $n = 30$ ; this allowed the procurement of parameters of the RC ladder network elements predicted by the program: resistance values of the resistors and capacitances values of the capacitors.

Due to the limited availability of the elements with the desired parameters on the market and discrepancies between the values declared by the manufacturer and the measured ones, the resulting resistances and capacitances provided by the program had to be obtained by building equivalent systems. In most cases, it was sufficient to select pairs of elements, which were then connected in series or parallel. To this end, the program was developed for selecting equivalent resistances and capacitances as well as an appropriate way of combining them – so as to obtain the value as close as possible to that anticipated by the program. This procedure allowed parameters to be selected with an error of less than 1%. Tabs. 1 and 2 summarise the parameters for the ladder network of  $\alpha_1 = 0.5$ . The second and third columns contain the measured values of resistive elements (Tab. 1) and capacitances (Tab. 2) used to build the ladder network. The fourth column shows connection of the elements. The fifth column contains the parameters of the equivalent systems, while the sixth column contains the parameters determined by the algorithm. The software used for the calculations (and plotting) was Wolfram Mathematica 9.0.

MLCC ceramic capacitors were used to build the ladder circuit model. Resistance and capacitance measurements were made with the LCR meter by HM8118 Rohde & Schwarz at 120 Hz.

Similar to the present method, a row RC ladder network of an order  $\alpha_2 = 0.7$  was designed. For the purpose of the algorithm, the following assumptions were made: scaling constant  $K_2 = 1010 \Omega$ , centre frequency  $f_0 = 100$  Hz and number of capacitors  $n = 30$ .

Tab. 1. Equivalent capacitances and their connection

No.	$C_a$	$C_b$	Connection	$C_{ab}$	$C$
1	34.08 nF	3.42 nF	Parallel	37.5 nF	37.5 nF
2	10.2 $\mu$ F	88.4 nF	Series	87.6 nF	87.6 nF
3	137 nF	1.43 nF	Parallel	138 nF	138 nF
4	99.4 nF	89.4 nF	Parallel	189 nF	189 nF
5	945 nF	322 nF	Series	240 nF	240 nF
6	225 nF	67.3 nF	Parallel	293 nF	293 nF
7	346 nF	-	None	346 nF	346 nF
8	337 nF	63.3 nF	Parallel	401 nF	401 nF
9	1.51 $\mu$ F	654 nF	Series	457 nF	457 nF
10	474 nF	40.6 nF	Parallel	514 nF	514 nF
11	348 nF	226 nF	Parallel	574 nF	574 nF
12	637 nF	-	None	637 nF	636 nF
13	661 nF	40.1 nF	Parallel	702 nF	702 nF
14	1.54 $\mu$ F	1.54 $\mu$ F	Series	770 nF	770 nF
15	633 nF	210 nF	Parallel	843 nF	842 $\mu$ F
16	10.1 $\mu$ F	1.01 $\mu$ F	Series	920 nF	919 nF
17	983 nF	19.3 nF	Parallel	1.00 $\mu$ F	1.00 $\mu$ F
18	675 nF	416 nF	Parallel	1.09 $\mu$ F	1.09 $\mu$ F
19	975 nF	212 nF	Parallel	1.19 $\mu$ F	1.19 $\mu$ F
20	663 nF	632 nF	Parallel	1.30 $\mu$ F	1.30 $\mu$ F
21	954 nF	458 nF	Parallel	1.41 $\mu$ F	1.42 $\mu$ F
22	1.50 $\mu$ F	46.7 nF	Parallel	1.55 $\mu$ F	1.55 $\mu$ F
23	1.02 $\mu$ F	685 nF	Parallel	1.71 $\mu$ F	1.71 $\mu$ F
24	1.55 $\mu$ F	348 nF	Parallel	1.89 $\mu$ F	1.89 $\mu$ F
25	1.49 $\mu$ F	629 nF	Parallel	2.12 $\mu$ F	2.12 $\mu$ F
26	1.49 $\mu$ F	909 nF	Parallel	2.40 $\mu$ F	2.40 $\mu$ F
27	719 nF	1.03 $\mu$ F	Parallel	2.78 $\mu$ F	2.78 $\mu$ F
28	10.6 $\mu$ F	4.88 $\mu$ F	Parallel	3.34 $\mu$ F	3.34 $\mu$ F
29	434 nF	2.28 $\mu$ F	Parallel	4.29 $\mu$ F	4.28 $\mu$ F
30	5.15 $\mu$ F	1.45 $\mu$ F	Parallel	6.60 $\mu$ F	6.59 $\mu$ F

Tab. 2. Equivalent resistances and their connection

No.	$R_a$	$R_b$	Connection	$R_{ab}$	$R$
0	739 $\Omega$	35.9 $\Omega$	Parallel	34.2 $\Omega$	34.2 $\Omega$
1	802 $\Omega$	218 $\Omega$	Parallel	171 $\Omega$	171 $\Omega$
2	5.07 k $\Omega$	329 $\Omega$	Parallel	309 $\Omega$	309 $\Omega$
3	2.35 k $\Omega$	553 $\Omega$	Parallel	447 $\Omega$	447 $\Omega$
4	555 $\Omega$	32.8 $\Omega$	Series	587 $\Omega$	588 $\Omega$
5	662 $\Omega$	67.2 $\Omega$	Series	730 $\Omega$	729 $\Omega$
6	612 $\Omega$	262 $\Omega$	Series	874 $\Omega$	874 $\Omega$
7	2.14 k $\Omega$	1.96 k $\Omega$	Parallel	1.02 k $\Omega$	1.02 k $\Omega$
8	272 k $\Omega$	1.18 k $\Omega$	Parallel	1.17 k $\Omega$	1.17 k $\Omega$
9	12.9 k $\Omega$	1.48 k $\Omega$	Parallel	1.33 k $\Omega$	1.33 k $\Omega$
10	9.80 k $\Omega$	1.76 k $\Omega$	Parallel	1.49 k $\Omega$	1.49 k $\Omega$
11	5.54 k $\Omega$	2.36 k $\Omega$	Parallel	1.66 k $\Omega$	1.66 k $\Omega$
12	4.19 k $\Omega$	3.26 k $\Omega$	Parallel	1.83 k $\Omega$	1.83 k $\Omega$
13	1.96 k $\Omega$	55.0 $\Omega$	Series	2.01 k $\Omega$	2.01 k $\Omega$
14	13.0 k $\Omega$	2.66 k $\Omega$	Parallel	2.21 k $\Omega$	2.21 k $\Omega$
15	2.36 k $\Omega$	50.4 $\Omega$	Series	2.41 k $\Omega$	2.41 k $\Omega$
16	8.05 k $\Omega$	3.90 k $\Omega$	Parallel	2.63 k $\Omega$	2.63 k $\Omega$
17	1.77 k $\Omega$	1.10 k $\Omega$	Series	2.86 k $\Omega$	2.86 k $\Omega$
18	2.92 k $\Omega$	195 $\Omega$	Series	3.12 k $\Omega$	3.12 k $\Omega$
19	17.7 k $\Omega$	4.21 k $\Omega$	Parallel	3.40 k $\Omega$	3.40 k $\Omega$
20	30.1 k $\Omega$	4.23 k $\Omega$	Parallel	3.71 k $\Omega$	3.71 k $\Omega$
21	3.84 k $\Omega$	215 $\Omega$	Series	4.06 k $\Omega$	4.05 k $\Omega$
22	38.5 k $\Omega$	5.04 k $\Omega$	Parallel	4.45 k $\Omega$	4.45 k $\Omega$
23	2.95 k $\Omega$	1.97 k $\Omega$	Series	4.92 k $\Omega$	4.92 k $\Omega$
24	240 k $\Omega$	5.60 k $\Omega$	Parallel	5.47 k $\Omega$	5.47 k $\Omega$
25	26.4 k $\Omega$	8.03 k $\Omega$	Parallel	6.16 k $\Omega$	6.16 k $\Omega$
26	6.82 k $\Omega$	235 $\Omega$	Series	7.05 k $\Omega$	7.05 k $\Omega$
27	55.4 k $\Omega$	9.76 k $\Omega$	Parallel	8.29 k $\Omega$	8.29 k $\Omega$
28	8.95 k $\Omega$	1.29 k $\Omega$	Series	10.2 k $\Omega$	10.2 k $\Omega$
29	29.89 k $\Omega$	26.4 k $\Omega$	Parallel	14.0 k $\Omega$	14.0 k $\Omega$
30	738 k $\Omega$	29.9 k $\Omega$	Parallel	28.7 k $\Omega$	28.7 k $\Omega$

## 5. FREQUENCY RESPONSE OF THE LADDER CIRCUIT MODEL

Due to the complexity of the ladder networks and the number of their elements, Bode plots of incomplete systems, spanning four decades (1–10 kHz), were investigated. Figs. 2 and 3 present the amplitude and phase characteristics for an RC ladder model of an order  $\alpha_1 = 0.5$  and pseudocapacitance  $C_{\alpha_1} = 19.1 \mu\text{F/s}^{0.5}$ .

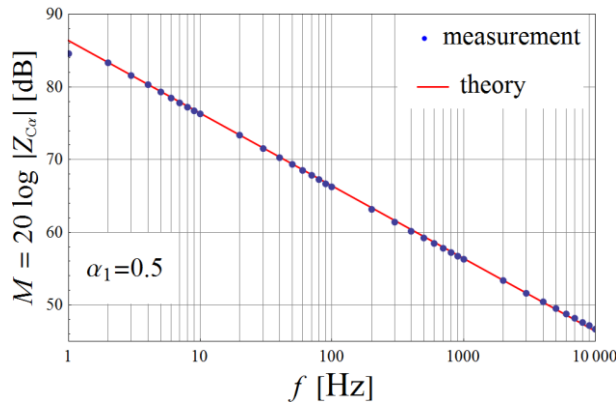


Fig. 2. Bode magnitude plot for the RC ladder circuit of an order  $\alpha_1 = 0.5$

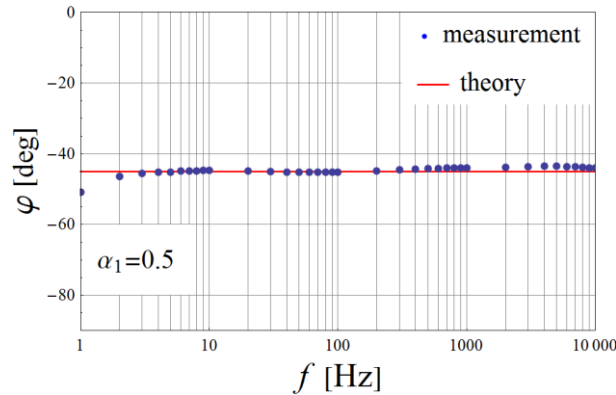


Fig. 3. Bode phase plot for the RC ladder circuit of an order  $\alpha_1 = 0.5$

In turn, Figs. 4 and 5 depict the frequency responses of the ladder network of an incomplete order  $\alpha_2 = 0.7$  and pseudocapacitance  $C_{\alpha_2} = 10.9 \mu\text{F/s}^{0.5}$ .

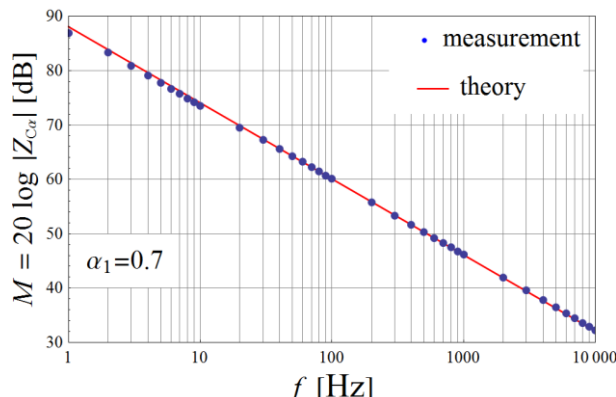


Fig. 4. Bode magnitude plot for the RC ladder circuit of an order  $\alpha_2 = 0.7$

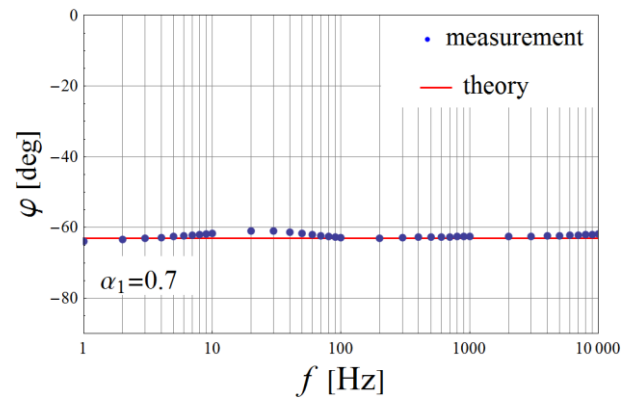


Fig. 5. Bode phase plot for the RC ladder circuit of an order  $\alpha_2 = 0.7$

The obtained phase characteristics for the RC ladder with an order of 0.5 deviate from the theoretical value ( $-45^\circ$ ) by no more than  $1.5^\circ$ . In contrast, the measured magnitude deviates from the theoretical line by less than 0.7%. The measured phase characteristic for the RC ladder of a fractional order of  $\alpha_2 = 0.7$  deviates from the theoretical value ( $-63^\circ$ ) by no more than  $2.2^\circ$ . The Bode magnitude plot for the system of  $\alpha_2$ , based on the measurement, is consistent with the theoretical response, differing less than 0.8%.

## 6. ELECTRICAL FRACTIONAL CIRCUIT

The diagram of the measuring system, shown in Fig. 6, consists of three external resistors  $R_1$ ,  $R_2$  and  $R_3$ , constant voltage source  $e$  and two elements of orders  $\alpha_1$  and  $\alpha_2$ .

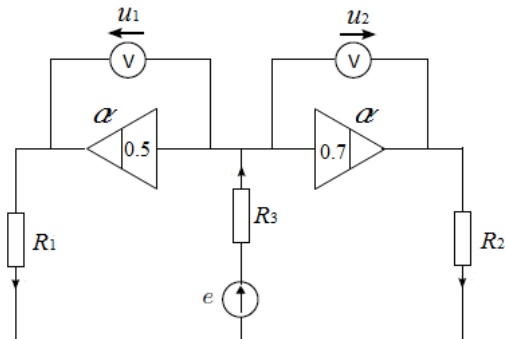


Fig. 6. Diagram of the RC electrical circuit

The dynamics of the voltages at the terminals of both ladder circuits are given by the state-space representation (Eq. [18]):

$$\begin{bmatrix} D_t^{\alpha_1} u_1(t) \\ D_t^{\alpha_2} u_2(t) \end{bmatrix} = \begin{bmatrix} a_{11} & a_{12} \\ a_{21} & a_{22} \end{bmatrix} \begin{bmatrix} u_1(t) \\ u_2(t) \end{bmatrix} + \begin{bmatrix} b_1 \\ b_2 \end{bmatrix} e(t) \quad (18)$$

where:

$$A = \begin{bmatrix} a_{11} & a_{12} \\ a_{21} & a_{22} \end{bmatrix} = \begin{bmatrix} -\frac{R_2+R_3}{R^2 C_{\alpha_1}} & \frac{R_3}{R^2 C_{\alpha_1}} \\ \frac{R_3}{R^2 C_{\alpha_2}} & -\frac{R_1+R_3}{R^2 C_{\alpha_2}} \end{bmatrix} \quad (19a)$$

$$B = \begin{bmatrix} b_1 \\ b_2 \end{bmatrix} = \begin{bmatrix} \frac{R_2}{R^2 C_{\alpha_1}} \\ \frac{R_1}{R^2 C_{\alpha_2}} \end{bmatrix} \quad (19b)$$

$$R^2 = R_1 R_2 + R_2 R_3 + R_1 R_3 \quad (19c)$$

The solution of the equation of state (Eq. [20]) is as follows:

$$x(t) = \Phi_0(t)x_0 + \int_0^t [\Phi_1(t-\tau)\tilde{B}_1 + \Phi_2(t-\tau)\tilde{B}_2]e(\tau)d\tau \quad (20)$$

where  $x(t) = \begin{bmatrix} u_1(t) \\ u_2(t) \end{bmatrix}$  is a state vector with  $x_0 = x(0)$ , while

$$\tilde{B}_1 = \begin{bmatrix} b_1 \\ 0 \end{bmatrix}, \tilde{B}_2 = \begin{bmatrix} 0 \\ b_2 \end{bmatrix} \quad (21)$$

Time-dependent functions  $\Phi_k(t)$  for  $k = 0, 1, 2$ , occurring in the solution of Eq. (19), are given by functional series, as presented in Eq. (22):

$$\begin{aligned} \Phi_0(t) &= \sum_{k_1=0}^{\infty} \sum_{k_2=0}^{\infty} T_{k_1 k_2} \frac{t^{k_1 \alpha_1 + k_2 \alpha_2}}{\Gamma(k_1 \alpha_1 + k_2 \alpha_2 + 1)} \\ \Phi_1(t) &= \sum_{k_1=0}^{\infty} \sum_{k_2=0}^{\infty} T_{k_1 k_2} \frac{t^{(k_1+1) \alpha_1 + k_2 \alpha_2 - 1}}{\Gamma[(k_1+1) \alpha_1 + k_2 \alpha_2]} \\ \Phi_2(t) &= \sum_{k_1=0}^{\infty} \sum_{k_2=0}^{\infty} T_{k_1 k_2} \frac{t^{k_1 \alpha_1 + (k_2+1) \alpha_2 - 1}}{\Gamma[k_1 \alpha_1 + (k_2+1) \alpha_2]} \end{aligned} \quad (22)$$

where data in the form of matrices  $T_{k_1 k_2}$  are provided in terms of the following recursive relationship (Eq. [23]):

$$f(x) = \begin{cases} I_N & \text{for } k_1 = k_2 = 0 \\ \tilde{A}_1 T_{k_1-1, k_2} + \tilde{A}_2 T_{k_1, k_2-1} & \text{for } k_1, k_2 \geq 0 \\ & \text{and } k_1 = k_2 = 0 \\ 0 & \text{for } k_1 < 0 \\ & \text{and/or } k_2 < 0 \end{cases} \quad (23)$$

where

$$\tilde{A}_1 = \begin{bmatrix} a_{11} & a_{12} \\ 0 & 0 \end{bmatrix}, \tilde{A}_2 = \begin{bmatrix} 0 & 0 \\ a_{21} & a_{22} \end{bmatrix} \quad (24)$$

## 7. MEASUREMENTS OF THE ELECTRICAL CIRCUIT

The RC ladder network of fractional orders  $\alpha_1 = 0.5$  and  $\alpha_2 = 0.7$  was assembled (Fig. 7) according to the scheme presented in Fig. 6. The values of the parameters of the circuit elements are presented in Tab. 3.

Tab. 3. Parameters of the circuit

Circuit parameters	Values
$R_1$	996.8 $\Omega$
$R_2$	1183.0 $\Omega$
$R_3$	893.8 $\Omega$
$\alpha_1$	0.5
$\alpha_2$	0.7
$C_{\alpha_1}$	19.1 $\mu\text{F}/\text{s}^{0.5}$
$C_{\alpha_2}$	10.9 $\mu\text{F}/\text{s}^{0.3}$
$e$	10 V

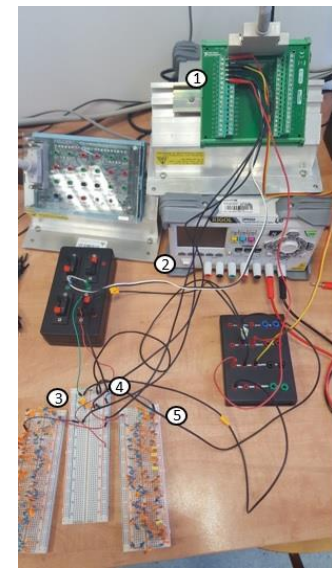


Fig. 7. Measuring station used in the experiment: 1 – measuring card; 2 – DC power supply; 3 – ladder network of  $\alpha_1 = 0.5$ ; 4 – boards with external resistors; 5 – ladder network of  $\alpha_2 = 0.7$

The RC ladder network and DC voltage terminals were connected to the measuring card. The discharged circuit was fed with a step voltage of 10 V. During the experiment, the dynamics of terminal voltage of the ladder circuits with a time step of 1 ms were measured.

Figs. 8 and 9 present the step responses of the fractional-order RC circuit; further, Tab. 3 presents theoretical curves based on Eq. (19) and parameters of the tested circuit elements.

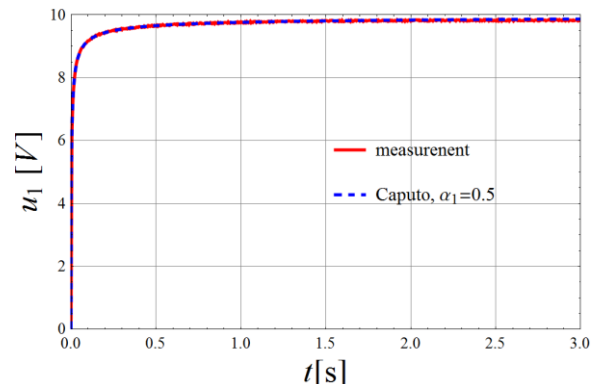


Fig. 8. Measured and theoretical step response of the RC ladder circuit of  $\alpha_1 = 0.5$

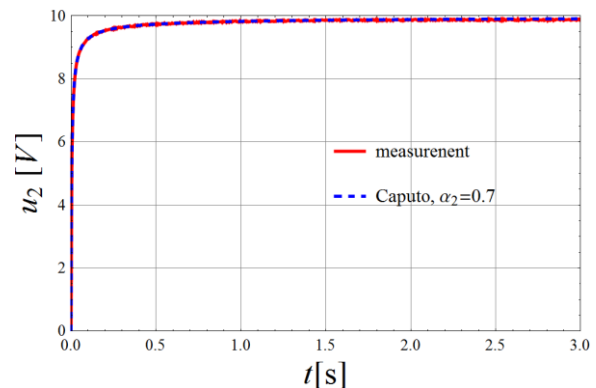


Fig. 9. Measured and theoretical step response of the RC ladder circuit of  $\alpha_2 = 0.7$

The accuracy of the results is analysed through a comparison of theoretical and measured values of both curves using relative error (Eq. [25]):

$$\varepsilon = \left| \frac{u_{\text{theoretical}} - u_{\text{measured}}}{u_{\text{measured}}} \right| \cdot 100\% \quad (25)$$

The relative error curves are presented in Figs. 10 and 11.

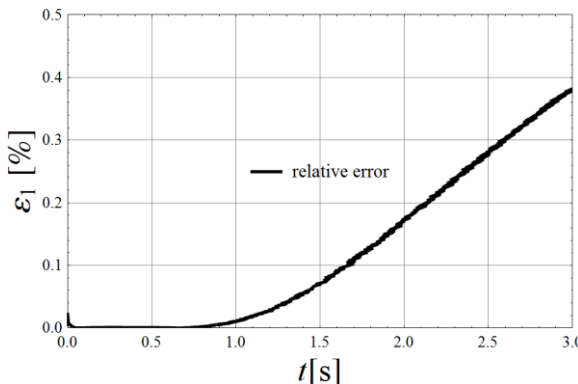


Fig. 10. Relative error function of the RC ladder circuit of  $\alpha_1 = 0.5$

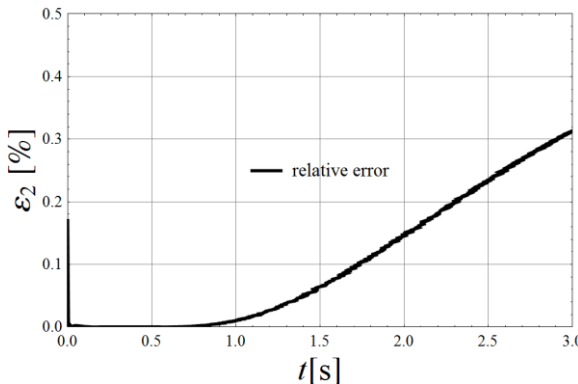


Fig. 11. Relative error function of the RC ladder circuit of  $\alpha_2 = 0.7$

The relative error in both the cases did not exceed 0.5%.

## 8. CONCLUSIONS

Realisation methods of an RC ladder circuit of fractional order, associated with the appropriate selection of its resistance and capacitance, were discussed. Previous approaches described by Khazali and Tawalbeh [5], as well as Petras, Sierociuk and Podlubny [16], have significant restrictions as to the choice of order of derivative  $\alpha$ . Despite their simplicity, consisting in a small variation of the parameters of the selected elements, the above methods require the construction of systems of considerable length in order to obtain a wide frequency range in which RC ladder behaves in a manner as close as possible to the ideal element of the order  $\alpha_1 = 0.5$ .

For this reason, the paper considers the case when  $\alpha$  is different from 0.5 (in this case  $\alpha = 0.7$ ) and compares the obtained results with the results of  $\alpha = 0.5$ . In this way, the description and development of the ladder electrical circuits with  $\alpha$  other than 0.5 were presented, thereby enabling a wider application of fractional differential calculus. An approximation based on CFE was used, which made it possible to shorten the ladder calculations of elec-

trical circuits. The definition of fractional order by Caputo was also used.

In order to obtain the values of the resistance and capacitance of the RC ladder network, consistent with the theoretical values calculated based on CFE, a program was developed that selects the equivalent, actual resistors and capacitors with the measured values and the way of their connection. As a result, the discrepancy between the actual and theoretical values was at most 1%.

In this way, the circuits consisting of fewer meshes and having a wider range of Bode plot compatibility were obtained and compared with the results derived by the aforementioned authors. The study also shows that for the circuit comprising two real fractional elements, the theoretical predictions do not differ from the experimental results by more than 0.5% of the measured value.

## REFERENCES

1. Alsaedi A, Nieto JJ, Venkatesh V. Fractional electrical circuits. *Advances in Mechanical Engineering*. 2015 Dec 1; 7 (12): 168781401561812.
2. Al-Refai M, Abdeljawad T. Analysis of the fractional diffusion equations with fractional derivative of non-singular kernel. *Adv Differ Equ*. 2017; (1): 315.
3. M. Batiha I, A. Njadat S, M. Batyha R, Zraiqat A, Dababneh A, Momani S. Design Fractional-order PID Controllers for Single-Joint Robot Arm Model. *ijasca*. 2022 Aug 1; 14 (2): 97–114.
4. Chen W, HongGuang S, Xicheng L. *Fractional Derivative Modeling in Mechanics and Engineering*. 1st ed. Springer; 2022. 385 p.
5. El-Khazali R, Tawalbeh N. Realization of Fractional-Order Capacitors and Inductors. In: *Proceedings of The 5th Workshop on Fractional Differentiation and its Applications*. Hohai University, Nanjing, China; 2012; 1–6.
6. Correa-Escudero IL, Gómez-Aguilar JF, López-López MG, Alvarado-Martínez VM, Baleanu D. Correcting dimensional mismatch in fractional models with power, exponential and proportional kernel: Application to electrical systems. *Results in Physics*. 2022 Sep; 40:105867.
7. Evangelista LR, Lenzi EK. *An introduction to anomalous diffusion and relaxation*. Cham, Switzerland: Springer Nature; 2023. 400 p.
8. Hidalgo-Reyes JI, Gómez-Aguilar JF, Escobar-Jiménez RF, Alvarado-Martínez VM, López-López MG. Classical and fractional-order modeling of equivalent electrical circuits for supercapacitors and batteries, energy management strategies for hybrid systems and methods for the state of charge estimation: A state of the art review. *Microelectronics Journal*. 2019 Mar; 85:109–28.
9. Hidalgo-Reyes JI, Gómez-Aguilar JF, Escobar-Jimenez RF, Alvarado-Martinez VM, Lopez-Lopez MG. Determination of supercapacitor parameters based on fractional differential equations. *Int J Circ Theor Appl*. 2019 May 22; cta.2640.
10. Kaczorek T. Analysis of Fractional Electrical Circuits in Transient States. In *Logitrans - VII Konferencja Naukowo-Techniczna*; 2010; 1695–704.
11. Kaczorek T, Rogowski K. *Fractional Linear Systems and Electrical Circuits*. Springer International Publishing; 2015. (Studies in Systems, Decision and Control; vol. 13). <https://link.springer.com/10.1007/978-3-319-11361-6>
12. Krishna BT, Reddy KVVS. Active and Passive Realization of Fractance Device of Order 1/2. *Active and Passive Electronic Components*. 2008;2008:1–5.
13. Kumar N, Upadhyay DK. Fractional Order Digital Differentiator with Linear Phase and Low Absolute Error. *International Journal of Electronic and Electrical Engineering*. 2014;7(5):491–6.
14. Mitkowski W, Bauer W, Zagórowska M. RC-ladder networks with supercapacitors. *Archives of Electrical Engineering*. 2018; 67 (2): 377–89.

15. Mitkowski W, Długosz M, Skruch P. Selected Engineering Applications of Fractional-Order Calculus. In: Kulczycki P, Korbicz J, Kacprzyk J, editors. Fractional Dynamical Systems: Methods, Algorithms and Applications [Internet]. Cham: Springer International Publishing; 2022 [cited 2023 Sep 7]. p. 333–59. (Studies in Systems, Decision and Control; vol. 402). Available from: [https://link.springer.com/10.1007/978-3-030-89972-1\\_12](https://link.springer.com/10.1007/978-3-030-89972-1_12)
16. Petras I, Sierociuk D, Podlubny I. Identification of Parameters of a Half-Order System. *IEEE Trans Signal Process*. 2012 Oct; 60 (10): 5561–6.
17. Piotrowska E. Analysis of fractional capacitor and coil by the use of the Conformable Fractional Derivative and Caputo definitions. In: 2018 International Interdisciplinary PhD Workshop (IIPhDW). Swinoujście: IEEE. 2018; 103–7. <https://ieeexplore.ieee.org/document/8388335/>
18. Piotrowska E, Rogowski K. Analysis of Fractional Electrical Circuit Using Caputo and Conformable Derivative Definitions. In: Ostalczyk P, Sankowski D, Nowakowski J, editors. Non-Integer Order Calculus and its Applications: Springer International Publishing; 2019, p. 183–94. (Lecture Notes in Electrical Engineering; vol. 496). [http://link.springer.com/10.1007/978-3-319-78458-8\\_16](http://link.springer.com/10.1007/978-3-319-78458-8_16)
19. Podlubny I, Petráš I, Vinagre BM, O'Leary P, Dorčák L. Analogue Realization of Fractional-Order Controllers. *Nonlinear Dynamics*. 2002;29(1/4):281–96.
20. Pu Yifei, Yuan Xiao, Liao Ke, Zhou Jiliu, Zhang Ni, Zeng Yi, et al. Structuring Analog Fractance Circuit for 1/2 Order Fractional Calculus. In: 2005 6th International Conference on ASIC. Shanghai, China: IEEE; 2005, 1039–42. <http://ieeexplore.ieee.org/document/1611507/>
21. Sene N, Gómez-Aguilar JF. Analytical solutions of electrical circuits considering certain generalized fractional derivatives. *Eur Phys J Plus*. 2019 Jun;134(6):260.
22. Sierociuk D, Skovranek T, Macias M, Podlubny I, Petras I, Dzieliński A, et al. Diffusion process modeling by using fractional-order models. *Applied Mathematics and Computation*. 2015; 257:2–11.
23. Sierociuk D, Dzieliński A. Ultracapacitor Modelling and Control Using Discrete Fractional Order State-Space Model. *Acta Montanistica Slovaca*. 2008;13(1):136–45.
24. Skovranek T, Macias M, Sierociuk D, Malesza W, Dzieliński A, Podlubny I, et al. Anomalous diffusion modeling using ultracapacitors in domino ladder circuit. *Microelectronics Journal*. 2019; 84:136–41.
25. Tapadar A, Khanday FA, Sen S, Adhikary A. Fractional calculus in electronic circuits: a review. In: Fractional Order Systems [Internet]. Elsevier; 2022 [cited 2023 Sep 7]. p. 441–82. Available from: <https://linkinghub.elsevier.com/retrieve/pii/B978012824293300018>
26. Yang XJ. General fractional derivatives: theory, methods and applications. Boca Raton, FL: CRC Press, Taylor & Francis Group; 2019.

Ewa Piotrowska:  <https://orcid.org/0000-0003-3163-0753>

Rafał Melnik:  <https://orcid.org/0000-0003-2900-784X>



This work is licensed under the Creative Commons BY-NC-ND 4.0 license.

# A FRACTIONAL STUDY OF MHD CASSON FLUID MOTION WITH THERMAL RADIATIVE FLUX AND HEAT INJECTION/SUCTION MECHANISM UNDER RAMPED WALL CONDITION: APPLICATION OF RABOTNOV EXPONENTIAL KERNEL

Aziz Ur REHMAN\*, Fahd JARAD\*\*/\*\*\*, Muhammad Bilal RIAZ\*

\*Department of Mathematics, University of Management and Technology Lahore, Pakistan

\*\*Department of Mathematics, Cankaya University, ETES 06790, Ankara, Turkey

\*\*\*Department of Medical Research, China Medical University, Taichung 40402, Taiwan

\*\*\*\*Department of Computer Science and Mathematics, Lebanese American University, Byblos, Lebanon

[prof.azizkhan@gmail.com](mailto:prof.azizkhan@gmail.com), [fahd@cankaya.edu.tr](mailto:fahd@cankaya.edu.tr), [bilal.riaz@umt.edu.pk](mailto:bilal.riaz@umt.edu.pk)

received 29 April 2023, revised 16 June 2023, accepted 28 June 2023

**Abstract:** The primary objective of this research is to extend the concept of fractionalized Casson fluid flow. In this study, a comprehensive analysis of magnetohydrodynamic (MHD) natural convective flow of Casson fluid is conducted, focusing on obtaining analytical solutions using the non-integer-order derivative known as the Yang–Abdel-Aty–Cattani (YAC) operator. The YAC operator utilized in this research possesses a more generalized exponential kernel. The fluid flow is examined in the vicinity of an infinitely vertical plate with a characteristic velocity denoted as  $u_0$ . The mathematical modelling of the problem incorporates partial differential equations, incorporating Newtonian heating and ramped conditions. To facilitate the analysis, a suitable set of variables is introduced to transform the governing equations into a dimensionless form. The Laplace transform (LT) is then applied to the fractional system of equations, and the obtained results are presented in series form and also expressed in terms of special functions. The study further investigates the influence of relevant parameters, such as  $\alpha$ ,  $\beta$ ,  $P_r$ ,  $Q$ ,  $G_r$ ,  $M$ ,  $N_r$  and  $K$ , on the fluid flow to reveal interesting findings. A comparison of different approaches reveals that the YAC method yields superior results compared to existing operators found in the literature. Graphs are generated to illustrate the outcomes effectively. Additionally, the research explores the limiting cases of the Casson and viscous fluid models to derive the classical form from the YAC fractionalized Casson fluid model.

**Key words:** YAC derivative, series solution, heat transfer, Laplace transformation, Rabotnov exponential functions, system parameters

## 1. INTRODUCTION

Non-Newtonian fluids have gained significant importance among researchers and scientists in recent decades due to their wide range of applications in various fields. The complex nature of these fluids prevents the characterization of their mechanical properties using the Navier–Stokes equation, making a single constitutive equation inadequate for describing their rheological behaviour. The rheological behaviour of non-Newtonian fluids is of great significance in industrial and technological applications, such as petroleum, biological, plastic manufacturing, chemical, textile and cosmetic industries. Several models, including the viscoplastic model, second-grade fluid model, Williamson fluid, Bingham plastic model, power law model, Jeffery model, Brinkman type fluid, Oldroyd-B model, Maxwell model, Walters-B fluid model, tangent hyperbolic fluid and Casson model (shear thinning liquid), have been developed to explain the diverse nature of non-Newtonian fluids [1–6].

Among these models, the Casson fluid is considered the simplest generalization of a Newtonian fluid. Casson fluid, introduced by Casson in 1959 to analyse the regime of pigment-oil suspensions, is one of the most common types of non-Newtonian fluids [7]. The Casson fluid model allows for the determination of viscous fluid behaviour by considering the impacts of its generalized

parameters. Due to its important properties and wide range of applications, Casson fluid finds application in biological sciences, such as plasma and the handling of biological fluids like blood, as well as in mechanics due to its viscoelastic behaviour. Given the current scientific challenges, mathematicians, researchers, scientists and engineers are particularly focused on studying Casson fluid in fields like biology, engineering, chemistry, petroleum industries and physiology, considering its natural behaviour. Hussain et al. [8] employed the Homotopy analysis method, an analytical technique, to investigate series solutions for magnetohydrodynamic (MHD) Casson fluid in the thermal boundary layer flow over a moving stretching porous wedge. Additionally, Hussain et al. [9] discussed the solution of the MHD thermal boundary layer flow of Casson liquid over a penetrable extending wedge with ohmic heating and convective boundary conditions.

Ramped conditions refer to a flow condition where the shear rate of a fluid gradually changes over time. This approach is commonly employed in the investigation of non-Newtonian fluids to gain insights into their flow behaviour and properties under different circumstances. In the pharmaceutical industry, ramped conditions are utilized to study the rheological behaviour of complex fluids like suspensions and emulsions, which often exhibit non-Newtonian characteristics. The application of ramped conditions extends to the oil and gas industry, where they are employed

to model the flow of non-Newtonian fluids. Understanding the rheological behaviour of drilling mud and other fluids is crucial for optimizing drilling operations. In the field of biomedical engineering, ramped conditions are used to study blood flow in arteries and veins. The behaviour of non-Newtonian fluids plays a critical role in comprehending the pathophysiology of diseases such as atherosclerosis. Ali et al. [10] developed a mathematical model to examine blood flow through a cylindrical stenosed blood vessel. Overall, ramped conditions have significant applications in the study of non-Newtonian fluids. They enable researchers to gain a better understanding of the flow behaviour of these fluids under various conditions, which is essential for optimizing their performance in diverse applications. Khalid et al. [11] investigated the MHD unsteady free convectional transport of the Casson model, considering computational aspects in porous media. Hussain et al. [12] discussed the effects of chemical reactions and suction/injection on the flow of Williamson fluid along a porous stretching wedge. Bhattacharyya et al. [13] described the MHD flow of Casson fluid velocity in the presence of an exponentially stretching surface. Oka [14] conducted the first-time analysis of Casson fluid movement, considering convective conditions at the boundary through a permeable stretching sheet, and analysed the results theoretically. Riaz et al. [15] investigated the impacts of heat generation on MHD Maxwell fluid in a permeable medium. Hussain et al. [16] analyzed the flow of a hybrid nanofluid under the influence of MHD, variable viscosity and mixed convection. Mernone et al. [17] examined the two-dimensional peristaltic flow of Casson fluid in a channel. Arthur et al. [18] investigated the generalized peristaltic flow of Casson fluid in a permeable channel subjected to chemical reaction effects. Mukhopadhyay [19] examined the heat transfer phenomenon of MHD Casson fluid with heat suction/blowing passing over a stretching plate. Mustafa et al. [20] analysed the unsteady flow of the Casson model using the homotopy analysis method to study heat transfer over a movable flat plate. Similar studies on MHD Casson fluid can be found in the literature [21–23] and references therein.

Fractional calculus has diverse and significant impacts in various fields such as electrical engineering, electrochemistry, control theory, electromagnetism, mechanics, image processing, bioengineering, physics, finance and fluid dynamics. It is a valuable tool for research and study due to its wide-ranging applications. Fractional derivatives not only capture the present behaviour of systems but also account for their past behaviour, making them particularly suitable for systems with long-term memory. Its applications extend beyond physical sciences to areas like biology, astrophysics, ecology, geology and chemistry. In the past decades, fractional calculus has successfully elucidated the mechanisms of non-Newtonian models by providing a simple and elegant description of their complex behaviour. One well-known type of non-Newtonian fluid is viscoelastic fluid, which exhibits both elasticity and viscosity. These fluid models have significant implications in polymerization, industrial and mechanical engineering, as well as the automobile industry, due to their inherent characteristics. Fractional calculus plays a crucial role in interpreting the viscoelastic nature of materials. Given these remarkable properties, researchers have dedicated attention to analysing the fractional behaviour of different fluid models, either directly or indirectly, particularly when considering non-integer-order derivatives. For example, Kumar et al. [24] illustrated the multidimensional heat equations of arbitrary order using the analytical approaches of the homotopy perturbation transform method (HPTM) and residual power series method, employing a new fractional operator in the

Yang–Abdel-Aty–Cattani (YAC) sense. Bagley and Torvik [25] explored the application of fractional calculus to viscoelastic fluids. Rehman et al. [26] investigated the fractional Maxwell fluid and obtained closed solutions for shear stress and velocity. Riaz et al. [27] analysed the influence of MHD on the heat transfer of fractionalized Oldroyd-B fluid. Additionally, Rehman et al. [28] studied certain features of Maxwell fluid, considering the impact of Newtonian heating and developed a fractional model using the Prabhakar fractional approach. Mohammadi et al. [29] utilized the Euler method for fractional-order Caputo Fabrizio derivative to approximate the system's solution and analyse the effects of the mumps virus. Rehman et al. [30] performed a comparative analysis of ABC, CF and CPC methods for a second-grade fluid under the influence of Newtonian heating, obtaining series solutions. Kumar et al. [31] proposed a new generalized fractional derivative that produces different types of singular and nonsingular fractional derivatives based on various kernels. Jleli et al. [32] presented a general framework of the HPTM for the analytic treatment of time-fraction partial differential equations following the YAC approach. Furthermore, Hayat et al. [33] obtained a series solution for the flow of Jeffery fluid, highlighting the contributions of fractional calculus to viscoelastic fluids in various studies [34–39].

In a recent study, Anwar et al. [40] investigated the classical version of the Casson fluid model with ramped boundary conditions using the Laplace transformation method. This method is efficient for non-uniform boundary conditions, but it does not consider the fractional behaviour effect in the presented model. It was observed that the Casson fluid model with the innovative fractional operator, known as the YAC operator, which has a non-local and singular kernel, has not been previously studied in conjunction with ramped boundary conditions for velocity and energy distribution through porous media in the literature on fractional models in fluid mechanics. Motivated by these findings, this article focuses on the heat transfer analysis of the MHD fractional Casson fluid in a channel with ramped conditions. The integer-order derivative Casson fluid model is transformed into the non-integer-order derivative YAC model. The Laplace transform (LT) is used to obtain analytical solutions for the problem at hand. The velocity and temperature are evaluated in series form, providing exact solutions that have not been reported in the previous literature. Therefore, this article contributes valuable insights to the existing literature by presenting a wide range of exact solutions for the Casson fluid with appropriate boundary conditions. The influence of embedded parameters, including the YAC fractional parameter  $\alpha$ , porosity parameter  $K$ , Casson fluid parameter  $\beta$ , Prandtl parameter  $P_r$ , magnetic number  $M$ , heat injection/suction parameter  $Q$ , Grashof number  $G_r$ , and radiation parameter  $N_r$ , on the velocity profile and heat distribution, are analysed using graphical representations.

## 2. MATHEMATICAL MODEL

In this study, we investigate the heat transfer phenomenon in the convective flow of an MHD Casson fluid over a vertically oriented infinite plate. The coordinate axis system is set up such that the plate is fixed along the  $x$ -axis, and the  $\phi$ -axis is perpendicular to the plate (as depicted in Fig. 1). Initially, at time  $t = 0$ , the fluid is at rest with the ambient temperature  $T_\infty$ . Ramped conditions are applied to the velocity for  $t > 0$ , with the wall temperature set as  $T_w$ .

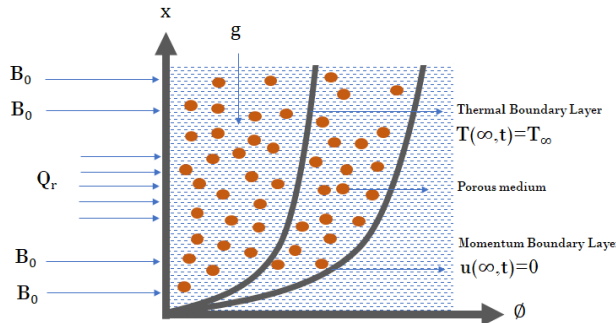


Fig. 1. Schematic drawing of the flow model

The velocity component  $u(\varphi, t)$  is considered along the  $x$ -axis, where  $u_0$  represents the characteristic velocity, and the fluid flow is confined to  $\varphi > 0$ . We make certain assumptions in our model. First, a vertical transverse magnetic force is introduced and exerted on the fluid flow, and the fluid motion is assumed to be unidirectional. We neglect the influence of the induced magnetic field due to the small value of the Reynolds parameter/number. Viscous dissipation, Joule heating, radiative heat flux ( $Q_r$ ) and any other external heat sources are also disregarded. Additionally, we assume that the fluid velocity in this problem is only dependent on the two parameters,  $\varphi$  and  $t$ . Under these assumptions, the governing equations for the fluid flow, using Boussinesq's approximation [41, 42], can be expressed as follows:

The following equations represent the momentum and energy equations:

$$\frac{\partial u(\varphi, t)}{\partial t} = v \left( 1 + \frac{1}{\beta} \right) \frac{\partial^2 u(\varphi, t)}{\partial \varphi^2} + g \beta_T (T(\varphi, t) - T_\infty) - \frac{\sigma}{\rho} B_0^2 u(\varphi, t) - v \left( 1 + \frac{1}{\beta} \right) \frac{\zeta}{k_p} u(\varphi, t), \quad (1)$$

$$\rho C_p \frac{\partial T(\varphi, t)}{\partial t} = - \frac{\partial q(\varphi, t)}{\partial \varphi} - \frac{\partial Q_r}{\partial \varphi} + Q_0 (T(\varphi, t) - T_\infty), \quad (2)$$

where

$$\left[ Q_r = - \frac{4\sigma_1}{3k_1} \frac{\partial T^4}{\partial \varphi}; T^4 \approx 4T_\infty^3 T - 3T_\infty^4 \right].$$

Fourier's Law of thermal flux is written as

$$q(\varphi, t) = -k \frac{\partial T(\varphi, t)}{\partial \varphi}. \quad (3)$$

The mathematical representation of the given problem, including the associated initial conditions and ramped boundary conditions, is presented as follows:

$$\begin{aligned} u(\varphi, 0) &= 0, \quad T(\varphi, 0) = T_\infty, \quad \varphi \geq 0, \\ u(0, t) &= \begin{cases} u_0 \frac{t}{t_0}, & 0 < t \leq t_0; \\ u_0, & t > t_0 \end{cases}, \\ T(0, t) &= \begin{cases} T_\infty + (T_w - T_\infty) \frac{t}{t_0}, & 0 < t \leq t_0; \\ T_w, & t > t_0 \end{cases}, \\ u(\varphi, t) &\rightarrow 0, T(\varphi, t) \rightarrow T_\infty, \text{ as } \varphi \rightarrow \infty \text{ and } t > 0. \end{cases} \quad (4)$$

A new set of quantities is introduced to non-dimensionalise the problem equations. This allows for a more convenient representation of the equations without specific units. By utilizing these non-dimensional quantities, the problem can be analysed and compared across different scales or systems.

$$\begin{aligned} t^* &= \frac{u_0^2 t}{v}, \quad \varphi^* = \frac{u_0 \varphi}{v}, \quad u^* = \frac{u}{u_0}, \quad q^* = \frac{q}{q_0}, \quad T^* = \frac{T - T_\infty}{T_w - T_\infty}, \\ q_0 &= \frac{k(T_w - T_\infty)u_0}{v}, \quad Q = \frac{Q_0 v}{\rho C_p u_0^2}, \quad Gr = \frac{g \beta_T (T_w - T_\infty)}{u_0^3}, \\ Pr &= \frac{\mu C_p}{k}, \quad M = \frac{\sigma C_p^2 v}{\rho u_0^2}, \quad N_r = \frac{16\sigma_1 T_\infty^3}{3kK_1}, \quad \frac{1}{K} = \frac{v^2 \zeta}{k_p u_0^2}. \end{aligned} \quad (5)$$

Upon substituting the newly introduced entities, as defined in Eq. (5), into Eqs (1) and (2), and subsequently omitting the  $*$  symbol, the equations undergo a transformation that results in a revised form. This process involves replacing the relevant variables or terms with their corresponding values based on the definitions provided in Eq. (5).

By applying these substitutions and simplifications, the equations are modified to better represent the desired form or structure, allowing for clearer mathematical expressions and further analysis. The specific details of the transformations depend on the specific equations and substitutions involved, as well as the context in which they are applied.

$$\frac{\partial u(\varphi, t)}{\partial t} = b \frac{\partial^2 u(\varphi, t)}{\partial \varphi^2} - \left[ M + \frac{b}{K} \right] u(\varphi, t) + Gr T(\varphi, t), \quad (6)$$

$$\frac{\partial T(\varphi, t)}{\partial t} = - \left( \frac{1+N_r}{Pr} \right) \frac{\partial q(\varphi, t)}{\partial \varphi} + QT, \quad (7)$$

$$q(\varphi, t) = - \frac{\partial T(\varphi, t)}{\partial \varphi}. \quad (8)$$

The non-dimensional forms of the initial and boundary conditions are also considered in this context

$$u(\varphi, 0) = 0, \quad T(\varphi, 0) = 0, \text{ for } \varphi \geq 0, \quad (9)$$

$$u(0, t) = T(0, t) = \begin{cases} t & 0 < t \leq 1 \\ 1 & t > 1 \end{cases}, \quad (10)$$

$$u(\varphi, t) \rightarrow 0, \quad T(\varphi, t) \rightarrow 0 \text{ as } \varphi \rightarrow \infty \text{ and } t > 0, \quad (11)$$

where

$$a = b\theta Q, \quad b = 1 + \frac{1}{\beta}, \quad c = M + \frac{b}{K}, \quad d = 1 - b\theta, \quad \theta = \frac{Pr}{1+N_r}.$$

In this context, the term Grashof number is used to represent the parameter  $Gr$ , the Prandtl number is denoted by  $Pr$ , the radiation parameter is represented by  $N_r$ , the magnetic number is denoted as  $M$ , permeability is represented by  $k_p$ , thermal conductivity is denoted by  $k$ , the coefficient of Rossland absorption is denoted by  $k_1$ , the Stefan–Boltzmann constant is represented by  $\sigma_1$ , porosity is denoted by  $\zeta$ , radiative heat flux is represented by  $Q_r$  and porosity is defined as  $K$ .

### 3. PRELIMINARIES

In this article, the non-integer YAC time derivative is applied which is defined as

$${}^{YAC} D_t^\alpha f(t) = \int_0^t \Psi_\alpha(-\vartheta(t-\tau)^\alpha) f'(\tau) d\tau, \quad (12)$$

for  $t > 0, 0 < \alpha < 1$ ,

where

$$\Psi(\vartheta z^\alpha) = \sum_{n=0}^{\infty} \frac{\vartheta^n z^{(n+1)(\alpha+1)-1}}{\Gamma(n+1)(\alpha+1)}, \quad z \in \mathbb{C},$$

and  $\Psi_\alpha$  denotes the Rabotnov exponential function of order  $\alpha$ .

Laplace transformation of this newly developed operator is defined as follows:

$$L\{YACD_t^\alpha f(t)\} = \frac{1}{\eta^{\alpha+1}} \frac{\eta L\{f(t)\} - f(0)}{1 + \varphi \eta^{-(\alpha+1)}}, \quad (13)$$

where  $\eta$  represents LT parameter and  $\alpha$  used as a fractional parameter.

## 4. FRACTIONAL FORMULATION OF GOVERNING EQUATIONS AND SOLUTIONS

By replacing the regular time derivative with the YAC fractional derivative in Eqs. (6)–(8), the modified equations for the time-fractional rate-type fluid model describing velocity and energy are obtained. This substitution allows for a more accurate representation of fractional behaviour, as the YAC fractional derivative incorporates non-local and singular kernels. Hence, the resulting equations provide a comprehensive framework for understanding the dynamics of the fluid in terms of velocity and energy within the context of a time-fractional rate-type fluid model.

$$^{YAC}D_t^\alpha u(\varphi, t) = b \frac{\partial^2 u(\varphi, t)}{\partial \varphi^2} - cu(\varphi, t) + GrT(\varphi, t), \quad (14)$$

$$^{YAC}D_t^\alpha T(\varphi, t) = \frac{1}{\theta} \frac{\partial^2 T(\varphi, t)}{\partial \varphi^2} + QT(\varphi, t). \quad (15)$$

The YAC fractional operator, denoted as  $^{YAC}D_t^\alpha$ , is utilized in the context mentioned above. More details regarding the properties of the YAC operator can be found in the study referenced as [43].

### 4.1. Investigation of exact solution for temperature profile

By applying the LT to Eq. (15) while considering the transformed conditions specified in Eqs (9)–(11), we obtain

$$\frac{\eta \bar{T}(\varphi, \eta) - \bar{T}(\varphi, 0)}{\eta^{\alpha+1} + \varphi} = \frac{1}{\theta} \frac{\partial^2 \bar{T}(\varphi, \eta)}{\partial \varphi^2} + Q\bar{T}(\varphi, \eta). \quad (16)$$

With transformed boundary conditions

$$\bar{T}(\varphi, 0) = 0, \quad \bar{T}(0, \eta) = \frac{1 - e^{-\eta}}{\eta^2}$$

$$\text{and } \bar{T}(\varphi, \eta) \rightarrow 0 \text{ as } \varphi \rightarrow \infty. \quad (17)$$

By applying the Laplace transformation to Eq. (16), the solution for the energy can be derived as follows:

$$\bar{T}(\varphi, \eta) = e_1 e^{-\varphi \sqrt{\theta \left( \frac{\eta}{\eta^{\alpha+1} + \varphi} - Q \right)}} + e_2 e^{\varphi \sqrt{\theta \left( \frac{\eta}{\eta^{\alpha+1} + \varphi} - Q \right)}}. \quad (18)$$

After implementing the transformed boundary conditions, the energy solution can be expressed as follows:

$$\begin{aligned} \bar{T}(\varphi, \eta) &= \left( \frac{1 - e^{-\eta}}{\eta^2} \right) e^{-\varphi \sqrt{\theta \left( \frac{\eta}{\eta^{\alpha+1} + \varphi} - Q \right)}}, \\ &= \bar{T}_1(\varphi, \eta) - e^{-\eta} \bar{T}_1(\varphi, \eta). \end{aligned} \quad (19)$$

To transform the solution in time variable again, we have to employ inverse Laplace transformation technique on Eq. (19).

$$T(\varphi, t) = T_1(\varphi, t) - T_1(\varphi, t)P(t - 1). \quad (20)$$

In the above expression,  $P(t - 1)$  represents a Heaviside function and

$$T_1(\varphi, t) = \text{?} \quad (21)$$

The current form of Eq. (21) makes it challenging to compute the Laplace inverse. Therefore, it is necessary to convert it into a series form, which will yield the following expression:

$$\begin{aligned} T_1(\varphi, t) &= L^{-1} \left\{ \frac{1}{\eta^2} \sum_{\chi=0}^{\infty} \sum_{n=0}^{\infty} \frac{(-\varphi)^\chi (\theta)^{\frac{\chi}{2}} (-Q)^{\frac{\chi}{2} - n} \Gamma(\frac{\chi}{2} + 1) (\eta)^n}{\chi! n! \Gamma(\frac{\chi}{2} - n + 1) (\eta^{\alpha+1} + \varphi)^n} \right\}, \\ &= \sum_{\chi=0}^{\infty} \sum_{n=0}^{\infty} \frac{(-\varphi)^\chi (\theta)^{\frac{\chi}{2}} (-Q)^{\frac{\chi}{2} - n} \Gamma(\frac{\chi}{2} + 1)}{\chi! n! \Gamma(\frac{\chi}{2} - n + 1)} t^{n\alpha+1} E_{\alpha+1, n\alpha+2}^n(-\varphi t^{\alpha+1}), \\ &\text{by using } L^{-1} \left\{ \frac{\eta^{\alpha\gamma - \beta}}{(\eta^{\alpha} - \varphi)^\gamma} \right\} = t^{\beta-1} E_{\alpha, \beta}^\gamma(\varphi t^\alpha). \end{aligned}$$

### 4.2. Investigation of exact solution for fluid velocity

Applying the Laplace transformation into Eq. (14) with appropriate transformed conditions as defined in Eqs. (9)–(11), we get

$$\frac{\eta \bar{u}(\varphi, \eta) - \bar{u}(\varphi, 0)}{\eta^{\alpha+1} + \varphi} = b \frac{d^2 \bar{u}(\varphi, \eta)}{d \varphi^2} - c \bar{u}(\varphi, \eta) + Gr \bar{T}(\varphi, \eta), \quad (22)$$

with conditions are

$$\bar{u}(\varphi, 0) = 0, \quad \bar{u}(0, \eta) = \frac{1 - e^{-\eta}}{\eta^2}$$

$$\text{and } \bar{u}(\varphi, \eta) \rightarrow 0 \text{ as } \varphi \rightarrow \infty. \quad (23)$$

By substituting the computed temperature  $\bar{T}(\varphi, \eta)$  obtained from Eq. (19) into Eq. (22), the resulting solution can be expressed in a simplified form as follows:

$$\begin{aligned} \bar{u}(\varphi, \eta) &= e_5 e^{-\varphi \sqrt{\frac{1}{b} \left( \frac{\eta}{\eta^{\alpha+1} + \varphi} + c \right)}} + e_6 e^{\varphi \sqrt{\frac{1}{b} \left( \frac{\eta}{\eta^{\alpha+1} + \varphi} + c \right)}} \\ &+ Gr \left( \frac{1 - e^{-\eta}}{\eta^2} \right) \frac{e^{-\varphi \sqrt{\theta \left( \frac{\eta}{\eta^{\alpha+1} + \varphi} - Q \right)}}}{a + \frac{d\eta}{\eta^{\alpha+1} + \varphi}}. \end{aligned} \quad (24)$$

By utilizing the transformed boundary conditions, we can ascertain the unknown constant. Subsequently, the solution for the velocity in Eq. (24) can be expressed as follows:

$$\begin{aligned} \bar{u}(\varphi, \eta) &= \left( \frac{1 - e^{-\eta}}{\eta^2} \right) e^{-\varphi \sqrt{\frac{1}{b} \left( \frac{\eta}{\eta^{\alpha+1} + \varphi} + c \right)}} \\ &+ \frac{Gr(1 - e^{-\eta})}{\eta^2 \left( a + \frac{d\eta}{\eta^{\alpha+1} + \varphi} \right)} \left[ e^{-\varphi \sqrt{\theta \left( \frac{\eta}{\eta^{\alpha+1} + \varphi} - Q \right)}} - e^{-\varphi \sqrt{\frac{1}{b} \left( \frac{\eta}{\eta^{\alpha+1} + \varphi} + c \right)}} \right]. \end{aligned} \quad (25)$$

To find Laplace inverse of Eq. (25), first we write it in the following form:

$$\begin{aligned} \bar{u}(\varphi, \eta) &= \bar{\Omega}(\varphi, \eta) \\ &+ Gr \bar{\Phi}(\varphi, \eta) [\bar{T}(\varphi, \eta) - \bar{\Omega}(\varphi, \eta)] \end{aligned} \quad (26)$$

and

$$\bar{\Omega}(\varphi, \eta) = \bar{\Omega}_1(\varphi, \eta) - e^{-\eta} \bar{\Omega}_1(\varphi, \eta). \quad (27)$$

The inverse Laplace of Eq. (27) is obtained as

$$\Omega(\varphi, t) = \Omega_1(\varphi, t) - \Omega_1(\varphi, t)P(t - 1), \quad (28)$$

where

$$\begin{aligned}\Omega_1(\varphi, t) &= L^{-1}\{\overline{\Omega_1}(\varphi, \eta)\} = L^{-1}\left\{\frac{1}{\eta^2} e^{-\varphi \sqrt{\frac{1}{b} \left(\frac{\eta}{\eta^{\alpha+1}+\varrho}+c_1\right)}}\right\}, \\ &= L^{-1}\left\{\frac{1}{\eta^2} \sum_{\chi=0}^{\infty} \sum_{n=0}^{\infty} \frac{(-\varphi)^{\chi(c)} \frac{\chi}{2}^{-n} \Gamma(\frac{\chi}{2}+1)(\eta)^n}{\chi! n! (b)^{\frac{\chi}{2}} \Gamma(\frac{\chi}{2}-n+1)(\eta^{\alpha+1}+\varrho)^n}\right\}, \\ &= \sum_{\chi=0}^{\infty} \sum_{n=0}^{\infty} \frac{(-\varphi)^{\chi(c)} \frac{\chi}{2}^{-n} \Gamma(\frac{\chi}{2}+1)}{\chi! n! (b)^{\frac{\chi}{2}} \Gamma(\frac{\chi}{2}-n+1)} t^{n\alpha+1} E_{\alpha+1, n\alpha+2}^n(-\varrho t^{\alpha+1}), \\ \Phi(\varphi, t) &= L^{-1}\{\overline{\Phi}(\varphi, \eta)\} = L^{-1}\left\{\frac{1}{a_1 + \frac{d\eta}{\eta^{\alpha+1}+\varrho}}\right\}, \\ &= L^{-1}\left\{\sum_{m=0}^{\infty} \frac{(-1)^m (d)^m (\eta)^m}{(a)^{m+1} (\eta^{\alpha+1}+\varrho)^m}\right\}, \\ &= \sum_{m=0}^{\infty} \frac{(-1)^m (d)^m}{(a)^{m+1}} t^{m\alpha-1} E_{\alpha+1, m\alpha}^m(-\varrho t^{\alpha+1}).\end{aligned}$$

The required velocity solution after employing the definition of inverse Laplace operator in Eq. (26) is

$$u(\varphi, t) = \Omega(\varphi, t) + Gr\Phi(\varphi, t) * [T(\varphi, t) - \Omega(\varphi, t)]. \quad (29)$$

### 4.3. Limiting models

This section focuses on specific cases that arise when certain physical parameters are not present. These cases provide an opportunity to examine the influence of different circumstances on the solutions. By exploring these scenarios, we can gain valuable insights into the system's behaviour and characteristics when specific parameters are disregarded. This analysis contributes to a holistic understanding of the problem and deepens our knowledge of its dynamics.

#### 4.3.1 Solution in the absence of Casson parameter

In this case, let us assume that the Casson fluid parameter, denoted as  $\beta$ , is chosen to be extremely large, meaning  $1/\beta \rightarrow 0$ . After this transformation, the velocity field solution of the newly derived viscous fluid, obtained from the previously calculated velocity Eq. (25), can be expressed as

$$\begin{aligned}\bar{u}(\varphi, \eta) &= \left(\frac{1-e^{-\eta}}{\eta^2}\right) e^{-\varphi \sqrt{\frac{1}{b} \left(\frac{\eta}{\eta^{\alpha+1}+\varrho}+c_1\right)}} \\ &+ \frac{Gr(1-e^{-\eta})}{\eta^2 \left(a_1 + \frac{d\eta}{\eta^{\alpha+1}+\varrho}\right)} \left[ e^{-\varphi \sqrt{\theta \left(\frac{\eta}{\eta^{\alpha+1}+\varrho}-Q\right)}} - e^{-\varphi \sqrt{\left(\frac{\eta}{\eta^{\alpha+1}+\varrho}+c_1\right)}} \right],\end{aligned} \quad (30)$$

where  $a_1 = \theta Q + c_1$ ,  $c_1 = M + \frac{1}{K}$ ,  $d_1 = 1 - \theta$ .

To find Laplace inverse of Eq. (30), first we write it in the following form:

$$\bar{u}(\varphi, \eta) = \bar{\omega}(\varphi, \eta) + Gr\bar{\Psi}(\varphi, \eta) [\bar{T}(\varphi, \eta) - \bar{\omega}(\varphi, \eta)] \quad (31)$$

and

$$\bar{\omega}(\varphi, \eta) = \overline{\omega_1}(\varphi, \eta) - e^{-\eta} \overline{\omega_1}(\varphi, \eta). \quad (32)$$

After the application of Laplace inverse operator, Eq. (32) is turn out again in the time variable as

$$\omega(\varphi, t) = \omega_1(\varphi, t) - \omega_1(\varphi, t)P(t-1), \quad (33)$$

where

$$\begin{aligned}\omega_1(\varphi, t) &= L^{-1}\{\overline{\omega_1}(\varphi, \eta)\} = L^{-1}\left\{\frac{1}{\eta^2} e^{-\varphi \sqrt{\frac{1}{b} \left(\frac{\eta}{\eta^{\alpha+1}+\varrho}+c_1\right)}}\right\}, \\ &= L^{-1}\left\{\frac{1}{\eta^2} \sum_{\chi=0}^{\infty} \sum_{n=0}^{\infty} \frac{(-\varphi)^{\chi(c_1)} \frac{\chi}{2}^{-n} \Gamma(\frac{\chi}{2}+1)(\eta)^n}{\chi! n! (b)^{\frac{\chi}{2}} \Gamma(\frac{\chi}{2}-n+1)(\eta^{\alpha+1}+\varrho)^n}\right\}, \\ &= \sum_{\chi=0}^{\infty} \sum_{n=0}^{\infty} \frac{(-\varphi)^{\chi(c_1)} \frac{\chi}{2}^{-n} \Gamma(\frac{\chi}{2}+1)}{\chi! n! (b)^{\frac{\chi}{2}} \Gamma(\frac{\chi}{2}-n+1)} t^{n\alpha+1} E_{\alpha+1, n\alpha+2}^n(-\varrho t^{\alpha+1}), \\ \Psi(\varphi, t) &= L^{-1}\{\overline{\Psi}(\varphi, \eta)\} = L^{-1}\left\{\frac{1}{a_1 + \frac{d\eta}{\eta^{\alpha+1}+\varrho}}\right\}, \\ &= L^{-1}\left\{\sum_{m=0}^{\infty} \frac{(-1)^m (d_1)^m (\eta)^m}{(a_1)^{m+1} (\eta^{\alpha+1}+\varrho)^m}\right\}, \\ &= \sum_{m=0}^{\infty} \frac{(-1)^m (d_1)^m}{(a_1)^{m+1}} t^{m\alpha-1} E_{\alpha+1, m\alpha}^m(-\varrho t^{\alpha+1}).\end{aligned}$$

The inverse Laplace of Eq. (31), the required velocity field solution, is finally written as

$$u(\varphi, t) = \omega(\varphi, t) + Gr\Psi(\varphi, t) * [T(\varphi, t) - \omega(\varphi, t)]. \quad (34)$$

#### 4.3.2 Solution in the absence of magnetic and porosity parameter

In this scenario, let us assume that  $M = 0$  and  $\frac{1}{K} = 0$  in the velocity equation (25), resulting in the following simplified form:

$$\begin{aligned}\bar{u}(\varphi, \eta) &= \left(\frac{1-e^{-\eta}}{\eta^2}\right) e^{-\varphi \sqrt{\frac{1}{b} \left(\frac{\eta}{\eta^{\alpha+1}+\varrho}\right)}} \\ &+ \frac{Gr(1-e^{-\eta})}{\eta^2 \left(b\theta Q + \frac{d\eta}{\eta^{\alpha+1}+\varrho}\right)} \left[ e^{-\varphi \sqrt{\theta \left(\frac{\eta}{\eta^{\alpha+1}+\varrho}-Q\right)}} - e^{-\varphi \sqrt{\frac{1}{b} \left(\frac{\eta}{\eta^{\alpha+1}+\varrho}\right)}} \right].\end{aligned} \quad (35)$$

To find Laplace inverse of Eq. (35), first we write it in the following form:

$$\begin{aligned}\bar{u}(\varphi, \eta) &= \bar{\Psi}(\varphi, \eta) \\ &+ Gr\bar{\omega}(\varphi, \eta) [\bar{T}(\varphi, \eta) - \bar{\Psi}(\varphi, \eta)]\end{aligned} \quad (36)$$

and

$$\bar{\Psi}(\varphi, \eta) = \bar{\omega}_1(\varphi, \eta) - e^{-\eta} \bar{\omega}_1(\varphi, \eta). \quad (37)$$

After the application of Laplace inverse operator, Eq. (37) is turn out again in the time variable as

$$\Psi(\varphi, t) = \Psi_1(\varphi, t) - \Psi_1(\varphi, t)P(t-1), \quad (38)$$

where

$$\begin{aligned}\Psi_1(\varphi, t) &= L^{-1}\{\overline{\Psi_1}(\varphi, \eta)\} = L^{-1}\left\{\frac{1}{\eta^2} e^{-\varphi \sqrt{\frac{1}{b} \left(\frac{\eta}{\eta^{\alpha+1}+\varrho}\right)}}\right\}, \\ &= L^{-1}\left\{\frac{1}{\eta^2} \sum_{\chi=0}^{\infty} \sum_{n=0}^{\infty} \frac{(-\varphi)^{\chi} \Gamma(\frac{\chi}{2}+1)(\eta)^n}{\chi! n! (b)^{\frac{\chi}{2}} \Gamma(\frac{\chi}{2}-n+1)(\eta^{\alpha+1}+\varrho)^n}\right\}, \\ &= \sum_{\chi=0}^{\infty} \sum_{n=0}^{\infty} \frac{(-\varphi)^{\chi} \Gamma(\frac{\chi}{2}+1)}{\chi! n! (b)^{\frac{\chi}{2}} \Gamma(\frac{\chi}{2}-n+1)} t^{n\alpha+1} E_{\alpha+1, n\alpha+2}^n(-\varrho t^{\alpha+1}), \\ \bar{\omega}(\varphi, t) &= L^{-1}\{\overline{\omega}(\varphi, \eta)\} = L^{-1}\left\{\frac{1}{b\theta Q + \frac{d\eta}{\eta^{\alpha+1}+\varrho}}\right\}, \\ &= L^{-1}\left\{\sum_{m=0}^{\infty} \frac{(-1)^m (d)^m (\eta)^m}{(b\theta Q)^{m+1} (\eta^{\alpha+1}+\varrho)^m}\right\},\end{aligned}$$

$$= \sum_{m=0}^{\infty} \frac{(-1)^m (d)^m}{(b\theta Q)^{m+1}} t^{m\alpha-1} E_{\alpha+1, m\alpha}^m (-\beta t^{\alpha+1}).$$

The inverse Laplace of Eq. (36), the required velocity field solution, is finally written as

$$u(\varphi, t) = \Upsilon(\varphi, t) + Gr\omega(\varphi, t) * [T(\varphi, t) - \Upsilon(\varphi, t)]. \quad (39)$$

## 5. RESULTS AND DISCUSSION

This study focuses on analysing the heat transfer in the natural convective flow of Casson fluid under the influence of MHD. The aim is to derive analytical solutions using the non-integer-order derivative YAC model. The fluid flow occurs along the  $\varphi$ -axis, and a dimensionless system of equations representing the phenomenon is solved using integral LT. The results obtained are presented in series form and also expressed in terms of special functions. To visually depict the effects of various physical parameters, such as the memory parameter ( $\alpha$ ), Prandtl number ( $P_r$ ), Casson parameter ( $\beta$ ), heat absorption parameter ( $Q$ ), thermal Grashof number ( $G_r$ ), magnetic parameter ( $M$ ), chemical reaction rate ( $N_r$ ) and porosity parameter ( $K$ ), graphical illustrations are utilized. Figs. 2–11 portray the velocity and temperature distribution of the Casson fluid under different parameter values using graphical software.

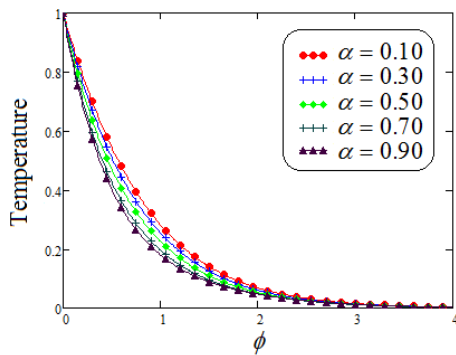


Fig. 2. Influence of Casson fluid temperature against  $\varphi$  for multiple values of  $\alpha$

Fig. 2 illustrates the influence of the memory parameter on the temperature profile. As the value of  $\alpha$  increases, the boundary layer thickens, leading to a decrease in temperature. The validity of the obtained result can be easily confirmed by considering the limit as  $\alpha \rightarrow 1$ . The Prandtl number is a dimensionless quantity that characterizes the relative importance of momentum diffusion to thermal diffusion in a fluid. It provides valuable information about the rate of heat transfer and the thermal boundary layer in various fluid flow systems. The prevalence of mass diffusivity in fluid flow leads to a decrease in the thermal boundary layer, consequently causing a reduction in temperature. These effects, as demonstrated in Fig. 3, can be attributed to the influence of the Prandtl number  $P_r$ . Fig. 4 depicts the influence of the radiation parameter  $N_r$  on the temperature distribution of Casson fluid for different values. The graphs reveal that the energy profile increases as the  $N_r$  values increase. Physically, as the heat flux changes, it leads to a reduction in  $k_1$  along the plate in the normal direction. This indicates that a greater amount of heat radiation is absorbed by the fluid, resulting in an elevated temperature profile.

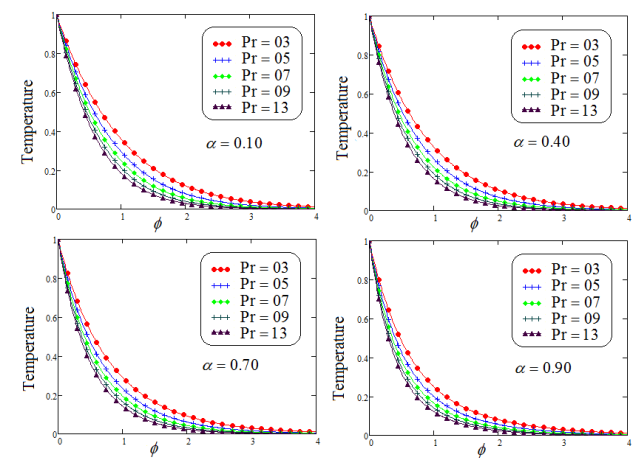


Fig. 3. Representation of Casson fluid temperature against  $\varphi$  for multiple values of  $P_r$

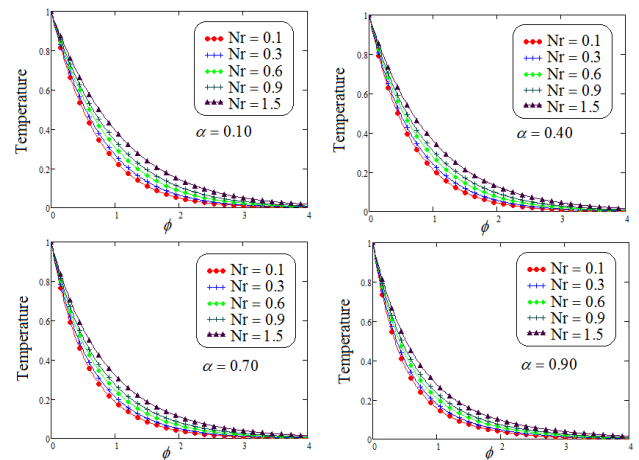


Fig. 4. Representation of Casson fluid temperature against  $\varphi$  for multiple values of  $N_r$

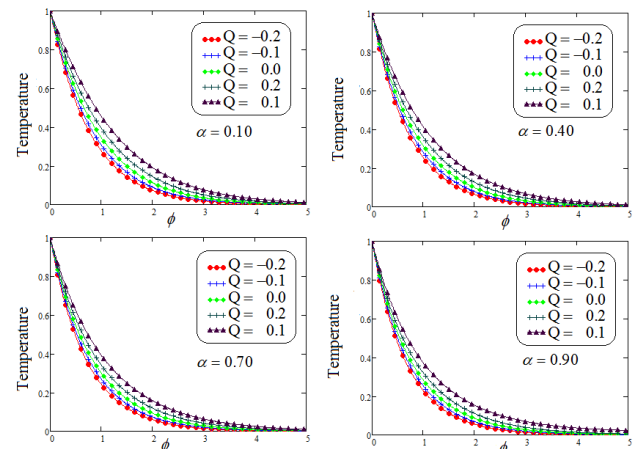


Fig. 5. Representation of Casson fluid temperature against  $\varphi$  for multiple values of  $Q$

Fig. 5 illustrates the correlation between the quantity of heat, whether extracted ( $Q < 0$ ) or supplied ( $Q > 0$ ), and temperature. It can be observed that the energy profile increases as the values of  $Q$  rise, indicating the considerable impact of heat extraction or generation in cooling and heating procedures. Furthermore, Fig. 6 exhibits the influence of parameter  $\alpha$  on the fluid

flow. The descending velocity curves provide a clear representation of how varying values of  $\alpha$  impact the flow behaviour. Fig. 7 describes the influence of the Casson fluid parameter,  $\beta$ , on the velocity graphs of the Casson fluid in relation to  $\phi$ . Various values of  $\beta$  were selected to examine the effects on different fluidic parameters.

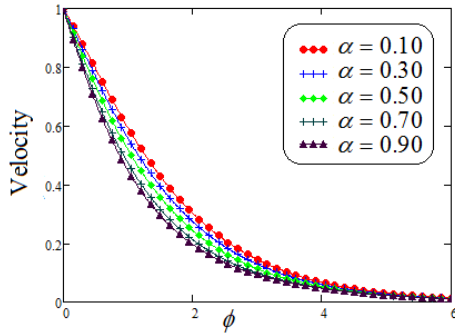


Fig. 6. Velocity representation for multiple values of  $\alpha$

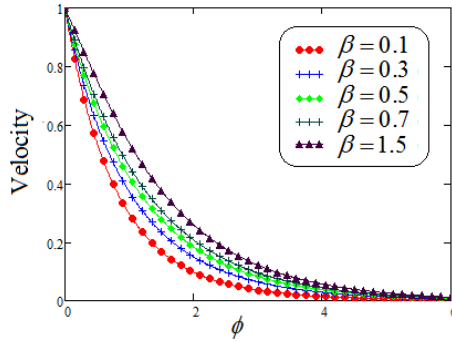


Fig. 7. Velocity representation for multiple values of  $\beta$

Fig. 8 depicts the effect of the Prandtl number, denoted as  $P_r$ , on the velocity of Casson fluid as a function of  $\phi$ , while considering different values of  $P_r$  at four distinct fractional parameter values of  $\alpha$ . It is noteworthy that the Prandtl number plays a significant role in determining the behaviour of the Casson fluid velocity profile within the boundary layer. As the values of  $P_r$  vary, noticeable changes in the velocity distribution within the boundary layer are observed as decay in the boundary layer of velocity noticed corresponding to rise in the distinct values of  $P_r$ . To provide a more comprehensive understanding of the impact of the Grashof number  $G_r$ , Fig. 9 has been plotted. The Grashof number represents the ratio between buoyancy force and viscous force. As  $G_r$  increases, indicating a higher fraction of buoyancy force compared to viscous force, the fluid velocity experiences a significant boost. This acceleration in fluid velocity is a direct result of the increasing value of  $G_r$ .

Fig. 10 elucidates the influence of the permeability parameter  $K$  on the velocity profiles of the Casson fluid with respect to  $\phi$ . Different values of  $K$  were chosen to examine the impact of small and large  $\alpha$  values. An increase in the porosity of the medium weakens the resistive force, leading to an enhancement in the flow regime due to momentum development. The graph clearly depicts an elevation in the velocity profile as  $K$  values increase under ramped conditions.

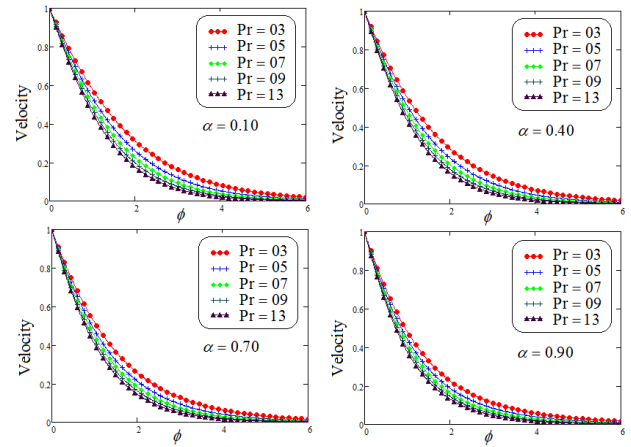


Fig. 8. Velocity representation for multiple values of  $P_r$

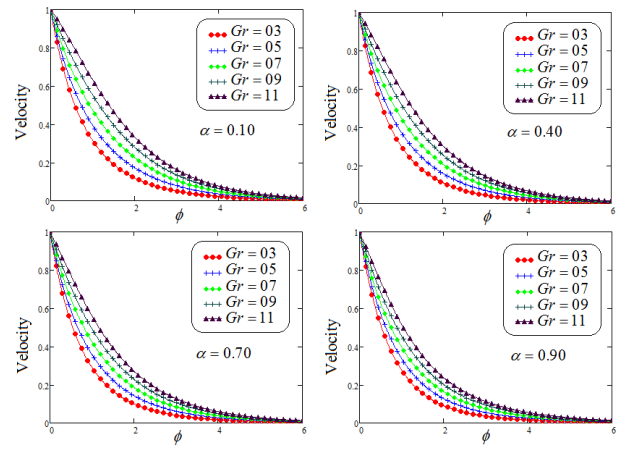


Fig. 9. Velocity representation for multiple values of  $G_r$

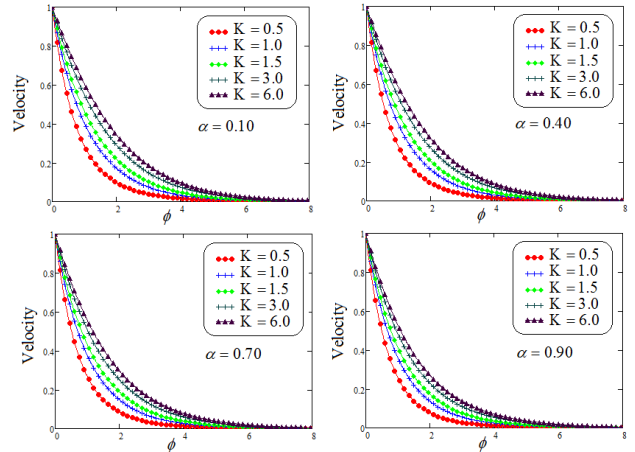


Fig. 10. Velocity representation for multiple values of  $K$

Fig. 11 interprets the influence of the magnetic number  $M$  on the momentum profile concerning  $\phi$ , by assigning different values of  $M$  in the velocity equation. This visualization aims to demonstrate the physical behaviour of the velocity of Casson fluid corresponding to various fractional parameter values. The results show that both the magnitude of the boundary layer thickness and the

velocity decrease when a strong magnetic field is applied. Consequently, this observation indicates that the fluid experiences a slow down as the magnetic number increases, as the dragging forces dominate over the flow-supporting forces. Ultimately, the velocity contour diminishes as the magnetic number values increase.

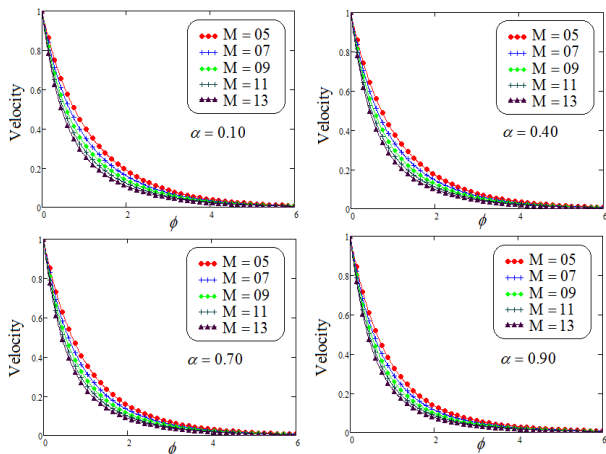


Fig. 11. Velocity representation for multiple values of  $M$

## 6. CONCLUSION

This research article aims to explore the behaviour of MHD natural convective flow of Casson fluid, a type of non-Newtonian fluid, by obtaining analytical solutions using the non-integer-order derivative known as YAC. The study focuses on the fluid flow in the vicinity of an infinitely vertical plate. To analyse the system of equations governing the flow, the LT technique is employed. This mathematical tool helps in transforming the equations into a different domain, where they can be solved more effectively. By applying the LT to the fractional system of equations, the researchers are able to derive solutions in a series form, which provides a mathematical representation of the behaviour of the Casson fluid under MHD natural convective flow conditions. Furthermore, the obtained solutions are presented using special functions, which are mathematical functions that have specific properties and are commonly used to describe complex phenomena. The use of special functions allows for a more concise and precise representation of the results. The researchers analyse the graphical behaviour of the solutions to gain insights into the characteristics of the Casson fluid flow. These graphical representations provide valuable information about various aspects of the flow, such as velocity profiles and heat distribution. By observing the trends and patterns in the graphs, important key points can be identified and expressed as follows:

- With an increase in the memory parameter  $\alpha$ , the velocity field and temperature experience a gradual decrease. In other words, higher values of  $\alpha$  result in lower velocities and temperatures.
- When the Prandtl number  $P_r$  increases, it indicates a higher ratio of momentum diffusivity to thermal diffusivity in a fluid. In practical terms, this means that the fluid is more efficient at transferring momentum than heat. As a result, both the velocity field and temperature exhibit a decreasing trend.
- As the values of the parameters  $N_r$  and  $Q$  increase, the effect on the temperature profile becomes more pronounced.

A higher  $N_r$  implies a greater influence of radiation, leading to elevated temperatures. Similarly, an increase in the heat injection/suction parameter  $Q$  amplifies the impact on the temperature distribution, resulting in higher temperatures.

- Elevated values of the parameters  $G_r$  and  $K$  have a positive effect on the velocity of the Casson fluid, resulting in an increase in its flow speed. The larger the values of  $G_r$  and  $K$ , the greater the enhancement observed in the velocity of the Casson fluid.
- When the magnetic number  $M$  increases, the impact of magnetic forces on the fluid becomes more significant. This increased influence results in a reduction in the fluid velocity. The magnetic forces act as a resistance, impeding the fluid flow and causing a decrease in velocity as the magnetic number increases.

## REFERENCES

1. Kahshan M, Lu D, Siddiqui AM. A Jeffrey fluid model for a porous-walled channel: Application to flat plate dialyzer, *Sci. Rep.* 2019;9(1):1-18.
2. Mohebbi R, Delouei AA, Jamali A, Izadi M, Mohamad AA. Pore-scale simulation of non-Newtonian power-law fluid flow and forced convection in partially porous media: Thermal lattice Boltzmann method, *Physica A*. 2019; 525: 642-656.
3. Riaz MB, Rehman AU, Wojciechowski A, Atangana A. Heat and mass flux analysis of magneto-free-convection flow of Oldroyd-B fluid through porous layered inclined plate. *Sci Rep.* 2023;13: 653. <https://doi.org/10.1038/s41598-022-27265-w>
4. Riaz MB, Abro KA, Abualnaja KM, Akgül A, Rehman AU, Abbas M, Hamed YS. Exact solutions involving special functions for unsteady convective flow of magnetohydrodynamic second grade fluid with ramped conditions, *Advances in Difference Equations*. 2021; 408. <https://doi.org/10.1186/s13662-021-03562-y>
5. Riaz MB, Awrejcewicz J, Rehman AU. Functional Effects of Permeability on Oldroyd-B Fluid under Magnetization: A Comparison of Slipping and Non-Slipping Solutions. *Appl. Sci.* 2021; 11: 11477 <https://doi.org/10.3390/app112311477>.
6. Khan Z, Tairan N, Mashwani WK, Rasheed HU, Shah ., Khan W. MHD and slip effect on two-immiscible third grade fluid on thin film flow over a vertical moving belt, *Open Phys.* 2019; 17 (1): 575-586.
7. Casso N. A flow equation for pigment-oil suspensions of the printing ink type. In *Rheology of Disperse Systems*. Ed. Mill, C. C. Pergamon Press, Oxford. 1959; 84-104.
8. Hussain M, Ali A, Ghaffar A. et al. Flow and thermal study of MHD Casson fluid past a moving stretching porous wedge. *J Therm Anal Calorim.* 2022;147:6959-6969. <https://doi.org/10.1007/s10973-021-10983-0>
9. Hussain M, Ghaffar A, Ali A, Shahzad A, Nisar KS, Alharthi MR, Jamshed W. MHD thermal boundary layer flow of a Casson fluid over a penetrable stretching wedge in the existence of nonlinear radiation and convective boundary condition, *Alexandria Engineering Journal*. 2021;60(6):5473—5483. <https://doi.org/10.1016/j.aej.2021.03.042>
10. Ali A, Hussain M, Anwar MS. et al. Mathematical modeling and parametric investigation of blood flow through a stenosis artery. *Appl. Math. Mech.-Engl. Ed.* 2021; 42:1675-1684. <https://doi.org/10.1007/s10483-021-2791-8>
11. Khalid A, Khan I, Khan A, Shafie S. Unsteady MHD free convection flow of Casson fluid past over an oscillating vertical plate embedded in a porous medium. *Eng. Sci. Technol. Int. J.* 2015;18(3):309-317.
12. Hussain M, Ali A, Inc M, Sene N, Hussain M. Impacts of Chemical Reaction and Suction/Injection on the Mixed Convective Williamson Fluid past a Penetrable Porous Wedge, *Journal of Mathematics*. 2022. <https://doi.org/10.1155/2022/3233964>
13. Bhattacharyya K, Hayat T, Alsaedi A. Analytic solution for magneto-hydrodynamic boundary layer flow of Casson fluid over a stretch-

ing/shrinking sheet with wall mass transfer. *Chin. Phys. B.* 2013;22(2): 024702.

14. Oka S. An approach to  $\alpha$  unified theory of the flow behavior of time-independent non-Newtonian suspensions. *Jpn. J. Appl. Phys.* 1971; 10(3): 287.
15. Riaz MB, Awrejcewicz J, Rehman AU, Abbas M. Special functions-based solutions of unsteady convective flow of a MHD Maxwell fluid for ramped wall temperature and velocity with concentration. *Advances in Difference Equations* 2021. <https://doi.org/10.1186/s13662-021-03657-6>
16. Hussain Z, Alshomrani AS, Muhammad T, Anwar MS. Entropy analysis in mixed convective flow of hybrid nanofluid subject to melting heat and chemical reactions, *Case Studies in Thermal Engineering*. 2022;34. <https://doi.org/10.1016/j.csite.2022.101972>.
17. Mermone AV, Mazumdar JN, Lucas SK. A mathematical study of peristaltic transport of a Casson fluid. *Math. Comput. Model.* 2002; 35(7-8): 895-912.
18. Arthur EM, Seini IY, Bortteir B. Analysis of Casson fluid flow over a vertical porous surface with chemical reaction in the presence of magnetic field. *J Appl. Math. Phys.* 2015;3:713-723.
19. Mukhopadhyay S. Effects of thermal radiation on Casson fluid flow and heat transfer over an unsteady stretching surface subjected to suction/blowing. *Chin. Phys. B.* 2013;22(11): 114702.
20. Mustafa M, Hayat T, Pop I, Aziz A. Unsteady boundary layer flow of a Casson fluid due to an impulsively started moving flat plate. *Heat Transf.* 2011;40(6): 563-576.
21. Rehman AU, Riaz MB, Khan I, Mohamed A. Time fractional analysis of Casson fluid with application of novel hybrid fractional derivative operator. *AIMS Mathematics*, 2023; 8(4): 8185-8209. <https://doi.org/10.3934/math.2023414>.
22. Riaz MB, Rehman AU, Awrejcewicz J, Akgül A. Power Law Kernel Analysis of MHD Maxwell Fluid with Ramped Boundary Conditions: Transport Phenomena Solutions Based on Special Functions. *Fractal Fract.* 2021;5:248. <https://doi.org/10.3390/fractfract5040248>.
23. Rehman AU, Riaz MB, Rehman W, Awrejcewicz J, Baleanu D. Fractional Modeling of Viscous Fluid over a Moveable Inclined Plate Subject to Exponential Heating with Singular and Non-Singular Kernels. *Math. Comput. Appl.* 2022; 27: 8. <https://doi.org/10.3390/mca27010008>
24. Kumar S, Ghosh S, Samet B, Doungmo Goufo EF. An analysis for heat equations arises in diffusion process using new Yang-Abdel-Aty-Cattani fractional operator. *Mathematical Methods in the Applied Sciences*. 2020;43(9):6062-6080. <https://doi.org/10.1002/mma.6347>.
25. Bagley RL, Torvik PJ. A theoretical basis for the application of fractional calculus to viscoelasticity, *J. Rheol.* 1983; 27 (3): 201-210.
26. Rehman AU, Riaz MB, Atangana A, Jarad F, Awrejcewicz J. Thermal and concentration diffusion impacts on MHD Maxwell fluid: A generalized Fourier's and Fick's perspective, *Case Studies in Thermal Engineering*. 2022;35. <https://doi.org/10.1016/j.csite.2022.102103>
27. Riaz MB, Awrejcewicz J, Rehman AU, Akgül A. Thermophysical Investigation of Oldroyd-B Fluid with Functional Effects of Permeability: Memory Effect Study Using Non-Singular Kernel Derivative Approach. *Fractal Fract.* 2021; 5: 124. <https://doi.org/10.3390/fractfract5030124>
28. Rehman AU, Jarad F, Riaz MB, Shah ZH. Generalized Mittag-Leffler Kernel Form Solutions of Free Convection Heat and Mass Transfer Flow of Maxwell Fluid with Newtonian Heating: Prabhakar Fractional Derivative Approach. *Fractal Fract.* 2022; 6: 98. <https://doi.org/10.3390/fractfract6020098>.
29. Mohammadi H, Kumar S, Rezapour S, Etemad S. A theoretical study of the Caputo-Fabrizio fractional modeling for hearing loss due to Mumps virus with optimal control. *Chaos, Solitons & Fractals*. 2021; 144. <https://doi.org/10.1016/j.chaos.2021.110668>.
30. Rehman AU, Riaz MB, Wojciechowski A. Thermo diffusion impacts on the flow of second grade fluid with application of (ABC), (CF) and (CPC) subject to exponential heating. *Sci Rep.* 2022; 12:18437 <https://doi.org/10.1038/s41598-022-21773-5>.
31. Kumar S, Nisar KS, Kumar R, Cattani C, Samet B. A new Rabotnov fractional-exponential function-based fractional derivative for diffusion equation under external force. *Mathematical Methods in the Applied Sciences*. 2020; 43(7): 4460-4471. <https://doi.org/10.1002/mma.6208>
32. Jleli M, Kumar S, Kumar R, Samet B. Analytical approach for time fractional wave equations in the sense of Yang-Abdel-Aty-Cattani via the homotopy perturbation transform method, *Alexandria Engineering Journal*. 2020; 59(5): 2859-2863. <https://doi.org/10.1016/j.aej.2019.12.022>
33. Hayat T, Sajjad R, Asghar S. Series solution for MHD channel flow of a Jeffery fluid, *Commun. Nonlin. Sci. Numer. Simulat.* 2010; 15(9):2400-2406. <https://doi.org/10.1016/j.cnsns.2009.09.033>.
34. Kumar S, Chauhan RP, Momani S., Hadid S. Numerical investigations on COVID-19 model through singular and non-singular fractional operators. *Numerical Methods for Partial Differential Equations*. <https://doi.org/10.1002/num.22707>.
35. Rehman AU, Riaz MB., Saeed ST, Jarad F, Jasim H N., Enver A. An Exact and Comparative Analysis of MHD Free Convection Flow of Water-Based Nanoparticles via CF Derivative, *Mathematical Problems in Engineering*. 2022. <https://doi.org/10.1155/2022/9977188>.
36. Riaz MB, Rehman AU, Awrejcewicz J. Double Diffusive Magnetofree-Convection Flow of a Maxwell Fluid Over a Vertical Plate: Special Functions Based Analysis using Local and Non-Local Kernels to Heat and Mass Flux subject to Exponential Heating, *Fractals*. 2022; 30(5). <https://doi.org/10.1142/S0218348X22401570>.
37. Rehman AU, Riaz MB, Atangana A. Time fractional analysis of Casson fluid with Rabotnov exponential memory based on the generalized Fourier and Fick... s law, *Scientific African*. 2022;17: e01385, <https://doi.org/10.1016/j.sciaf.2022.e01385>.
38. Kumar S, Kumar A, Samet B, Dutta H. A study on fractional host-parasitoid population dynamical model to describe insect species. *Numerical Methods for Partial Differential Equations*. 2021; 37(2): 1673-692. <https://doi.org/10.1002/num.22603>.
39. Anwar MS, Irfan M, Hussain M, Muhammad T, Hussain Z. Heat Transfer in a Fractional Nanofluid Flow through a Permeable Medium, *Mathematical Problems in Engineering*. 2022. <https://doi.org/10.1155/2022/3390478>
40. Anwar T, Kumam P, Watthayu W. Unsteady MHD natural convection flow of Casson fluid incorporating thermal radiative flux and heat injection/suction mechanism under variable wall conditions. *Sci Rep.* 2021;11: 4275. <https://doi.org/10.1038/s41598-021-83691-2>.
41. Khalid A, Khan I, Khan A, Shafie S. Unsteady MHD free convection flow of Casson fluid past over an oscillating vertical plate embedded in a porous medium. *Eng. Sci. Technol. Int. J.* 2015;18(3):309-317
42. Mustafa M, Khan JA. Model for flow of Casson nanofluid past a non-linearly stretching sheet considering magnetic field effects. *AIP Adv.* 2015;5(7): 077148.
43. Yang XJ, Abdel-Aty M, Cattani C. A new general fractional order derivative with Rabotnov fractional exponential kernel applied to model the anomalous heat. *Thermal Science*. 2019; 23(3A): 1677-1681.

Aziz Ur Rehman:  <https://orcid.org/0000-0002-8804-3915>Fahd Jarad:  <https://orcid.org/0000-0002-3303-0623>Muhammad Bilal Riaz:  <https://orcid.org/0000-0001-5153-297X>

This work is licensed under the Creative Commons BY-NC-ND 4.0 license.

## THE CO<sub>2</sub> CAPTURE SYSTEM WITH A SWING TEMPERATURE MOVING BED

Ewa KOZAK-JAGIEŁA<sup>\*ID</sup>, Monika RERAK<sup>\*ID</sup>, Wiesław ZIMA<sup>\*ID</sup>, Artur CEBULA<sup>\*ID</sup>, Sławomir GRĄDZIEL<sup>\*ID</sup>, Giorgia MONDINO<sup>\*\*ID</sup>, Richard BLOM<sup>\*\*ID</sup>, Lars O. NORD<sup>\*\*\*ID</sup>, Vidar T. SKJERVOLD<sup>\*\*\*ID</sup>

<sup>\*</sup>Politechnika Krakowska, Al. Jana Pawła II 37, 31-864 Kraków, Poland

<sup>\*\*</sup>SINTEF Industry, PO Box 124 Blindern, Oslo N0314, Norway

<sup>\*\*\*</sup>NTNU - Norwegian University of Science and Technology, Department of Energy and Process Engineering, Trondheim, Norway

[ewa.kozak@pk.edu.pl](mailto:ewa.kozak@pk.edu.pl), [monika.rerak@pk.edu.pl](mailto:monika.rerak@pk.edu.pl), [wieslaw.zima@pk.edu.pl](mailto:wieslaw.zima@pk.edu.pl), [artur.cebula@pk.edu.pl](mailto:artur.cebula@pk.edu.pl), [slawomir.gradziel@pk.edu.pl](mailto:slawomir.gradziel@pk.edu.pl),  
[giorgia.mondino@sintef.no](mailto:giorgia.mondino@sintef.no), [richard.blom@sintef.no](mailto:richard.blom@sintef.no), [lars.nord@ntnu.no](mailto:lars.nord@ntnu.no), [vidar.t.skjervold@ntnu.no](mailto:vidar.t.skjervold@ntnu.no),

received 28 February 2023, revised 19 June 2023 accepted 6 July 2023

**Abstract:** The reduction in CO<sub>2</sub> emissions is now a very popular topic. According to the International Energy Agency, CO<sub>2</sub> emitted in 2021 was 6% more than that emitted in 2020. Carbon capture and storage (CCS) is gaining popularity as a possible solution to climate change. Experts estimate that industry and power plants will be responsible for 19% of total CO<sub>2</sub> emissions by 2050. This paper presents the design of a semi-industrial-scale system for CO<sub>2</sub> capture based on the moving bed temperature swing adsorption technology. According to the results of laboratory tests conducted by the SINTEF industry, this technology demonstrates high capture efficiency (>85%). The CO<sub>2</sub> capture medium involved in adsorption is activated carbon passing through individual sections (cooling, heating, adsorption), where CO<sub>2</sub> is bonded and then released. The heat and mass transfer processes are realised on the developed stand. The heat exchangers use steam and water as the heating/cooling medium. The paper reviews the existing solutions and describes the developed in-house design of heat exchangers that will ensure heat transfer conditions being a trade-off between economic and efficiency-related issues of the CO<sub>2</sub> capture process. The designed test stand will be installed in a Polish power plant and is expected to meet the method energy intensity target, set at  $\leq 2.7$  MJ/kg CO<sub>2</sub>, with a capture efficiency exceeding 85%. The aim of the work was to develop and solve technical problems that would lead to the construction of a CO<sub>2</sub> capture station with parameters mentioned above. This stand uses an innovative method where CO<sub>2</sub> is captured by contacting the fluid (gases) with solid particles. The heat exchange associated with the heating and cooling of the adsorbent had to be solved. For this purpose, heat exchangers were designed with high thermal efficiency and to prevent the formation of mounds.

**Key words:** heat and mass transfer, CO<sub>2</sub> capture, moving bed temperature swing adsorption, test stand

### 1. INTRODUCTION

Reducing CO<sub>2</sub> emissions in line with the European Green Deal has become a very important topic. According to a report by the International Energy Agency, as much as 36.3 billion tons of CO<sub>2</sub> were produced in 2021, which is more than 6% than that produced the year before – which is the highest level ever [1]. The same agency estimates that the share of CO<sub>2</sub> emissions from industry and power plants will increase from 3% in 2020 to 19% in 2050 [2,3]. For this reason, the carbon capture and storage (CCS) technology has become one of the most promising and necessary solutions to combat climate change [4]. Carbon capture (CC) is a solution which makes it possible to continue the use of fossil fuels, minimising at the same time the amount of CO<sub>2</sub> released into the atmosphere, thus mitigating global climate changes. Great efforts are being made around the world to develop a highly efficient CO<sub>2</sub> capture technology consuming little energy.

The CO<sub>2</sub> capture technology mainly includes three methods: pre-combustion capture, oxy-combustion and post-combustion capture [5]. The first method involves avoiding the mixing of CO<sub>2</sub> with air, through conversion processes of carbon contained in the fuel to make it possible to remove CO<sub>2</sub> from the gases.

Such processes include coal gasification or reforming of oil and gas fuels.

Oxy-combustion involves the use of air significantly enriched

with oxygen. Such air is obtained by a prior process which removes nitrogen. The technology makes use of recirculation of a portion of combustion gases consisting mainly of CO<sub>2</sub> and O<sub>2</sub> to lower the furnace temperature and increase CO<sub>2</sub> concentration.

Post-combustion capture can be implemented, for example, by absorption, cryogenic separation, membrane process or adsorption [6,7]. Depending on the applied method, the process requires energy necessary for compression, cooling and extraction for the solvent regeneration and needs to ensure a highly efficient desulphurisation process. However, the main advantage of the post-combustion capture method is that it does not require major modifications to existing power plants [8].

The absorption process involves passing cooled and pre-treated combustion gases through an absorption column, where a significant portion of the CO<sub>2</sub> is absorbed through contact with a solvent. The CO<sub>2</sub>-rich solvent then passes through a desorber responsible for releasing carbon dioxide, which is compressed and purified in the next step.

Membrane separation is based on the occurrence of differences in the physicochemical and chemical interactions between the membrane material and the components of the gas mixture, which is related to the difference in the rate of permeation of the gas components through the membrane. The membrane is responsible for dividing combustion gases into the permeating stream and the stopped stream.

The cryogenic method involves compression and cooling of the gas to a temperature of about  $-56^{\circ}\text{C}$ , followed by separation of CO<sub>2</sub> in the liquid form. The selectivity of the cryogenic fractionation process results from the different conditions of condensation of individual components of combustion gases.

The last post-combustion capture method – adsorption – is based on physical attraction of gas and solids. The following materials with a large specific surface area are used as a CO<sub>2</sub> separation medium in the adsorption process: zeolites, activated carbon, aluminium oxide or silica and alumina gel. Three kinds of CO<sub>2</sub> adsorption are used for separation:

- pressure swing adsorption (PSA) – the adsorbent is regenerated through a reduction in pressure,
- temperature swing adsorption (TSA) – the adsorbent is regenerated through a rise in temperature,
- electric swing adsorption (ESA) – regeneration proceeds by passing a low-voltage electric current through the adsorbent.

Currently, adsorption is widely recognised as an attractive method for small and medium-sized CO<sub>2</sub> emitters due to its low energy consumption and low operating cost [9,10]. The moving bed temperature swing adsorption (MBTSA) is a promising technology for capturing CO<sub>2</sub> from combustion gases. In an MBTSA unit, selective adsorbing material circulates between the low-temperature stage, where it removes CO<sub>2</sub> from combustion gases, and the zone with a higher temperature, where it desorbs CO<sub>2</sub> with greater purity. Given these advantages, various solid adsorbents are used to capture CO<sub>2</sub>, including zeolites, metal-organic frameworks (MOFs), silica materials, carbon materials and functionalised adsorbents [11,12]. Studies have shown that activated carbon can successfully capture CO<sub>2</sub> because it has a large surface area per unit volume, as well as a large surface area of submicroscopic pores in which adsorption of impurities occurs. Moreover, activated carbon is stable in acidic and alkaline conditions. The activated carbon discussed here, with the trade name G-BAC, was manufactured by Kureha and has a spherical shape. The shape, as well as the particle size, of the activated carbon is significant here because of its adsorption properties. In an experiment conducted by a team from SINTEF [34], this activated carbon showed a high, up to 95%, capture rate. The experiment was conducted for synthetic flue gases with a CO<sub>2</sub> content of 3.5 vol%, which is much lower than that found in flue gases from coal-fired power plants. Simulations were also carried out in gProms software for the composition of the flue gas as in a coal-fired power station, as to ensure that the CO<sub>2</sub> capture efficiency was sufficient. On this basis, an activated carbon adsorbent-based CO<sub>2</sub> capture system was designed. Activated carbon is also cost-effective due to the possibility of regeneration and is therefore suitable for the removal of organic compounds [13]. However, the adsorption bed is a costly and energy-intensive part of the MBTSA system; so, an appropriate design of the heat exchanger responsible for cooling, heating and adsorption of the working medium is of key importance to improving the efficiency of the entire process. Creating gas-granulate or liquid-granulate heat exchangers is a major challenge. Efficient heat transfer is affected by the geometry of the exchanger (shape and arrangement of tubes, hydraulic diameter), operating conditions (fluid flow velocity, the heating/cooling fluid temperature) and the adsorbent specific properties (shape and size of particles, density).

There are three mechanisms of the heat transfer between freely falling granules and the heat exchanger immersed surfaces

– particle convection, gas convection and radiation. In most dense gas-solid fluidised beds, the mixing of solids is the main cause of the convective heat transfer by particles [14].

Several factors are responsible for the convective heat transfer to the flowing sorbent: the contact surface area between the sorbent and the hot surfaces, the sorbent residence time, the flow pattern and also the mixing of the particles. For these reasons, determining the exchanger performance and, in particular, estimating the coefficient of the heat transfer from the sorbent to the medium flowing in the exchanger tubes is a challenge for any designer. In this paper, this coefficient is estimated, and the exchangers intended for the CO<sub>2</sub> capture system are designed.

## 2. DESIGNING AND TESTING HEAT EXCHANGERS

Researchers all over the world have been making efforts to design more efficient heat exchangers for many years. In this part of the paper, attention will be focused on the literature analysis in terms of designing and testing heat exchangers operating with a fluidised bed.

Wang et al. [15] proposed a transient model for the analysis of cryogenic desublimation of CO<sub>2</sub> in a gas mixture. The model includes a counter-current tube-in-tube heat exchanger with three control volumes, a nitrogen (or helium) cooling medium, a wall with a solid CO<sub>2</sub> layer and a gas mixture. The deposition distribution, the capture rate and the energy consumption for the CO<sub>2</sub> desublimation process are analysed in different operating conditions. The Nusselt number in the simulations is calculated using equations derived from the model function. Bahremand and Bahrami [16] described a 2D analytical model for the design of sorbent-bed heat exchangers of sorption cooling systems. The model covered all relevant thermophysical and sorptive properties, the heat exchanger geometry and operating conditions. Contact thermal resistance at the phase interface in sorption beds was also taken into account. The convective heat transfer coefficient adopted in the computations was calculated based on the Gnielinski correlation. More information on heat exchanger modelling can be found in the paper by Golparvar et al. [17], where a detailed three-dimensional non-equilibrium model was developed to study the effects of the heat and mass transfer in annular and longitudinal finned tube adsorber beds filled with zeolite 13X particles. The convective heat transfer coefficient in this paper was calculated for a fully developed flow using the Dittus-Boelter correlation for smooth tubes. It was observed that larger temperature gradients occur in an adsorption bed with a bigger fin spacing, leading to non-uniform adsorption and desorption processes in the entire heat exchanger. The Dittus-Boelter correlation for smooth tubes was also used to calculate the heat transfer coefficient by Zhang [18]. The paper presents a mathematical model of the conjugate heat and mass transfer in an adsorber in an intermittent adsorption cooling system. The model includes four submodels: the heat transfer in the heating/cooling fluids, the heat transfer in the metal tube, the heat transfer in the fins and the heat and mass transfer in the adsorbent. The model of the heat and mass transfer in the adsorbent (zeolite 13X) is a three-dimensional non-equilibrium model that takes account of the mass transfer both internal and external resistance in the adsorbent. The paper by Clausse et al. [19] compares an adsorber cooled indirectly in a TSA system and other adsorbents

classically investigated in TSA systems. A numerical model is presented and then validated using experimental testing results. Based on testing, the advantages of indirectly cooled adsorbers are demonstrated. The paper also describes the possibility of omitting the cooling stage in TSA cycles.

Hofer et al. [20] investigated the heat transfer between bubbling fluidised beds and the immersed surface of heat exchangers with respect to continuous TSA processes used for post-combustion CO<sub>2</sub> capture. Heat transfer coefficients for gas and particle properties were calculated using the models proposed by Natusch and Molerus. Fluidised beds were also investigated by Pirkbauer et al. [21], who studied different process configurations of a multi-stage fluidised bed for continuous temperature swing adsorption. The aim of the studies was to determine the optimum energy of the process. When CO<sub>2</sub> is used as the regeneration medium, the total energy demand of the TSA process increases as compared with a multi-stage TSA system that operates with steam as the separation medium. This research provides clear information on what configurations of continuous TSA processes of CO<sub>2</sub> capture are the most energy efficient. The topic of moving bed adsorption (MBA) was also taken up by Kim et al. [22]. The authors described this process with heat integration. The adsorbent particles and the combustion gases flow in opposite directions in the adsorption bed. In this case, a scheme is also proposed in which the thermal energy removed from the adsorption bed is used in the desorption bed, which increases the presented method efficiency. Post-combustion CO<sub>2</sub> capture was also studied by Schöny et al. [23]. In this case, steam is used as the removing agent on the desorber side. The optimal number of stages on the adsorber and desorber sides is investigated to achieve high energy efficiency of the separation process. It is concluded that the larger the heat transfer surfaces of heat exchangers the higher the CO<sub>2</sub> capture efficiency.

Mitra et al. [24] described typical adsorption heat exchangers, i.e. tube-and-fin assemblies with adsorbents placed between the heat exchange surfaces. The research was conducted for activated carbon as the adsorbent. The results show that the optimal geometry of the heat exchanger depends on the size of the adsorbent particle. Exchangers were also investigated by Hofer et al. [25]. The authors tested devices consisting of a single tube and multiple tubes operating in post-combustion CC processes. The authors developed design requirements for TSA stages based on the heat transfer coefficients achievable in bubbling fluidised beds. The testing results show that the heat transfer coefficients obtained experimentally for single tubes are in good agreement with the modelled values. The results obtained for tube banks could be applied for the heat transfer between bubbling fluidised beds and immersed surfaces of the heat exchanger. Sharafian et al. [26] carried out experimental testing of the effect of fin spacing on the temperature distribution of two adsorption beds using finned tubes with different fin spacing. The works included comparing the adsorption bed/adsorbent mass ratio and the temperature differences between the fins depending on the fin spacing. The researchers concluded that the optimal fin spacing of 6 mm was the best fit design for a finned tube adsorber filled with 2–4 mm silica gel particles.

It follows from the presented literature review that there are various designs of exchangers intended for CO<sub>2</sub> capture plants. Most of them are exchangers with an increased heat transfer surface area (finned tubes). This paper presents a CO<sub>2</sub> capture system based on the MBTSA technology which does not work as

a fluidised bed. In the presented system, the adsorbent is transported to individual sections where it is heated or cooled. In addition to a high coefficient of the heat transfer from the granulate to the surface of the tubes, the exchanger must ensure that the adsorbent flows through freely and is prevented from settling on the tubes. This rules out the use of fins, as they would create spaces for the adsorbent to accumulate, which would render the exchanger inefficient. The developed exchangers must reconcile the adsorbent transport with a high coefficient of the heat transfer from the granulate. The system with the developed in-house heat exchangers will be installed in one of the Polish power plants. The CO<sub>2</sub> capture system with the heat exchanger design is presented in Section 2.1 below.

## 2.1. Description of the CO<sub>2</sub> capture system

The method of CO<sub>2</sub> capture from combustion gases arising in the process of gas combustion and based on the MBTSA was described, among others, by SINTEF Industry in Norway [27]. The method was adapted to capture CO<sub>2</sub> in the case of pulverised coal combustion in a power boiler [28].

The method is based on using activated carbon in the moving bed adsorption process. This type of adsorbent was chosen for its properties. Activated carbons are considered suitable materials for CO<sub>2</sub> adsorption due to their porous structure - they have well-developed micro-porosity and mesoporosity. The high CO<sub>2</sub> adsorption capacity of activated carbons is due to their large surface area per unit volume, as well as the large area of submicroscopic pores in which impurities can be adsorbed. Carbon materials show lower sorption capacity and selectivity than zeolites but are nevertheless used in CO<sub>2</sub> gas purification processes. This is due to the interactions between activated carbon and CO<sub>2</sub>, which are much weaker than the bonding of carbon dioxide to zeolites. This has the effect of requiring less energy to carry out the desorption process and is more easily regenerated. The advantage of activated carbons is that they are regenerative, they do not wear out during multi-stage adsorption/desorption cycles and are therefore ideal for MBTSA adsorption plants. In addition, activated carbon does not require prior removal of moisture from the flue gas [33]. The main advantages of the MBTSA method are low pressure drops in the adsorption zone and the possibility of a faster rate of the adsorbent heating compared with standard adsorption technologies [13]. Preliminary results of the MBTSA simulations [29] allow a conclusion that the degree of CO<sub>2</sub> capture achieved in this method is higher than that of the existing methods based on chemical adsorption (MEA and DAE). In order to examine the method suitability for rapid changes in the power unit load, with a particular focus on a rapid increase in power, it is necessary to design and build a test stand for the proposed method for CO<sub>2</sub> capture from hard coal combustion gases. SINTEF Industry in Norway is now in possession of a laboratory-scale system, a schematic diagram of which is shown in Fig. 1. The system was re-designed to a semi-industrial scale. The exchangers on the laboratory-scale test stand were made using a 3D printer. Considering high printing costs, it was necessary to find an alternative, cheaper solution. Due to that, the semi-industrial system makes use of tube exchangers in a staggered configuration. Fig. 2 and Fig. 3 present the heat exchangers arranged in a triangular configuration. Such arrangement of the exchangers was selected due to the limitations imposed by the room height and to ensure uniform loading of the floor. Activated

carbon in the form of granules with the diameter of 0.7 mm was used as the moving bed. The granules are shown in Fig. 4. Due to the formation of bed mounds, preliminary tests were carried out to eliminate the phenomenon of the adsorbent getting stuck in between the exchangers. As a result, the tube diameter no bigger than 13.5 mm was selected.

The exchanger thermal calculations are presented in Section 2.2.

The test stand will be installed in a Polish power plant. In order to confirm the method suitability for close-to-real conditions, the measurements will be performed during the system operation in steady- and transient-state conditions.

## 2.2. Determination of the heat transfer coefficient

The heat exchanger design process was based on the classical logarithmic mean temperature difference method for a cross-flow heat exchanger, in which the exchanger power is calculated from the following basic equation (1):

$$\dot{Q} = \frac{\Delta T_{LM}}{R_{tot}}, \quad (1)$$

where:  $R_{tot}$  is heat transfer total resistance,  $\Delta T_{LM}$  is logarithmic mean temperature difference for the counter current system.

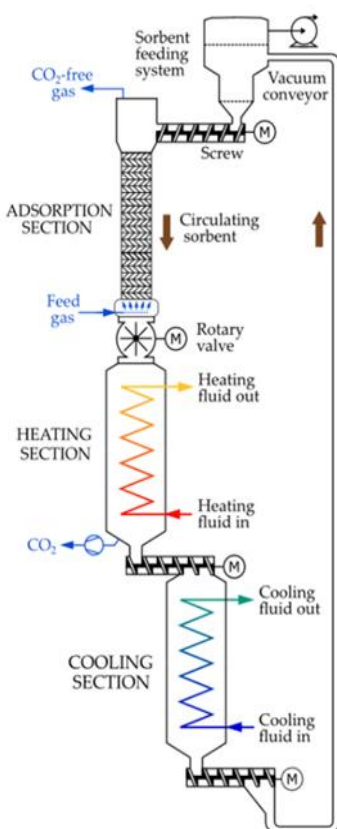


Fig. 1. Diagram of the laboratory system

The method was selected due to the fact that the adsorber temperatures at the inlets and outlets of the heating and cooling sections are known and result from the adsorber CO<sub>2</sub> capture property. According to the art of engineering, the following assumptions are adopted:

- steady-state operation of the exchanger,
- no heat losses to the environment,
- identical heat transfer coefficient across the entire heat transfer surface area,
- constant physicochemical properties of the working mediums.

Total thermal resistance was calculated from equation (2):

$$R_{tot} = R_w + R_t + R_s + R_{f,i} + R_{f,o} = \frac{1}{A_w \cdot h_w} + \frac{\ln(\frac{d_o}{d_i})}{2\pi \cdot r \cdot l} + \frac{1}{A_s \cdot h_s} + R_{f,i} + R_{f,o}, \quad (2)$$

where:  $R_w$  is resistance of the convective heat transfer from the inner surfaces of tubes to water,  $R_t$  is resistance of heat conduction through the tube walls,  $R_s$  is resistance of the heat flow on the sorbent side,  $R_{f,i}$  is resistance of heat conduction through impurities on the inner side and  $R_{f,o}$  is resistance of heat conduction through impurities on the outer side.

Equation (2) takes account of the resistance of impurities both on the inner and outer side of tubes. On the inner side, resistance  $R_{f,i}$  takes values like for boiling water: 0.0002 (m<sup>2</sup>·K)/W, whereas on the outer side,  $R_{f,o}$ , being the resistance of the activated carbon deposit, is adopted according to [30] at the level of 0.002 (m<sup>2</sup>·K)/W.

The coefficient of the heat transfer from the water flowing inside the tubes is calculated like for a transient flow because the calculated Reynolds number is included in the range from Re=300 to Re=3000. Due to that, a correlation is used based on function  $Nu=f(Re,Pr)$  for the following ranges of the dimensionless numbers: 2300≤Re≤106, 0.1≤Pr≤1000 [31]. The dimensionless numbers Nu, Re and Pr are defined as follows:

$$Nu = \frac{h d_w}{k}, \quad Re = \frac{w_m \cdot d_w}{v}, \quad Pr = \frac{c_p \cdot \mu}{k}. \quad (3)$$

The heat transfer coefficient on the side of the granulate was established experimentally on the laboratory stand in Norway and totals ~90 W/m<sup>2</sup>·K.

Assuming that the flow changes from laminar to transient at Re=2300, for which the Nusselt number is Nu=4.36, the correlation for the heat transfer coefficient is expressed by the following formula:

$$Nu = 4.36 + \frac{\frac{\xi}{8}(Re-2300)Pr^{x_1}}{x_2 + x_3 \sqrt{\frac{\xi}{8}(Pr^{\frac{2}{3}}-1)}}, \quad (4)$$

where friction factor  $x$  is given by Filonienko [32] and can be calculated according to Taler [31].

$$\xi = \frac{1}{(1.2776 \log Re - 0.406)^{2.246}} \cdot 2.10^3 \leq Re \leq 10^7. \quad (5)$$

The unknown values of friction factor  $x = (x_1, \dots, x_m)^T$  in equation (4) can be found using the least squares method:

$$S(x) = \sum_{i=1}^{n_{Re}} \sum_{j=1}^{n_{Pr}} (Nu_{ij}^m - Nu_{ij}^c)^2 = \min, \quad (6)$$

where:  $Nu_{ij}^m = Nu^m(Re_i, Pr_j)$  and  $Nu_{ij}^c = Nu(Re_i, Pr_j)$ ,  $i = 1, \dots, n_{Re}$ ,  $j = 1, \dots, n_{Pr}$  are the appropriately given, and approximated values of the Nusselt, Reynolds and Prandtl numbers are adopted as  $n_{Re} = 10$  and  $n_{Pr} = 16$ . The values of the factors obtained using the least squares method are as follows:

$$x_1 = 1.008 \pm 0.0050, x_2 = 1.08 \pm 0.0089, x_3 = 12.39 \pm 0.0080 [31].$$

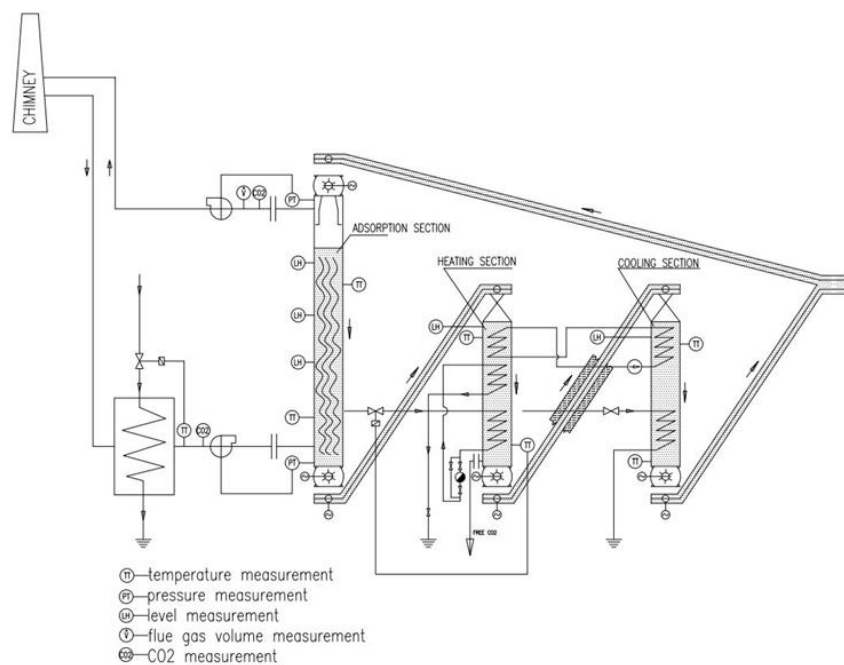


Fig. 2. Diagram of the semi-industrial system

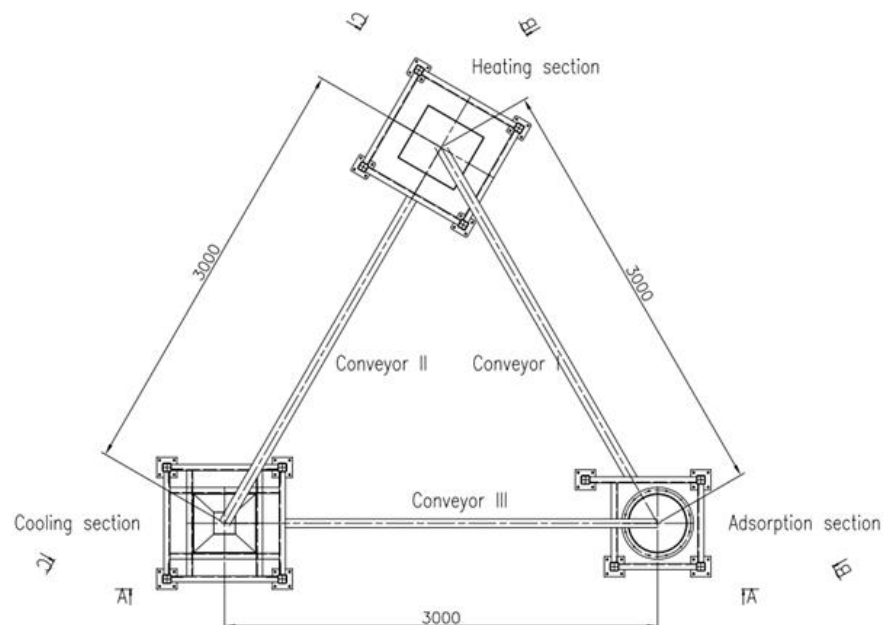


Fig. 3. Vertical projection of the semi-industrial system



Fig. 4. Activated carbon ([www.kureha.co.jp](http://www.kureha.co.jp))

### 2.3. Calculations of heat exchangers

The outcome of the thermal calculations and the applied equation (4) is the heat transfer surface area. The design details and the heat transfer surface area will be the subject of patent proceedings, and for this reason, they cannot be disclosed. Knowing the heat transfer surface area and the diameter of the tubes that will minimise the occurrence of the bed mound formation, it was possible to design the exchanger presented in Fig. 5 and Fig. 6. The described semi-industrial system was developed based on the SINTEF laboratory-scale stand located in Norway. The research system was made as a vertical column with the cooling, heating and adsorption section where the sorbent is fed by pneumatic conveyors (Fig. 1). In the target system, tube exchangers are used in a staggered configuration (Fig. 2), and the sorbent is transported by inclined belt conveyors. Such a solution is cheaper and does not require a big height of the room where it is located. Moreover, the designed exchangers have a module structure, which means that in the event of failure, a single module can be replaced without the need to replace the entire unit. The adopted assumptions made it possible to develop a compact design on a triangular plan, which minimised the system height. The system has three sections: the adsorption, heating and cooling section. The adsorbent with the inlet temperature of 30°C gets into the adsorption section and captures CO<sub>2</sub> from the combustion gases. From the adsorption section, it gets into the heating section, where it is heated to the temperature of 180°C. When this temperature is reached, CO<sub>2</sub> is released from the combustion gases and removed from the system through a connecting pipe. The adsorbent heating is realised in the developed exchangers, where the heating medium is saturated steam with the temperature of ~200°C. After CO<sub>2</sub> is released, the adsorbent gets to the cooling section, where the temperature is lowered to 30°C using cooling water supplied to the exchanger. At the same time, the water in the system is heated to the temperature of ~130°C and returned to the boiler cycle for regenerative heating of feed water. This is a procedure that will make it possible to reduce the method energy intensity to an expected value of less than 2.7 MJ/kg CO<sub>2</sub>. The study was carried out according to [13] in gProms software, where the operation of the test stand was modelled. Data related to the flow velocity of the granule in the exchangers are presented in [13] for different operating conditions. The velocity value used in the calculations in the gProms programme determined for the granule transfer through the Mellapak was 5.7 mm/s.

During the development of the test stand, some limitations and challenges were diagnosed and worth considering. The main limitation of the installation is its size and dimensions. The test stand presented in this paper was designed for flue gas volume fluxes of several tens of m<sup>3</sup>/h. These fluxes under actual power plant operating conditions are much higher, which implies a correspondingly larger CO<sub>2</sub> installation. A solution to the problem may be to install all sections of the test stand vertically (but this will require an enclosed room or a specially placed high container).

Challenges may include designing an efficient sorbent transport. A good solution seems to be (compared with the one proposed in the paper) pneumatic transport. However, due to the internal heat recovery, this transport can generate high heat loss due to the low temperature of the air transporting the adsorbent. It

is also a challenge to minimise the loss of activated carbon through the use of suitable seals. This is related to its granularity (0.7 mm diameter) and any kind of leakage in the transport system which causes its loss.

Another challenge is to maximise the heat available after the adsorbent has cooled from about 180 °C to about 30 C. Under actual power plant operating conditions, there will be large amounts of this heat. It is planned to turn this heat back to regenerate the boiler feed water temperature.



Fig. 5. Fragment of the cooling section



Fig. 6. Cooling section exchangers

### 3. SUMMARY

This paper presents a CO<sub>2</sub> capture system using activated carbon with sections designed to exchange heat with exchangers ensuring high thermal efficiency.

The design work on the heat exchanger was focused on ensuring a high coefficient of the heat transfer from the side of the working mediums, i.e. the adsorbent, water and steam, minimising at the same time the phenomenon of the formation of granulate mounds over the tubes.

It is assumed that it will be possible to achieve the low energy intensity method of less than 2.7 MJ/kg CO<sub>2</sub> utilising hot water from the cooling section.

The designed test stand is now being built in a Polish power plant. The first tests of the stand are planned in the near future, together with the testing of the efficiency of CO<sub>2</sub> capture from pulverised hard coal combustion gases. In the future, the performance, cost and scalability of the developed system will be investigated and compared with current CO<sub>2</sub> capture technologies.

## REFERENCES

1. Global Energy Review: CO<sub>2</sub> Emissions in 2021 Global emissions rebound sharply to highest ever level. 2021.
2. Gibbins J, Chalmers H. Carbon capture and storage. *Energy Policy*. 2008;36(12):4317–22. Available from: <http://dx.doi.org/10.1016/j.enpol.2008.09.058>
3. De Coninck H, Stephens JC, Metz B. Global learning on carbon capture and storage: A call for strong international cooperation on CCS demonstration. *Energy Policy*. 2009;37(6):2161–5. Available from: <http://dx.doi.org/10.1016/j.enpol.2009.01.020>
4. Zhao L, Zhao R, Deng S, Tan Y, Liu Y. Integrating solar Organic Rankine Cycle into a coal-fired power plant with amine-based chemical absorption for CO<sub>2</sub> capture. *Int J Greenhouse Gas Control*. 2014;31:77–86. Available from: <http://dx.doi.org/10.1016/j.ijggc.2014.09.025>
5. Jiang L, Wang RQ, Gonzalez-Diaz A, Smallbone A, Lamidi RO, Roskilly AP. Comparative analysis on temperature swing adsorption cycle for carbon capture by using internal heat/mass recovery. *Appl Therm Eng*. 2020;169(114973):114973. Available from: <http://dx.doi.org/10.1016/j.aplthermaleng.2020.114973>
6. Mondal MK, Balsora HK, Varshney P. Progress and trends in CO<sub>2</sub> capture/separation technologies: A review. *Energy (Oxf)*. 2012;46(1):431–41. Available from: <http://dx.doi.org/10.1016/j.energy.2012.08.006>
7. Zhao R, Deng S, Liu Y, Zhao Q, He J, Zhao L. Carbon pump: Fundamental theory and applications. *Energy (Oxf)*. 2017;119:1131–43. Available from: <http://dx.doi.org/10.1016/j.energy.2016.11.076>
8. Lian Y, Deng S, Li S, Guo Z, Zhao L, Yuan X. Numerical analysis on CO<sub>2</sub> capture process of temperature swing adsorption (TSA): Optimization of reactor geometry. *Int J Greenhouse Gas Control*. 2019;85:187–98. Available from: <http://dx.doi.org/10.1016/j.ijggc.2019.03.029>
9. He J, Deng S, Zhao L, Zhao R, Li S. A numerical analysis on energy-efficiency performance of temperature swing adsorption for CO<sub>2</sub> capture. *Energy Procedia*. 2017;142:3200–7. Available from: <http://dx.doi.org/10.1016/j.egypro.2017.12.490>
10. Wang YN, Pfotenhauer JM, Zhi XQ, Qiu LM, Li JF. Transient model of carbon dioxide desublimation from nitrogen-carbon dioxide gas mixture. *Int J Heat Mass Transf*. 2018;127:339–47. Available from: <http://dx.doi.org/10.1016/j.ijheatmasstransfer.2018.07.068>
11. Lee S-Y, Park S-J. A review on solid adsorbents for carbon dioxide capture. *J Ind Eng Chem*. 2015;23:1–11. Available from: <http://dx.doi.org/10.1016/j.jiec.2014.09.001>
12. Younas M, Sohail M, Leong LK, Bashir MJK, Sumathi S. Feasibility of CO<sub>2</sub> adsorption by solid adsorbents: a review on low-temperature systems. *Int J Environ Sci Technol (Tehran)*. 2016;13(7):1839–60. Available from: <http://dx.doi.org/10.1007/s13762-016-1008-1>
13. Mondino G, Grande CA, Blom R, Nord LO. Evaluation of MBTSA technology for CO<sub>2</sub> capture from waste-to-energy plants. *Int J Greenhouse Gas Control*. 2022;118(103685):103685. Available from: <http://dx.doi.org/10.1016/j.ijggc.2022.103685>
14. Kadambi JR. Principles of gas-solid flows by L.-S. Fan and C. Zhu, Cambridge University Press, 1998; p. 557. *Int J Multiph Flow*. 2001;27(5):947–8. Available from: [http://dx.doi.org/10.1016/s0301-9322\(00\)00072-0](http://dx.doi.org/10.1016/s0301-9322(00)00072-0)
15. Wang J, Yuan X, Deng S, Zeng X, Yu Z, Li S, et al. Waste polyethylene terephthalate (PET) plastics-derived activated carbon for CO<sub>2</sub> capture: a route to a closed carbon loop. *Green Chem*. 2020;22(20):6836–45. Available from: <http://dx.doi.org/10.1039/d0gc01613f>
16. Bahremand H, Bahrami M. An analytical design tool for sorber bed heat exchangers of sorption cooling systems. *Int J Refrig*. 2019;100:368–79. Available from: <http://dx.doi.org/10.1016/j.ijrefrig.2019.02.003>
17. Golparvar B, Niazmand H, Sharafian A, Ahmadian Hosseini A. Optimum fin spacing of finned tube adsorber bed heat exchangers in an exhaust gas-driven adsorption cooling system. *Appl Energy*. 2018;232:504–16. Available from: <http://dx.doi.org/10.1016/j.apenergy.2018.10.002>
18. Zhang LZ. A three-dimensional non-equilibrium model for an intermittent adsorption cooling system. *Sol Energy*. 2000;69(1):27–35. Available from: [http://dx.doi.org/10.1016/s0038-092x\(00\)0010-4](http://dx.doi.org/10.1016/s0038-092x(00)0010-4)
19. Clausse M, Bonjour J, Meunier F. Adsorption of gas mixtures in TSA adsorbers under various heat removal conditions. *Chem Eng Sci*. 2004;59(17):3657–70. Available from: <http://dx.doi.org/10.1016/j.ces.2004.05.027>
20. Hofer G, Fuchs J, Schöny G, Pröll T. Heat transfer challenge and design evaluation for a multi-stage temperature swing adsorption process. *Powder Technol*. 2017;316:512–8. Available from: <http://dx.doi.org/10.1016/j.powtec.2016.12.062>
21. Pirklbauer J, Schöny G, Pröll T, Hofbauer H. Impact of stage configurations, lean-rich heat exchange and regeneration agents on the energy demand of a multistage fluidized bed TSA CO<sub>2</sub> capture process. *Int J Greenhouse Gas Control*. 2018;72:82–91. Available from: <http://dx.doi.org/10.1016/j.ijggc.2018.03.018>
22. Mondino G, Grande CA, Blom R, Nord LO. Moving bed temperature swing adsorption for CO<sub>2</sub> capture from a natural gas combined cycle power plant. *Int J Greenhouse Gas Control*. 2019;85:58–70. Available from: <http://dx.doi.org/10.1016/j.ijggc.2019.03.021>
23. Schöny G, Dietrich F, Fuchs J, Pröll T, Hofbauer H. A Multi-Stage Fluidized Bed System for Continuous CO<sub>2</sub> Capture by Means of Temperature Swing Adsorption – First Results from Bench Scale Experiments. *Powder Technology* 2007;316:519–27. Available from: <https://doi.org/10.1016/j.powtec.2016.11.066>
24. Mitra S, Muttakin M, Thu K, Saha BB. Study on the influence of adsorbent particle size and heat exchanger aspect ratio on dynamic adsorption characteristics. *Appl Therm Eng*. 2018;133:764–73. Available from: <http://dx.doi.org/10.1016/j.aplthermaleng.2018.01.015>
25. Hofer G, Schöny G, Fuchs J, Pröll T. Investigating wall-to-bed heat transfer in view of a continuous temperature swing adsorption process. *Fuel Process Technol*. 2018;169:157–69. Available from: <http://dx.doi.org/10.1016/j.fuproc.2017.09.024>
26. Sharafian A, McCague C, Bahrami M. Impact of fin spacing on temperature distribution in adsorption cooling system for vehicle A/C applications. *Int J Refrig*. 2015;51:135–43. Available from: <http://dx.doi.org/10.1016/j.ijrefrig.2014.12.003>
27. Mondino G, Grande CA, Blom R, Nord LO. Moving bed temperature swing adsorption for CO<sub>2</sub> capture from a natural gas combined cycle power plant. *SSRN Electron J*. 2019; Available from: <http://dx.doi.org/10.2139/ssrn.3366315>
28. Zima W, Grądziel G, Cebula A, Rerak M, Kozak-Jagiela E, Nord LO, et al. Mathematical Model of a Power Boiler Operation Under Rapid Load Changes, PRES'21 0484 Proceedings of the 24th Conference on Process Integration, Modelling and Optimisation for Energy Saving and Pollution Reduction. Vol. 1. Brno, CZ; 2021.
29. Mondino G, Grande CA, Blom R. Effect of gas recycling on the performance of a moving bed temperature-swing (MBTSA) process for CO<sub>2</sub> capture in a coal fired power plant context. *Energies*. 2017;10(6):745. <http://dx.doi.org/10.3390/en10060745>
30. Zhao B, Wang X, Xu Y, Liu B, Cao S, Zhao Q. Reduction of dust deposition in air-cooled condensers in thermal power plants by Ni–P-based coatings. *Clean Technol Environ Policy*. 2021;23(6):1727–36. Available from: <http://dx.doi.org/10.1007/s10098-021-02055-6>

31. Taler D. A new heat transfer correlation for transition and turbulent fluid flow in tubes. *Int J Therm Sci.* 2016;108:108–22. Available from: <http://dx.doi.org/10.1016/j.ijthermalsci.2016.04.022>
32. Filonienko GK. Friction factor for turbulent pipe flow. *Teploenergetika.* 1954;40–4.
33. Majchrzak A. Testowanie i optymalizacja stałych sorbentów do usuwania CO<sub>2</sub> ze spalin, PhD thesis. 2017.
34. Mondino G, Nord LO, Grande CA, Arstad B, Plassen M, Håkonsen S, et al. Initial operation of a continuous lab-scale MBTSA pilot using activated carbon adsorbent. *SSRN Electron J.* 2021; Available from: <http://dx.doi.org/10.2139/ssrn.3812354>

The research leading to these results has received funding from the Norway Grants 2014bon adsorbent. SSRN EI Center for Research and Development (Grant NOR/POLNORCCS/0015/20195/201

Ewa Kozak-Jagiela:  <https://orcid.org/0000-0002-8236-2392>

Monika Rerak:  <https://orcid.org/0000-0003-3580-516X>

Wiesław Zima:  <https://orcid.org/0000-0002-9424-3104>

Artur Cebula:  <https://orcid.org/0000-0002-2180-314X>

Sławomir Grądziel:  <https://orcid.org/0000-0002-9916-1597>

Giorgia Mondino:  <https://orcid.org/0000-0002-5114-2020>

Richard Blom:  <https://orcid.org/0000-0001-8675-0774>

Lars O.Nord:  <https://orcid.org/0000-0002-2734-5821>

Vidar T. Skjervold:  <https://orcid.org/0000-0003-1572-7774>



This work is licensed under the Creative Commons BY-NC-ND 4.0 license.